THE SYNTHESIS AND STUDY OF 4-AZA-ACRIDINE TYPE LIGANDS AND THEIR RU(II) COMPLEXES

A Dissertation

Presented to

the Faculty of the Department of Chemistry

University of Houston

In Partial Fulfillment

of the Requirements for the Degree

Doctor of Philosophy

By

Rubabe Haberdar

May 2013

THE SYNTHESIS AND STUDY OF 4-AZA-ACRIDINE TYPE LIGANDS AND THEIR RU(II) COMPLEXES

Rubabe Haberdar

APPROVED:

Dr. Randolph P. Thummel, Chairman

Dr. Chengzhi Cai

Dr. David M. Hoffman

Dr. Ognjen Š. Miljanić

Dr. Jiming Bao

Dean, College of Natural Sciences and Mathematics

ACKNOWLEDGEMENTS

This dissertation is the end of my journey in obtaining my PhD, which was kept on track to completion with the support and encouragement of numerous people, including my well wishers, my friends, colleagues, and professors. I would also like to thank all my instructors and teachers, who throughout my educational career have supported and encouraged me to believe in my abilities. They have directed me through various situations, allowing me to reach this accomplishment. It is a pleasant task to express my thanks to all those who contributed in many ways to the success of this study and made it an unforgettable experience for me.

Foremost, I would like to express my sincere gratitude to my advisor Prof. Randolph Thummel for the continuous support of my PhD study and research, for his patience, motivation, enthusiasm, and immense knowledge. His guidance helped me all the time in my research and writing of this dissertation. I could not have imagined having a better advisor and mentor for my PhD study.

Besides my advisor, I would like to thank the rest of my committee: Profs. Chengzhi Cai, David Hoffman, Ognjen Miljanić, and Jiming Bao for their encouragement and insightful comments.

My sincere thanks also go to Dr. Charles Anderson for assistance in interpreting NMR spectra and Dr. James Korp for assistance with X-ray structure determination and analysis.

Very special thanks to my labmates Drs. Maya El-Ojaimi, Ruifa Zong, Lars Kohler, Natt Kaveevivitchai, Richard Hammitt, Chris Dorsey, and Anna Reynal for the stimulating discussions and for all the fun we have had in the last five years. Also I thank my colleague Patrik Johansson.

Last but not the least, I would like to thank my family: my mother Umran and father Hasan for giving birth to me at the first place, my brother Mustafa, and my precious nieces Gülin, Duru, and Bennu, for supporting me throughout my life.

Six years ago, Hakan and I decided that I would enroll in the PhD program, and throughout this time I always knew this project belonged to us both. My shadow and my light, he encouraged, supported, understood, and loved me at every moment, and I am intellectually indebted to his ideas and our conversations. None of this could have happened without Hakan. This dissertation is dedicated to him and my little Raspberry.

THE SYNTHESIS AND STUDY OF 4-AZA-ACRIDINE TYPE LIGANDS AND THEIR RU(II) COMPLEXES

An Abstract of a Dissertation

Presented to

the Faculty of the Department of Chemistry

University of Houston

In Partial Fulfillment

of the Requirements for the Degree

Doctor of Philosophy

By

Rubabe Haberdar

May 2013

ABSTRACT

With increasing human population and energy consumption, it is obvious that we need to find alternative sources of energy. Of all renewable energy sources, solar power is one of the most easily exploitable. It is abundant and adaptable to a wide variety of applications that produce energy. To be able to use the sun as an energy source, an effective photosensitizer will play a critical role.

We find that polypyridine complexes of Ru(II) show excited state characteristics that are favorable for certain photoredox behavior. In this dissertation we will consider two applications of this property:

1. Use of Ru(II) polypyridine complexes as sensitizers for dye sensitized solar cells (DSSCs). The photoexcited complex can inject an electron into the conduction band of a semi-conductor as the critical step in a possible solar cell.
2. The use of the excited state properties Ru(II) polypyridine complexes to facilitate the bond breaking and bond making steps in the decomposition of water into its elements, thus accomplishing artificial photosynthesis.

The incorporation of an additional non-coordinating nitrogen into the 4-position of 2,2'-bipyridine is anticipated to lower the π^* level of the ligand, causing a red-shift of the MLCT band which might increase the light-harvesting efficiency. To this purpose, a series of alkyl substituted 4-(pyrid-2'-yl)-pyrimidines and 2-(pyrid-2'-yl)-quinoxalines and their ruthenium polypyridyl complexes were synthesized. To extend the absorption

spectrum further into the IR region [Ru(**48**)$(NCS)_3$] was synthesized as an analog to the "black dye". The operating principles of the DSSC, design, synthesis, characterization, and photophysical properties of the studied dyes are discussed in Chapter 3.

The 2,2'-polymethylene-3,3'-bi-4-azaacridines **76a-d** and [Ru(**76a-d**)(tpy)$(H_2O)]^{2+}$ and [Ru(**76a-d**)$(bpy)_2]^{2+}$ complexes were synthesized to study possible excited-state proton coupled electron transfer (PCET) reactions. An additional benzo ring fused to the 6,7-position of the 1,8-naphthyridine unit extends the π-conjugation and is expected to help stabilize an intermediate radical anion that might be formed in the excited state. The synthesis, characterization and properties of these complexes are discussed in Chapter 4.

The ruthenium complexes of [Ru(**84-85,102**)$(4\text{-pic})_2(H_2O)]^{2+}$ have been studied for water oxidation. The synthesis, characterization, properties, and catalytic activity of these complexes are discussed in Chapter 5.

Table of Contents

List of Figures

List of Tables

List of Schemes

LIST OF ACRONYMS AND ABBREVIATIONS

(NN)	Bidentate Chelate Nitrogen-containing Ligand
(NNN)	Tridentate Chelate Nitrogen-containing Ligand
binap	Binapthyridine
biq	Biquinoline
bpy	2,2'-Bipyridine
cal	Calories
CB	Conduction Band
COSY	Correlated Spectroscopy
CT	Charge Transfer
CV	Cyclic Voltammetry
dcbpy	4,4'-Dicarboxy-2,2'-bipyridine
DMF	Dimethyl Formamide
DMSO	Dimethyl Sulfoxide
DSSC	Dye Sensitized Solar Cell
EtOH	Ethanol
FTO	Fluorine-doped Tin Oxide
HOMO	Highest Occupied Molecular Orbital
IPCE	Incident Photon to Current Conversion Efficiency
IR	Infrared Spectroscopy
ITO	Tin-doped Indium Oxide
L	Ligand
LC	Ligand-centered

LUMO	Lowest Unoccupied Molecular Orbital
M	Metal
MALDI-TOF	Matrix-assisted Laser Desorption/Ionization Time-of-Flight
MC	Metal-centered
MeCN	Acetonitrile
MLCT	Metal-to-Ligand Charge Transfer
MS	Mass Spectroscopy
MW	Microwave
nap	1,8-Naphthyridine
NMR	Nuclear Magnetic Resonance
OEC	Oxygen-evolving Catalyst
ORTEP	Oak Ridge Thermal Ellipsoid Program
4-pic	4-Picoline
Phen	1,10-Phenantroline
PV	Photovoltaic
SCE	Saturated Calomel Electrode
TiO_2	Titanium Dioxide
$TBAPF_6$	Tetra-*n*-butyl Ammonium Hexafluorophosphate
tpy	2,2';6'2"-Terpyridine
UV-vis	UltraViolet-Visible Spectroscopy
VB	Valence Band
VT	Variable Temperature

1. INTRODUCTION

In 2008, energy consumption in the world was 5.33 x 10^{20} J.[1] In 2020 this energy consumption is expected to increase to 6.53 x 10^{20} J and total world energy use in the future will continue to rise as a result of population and economic growth.[1]

Over the past several decades mankind has come to a realization that we must drastically modify the ways that we create and consume energy. Our main supply to meet current energy needs comes from fossil fuels (coal, liquid fuels, and natural gas). In our fast-growing world, alternative energy sources must soon make a major contribution. To face future energy demands the solution would be to use sustainable, clean and secure energy sources including solar, wind, and biomass. Of the various renewable energy sources, by far the largest resource to support life is provided by the sun. Sunlight which strikes the earth during one minute contains enough energy (7.2 x 10^{18} J/min)[2] to supply the world's needs for one year (4.1 x 10^{20} J in 2001).[3,4] Solar energy promises to satisfy human energy demands and we can consider solar energy as the best possible renewable energy source for the future. Solar energy is abundant, free, the largest non-carbon-based energy source, and does not produce noise, harmful emissions, or polluting gases. However, it has to be converted to useful energy at reasonably low cost.

Two fundamental chemical approaches deserve consideration: the direct conversion of sunlight into electricity (photovoltaics or "solar cells") and the photochemical decomposition of water (artificial photosynthesis) to produce hydrogen as a combustible

fuel. To be able to use the sun as an energy source, an effective photosensitizer will play a critical role.

The first approach of using sun as the energy source is solar cells. Solar cells are devices that convert sunlight into electrical energy. The first solar cell had ~1% power conversion efficiency and was made by Charles Fritts in 1883.[5a] More recently, solar cell technology has made remarkable progress.[5b] Silicon-based cells show high efficiency and still dominate the commercial solar panel market. There are several limitations to these devices including high manufacturing costs, fragility, and high labor input to make the devices. To simplify manufacturing and reduce costs, a new class of solar cells has been developed.[6,7]

A very promising alternative to the silicon-based solar cell is the nanoporous dye sensitized solar cell (DSSC), introduced by O'Regan and Grätzel in 1991.[8] These cells exhibit impressive white light energy efficiencies of up to 10% while they are based on relatively inexpensive starting materials and simple printing techniques.[9] In spite of the fact that their conversion efficiency is less than the best silicon-based cells, their price/performance ratio is good enough to allow them to compete with fossil fuel electricity generation.[10]

The second approach to implement solar energy is light driven water decomposition ($2\ H_2O + h\nu \rightarrow 4H^+ + 4e^- + O_2$). Green plants have developed complex catalytic systems for the decomposition of water into its elements, and our understanding of these systems is pointing the way to the design of simpler catalysts. Four-electron water oxidation in photosynthetic organisms is achieved by an inorganic molecule bound to polypeptides of

photosystem II (PSII).[11,12] Decomposition of water into hydrogen and oxygen requires a molecular catalyst to facilitate the bond breaking and bond making steps. The half-filled highest occupied molecular orbital (HOMO) and lowest unoccupied molecular orbital (LUMO) orbitals of the catalyst's photoexcited state allow it to undergo sequential oxidation and reduction (not necessarily in that order), ultimately regenerating the original catalyst. The oxygen-evolving catalyst (OEC) of PSII is a tetranuclear manganese cluster that uses a high oxidation state of the metal to promote the conversion of metal-aquo to metal-oxo species leading to dioxygen. Synthetic analogues of this OEC have been prepared which show modest catalytic activity toward water oxidation.[13]

Polypyridine derivatives of Ru(II) are the most widely studied of all transition metal complexes. Interest in these systems stems from the well understood nature of their photophysical and electrochemical properties as well as their ease of synthesis, leading to the availability of a wide variety of substituted analogues.[14]

2. COORDINATION CHEMISTRY OF RUTHENIUM POLYPYRIDINE COMPLEXES

2.1. Introduction to Bipyridines and Terpyridines

Pyridine is an important nitrogen-containing aromatic compound and the pyridine ring is present in many natural products and synthetic molecules.[15] Pyridyl moieties are versatile building blocks for the preparation of polypyridyl ligands.[16]

Polypyridines are molecules of great importance due to their ability to form stable complexes with numerous metal-centers. The structure of these ligands strongly affects the optical and electrochemical properties of their metal complexes. The functionalization of polypyridyl ligands with different groups allows their use in a wide range of applications, which exploit a variety of photophysical, photochemical, and redox properties.

Bipyridines and terpyridines are heterocyclic aromatic molecules based on 6-membered nitrogen-containing rings, linked by single bonds between the pyridine rings. The most useful and most widely studied bipyridine is the bidentate 2,2'-bipyridine (bpy) due to its ability to form stable complexes with a wide variety of metals.[17,18]

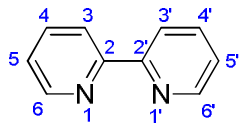

2,2'-bipyridine
(bpy)

Linking of a pyridine ring by a single bond to the 6 position of the bipyridine gives terpyridines. Specifically, 2,2':6',2''-terpyridine (tpy) is an important isomer due to its ability to act as a tridentate ligand in the formation of coordination compounds with a wide range of metal-centers.[19] This molecule contains three nitrogen atoms with the pyridyl rings attached through their *ortho*-positions.

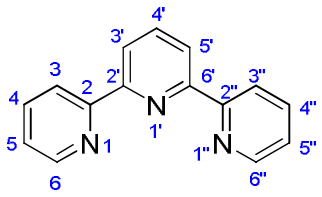

2,2':6',2''-terpyridine
(tpy)

Numerous derivatives have been prepared from the basic bipyridine and terpyridine structures by functionalization with different groups (Figure 1). Synthetic approaches to polypyridyl derivatives include both the functionalization at different positions on the aromatic rings and the incorporation of fused aromatic or aliphatic rings.

Phenanthrolines are aromatic molecules composed of three fused benzene rings with two carbons replaced by two nitrogen atoms in a peripheral position in each of the two outer rings. The most common isomer is the 1,10-phenanthroline (phen).

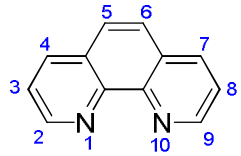

1,10-phenanthroline
(phen)

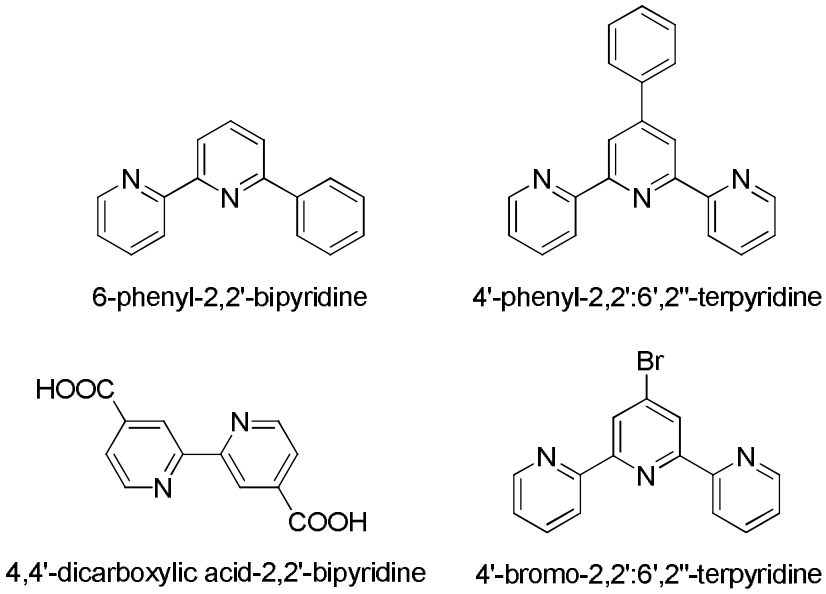

Figure 1. Polypyridyl bidentate and tridentate ligands derived from bipyridine and terpyridine units.

Pyrimidine is a heterocyclic aromatic organic compound containing two nitrogen atoms at positions 1 and 3 of the six-member pyridine ring. It is isomeric with two other forms of diazine: pyridazine with the nitrogen atoms in positions 1 and 2; and pyrazine with the nitrogen atoms in positions 1 and 4. Diazines are better π-acceptor ligands than pyridine.

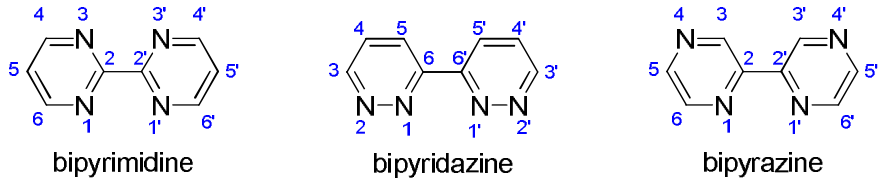

The 2- and 4-(pyridine-2-yl)pyrimidine ligands, which have both the pyridine and pyrimidine rings, are analogous to bpy in terms of the chelating site and are expected to be good ligands for the formation of ruthenium complexes.

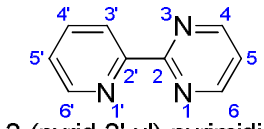

2-(pyrid-2'-yl)-pyrimidine

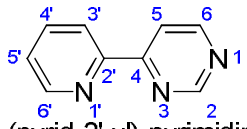

4-(pyrid-2'-yl)-pyrimidine

Selective functionalization of polypyridyl ligands with electron-donating or electron-withdrawing groups is often used to modify the redox and photophysical properties of their coordination complexes, as well as to anchor the ligands or their metal complexes to solid surfaces.[20] However, the introduction of substituents at certain positions can break the symmetry of the ligand, leading to the formation of various isomers when coordinated to metals. The different isomers of polypyridyl metal complexes can show divergent photophysical, photochemical, and electrochemical properties. Furthermore, having isomer mixtures can be a disadvantage for some applications such as biological labeling and some catalytic processes.

2.2. Coordination Chemistry

An important application of nitrogen containing aromatic heterocycles involves the formation of complexes with numerous metal-centers.[17,19,21] Polypyridyl ligands interact with the d orbitals of transition metals through both σ–donor and π–acceptor molecular orbitals located on the nitrogen atoms and the conjugated aromatic system, respectively. Furthermore, the geometry and the angle between the different nitrogen donor atoms strongly affect the nature of the bond between the pyridine-based chelating ligands and the metal-center.[16]

Bpy exists in two planar conformations: *anti* and *syn*. Theoretical calculation has revealed that the *anti* form is preferred in the solid state, but it is the *syn* form that bidentate chelating occurs. In solution or the gas phase, it is the *anti* conformation of bpy that is most stable since it avoids both the H3-H3' and N-N' repulsive interactions. However it is the less stable cisoid conformation that is required for effective coordination. The pyridyl moieties of non-coordinated 2,2'-bipyridine can rotate around the inter-ring C–C bond, reaching a minimum energy when the two pyridyl moieties are coplanar and with the nitrogens in a *anti* conformation.[22] This planar disposition is favorable due to the π-conjugation between the two rings, while the repulsive interaction between the nitrogen lone pair electrons induces a twist of 180 ^{o} to the angle between the pyridyl rings. On the other hand, this molecule adopts a *syn* planar conformation when linked in a bidentate mode to a metal-center (M), forming a stable five-membered ring (Figure 2).[22]

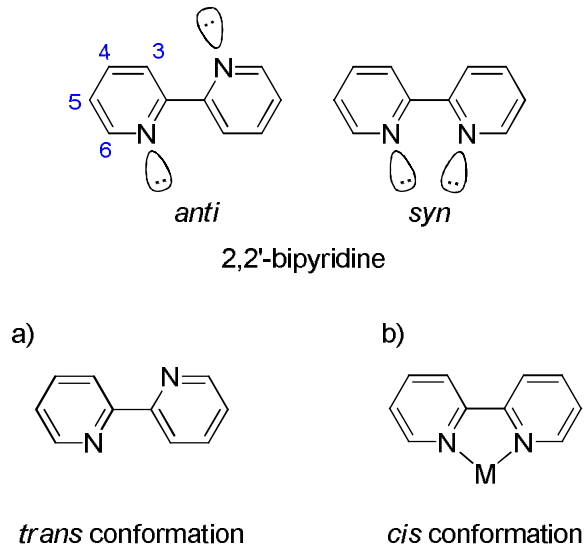

Figure 2. Molecular conformation of 2,2'-bipyridine as a) free ligand and b) coordinated to a metal-center (M).

The 2,2':6',2''-terpyridine molecule commonly acts as tridentate meridional ligand in the formation of coordination compounds with a wide range of metal-centers.[19] Moreover, the mono- and bidentate species are thought to be intermediates in the formation of the complexes. Terpyridines, in the solid state, adopt a planar conformation with the nitrogen atoms in a *trans*, *trans* relative spatial disposition to one other, in order to minimize the repulsion of the nitrogen lone pair electrons. However, when a terpyridine is coordinated to a metal-center (M) in a tridentate mode, the ligand adopts a planar *cis*,*cis* conformation, resulting in a change in the angle between the central and the terminal rings and in the bond lengths (Figure 3).[23]

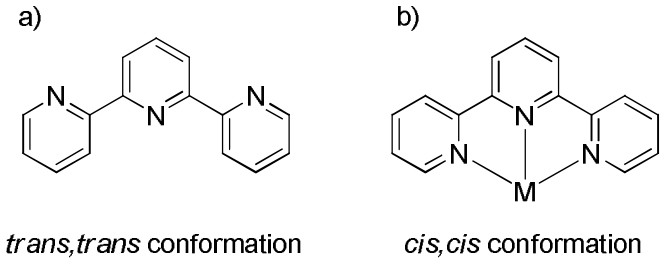

Figure 3. Molecular conformation of 2,2':6',2''-terpyridine as a) free ligand and b) coordinated to a metal-center.

Most of the phenanthrolines are solids, with a rigid structure due to the presence of the central ring. Therefore, the two nitrogen atoms are forced into a *cis* conformation allowing a faster complexation with metals.

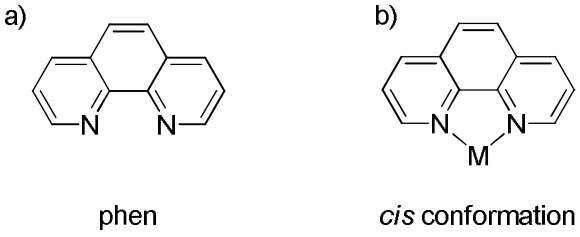

2.3. Main Characteristics and Applications

Polypyridyl ligands exhibit intense absorption bands in the ultraviolet (UV) region. The absorption spectrum is red shifted under acidic conditions, due to protonation of the nitrogen atoms.[24] The presence of low lying π^* molecular orbitals in most of the bipyridines and terpyridines allows for a non-radiative relaxation of the excited state through an intersystem crossing and/or internal conversion and, thus, the molecules are not fluorescent in organic solvents.[25,26,27] However, the introduction of substituents, such as highly extended conjugated moieties or electron donor groups can increase the luminescence quantum yield.[28]

As previously mentioned, 2,2'-bipyridines and 2,2':6',2"-terpyridines can interact through the nitrogen atoms as bi- or tridentate chelate ligands, respectively, to form five-membered rings with a large number of metals of different sizes and charges.[21] However, it must be mentioned that other isomers of this group of molecules can act as a bridge between two metal-centers or as monodentate ligands.[29] This group of nitrogen containing heterocyclic molecules contains neutral ligands that form charged complexes when coordinated to metal cation. Although this kind of ligand can stabilize a wide range of different oxidation states, the greater part of transition metal ions coordinated to nitrogen-containing heterocyclic ligands are found in the +2 or +3 oxidation states, acquiring an octahedral, tetrahedral, or square planar geometry.[19]

The optical properties of polypyridyl ligands, together with their ability to form coordination complexes with a variety of metal ions, allow their application in analytical

chemistry as fluorescent or colorimetric chemosensors,[30] supramolecular chemistry,[31] solar light-harvesting,[32] luminescence labeling of biological molecules,[33] catalysis,[34] and light-emitting devices[35]. The characteristics and main applications of ruthenium complexes are further discussed in the following section.[14a,36]

2.3.1. Solar energy conversion application

The potential of Ru polypyridyl complexes to act as photosensitizers in the conversion of solar energy into electrical energy has become an attractive subject of study.[32,37] Through appropriate molecular design, Ru polypyridyl complexes can exhibit a wide range of colors absorbing in different regions of the UV-vis spectrum, as well as having very different redox properties.

The breakthrough was achieved in 1991 with the first paper published by O'Regan and Grätzel, reporting a new type of solar cell based on the sensitization of a wide band gap mesoporous semiconductor.[38] Since then, dye sensitized solar cells have been extensively investigated.

The application of Ru polypyridyl complexes as photosensitizers is discussed in further detail in the following chapters.

2.3.2. Water splitting

The goal of artificial photosynthesis is to mimic the conversion of water and sunlight carried out by plants and other photosynthetic organisms to obtain

environmentally friendly energy sources.[39] An interesting reaction which results in the formation of carbon free fuels (H_2) is the splitting of water.

Light-induced homogeneous or partially homogeneous water splitting devices at a molecular level involve at least three essential components: (i) photosensitizer, (ii) water oxidation catalyst, and (iii) hydrogen reduction catalyst.[40] Ruthenium complexes play an important role when used as water oxidation catalysts and photosensitizers due to their ease of characterization.[41] To date, dimeric and monomeric ruthenium aqua polypyridine complexes are the most well studied and characterized oxidation catalysts due to their absorption of visible light, capacity to lose and gain electrons and protons, and their high number of stable oxidation states.[42,43,44]

2.3.3. Light-emitting devices

Organometallic complexes possessing a heavy transition metal element are strong phosphorescent emitters, making them suitable for employment in light-emitting devices.[45] These kinds of devices are very interesting for display and lighting applications.

Organic light-emitting diodes (OLEDs) are based on an emissive aromatic organic layer between two electrodes. When an electric potential is applied, the organic layer is oxidized at the anode and reduced at the cathode, and the recombination between the electrons and holes at the organic layer generates an exciton with energy similar to the difference between the HOMO and LUMO of the organic molecule.

Ruthenium complexes, such as the tris-(bidentate) $[Ru(NN)_3]^{2+}$ can be used in light-emitting devices in the form of a single emitting layer,[46,47] polymerized,[48] or incorporated into an inert solid matrix.[49] However, the emission of light is due to the recombination reaction between the oxidized $[Ru(NN)_3]^{3+}$ and the reduced $[Ru(NN)_3]^{+}$ forms of the ruthenium complex.[50]

2.4. Properties of Ruthenium (II) Complexes with Polypyridyl Ligands

Ruthenium is a d^8 transition metal. In its most common Ru(II) oxidation state it has six d-electrons (d^6) and thus requires an additional 12 electrons to complete its outer coordination sphere. This requirement can be met by coordination with six ligands each of which contributes two electrons. Having six symmetrically oriented ligands requires Ru(II) to thus have octahedral geometry with each ligand ideally oriented along an orthogonal axis.

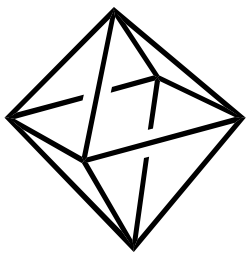

Octahedral geometry for Ru(II)

An important and useful ligand for Ru(II) is pyridine which has an unshared pair of electrons in an sp^2 orbital available for σ-bonding to the metal as well as an aromatic π-system that can participate in back-bonding to the metal d-orbitals.[51] However, pyridine does not form very robust complexes with Ru(II) and the metal-pyridine bond can easily

fragment. To overcome this deficiency two pyridine molecules can be connected through their *ortho*-positions to form the 2,2'-bipyridine molecule. If both pyridines bind to Ru(II), they are necessarily oriented *cis* to one another and thus form a chelate ring. The chelate ring lends considerable thermodynamic stability to its metal complexes.

2.4.1. Photophysical and photochemical properties of Ru (II) polypyridyls

A photochemical or photophysical process takes place when a molecule absorbs a photon of light with the proper energy and promotes an electron from the ground state to excited state. This high energy state is unstable and thus, the molecule tends to undergo some type of deactivation process. Excited state deactivation can occur by four different processes: (i) disappearance of the original molecule and formation of a new species (photochemical reaction), (ii) emission of light (luminescence), (iii) degradation of the excess energy into heat (radiationless decay or heat deactivation), and (iv) interaction with other species present in the solution (quenching process) (Figure 4).[52]

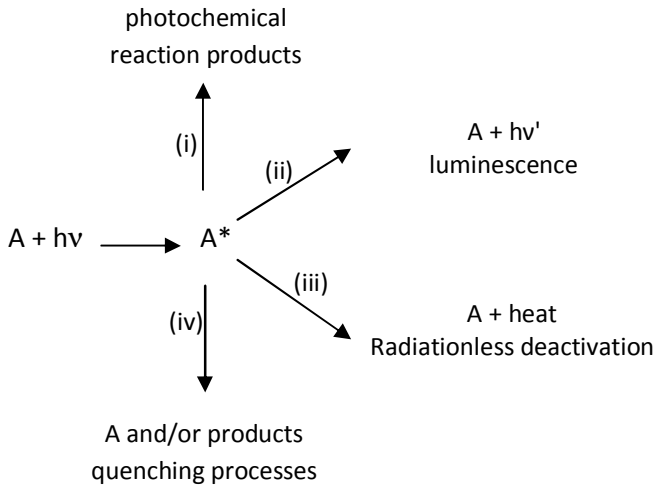

Figure 4. Schematic representation of excited state deactivation.

2.4.1.1. Absorption spectroscopy

The spectroscopic and electrochemical properties of ruthenium complexes are usually described through a simplified linear combination of atomic orbitals (Figure 5).[53] Each atomic orbital is denominated as metal (M) or ligand (L) in agreement with its prevalent localization. For example, the low-energy σ-bonding molecular orbitals, which result from the combination of metal and ligand orbitals of appropriate symmetry, are labeled L since they receive the greatest contribution from the ligand orbitals.

The molecular orbital diagram for an octahedral complex of a transition metal such as Ru(II) indicates that different transitions between the different chelating ligands and metal orbitals can take place upon the absorption of light. These transitions can be classifies as: (i) metal-centered (MC) or d-d transitions, when the electrons are promoted from a π_M metal orbital to a σ^*_M orbital, (ii) ligand-centerd (LC) or π-π* ligand to ligand transitions, for transitions that mainly localized on the chelating ligands, and (iii) transitions between molecular orbitals which causes the displacement of the electronic charge with different localization is called charge transfer (CT) and can be categorized as metal-to-ligand charge transfer (MLCT) or ligand-to-metal charge transfer (LMCT).[53]

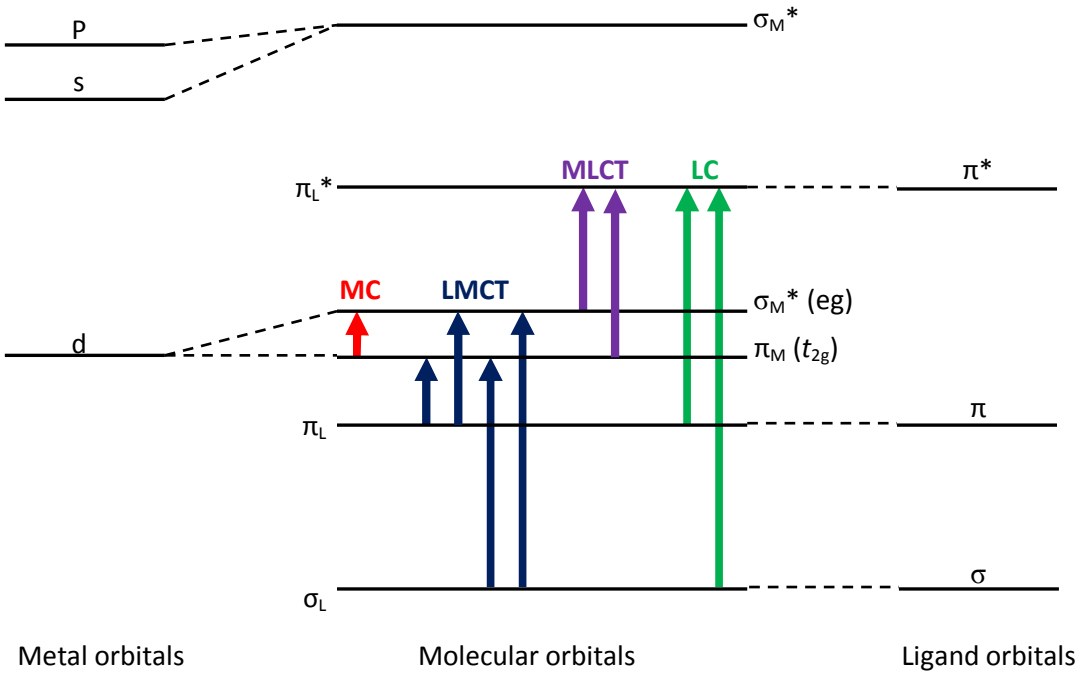

Figure 5. Simplified molecular orbital diagram for an octahedral transition metal complex. Different electronic transitions are also indicated.

The MC, MLCT, and LC transitions of an octahedral transition metal complex are related to the ligand field strength, the redox potential of the metal complex, and the intrinsic properties of the ligands, respectively.[54] For this reason, changes in the molecular structure of the ligands attached to the ruthenium metal ion can vary dramatically the relative energy positions of the excited states, with the consequent change in their photophysical properties.[55]

The absorption spectra of the $[Ru(bpy)_3]^{2+}$ complex is presented in Figure 6. The dication $[Ru(bpy)_3]^{2+}$ forms salts with a wide variety of anions and these ionic compounds, when dissolved in an appropriate solvent, absorb light in the blue region of the visible spectrum so that the complexes often appear red in color. The complete UV-

vis spectrum shows number of strong bands in the region of 220-350 nm which are associated with π-π* absorptions of the bpy ligands.[56] The lowest energy absorption is at 460 nm and represents the HOMO-LUMO transition for the complex. This transition has been assigned to a d-π* metal-to-ligand charge transfer state that defines the photochemically active form of the complex. This MLCT state is relatively long-lived and can decay through several important processes. The shoulders around 330 nm and 355 nm might be due to charge transfer or d-d metal-centered transitions.

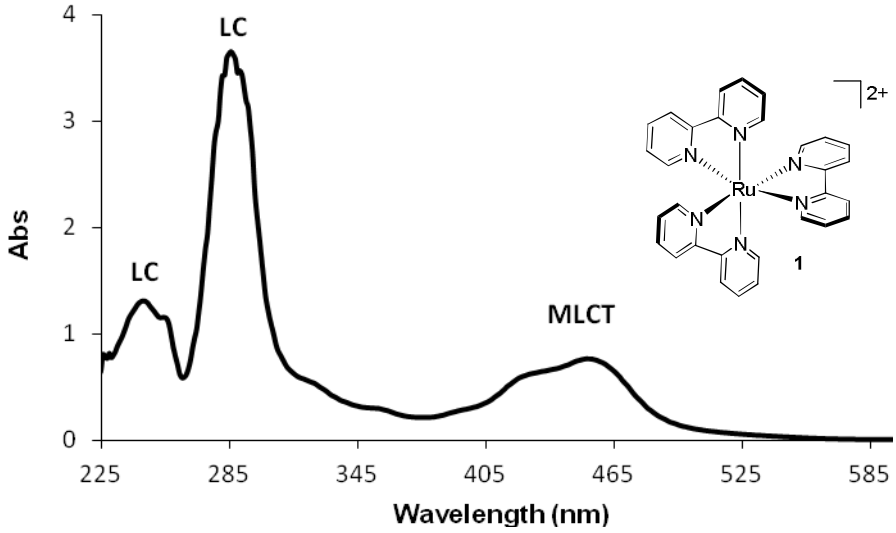

Figure 6. Electronic absorption spectrum of $[Ru(bpy)_3](PF_6)_2$ in CH_2Cl_2.

2.4.1.2. Emission spectroscopy

The behavior of excited species is usually represented in a Jablonski diagram (Figure 7). In most of the ruthenium polypyridyl complexes, three states are involved in the photochemical activation process: (i) singlet ground state, (ii) singlet excited state, and (iii) triplet excited state.

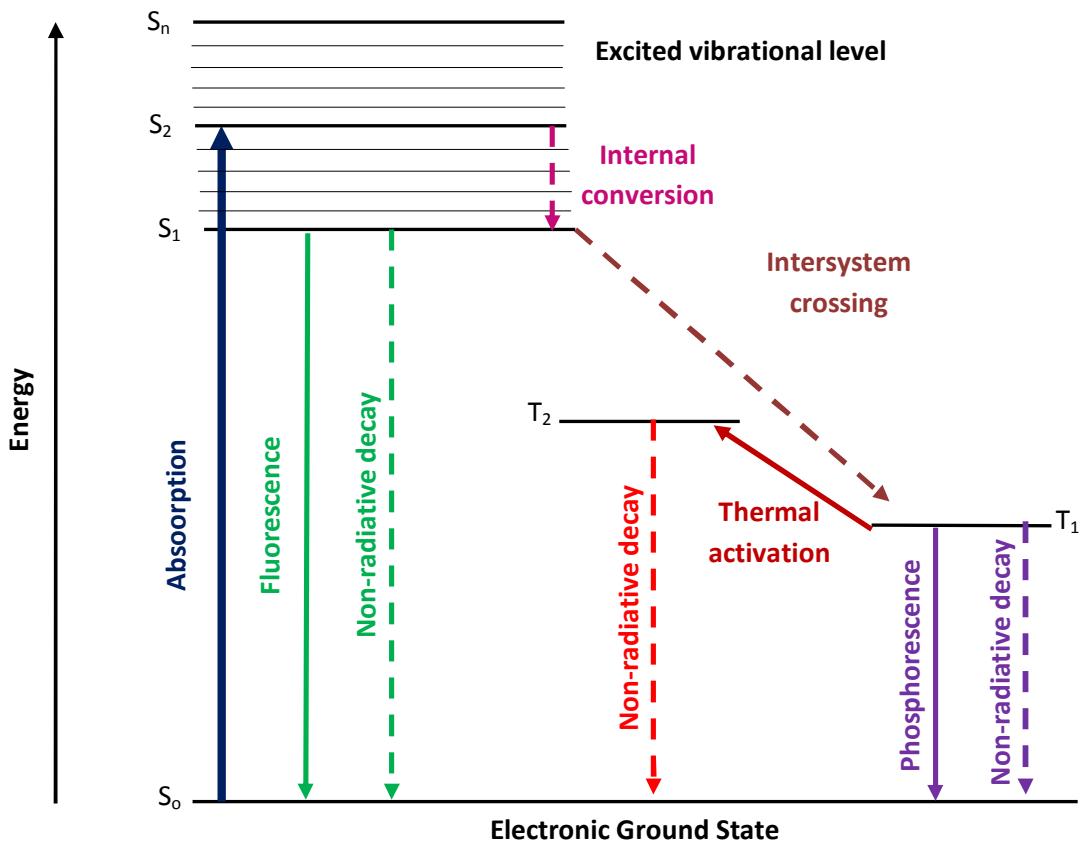

Figure 7. Jablonski diagram for ruthenium polypyridyl complexes.

The multiplicity of the ground state for most Ru(II) polypyridyl complexes is a singlet (S_o) and the absorption of a photon leads to the promotion of an electron from an occupied orbital to a higher energy unoccupied orbital with the same spin multiplicity (S_1). However, the lowest excited state is often a triplet (T_1) and, although it cannot be populated with excited electrons directly by light absorption, it can be populated through the deactivation of higher excited states. The S_1 state rapidly decays *via* intersystem crossing to the T_1 due to the strong spin-orbital coupling in metal complexes.[14a] The photo-excited state deactivation occurs through both a radiative (phosphorescence) and a non-radiative pathway.

Most ruthenium bipyridyl complexes show the lowest energy excited state as a triplet T_1, whose deactivation results in an intense long-lived luminescence. However, at higher temperatures, radiationless deactivation can take place *via* a thermally activated T_2 metal-centered excited state.

$[Ru(bpy)_3]^{2+}$ has an emission at 610 nm and long lifetime excited state for redox reaction. The emission spectra of the $[Ru(bpy)_3]^{2+}$ complex is presented in Figure 8. The excited state of $[Ru(bpy)_3]^{2+}$ may also be considered as $[Ru(bpy)_2(bpy\text{-}\cdot)]^{3+}$ with the excited electron in a π^*-orbital on the bpy and the ruthenium having lost and electron thus formally adopting a 3+ charge. As such this species is both a good electron donor and a good electron acceptor and it would be expected to participate in many useful photoredox reactions. If the excited $[Ru(bpy)_3]^{2+}$ reacts with an electron acceptor we call this electron loss oxidative quenching of the excited state and if the excited $[Ru(bpy)_3]^{2+}$ reacts with an electron donor we call this reductive quenching.

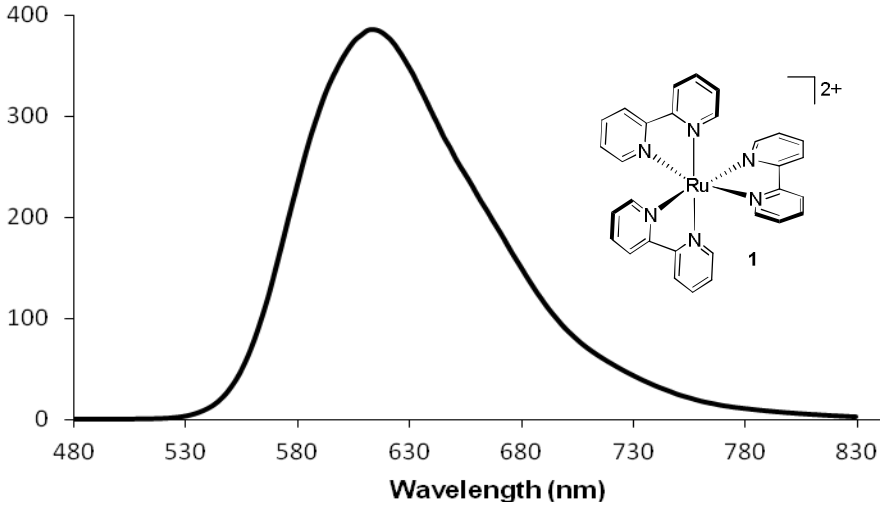

Figure 8. Emission spectrum of $[Ru(bpy)_3](Cl)_2$ in H_2O.

The behavior of ruthenium terpyridine complexes is different from their bipyridyl analogues.[57] No emission is detected at room temperature in ruthenium terpyridyl complexes due to a non-radiative relaxation of the excited state (T_1) *via* a transition by a T_2 metal-centered excited state to the ground state. However, when the temperature decreases, the transition is less efficient and some luminescence can be observed. Furthermore, the optical properties of these complexes can be modified by introduction of substituents on the ligands, allowing improvements in the luminescence quantum efficiency and/or lifetime.[58]

2.4.2. Redox properties of Ru (II) polypyridyls

One method that is used to characterize the electronic properties of Ru(II) polypyridyl complexes is cyclic voltammetry (CV).[59] CV measures the potential at which a molecule is either oxidized or reduced. For a simple two orbital model of a molecule with one filled lower energy orbital and one empty higher energy orbital, oxidation is the transfer of an electron from the lower energy filled orbital to the electrode and reduction is the transfer of an electron from the electrode to the higher energy empty orbital of the compound (Figure 9). In CV, the potential of the electrode is cycled through the region where oxidations and reductions occur for the compound in solution and the current is measured as electrons flow to or from the electrode. As the voltage of the electrode is scanned and the electrode potential exceeds energy of the empty orbital of the compound, electrons are transferred from the electrode to the species in solution. As the electrode potential becomes less than the energy of the electrons in the HOMO of the compound, electrons are transferred from the compound to the electrode. Since the electrode

potential is related to the energy of the electrons by $\Delta G = - n.F.E$ (Eq. 2.1), it is possible to determine the energy of the orbitals of a compound by measuring the oxidation and reduction potentials.

$$\Delta G = - n.F.E \qquad \text{Eq. 2.1}$$

ΔG: the Gibbs free energy
n : the number of electrons transferred
F : Faraday's constant
E : the potential

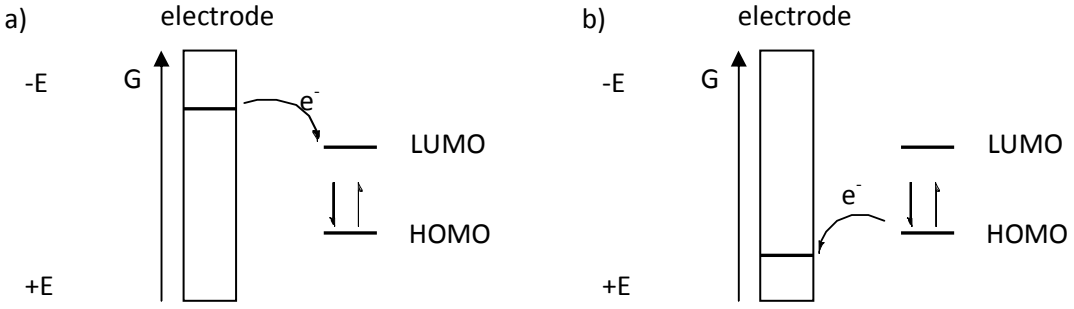

Figure 9. Electrochemical a) reduction and b) oxidation of a species at an electrode surface.

Ru(II) polypyridyl compounds are octahedral and diamagnetic complexes, with a t_{2g}^6 configuration. However, due to their high number of stable oxidation states, Ru polypyridyl complexes can serve as both an electron acceptor and electron donor.[60]

The oxidation of a d^6 Ru^{2+} polypyridyl complex involves removal of an electron from the HOMO, usually a π_M (t_{2g}) metal-centered orbital, with the formation of paramagnetic low spin d^5 Ru^{2+} complexes, which are inert to ligand substitution (Eq. 2.2).

$$[Ru^{II}(NN)_3]^{2+} \rightarrow [Ru^{II}(NN)_3]^{3+} + e^- \qquad \text{Eq. 2.2}$$

On the other hand, the reduction of a Ru^{II} polypyridyl complex may involve the introduction of one electron into the lowest unoccupied molecular orbital (LUMO), located either on a metal-centered orbital (σ^*_M) or on a ligand-centered orbital (π^*_L), depending on their relative energy level arrangement. Generally, polypyridine ligands coordinated to ruthenium ions are easily reduced, and the reduction takes place on the ligand (Eq. 2.3). In this case, ruthenium ions maintain their d^6 low spin configuration. These species are usually inert and the reduction reaction is reversible. However, when the lowest energy empty orbital is a metal-centered orbital, the electron is added to the metal-centered orbital. The reduction of these complexes produces an unstable low spin d^7 electronic configuration which leads to a rapid ligand dissociation, which makes the reaction irreversible (Eq. 2.4).

$$[Ru^{II}(NN)_3]^{2+} + e^- \rightarrow [Ru^{II}(NN)_2(NN)^-]^{2+} \qquad \text{Eq. 2.3}$$

$$[Ru^{II}(NN)_3]^{2+} + e^- \rightarrow [Ru^{I}(NN)_3]^{+} \rightarrow [Ru^{I}(NN)_2]^{+} + NN \qquad \text{Eq. 2.4}$$

The electrochemical behavior of polypyridyl ruthenium complexes depends on the nature of the ligands surrounding the metal ion. The redox potentials of a metal couple can be predicted by using the ligand electrochemical parameters (E_L) described by Lever in 1990.[61] E_L is a function of the σ and π donor and acceptor properties of the ligand and is independent of the metal to which the ligand is bound.[62]

2.4.3. Spectral tuning in polypyridyl Ru(II) complexes

To illustrate tuning of MLCT transitions in a Ru(II) polypyridyl complex, let us consider *tris*-4,4'-dicarboxy-2,2'-bipyridine (**2**). This complex shows a strong absorption

band in the visible region at 464 nm, due to CT transition from metal t_{2g} (HOMO) to π* (LUMO) of the ligand. The oxidation potential of $Ru^{2+/3+}$ is 1.3 V, and the ligand-based reduction potential is -1.5 V vs. SCE. The energy gap between the metal t_{2g} orbital and π* orbital can be reduced either by raising the energy level of t_{2g} or by decreasing the energy level of the π* orbital with donor or acceptor ligands, respectively.

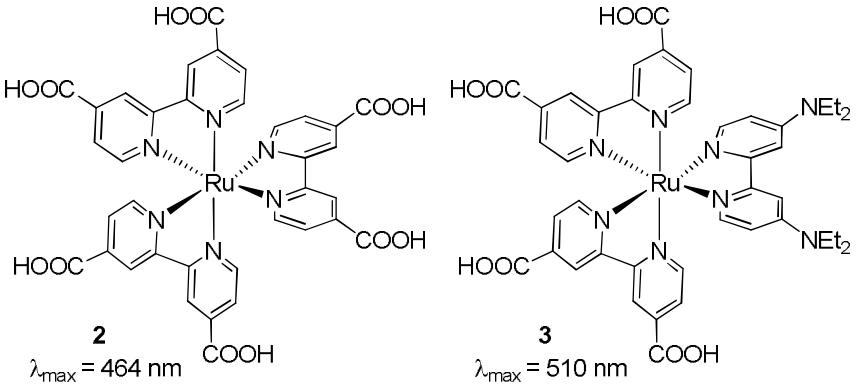

The MLCT transition energy of complex **2** can be lowered so that it absorbs more in the red region of visible spectrum by substituting one of the bidentate ligands with a donor ligand. The remaining two electron withdrawing bidentate ligands act as acceptor ligands. In this way, the absorption maxima of the complexes **2-5**, is tuned from 446 nm

to 560 nm by introducing a different donor ligand.[55] The oxidation potential in these complexes is tuned from 1.3 V to 0.3 V vs. SCE, on going from **2** to **5**. Thus the energy of the HOMO is varied over a range of 1 ev in this series.[55]

The spectral properties of the Ru polypyridyl complexes can also be tuned by introducing a nonchromophoric donor ligand such as NCS, which destabilizes the metal t_{2g} orbitals. A comparison of the visible absorption spectra of complexes **6**, **4**, **7**, and **8**, where the number of nonchromophoric ligands is varied from one to three, shows that the most intense MLCT transition maxima are at 500, 525, 570, and 620 nm, respectively. The 70 nm red shift in complex **7** compared to complex **6** is due to an increasing in the energy of the metal t_{2g} orbitals caused by the additional NCS ligands. Complex **8** compared to complex **7** reflects a decrease in the LUMO energy level, due to the incorporation of electron withdrawing carboxylic acid groups at the 4,4',4''-positions of the 2,2':6',2''-terpyridine as compared to the unsubstituted terpyridine.[63,64,65]

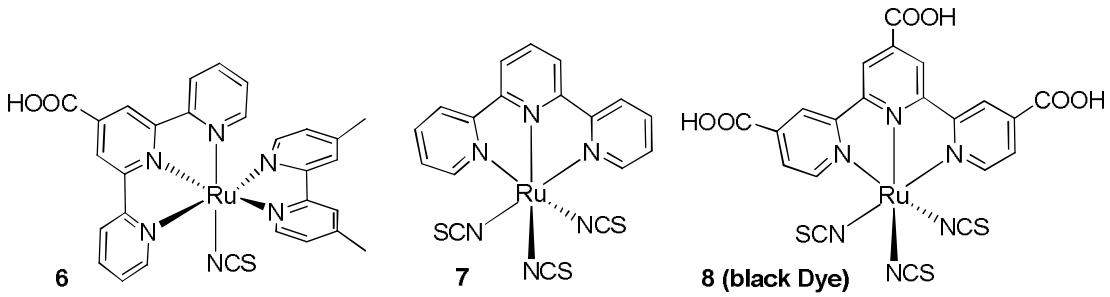

6 λ_{max} = 500 nm

7 λ_{max} = 570 nm

8 (black Dye) λ_{max} = 620 nm

3. SOLAR CELLS

3.1. Introduction

Fossil fuels such as oil, natural gas, and coal have a limited lifetime as our major source of energy and alternatives will have to make a major contribution in the near future. The sun as the source of solar energy is vital to all life on Earth. Solar cells are devices that convert sunlight into electricity. Solar cells are of particular interest because they have many advantages over presently used methods of electrical power generation.

Currently, only 0.05% of the world's energy is produced directly from sunlight.[66] This fact brings us to the question, "Why are we not using the sun to power the planet?" The answer to this question is cost. Solar energy is more expensive than conventional sources of energy. In 2007, in California, the cost of electricity produced by coal was 0.074-0.088 cents per kilowatt hour, and the cost of solar electricity was 0.116-0.312 cents per kilowatt hour.[67] The high cost of solar electricity explains why 80-90% of the world's energy comes from fossil fuels.[68] In order to overcome the high costs, solar cells must either be made from cheaper materials, or become more efficient.

Sunlight consists of visible light, infrared (IR), and ultraviolet (UV). Solar emission has a maximum at 500 nm and extends into the IR and the UV regions of the electromagnetic spectrum. UV light is partly filtered by ozone, while water and CO_2 absorb mainly in the IR causing dips in the solar spectrum at ~900, 1100 and 1400 nm. The solar radiation spectrum at the earth's surface is shown in Figure 10.[69] The region between 400 and 1100 has the highest photon density in the air mass 1.5 (AM 1.5) solar

spectrum. A material that can absorb sunlight between 400 and 1000 nm would be the ideal absorber.

The direct conversion of light into electricity using semiconductors is called the photovoltaic (PV) effect. The PV effect was first observed by Becquerel in 1839,[70] who found a light-dependent voltage between electrodes immersed in an electrolyte. The PV concept has provided a new source for alternative energy generation. Apart from the abundance of potentially exploitable solar energy, PV cells or solar cells also have other competitive advantages such as little need for maintenance, off-grid operation, and silence.

In order to be as efficient as possible a solar cell must be able to use the solar spectrum over a wide absorption range (Figure 10). The amount of the energy that reaches from sun to the surface of earth every hour (4.3×10^{20} J/h) is greater than the total amount of energy used (4.1×10^{20} J/year) in 2001.[3,71] Some solar powered systems generate heat energy while others convert light into electricity. Therefore, if we could utilize a fraction of the solar energy reaching the Earth, we could possibly solve the energy supply and environmental problems associated with our reliance on fossil fuels.[71]

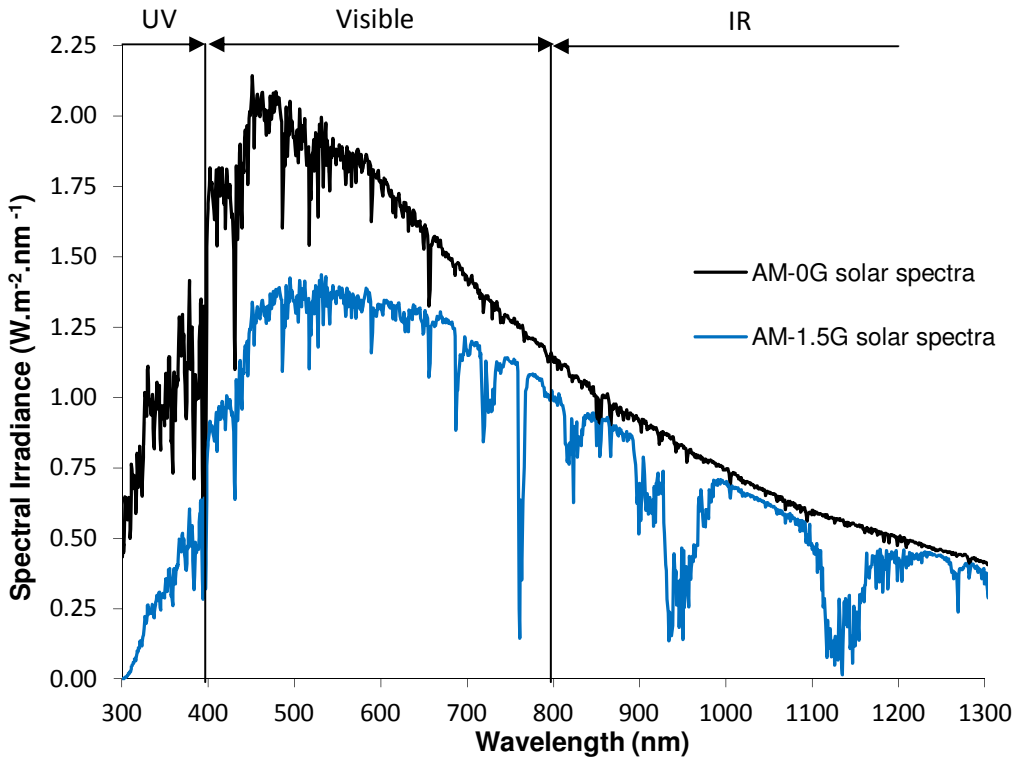

Figure 10. Spectral irradiance of the Sun on Earth: AM 1.5 (blue) and AM 0 (black). AM is the shortest path length from the sun through the atmosphere to the earth.

Solar cells are expensive because they are constructed from extremely pure silicon (Si). Solar cells based on silicon are known as *first generation solar cells*. Silicon is very abundant, making up ~26% of the earth's crust by mass. Even though silicon is very abundant, a significant amount of refining is required to obtain solar cell grade silicon. To be effectively used in solar cells silicon needs to be pure to parts per billion (ppb). To produce mono-crystalline, raw silicon must be refined to metallurgical grade silicon, then refined to semiconductor grade silicon, and further refined to create a large single crystal of silicon. Each process requires heating to 1000-1900 ^{o}C. Finally, the purified silicon ingots are cut into wafers and polished which destroys approximately 50% of the silicon. All these processes increase the cost of silicon solar cells.

Today the photovoltaic market is dominated by silicon in its multi-crystalline and mono-crystalline form. Current silicon research is concentrated on thin-film crystalline silicon, which avoids the costly crystal growing and sawing processes. The problems arising for this material are maintaining adequate light absorption, good crystal quality, and purity of the films.

Other inorganic materials used for PV devices belong to the group of chalcogenides such as copper indium diselenide ($CuInSe_2$) and cadmium telluride (CdTe). The interest has expanded from $CuInSe_2$ to $CuGaSe_2$, $CuInS_2$, and their alloys $Cu(In,Ga)(S,Se)_2$. All these materials belong to the so called *second generation solar cell*. Laboratory efficiencies for small area devices approach 19% and large area modules have reached 12%. CdTe solar cells, which show only slightly lower efficiency, also offer great promise.

In the 1990s a new concept was introduced. The *third generation solar cell* includes dye sensitized solar cells (DSSCs), polymeric solar cells, and nanocrystalline solar cells. These cells are different from classical *p-n* junction cells since they consist of bulk junctions where charge separation takes place. This approach offers an alternative for low-cost solar cells.

3.2. *P-n* Junction

The conversion of light into electricity in a photovoltaic device relies on the formation of free electrons (e^-) and holes (h^+) upon light absorption. In a bulk crystalline semiconductor, the HOMO and LUMO of constituent atoms or molecules converge into

valence and conduction band (VB and CB). The Fermi level, E_F, is defined as the energy, at a given temperature, for which the probability of being occupied by an electron is 50%. Due to the low number of electrons in CB, the conductivity is limited. However, conductivity can be increased by doping, for example silicon doped with boron and silicon doped with phosphorus. The former is called *p*-type silicon, due to boron's valency of three, which is one electron less than that of silicon and thus results in electron depletion (positive "holes") in silicon's valence band. Analogously, the latter is called *n*-type silicon, due to the phosphorus valency of five, which results in excess electrons in silicon's conduction band. When these blocks are brought into physical contact, the "extra" electrons in the *n*-type silicon flow to fill the "holes" in the *p*-type silicon, thus leaving behind ionized dopant atoms, as well as creating those in the *p*-side, when boron's valency of three exceeds by one. These ionized dopants then create the internal electric field that creates a so-called depletion region around the *p*-*n* junction. When an electron-hole pair is generated in this region, the internal electric field sweeps the charge carriers on the opposite sides of the junction, thus preventing recombination. To extract electricity out of the system, the electrons and holes must be separated before recombination, after which they can be transferred to an external circuit. Illustration of the working principle of a PV cell is shown in Figure 11.

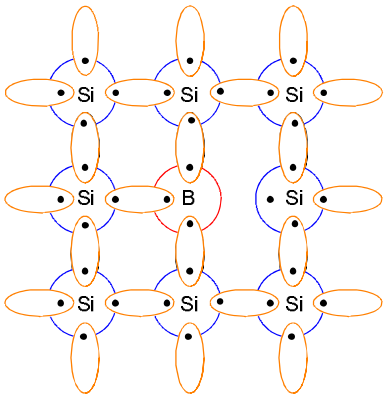

Boron: electron acceptor (*p*-type semiconductor)

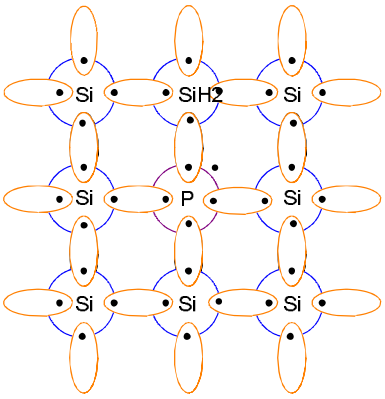

Phosphorus: electron donor (*n*-type semiconductor)

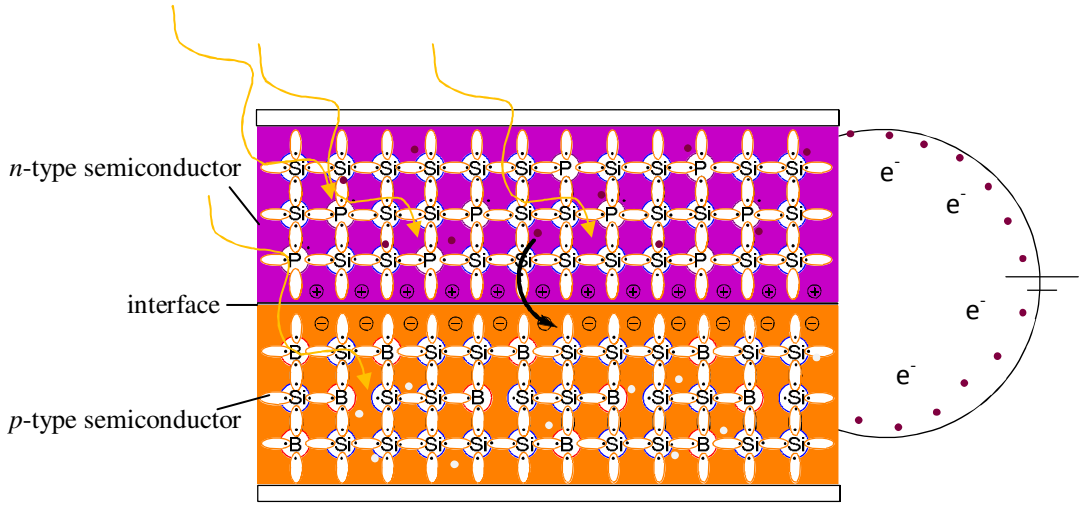

Figure 11. The operation principle of a basic photovoltaic cell.

3.3. Dye Sensitized Solar Cells

A very promising alternative to the silicon-based solar cell is the nanoporous DSSC, introduced by O'Regan and Grätzel in 1991.[8] These cells exhibit impressive energy efficiencies of up to 10% while they are based on relatively inexpensive starting materials and simple printing techniques.[9] In spite of the fact that their conversion efficiency is less than the best silicon-based cells, their price/performance ratio is good enough to allow them to compete with fossil fuel electricity generation.[10]

DSSCs are regenerative photoelectrochemical cells based on the sensitization of a nanocrystalline semiconductor containing a dye able to absorb a wide range of the solar spectrum.[72] DSSCs consist broadly of five components: (i) conductive mechanical support, (ii) semiconductor film, (iii) sensitizer, (iv) electrolyte containing the I^-/I_3^- redox couple, and (v) counter electrode with a platinum (Pt) coated catalyst.

DSSCs are based on the nanocrystalline titanium dioxide (TiO_2) semiconductor, covered by a photosensitizer dye, capable of absorbing sunlight and thus sensitizing the semiconductor. The TiO_2 coated electrode acts as the photoanode, or working electrode, and the counter electrode or photocathode is Pt coated conducting glass. To prepare the actual cell, an electrolyte solution (usually I^-/I_3^-) is sandwiched between the TiO_2 photoanode and the Pt photocathode (Figure 12).[73] The function of photosensitizer is to absorb a wide range of the solar spectrum and to inject excited state electrons into the conduction band of the semiconductor.[74] For this reason, the dye must be designed to fulfill several photophysical and electrochemical requirements.[75,76] The dye should include one or more anchoring groups, such as carboxylate or phosphonate, to graft the dye to the semiconductor surface.[37] The energy level of the excited state should be well matched with the conduction band of the semiconductor to minimize energy losses during the electron transfer. The redox potential of the dye should be sufficiently high that it can be regenerated via electron donation from the redox electrolyte.

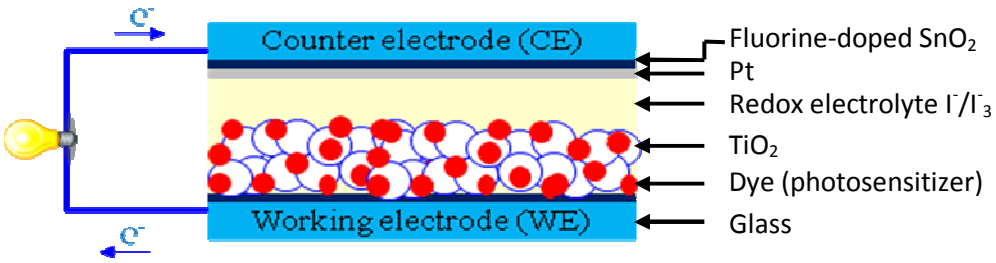

Figure 12. Schematic representation of the cross-section of a DSSC.

3.4. Operating Principles of Dye Sensitized Solar Cells

The schematic representation of the operating principle of a DSSC is shown in Figure 13. Upon absorption of light, the photosensitizer promotes an electron from its ground state to the excited state, corresponding to the metal-to-ligand charge transfer transition of the dye when Ru(II) polypyridine dyes are used (Eq. 3.1). This electron is subsequently injected into the conduction band of the semiconductor (Eq. 3.2), which arrives at the back contact and flows through an external circuit to the counter electrode. At the counter electrode, electrons are transferred to the redox pair presents in the electrolyte. The most commonly used electrolyte contains the I^-/I_3^- redox couple, and at the counter electrode triiodide is regenerated to iodide (Eq. 3.3). Finally, the cycle is completed with the regeneration of the oxidized dye by electron donation from the electrolyte (Eq. 3.4).[73]

dye photoexcitation: $S + h\nu \rightarrow S^*$ Eq. 3.1

electron injection: $S^* + TiO_2 \rightarrow S^+ + e^- – TiO_2$ Eq. 3.2

electrolyte regeneration: $I_3^- + 2e^- – Pt \rightarrow 3I^-$ Eq. 3.3

oxidized dye regeneration: $2S^+ + 3I^- \rightarrow I_3^- + 2S$ Eq. 3.4

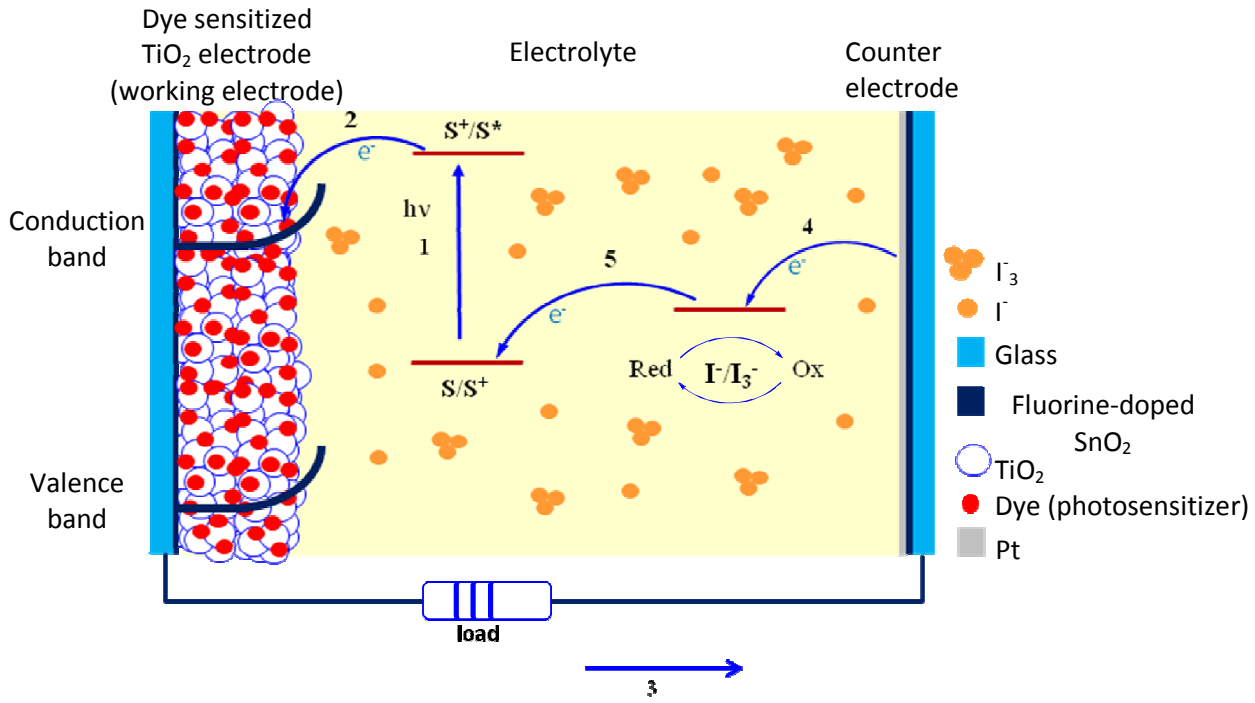

Figure 13. Schematic representation of the operating principle of a DSSC. S, S^+ and S* represent the photosensitizer (dye) in the ground, oxidized and excited states, respectively. (1) photoexcitation of the dye, (2) electron injection from the excited dye to the semiconductor, (3) external circuit, (4) regeneration of the electrolyte, and (5) regeneration of the oxidized dye.

However, this system has undesirable loss reactions, which decrease the total efficiency of the device (Figure 14). The three main loss reactions observed are (i) deactivation of the dye excited state (Eq. 3.5), (ii) recombination of photoinjected electrons in the semiconductor with the oxidized photosensitizer (Eq. 3.6), and (iii) recombination of photoinjected electrons in the semiconductor with the oxidized form of the redox mediator (Eq. 3.7). The latter recombination reaction is also called the "dark current ".

dye excited state deactivation: $S^* \rightarrow S + \text{heat/h}\nu$ Eq. 3.5

back electron transfer: $e^- - TiO_2 + S^+ \rightarrow TiO_2 + S$ Eq. 3.6

electron recombination with the redox couple: $2\ e^- - TiO_2 + I_3^- \rightarrow 2\ TiO_2 + 3I^-$ Eq. 3.7

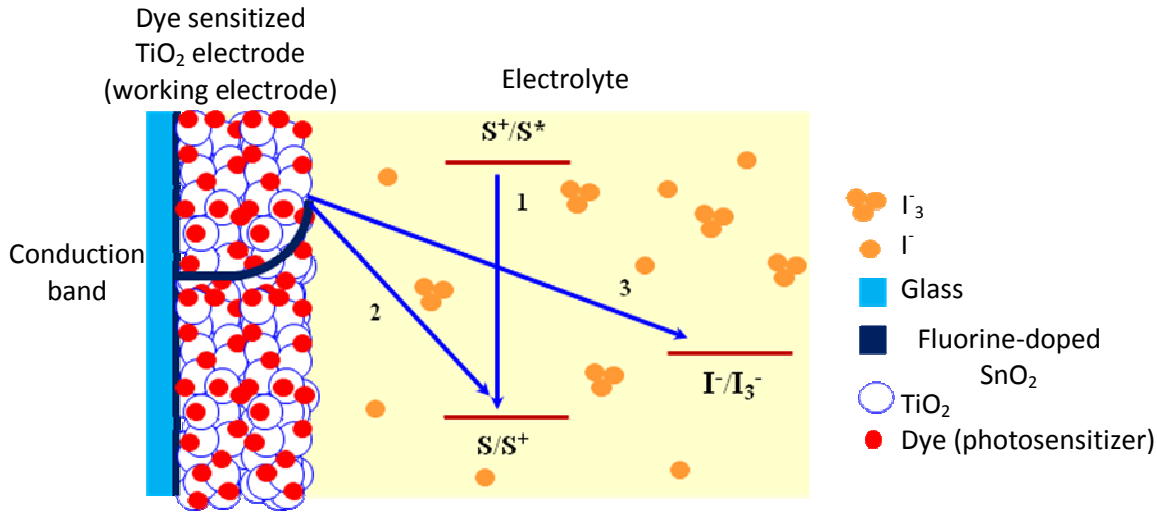

Figure 14. Scheme of the loss reactions occur in a DSSC. (1) dye excited state deactivation, (2) e^- –TiO_2/S^+ back electron transfer and (3) e^- –TiO_2/I_3^- recombination reaction.

Despite the loss processes which occur in a DSSC, the reason for the relatively high efficiencies observed in optimized devices is due to the rather favorably balanced kinetic competition which ensures forward electron transfer reactions dominate over the loss processes. For most of the dyes, the loss reactions are several orders of magnitude slower than the forward processes when the devices are working under normal operating conditions, allowing efficient charge separation to occur (Table 1).[77]

Table 1. Timescale processes in DSSC.[77]

Process	Time (s)
Injection of electron from the excited dye into the conduction band of TiO_2	$10^{-12} – 10^{-9}$
Dye regeneration by the redox electrolyte	$10^{-9} – 10^{-6}$
Electron recombination between the TiO_2 and the electrolyte	$10^{-3} – 10^{-1}$
Back electron transfer from the TiO_2 to the oxidized dye	$10^{-6} – 10^{-3}$
Excited state deactivation	$>10^{-9}$

3.5. Fundamental Constituents of DSSCs

DSSCs are devices composed of multiple components, and their overall efficiency depends on the individual properties of each constituent. A lot of effort has been spent on the optimization of the materials used in the fabrication of solar cells, such as the semiconductor metal oxide, the photosensitizer, the electrolyte, and the counter electrode.

3.5.1. Working electrode

In DSSCs, the semiconductor acts as a supporting material for dye adsorption and as an electron transport pathway. The TiO_2 nanoparticles are deposited onto a glass coated with a thin layer of a transparent conductive material. The most commonly used conductive material is fluorine-doped tin oxide (FTO). Although other metal oxides such as tin-doped indium oxide (ITO) present higher conductivities, the thermal instability of ITO strongly increases the resistance of the material when the glass is exposed high temperatures over a long period of time.

Three important processes take place at the working electrode: (i) light-harvesting, (ii) charge separation, and (iii) electron transport. Light-harvesting is performed by the chromophore or a photosensitizer dye. Charge separation occurs at the interface between the dye and the semiconductor, with electron travelling through TiO_2. Electron recombination also takes place at the interface between the surface of the semiconductor and either the dye or the electrolyte.

3.5.1.1. Band theory of solids

Basically, the band structure of a material is a description of its electronic energy levels. The electronic properties of solid materials are controlled by the nature and position of the valence and conduction bands. The band gap can be defined as the difference in energy between the VB and the CB.

For conducting materials, the two bands are overlapping and allow the free movement of electrons, while for semiconductors and insulators the two bands have different energy levels (Figure 15). Insulators have a large band gap where electrons cannot be promoted to the conduction band without applying extreme conditions. In semiconductors, electrons can be both thermally (increasing the temperature) or optically (absorption of light) excited to the conduction band, generating a hole in the valence band.[78]

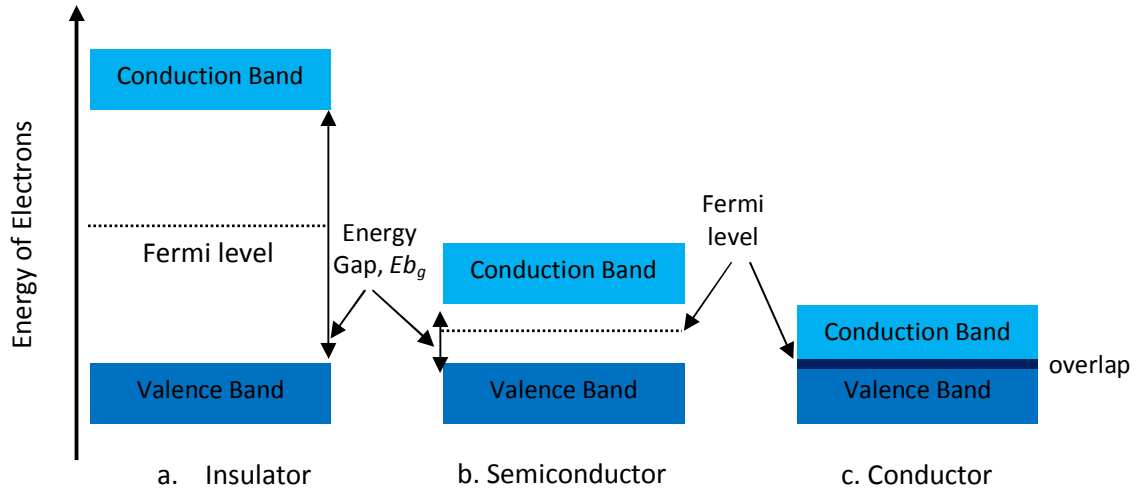

Figure 15. Energy level diagram for insulators, semiconductors, and conductors.

3.5.1.2. Characteristics of TiO_2

Among the several semiconductors such as TiO_2, ZnO, Zn_2SnO_4, SnO_2, and Nb_2O_5 that have been used for DSSCs, TiO_2 is the most common.[79,80] TiO_2 has many advantages for sensitized photochemistry and photo-electrochemistry: it is stable, cheap, abundant, non-toxic, and inert.[80] The three most common crystalline structures of TiO_2 are rutile, anatase, and brookite (Figure 16).[81] Pure brookite nanoparticles are difficult to prepare in the laboratory under mild conditions, therefore rutile and anatase are the most common crystalline forms.[80] Although rutile is the most thermodynamically stable crystalline form, anatase shows higher photocurrents in DSSCs due to its morphology, packing structure and electron transport properties. Anatase TiO_2 has a larger surface area due to smaller particle size, which allows the anchoring of larger amounts of dye and the higher conductivity between the different nanoparticles is associated with the better packing of the film.[82] The larger band gap of anatase compared to rutile prevents light absorption in the near UV-region (350-400 nm), which can cause long term degradation of the cell due to the strong oxidation effect of the formation of holes in the valence band.[83] Unless stated otherwise, TiO_2 in the anatase form is used in the entire dissertation.

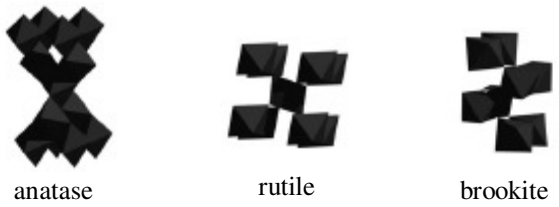

Figure 16. Structures of rutile, anatase, and brookite.

3.5.1.3. Titanium dioxide as a semiconductor in DSSCs

Semiconductors absorb light with an energy equal to the difference in energy between the valence and the conduction bands (E_{bg}, J) (Eq. 3.8), where h is plank's constant (h = 6.626 x 10^{-34} m^2.Kg.s^{-1}) and c is the light speed (c = 3 x 10^8 m.s^{-1}). For large band gap semiconductors such as TiO_2, the difference between the ground and excited state energy levels is of the order of 3 eV (rutile E_{bg} = 3.05 eV, anatase E_{bg} = 3.23 eV, brookite E_{bg} = 3.26 eV).[80] The energy needed to promote an electron from the valence to the conduction band is provided by UV light (λ < 400 nm). Therefore, in order to use sunlight as a source of energy, whose spectrum also includes visible and near IR, a dye is necessary to sensitize TiO_2 to these wavelengths, and to inject electrons into the conduction band of the semiconductor (Figure 17).

$$\lambda = \frac{h.c}{E_{bg}} \qquad \text{Eq. 3.8}$$

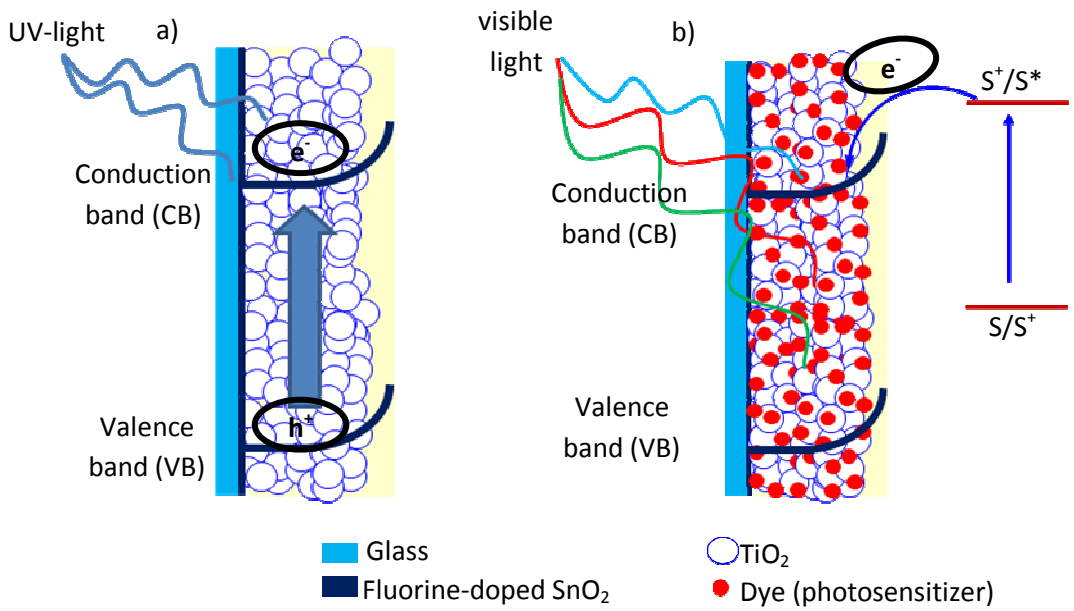

Figure 17. Schematic representation of a) the formation of an exciton in a semiconductor by the absorption of UV-light, b) electron injection into the conduction band of a semiconductor by the absorption of visible light by a photosensitizer.

The semiconductor in DSSCs is deposited in the form of mesoporous crystalline nanoparticles. The most important characteristics for an optimized TiO_2 film are the surface area,[84] porosity,[85] light scattering,[86] and electron diffusion.[87] In order to anchor as much dye as possible, the semiconductor must have a large surface area which is provided by TiO_2 nanoparticles. The size of the nanoparticles also affects the size of the pores and the light scattering properties of the nanoparticles. The porosity of the film has to be optimized in order to allow the electrolyte penetration through the film and to ensure fast dye regeneration. Furthermore, the porosity level has to be controlled in order to have enough interparticle connectivity so that electrons can diffuse through the film and reach the working electrode.

The diameter of the nanoparticles is in the range of 10-30 nm,[88] large enough to not exhibit quantum size effects. For this reason, the semiconductor film can be considered as a network composed of bulk nanocrystals.

At first glance, the properties of mesoporous nanocrystalline films would seem disadvantageous compared to their single crystal analogues because (i) the electrolyte penetrates into the pores of the semiconductor producing a huge junction contact area, increasing the probability of electron recombination, (ii) the low inherent conductivity of the film, (iii) the multiple traps present in the film decrease the electron diffusion coefficient, and (iv) the small size of the nanoparticles in contact with the electrolyte restricts the amount of electrical field.[89] However, such disadvantages are offset by the optical transparency of the nanoparticles and the enormous surface area of the films, which yields a high loading of photosensitizer, resulting in efficient light absorption.

3.5.2. Molecular sensitizer

3.5.2.1. Characteristics of molecular sensitizers

The function of the photosensitizer in a DSSC is to absorb a wide range of the solar spectrum and to inject electrons into the conduction band of the semiconductor. For this reason, the design of the dye must fulfill certain photophysical and electrochemical requirements.[75]

The absorption spectra of the sensitizers should cover a wide range of visible light including the near infrared region and possess a high molar extinction coefficient, to

maximize light absorption (Figure 10).[76] Solar radiation conditions are defined by the air mass (AM) value. Air mass zero (AM-0) corresponds to the radiation that a device receives in the absence of an atmosphere between the light source and the solar cell. However, the extraterrestrial solar spectrum is different from the sunlight spectrum that arrives at the surface of the Earth due to light scattering and absorption by H_2O, H_2, O_2, CO_2, O_3, and other species present in the atmosphere. Furthermore, the incident light falling on solar devices can be irradiated in the form of direct light, which comes straight from the sun, or in a diffuse form, which is light reflected off clouds, the ground or other objects. For this reason, AM-1.5G (global) is defined as the corrected solar spectrum, including both direct and diffuse radiation, considering the sun at an angle of 48.19^{o}. Although, the solar flux is 982 $W.m^{-2}$, it has been standardized to 1000 $W.m^{-2}$.[76]

The structure of the dye has to include one or more anchoring groups in order to bind it strongly to the surface of the semiconductor and ensure efficient electron injection. Photosensitizers can interact with the surface of metal oxides through covalent bonds, hydrogen bonding, electrostatic interactions, hydrophobic interaction, Van der Waals forces, or entrapment inside the pores.[37] However, the formation of covalent bonds between the hydroxyl groups present at the surface of the semiconductor nanoparticles and the different anchoring groups on the dyes increases (i) the amount of adsorbed dye, (ii) the stability of the cell, and (iii) the strength of the electronic coupling between the π^* molecular orbital of the dye and the orbitals of the TiO_2 semiconductor. Strong dye bonding also decreases the rate of dye desorption.[90] Many sensitizers are linked to the semiconductor surface through carboxylate groups. However, a variety of other groups

such as phosphonate,[91] boronate,[92] and other derivatives have been used. The attachment of dyes through carboxylate groups is reversible, and the sensitizers can be desorbed from the films under basic conditions. Furthermore, several binding modes of a carboxylate groups to the surface of a metal oxide are possible depending on the structure, the binding groups, the crystalline form of the metal oxide and the surface environment (Figure 18).[93,94]

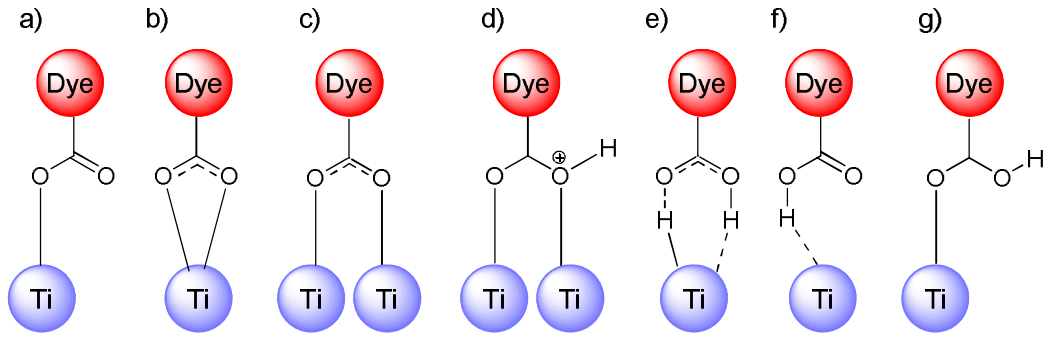

Figure 18. Possible binding modes of a carboxylic acid group to TiO_2. a) ester linkage, b) chelate binding, c and d) bidentate bridges, e and f) hydrogen bonding interactions, and g) monodentate binding through the CO.

The redox properties of the dye are also important for efficient charge separation: the LUMO energy level must be higher than the conduction band energy level of the semiconductor in order to be able to inject electrons into the TiO_2, and the HOMO must be sufficiently low to permit fast electron regeneration by the electrolyte redox couple. The HOMO–LUMO band gap should be about 1.5 eV[95] for optimum absorption of sunlight. Furthermore, the spatial orientation of the HOMO and LUMO influences not only the electron injection of the dye into the semiconductor conduction band and the photosensitizer regeneration but also the electron recombination between the photoinjected electrons in the TiO_2 and the oxidized dye.[96,97] The LUMO should be in

close contact with the semiconductor surface, while the dye cation should be separated from the electrode surface.

Another chemical aspect of photosensitizers regards their solubility in organic solvents. The dye should be soluble in a volatile solvent to permit their adsorption onto the surface of the semiconductor, but should not be desorbed by the electrolyte solution. Finally, the redox reactions involving the dyes must be reversible and the photosensitizers should be stable enough to permit many oxidation/reduction cycles without decomposition.

3.5.2.2. Types of molecular sensitizers

Many different dyes have been investigated for solar cell applications. They can be divided into three major groups: (i) transition metal containing complexes,[98] (ii) organic dyes,[99,100] and (iii) naturally occuring compounds[101].

Mononuclear and polynuclear transition metal complexes have been widely studied as photosensitizers.[102] Systematic optimization of the dye components such as the introduction of different anchoring ligands or the insertion of different chromophoric groups has been tested in dyes based on different metal ions, such as Ru(II),[103,104] Os(II),[105,106] Pt(II),[107,108] Re(I),[109] Cu(I),[110,111] and Fe(II)[112] (Figure 19).

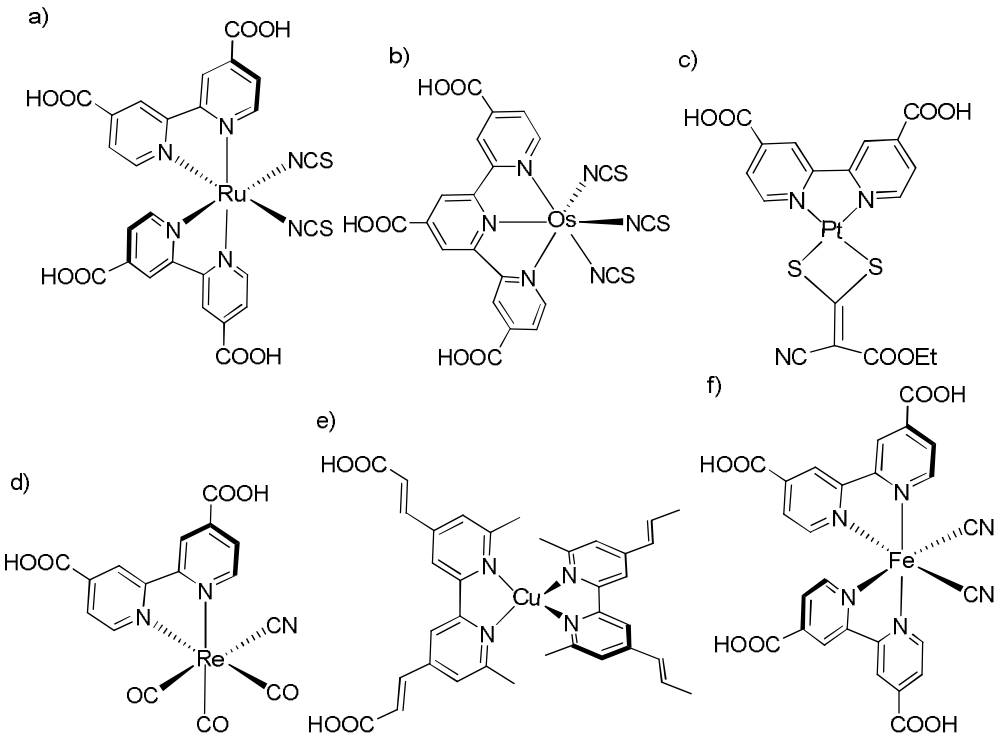

Figure 19. Molecular structures of metal based sensitizers. a) Octahedral Ru(II) complex,[113] b) Octahedral Os(II) complex,[114] c) Square planar Pt(II) complex,[107] d) Octahedral Re(I) complex,[109] e) Tetrahedral Cu(II) complex,[111] and f) Octahedral Fe(II) complex[112]

However, the most commonly used compounds in DSSCs are ruthenium complexes. The easily tunable redox and photophysical properties and the synthetic approach to these complexes, which allows the sequential introduction of different ligands, make these compounds excellent potential candidates for semiconductor sensitization.

In addition to metal complex sensitizers, a wide range of organic dyes have been explored. This kind of dye offers several advantages compared to metal containing analogues: higher molar extinction coefficients, low cost, relatively easy preparation, and purification techniques are a wide variety of different structures and chromophoric

groups. Organic dyes such as porphyrins, phthalocyanines, perylenes, squaraines, and conjugated donor-acceptor moieties have been explored (Figure 20).[99,100,115] However, the efficiencies obtained with devices prepared from organic dyes are still lower than Ru-based DSSCs. The most unfavorable characteristic of metal free dyes are their narrow absorption bands, causing poorer sunlight harvesting; their tendency to form aggregates, which prevents electron injection into the TiO_2 conduction band; and their lower stability compared to metal complexes.

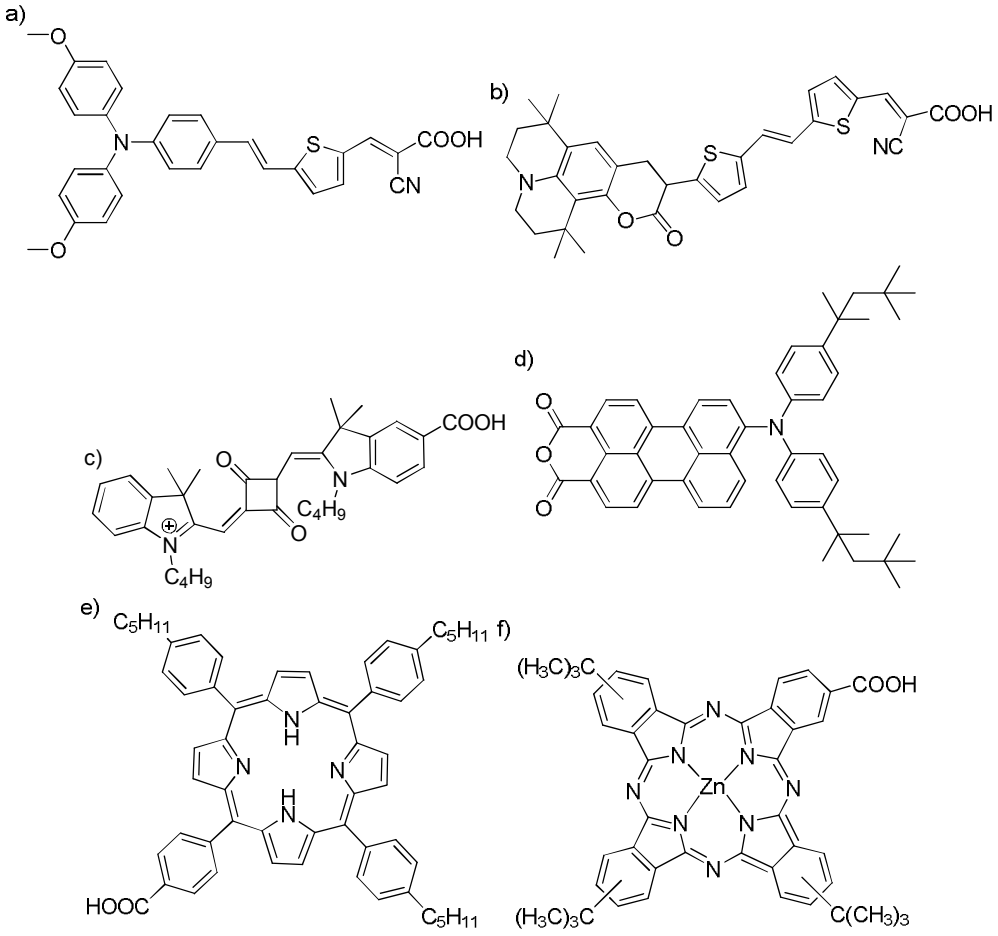

Figure 20. Molecular structures of a series of organic dyes. a) Donor-π-acceptor dye with a triphenyl amine donor moiety, [116] b) Donor-π-acceptor dye with a coumarin donor moiety, [117] c) Squaraine dye, [118] d) Perylene dye,[119] e) Porphyrin dye,[120] and f) Phthalocyanine dye[121]

Naturally occurring photosensitizers can also be used as dyes in photovoltaic devices. Naturally occurring dyes are pigments extracted from plants, flowers, and fruits that have been used for the preparation of DSSCs because of their ready availability, low cost, and environmentally friendliness. The overall efficiencies of such dyes are generally much lower than organic or metal complex sensitizers (Figure 21).[101,122,124]

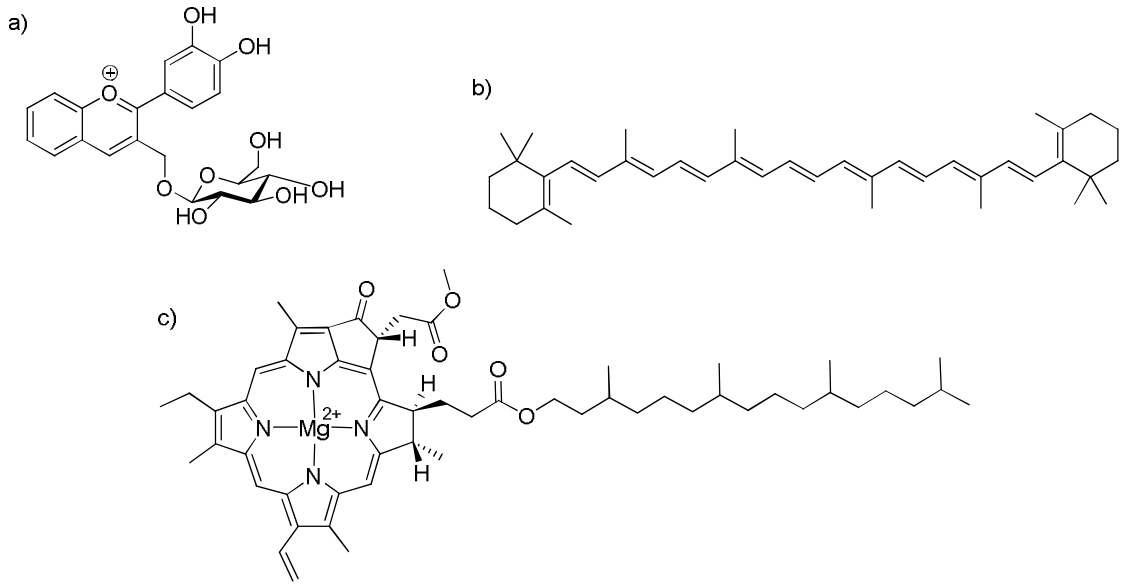

Figure 21. Molecular structures of naturally occuring dyes used in DSSCs. a) Cyanin dye,[101] b) β–carotene dye,[123] and c) Chlorophyll A dye[124]

3.5.3. Electrolyte

The electrolyte is the hole transporting material located between the surface of the semiconductor and the counter electrode. The electrolyte must have a good contact between the counter and working electrodes as well as high conductivity to permit fast charge transport between the Pt counter electrode and the oxidized dye. The electrolyte should also be thermally, optically, chemically, and electrochemically stable and have

adequate redox potentials to allow efficient dye regeneration. The electrolyte should not degrade, desorb the dye from the metal oxide surface, or absorb in the visible region of the spectra.

3.5.4. Counter electrode

The counter electrode reduces the oxidized species present in the electrolyte redox couple, or, from a different point of view, it collects the holes from the hole conducting material in a solid state DSSC. For efficient DSSCs, the counter electrode should possess low resistance and a high rate of reduction of the redox mediator present in the electrolyte.[125]

The material most widely used as the counter electrode is highly transparent FTO conductive glass coated with a thin layer of Pt. Although different deposition techniques have been tested to create the molecular catalyst, thin layer thermal deposition of a Pt thin film shows more stability and a higher triiodide reduction rate.[126]

Different materials have been used as a low cost alternative to the Pt coated counter electrode. Metal substrates such as steel or Ni have been tested. However, the I^-/I_3^- redox species present in the electrolyte is highly corrosive towards these metals. Carbon materials such as graphite or black carbon have also been tested.[127] Conducting polymers have also been used as a counter electrode, allowing the preparation of flexible devices.[128]

3.6. Quantitative Parameters for Solar Cell Performance

The performance of a DSSC can be quantified by several parameters: photocurrent and photovoltage generated by the solar cell, incident photon to current conversion efficiency (IPCE), and overall light to energy conversion efficiency.

3.6.1. Photocurrent and photovoltage

The photocurrent is the electric flux through a device under light irradiation. The maximum current flow is obtained when the cell is operated at short circuit, the external circuit is closed and the voltage is zero. The short circuit current (I_{sc}, A) increases with light intensity and is proportional to the area of the solar cell. The solar circuit current density (J_{sc}, mA.cm^{-2}) is defined as in Eq. 3.9, where I_{sc} is the short circuit photocurrent in mA and the cell area is given in cm^2.

$$J_{sc} = \frac{I_{sc}}{\text{cell area}} \qquad \text{Eq. 3.9}$$

The photovoltage is the electrical force generated upon radiation of light that can drive electrical current from one point to another one. Cell efficiency is measured under open circuit conditions, *i.e.* where the working and counter electrodes are not connected through an external circuit. Under such conditions the maximum voltage of a given cell is obtained when I_{sc}=0. In DSSCs, the open circuit voltage (V_{oc}) corresponds to the difference in energy between the Fermi level of the semiconductor under illumination and the redox potential of the mediator present in the electrode (Figure 22).[129]

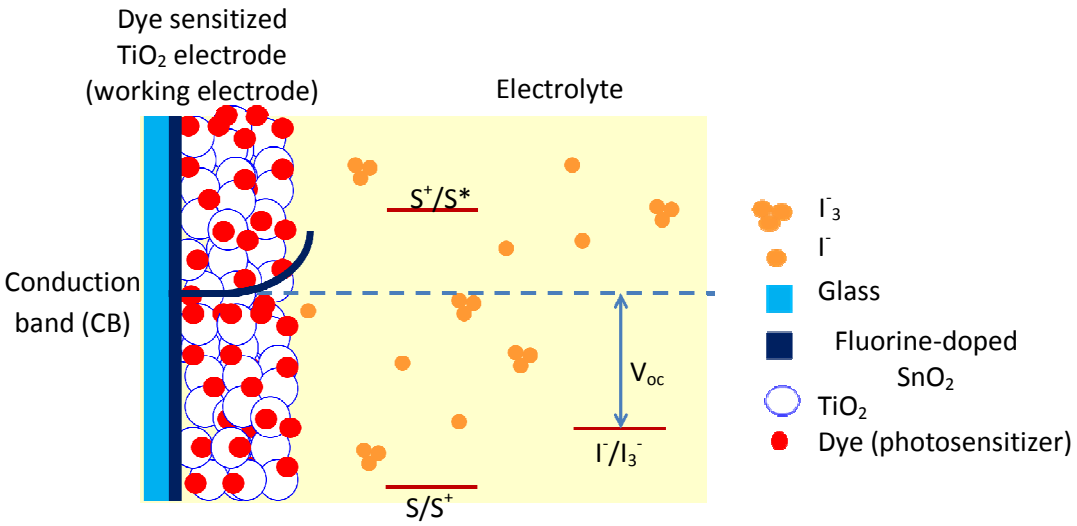

Figure 22. Energy level diagram of the working electrode and electrolyte of a DSSC.

However, the experimentally measured voltage in solar cells with most sensitizers is often different from the difference between the Fermi level and the redox potential, due to recombination process.[130] For this reason, the study of electron transfer reactions in a DSSC, particularly the recombination processes and the mechanisms which underpin these reactions are very important in the development of efficient devices. Furthermore, modifications of the semiconductor surface or changes to the electrolyte redox couple have strong effects on the V_{oc}.

3.6.2. Incident photon to current conversion efficiency

The incident photon to current conversion efficiency (IPCE, %) is used to describe the number of electrons generated by the solar cell and detected in the external circuit, as a ratio of the number incident photons which illuminate it for a given wavelength. It can be calculated from Eq. 3.10, where J_{sc} is the short circuit photocurrent

($mA.cm^{-2}$), λ is the incident light wavelength (nm), P_{lamp} is the power of the incident light ($W.m^{-2}$) and 1240 is the conversion factor for the energy of photons. The IPCE is strogly affected by (i) the light-harvesting efficiency of the dye (photosensitizer), which depends on the photophysical properties of the dye, (ii) the yield of electron injection into the conduction band of the semiconductor, which depends on both the redox potential and the injection kinetics of the excited photosensitizer, and (iii) the charge collection efficiency at the working electrode, which depends on the structure and morphology of the semiconductor film.

$$\text{IPCE} = \frac{1240 \cdot J_{sc}}{\lambda \cdot P_{lamp}} . 100 \qquad \text{Eq. 3.10}$$

3.6.3. Overall efficiency

The overall solar-to-electrical energy conversion efficiency (η_{eff}, %) of DSSC depends on the photocurrent measured at short circuit (J_{sc}, $mA.cm^{-2}$), the open circuit photovoltage (V_{oc}, V), the fill factor of the cell (FF, %) and the power of the incident light (P_{lamp}, $W.m^{-2}$). The overall efficiency can be calculated from Eq. 3.11.

$$\eta_{eff} = \frac{J_{sc} \cdot V_{oc} \cdot FF}{P_{lamp}} . 100 \qquad \text{Eq. 3.11}$$

The FF (%) is essentially a measurement indicative of the quality of a solar cell. It is obtained by dividing the maximum power density obtained by a solar cell (P_{FF}, $W.m^{-2}$) by the maximum theoretical power density (P_{max}, $W.m^{-2}$) (Eq. 3.12). The power can be obtained as the product between the current and the voltage (Eq. 3.13). The maximum

theoretical power density of a solar cell is therefore the product of V_{oc} (V) and I_{sc} (A) (Figure 23).

$$FF = \frac{P_{FF}}{P_{max}} = \frac{V_{FF} \cdot I_{FF}}{V_{oc} \cdot I_{sc}} . 100 \qquad \text{Eq. 3.12}$$

$$P = I \cdot V \qquad \text{Eq. 3.13}$$

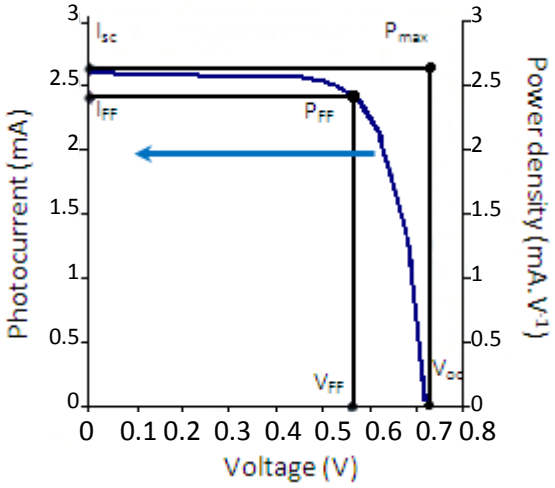

Figure 23. Current-voltage (I–V) curve and power-voltage (P–V) for a ruthenium polypyridyl dye (**N719**).[131]

3.7. Tuning of MLCT Transitions

The molecular design of ruthenium polypyridyl photosensitizers for solar cells presents a challenging task. The ideal sensitizer for a photovoltaic cell that converts sunlight into electricity should absorb all light below a threshold wavelength of about 900 nm. The dye should have suitable ground- and excited-state redox properties so that the two key electron-transfer steps (charge injection and regeneration of the dye) occur efficiently. It is very difficult to fulfill both requirements simultaneously. Systematic

tuning of the LUMO and HOMO energy levels of the ruthenium polypyridyl complexes are necessary to estimate the optimal threshold wavelength for maximum power conversion.[132]

The spectral and redox properties of Ru polypyridyl complexes can be tuned in two ways: (i) modification of the LUMO energy level by introducing a ligand with a low-lying π^* molecular orbital and (ii) by destabilization of the metal t_{2g} orbital (HOMO energy level) through the introduction of a strong donor ligand.[133] Meyer and co-workers have used these strategies to tune the MLCT transition in Ru complexes.[133,134] Controllable adjustments of the excited state energy levels can be performed with an appropriate selection of the ligands involved in the MLCT (*i.e.* $[Ru(bpy)_3]^{2+}$ (**1**) and $[Ru(bpy)_2(2,2'\text{-biquinoline})]^{2+}$ (**10**)). However, smaller changes in the LUMO energy levels are accomplished by the introduction of substituents on the aromatic rings of the ligands (*i.e.* $[Ru(bpy)_3]^{2+}$ (**1**) and $[Ru(4,4'\text{-dimethyl-}2,2'\text{-bipyridine})_3]^{2+}$ (**9**)). Furthermore, considerable changes in the spectral properties of the Ru polypyridyl complexes can be achieved upon substitution of a ligand not involved in the MLCT transition by a non-chromophoric donor ligand, which destabilizes the metal t_{2g} orbitals (*i.e.* $[Ru(bpy)_2(2,2'\text{-biquinoline})]^{2+}$ (**10**) and $[Ru(bpy)_2(CN)_2]^{2+}$ (**11**)) (Figure 24).[135]

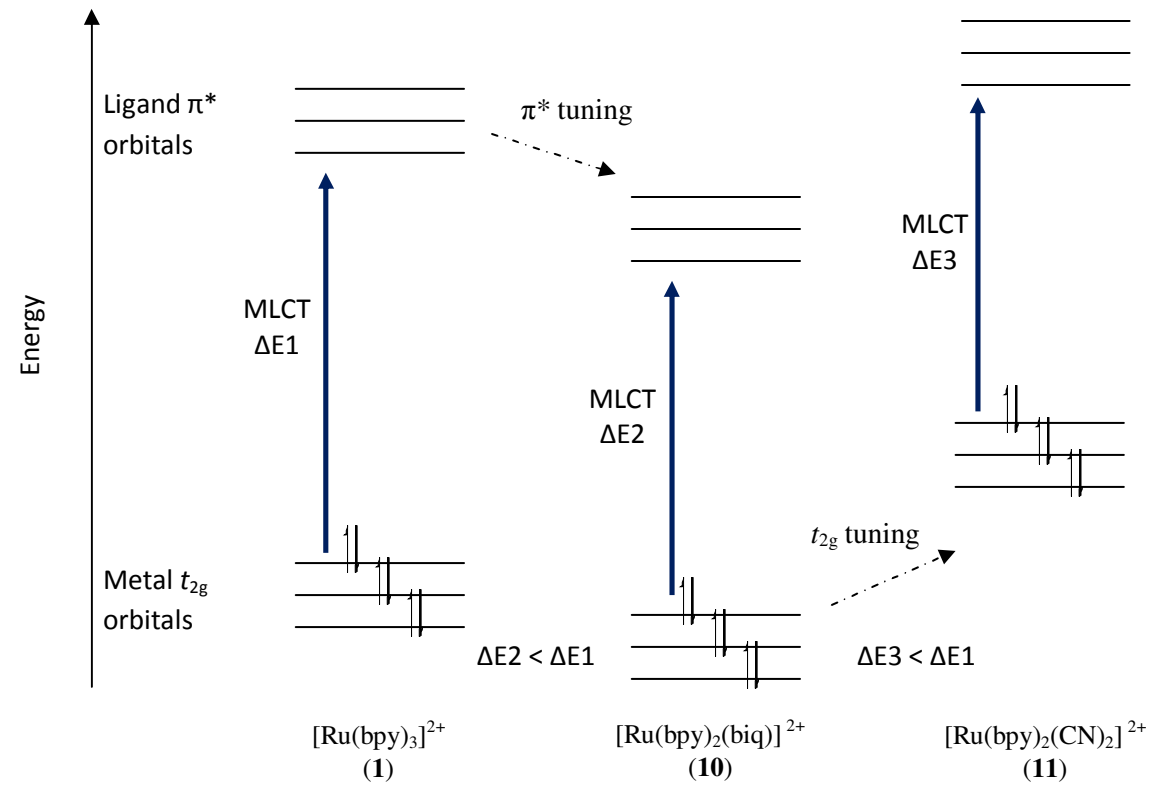

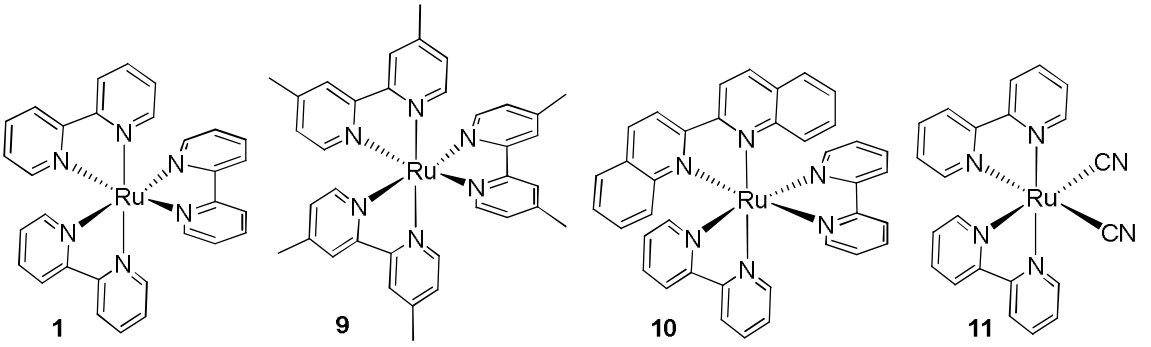

Figure 24. Tuning of HOMO (t_{2g}) and LUMO (π*) orbital energy in various ruthenium polypyridyl complexes (bpy = 2,2'-bipyridine, biq = 2,2'-biquinoline, CN = cyanide).

Heteroleptic complexes containing bidentate ligands with low lying π* orbitals, having strong σ-donating properties, can demonstrate impressive panchromatic absorption properties.[133] However, the extension of the spectral response into the near IR

is gained at the expense of shifting the LUMO orbital to levels where charge injection into the metal oxide (TiO_2) conduction band can no longer occur.[136,137]

A near infrared response can also be achieved by the upward shifting of the Ru t_{2g} (HOMO) levels. However, it turns out that the mere introduction of strong σ-donor ligands into the complex often does not lead to the desired spectral result as both the HOMO and LUMO are displaced in the same direction. Furthermore, the HOMO position cannot be varied freely because the redox potential of the dye must be maintained sufficiently positive to ensure rapid regeneration of the dye by electron donation from iodide following charge injection into the TiO_2.[134]

Based on the examination of several Ru(II) polypyridyl complexes, it has been discovered that the excited state oxidation potential of the sensitizer should be negative and at least -0.9 V vs. saturated calomel electrode (SCE), in order to inject electrons efficiently into the TiO_2 conduction band. The ground state oxidation potential should be about 0.5 V vs. SCE, in order for the dye to be regenerated rapidly by electron donation from the electrolyte (I_3^-/I^-). A significant decrease in electron injection efficiencies will occur if the excited- and ground-state redox potentials are lower than these values.[138]

3.8. Some Examples of Ruthenium Sensitizers

Ruthenium complexes have received particular interest as photosensitizers in DSSC application due to their favorable photoelectrochemical properties such as broad absorption spectrum, suitable excited and ground state energy levels, and high stability in the oxidized state, making practical applications feasible.[139] At present, *cis*-bis(4,4'-

dicarboxy-2,2'-bipyridine)dithiocyanato ruthenium(II) known as **N3** dye has become the paradigm of heterogeneous charge transfer sensitizers for solar cells with an IPCE of over 80% between 480 and 600 nm and overall power conversion efficiency of ~10%.[140,141] **N3** dye has been used as a standard in studies to compare the performance of new dye sensitizers. Furthermore, the 4,4'-dicarboxy-2,2'-bipyridine (dcbpy) and thiocyanate (NCS) ligands have subsequently been incorporated into many other complexes which are discussed later.

A drawback of **N3** dye is its lack of absorption in the near-IR region of the electromagnetic spectrum.[142] An efficient DSSC should absorb in the near-IR as well as over the entire visible region of the solar spectrum. For this reason, the structure of **N3** dye was modified by Grätzel and co-workers to give $[Ru^{II}(NCS)_3(tctpy)]$ (tctpy=4,4',4''-tricarboxy-2,2':6',2''-terpyridine) which is also known as **black dye**.[143,144] The MLCT band of **black** dye is red-shifted when compared to that of **N3** dye. This red-shift is due to the presence of three thiocyanato ligands which destabilize the Ru-based HOMO by electron donation, and also the ligand-based LUMO is stabilized by introducing the terpyridine ligand. This dye achieves very efficient sensitization over the whole visible range extending to the near-IR region up to 920 nm with IPCE values over 80%. The overall conversion efficiency of **black** dye is slightly higher than **N3** dye at 10.4%. The IPCE diagram of the **N3** and **black** dyes are shown in Figure 25. Both chromophores show very high IPCE values in the visible range. The response of the **black** dye extends 100 nm further into the IR than that of **N3**.

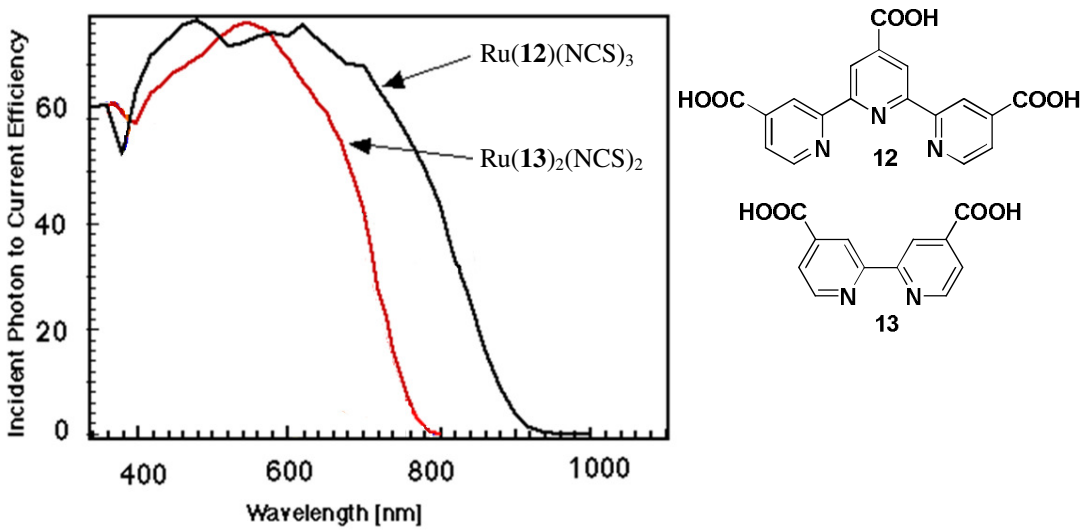

Figure 25. IPCE spectra of **N3** [Ru(**13**)$_2$(NCS)$_2$] (red) and black [Ru(**12**)(NCS)$_3$] (black) dyes.

The Ru(II)-polypyridyl sensitizer **N719**, $(Bu_4N)_2$[Ru(4,4'-dicarboxy-2,2'-bipyridine)$_2$ $(NCS)_2$], (Bu_4N= tetra-*n*-butylammonium) derived from the **N3** dye is presented in Figure 26.[113] **N719** is a doubly protonated form of **N3** and exhibits improved power conversion efficiency of over 11%.[139b] To this date, **N3**, **N719**, and **black** dyes are still the most efficient sensitizers employed in DSSC applications. Hence, these dyes have been used as templates for new Ru(II) polypyridyl sensitizers.

In the development of new sensitizers, many efforts have been made to extend the spectral wavelength as well as to enhance the molar extinction coefficient (ε).

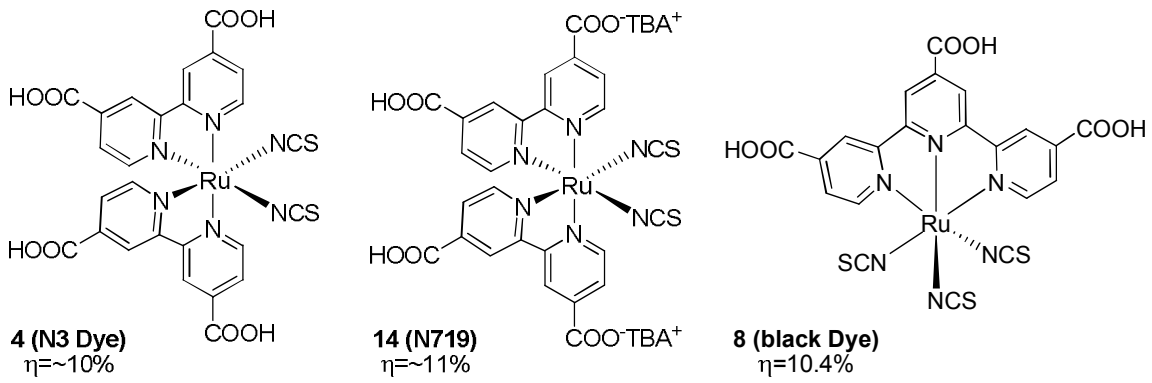

Figure 26. Molecular structures of **N3**, **N719**, and **black** dyes.

3.8.1. Thiocyanate ruthenium sensitizer for solar cells

A convenient and versatile new route is reported for the synthesis of the heteroleptic Ru complex, which plays a key role in achieving the high temperature stability.[145] The significance of using amphiphilic polypyridyl Ru sensitizers has been demonstrated to achieve enhanced stability in DSSCs at elevated temperatures. Therefore, it is interesting to design new ligands leading to the preparation of new amphiphilic Ru sensitizers.

The solar cell with the amphiphilic Ru sensitizer of *cis*-Ru(dcbpy)(L') $(SCN)_2$ (L'=4,4'-dinonyl-2,2'-bipyridine) (**Z907**, Figure 27) has an efficiency of >6%. The cell sustained heating for 1000 h at 80°C, maintaining 94% of its initial performance.

By varying the hydrocarbon chain length of an amphiphilic ruthenium dye (Figure 27), the efficiency can be improved significantly. The results reported here suggest that a slightly longer hydrocarbon chain length might be advantageous and could lead to even higher efficiencies, and a hydrophobic chain attached to the dye can be used to suppress

recombination.[146] The molecular structure of the some Ru(II)-complex photosensitizers are shown in Figure 27.[147] These amphiphilic Ru complexes have been successfully used as sensitizers for DSSCs.

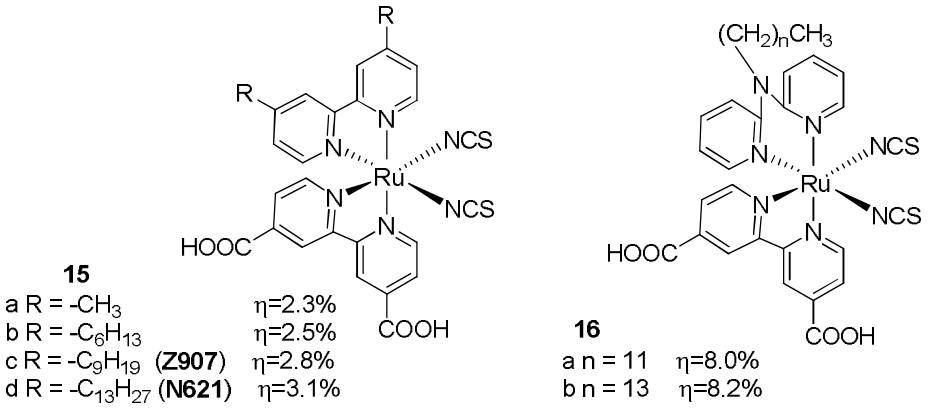

Figure 27. Molecular structure of some amphiphilic Ru-complex photosensitizers.

It is very important to develop transition-metal-based sensitizers with improved molar extinction coefficients which maintain the desirable stability under thermal stress and light soaking. New heteroleptic polypyridyl Ru complexes with extended conjugated π-systems are shown in Figure 28. These complexes with high molar extinction coefficients are **Z910** with $\varepsilon = 1.69 \times 10^4$ $M^{-1}.cm^{-1}$ and η=10.2%[148] and **K19** with $\varepsilon = 1.82 \times 10^4$ $M^{-1}.cm^{-1}$ and η=7.0% [149] power conversion efficiency.

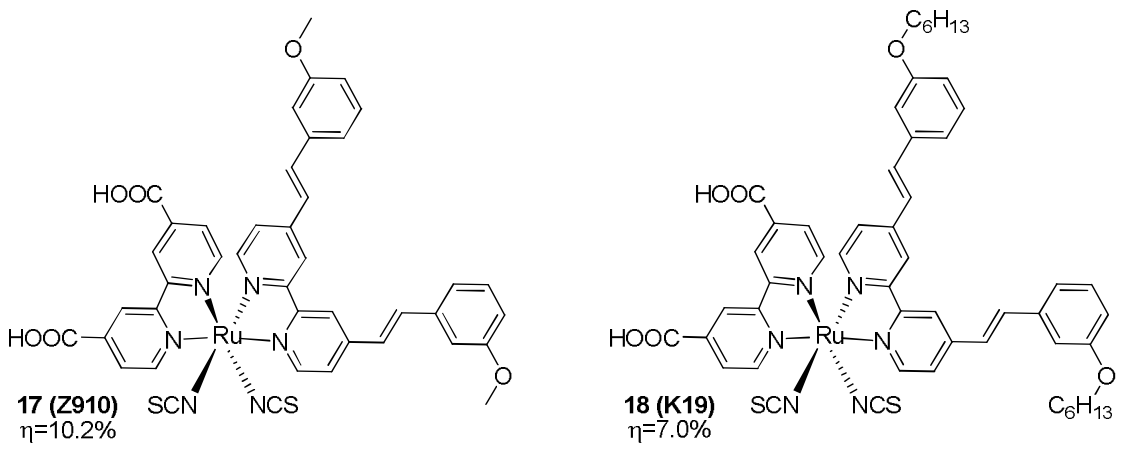

Figure 28. Molecular structure of **Z910** and **K19**.

To improve the effectiveness of the dye in both the visible and near-IR regions, Funaki and co-workers[150] synthesized a new class of cyclometallated Ru(II) complexes (Figure 29). These compounds can be used in DSSCs. Sensitizer **19b** shows a 10% IPCE at 900 nm.

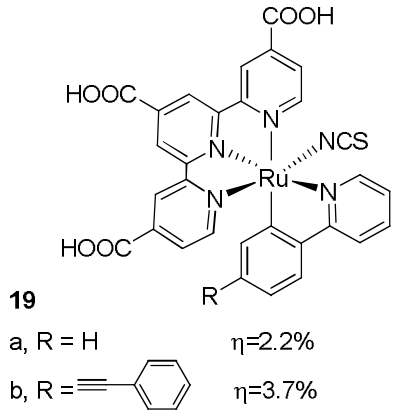

Figure 29. Molecular structures of cyclometalated Ru(II) complexes.

The replacement of the NCS groups with a cyclometalating ligand also offers the unique opportunity to independently tune both the metal-based HOMO and the ligand π*-based LUMO.[151] Because the NCS ligands of Ru sensitizers are labile in practical DSSC

devices,[15258] chelating cyclometalating ligands also offer a promising approach for increasing the stability of Ru sensitizers.

By adding a fused benzo group to 2,2'-bipyridine, Arakawa and co-workers designed 2-(pyrid-2'-yl)quinoline and 2,2'-biquinoline.[134,153] Attaching one or two carboxylic acid groups at the 4- and/or 4'- positions of these molecules provided ligands **20-22**. Although dyes made from these ligands had better light-harvesting capability at longer wavelengths because of the extended π conjugation, they showed decreased IPCEs and overall efficiencies compared with the **N3** dye.

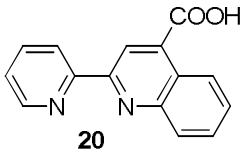

20

$[Ru(\mathbf{20})_2(NCS)_2]$
IPCE=52%
η=4.6%

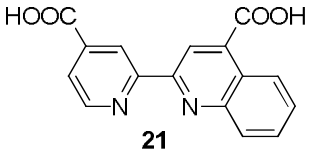

21

$[Ru(\mathbf{21})_2(NCS)_2]$
IPCE=54%
η=4.3%

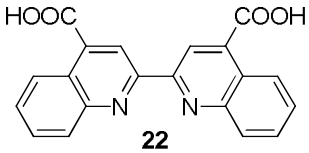

22

$[Ru(\mathbf{22})_2(NCS)_2]$
IPCE=76%
η=1.5%

Thummel and co-workers synthesized ligands **23-25** in which a fused pyrido group was incorporated instead of benzo group.[142] Compared with the **N3** dye, Ru(II) complexes of **23** and **25** exhibit better performance in light-harvesting efficiency over the whole visible region with lower IPCEs in the high energy region. The dye derived from ligand **24**, showed poor IPCE in the high energy region, indicating that the carboxylic group does play an important role in the light-harvesting process.

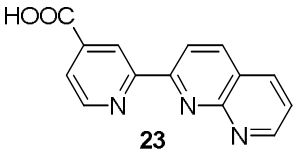

23

[Ru(**23**)$_2$(NCS)$_2$]
IPCE=71%

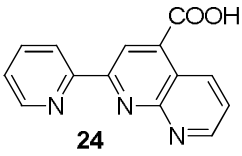

24

[Ru(**24**)$_2$(NCS)$_2$]
IPCE=43%

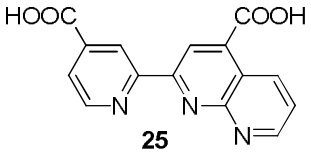

25

[Ru(**25**)$_2$(NCS)$_2$]
IPCE=58%

3.9. Objective of this Work

The focus of this part is the sensitizer component of the DSSC. The main theme is the designing of new ligands as well as their corresponding Ru complexes for use as a photosensitizer in a DSSC to improve the efficiency.

Efforts have been made to improve the cell performance achieved with the **N3** dye at longer wavelengths. The incorporation of an additional non-coordinating nitrogen into one of the ligands is anticipated to lower the π* level of the ligand, causing a red-shift of the MLCT band which might increase the light-harvesting efficiency. To this purpose, we designed a set of new dyes analogous to **N3** by substituting one 4,4'-dicarboxy-2,2'-bipyridine with an alkyl substituted 4-(pyrid-2'-yl)-pyrimidine. Also ligands involving 2-(pyrid-2'-yl)-quinoxalines were studied. The pyridine moiety needs to be present in order to maintain good performance in the high energy region. Schemes 1-3 shows the molecular structures of the ligands (L= **29a-b**, **34a-c**, **35a-b** and **37a-b**) and Scheme 4 shows their Ru(II) complexes, [Ru(**L**)(**13**)(NCS)$_2$].

The purpose of this research is to extend the absorption spectra further into the IR region. To achieve this, fused pyrido groups were incorporated onto the terminal pyridine

part of tpy in the **black** dye. Scheme 6 shows the molecular structure of the **black** dye analogue **51**, [Ru(**48**)$(NCS)_3$].

Our ultimate goal is to design a sensitizer which can efficiently absorb light in the region of 400-1000 nm, while maintaining sufficient thermodynamic driving forces for both the electron transfer and dye regeneration processes.

3.10. Results and Discussion

3.10.1. Synthesis of substituted 2-(pyrid-2'-yl)pyrimidine

The synthesis of ligands **29a** and **29b** started with the preparation of pyridine-2-carboxamidine derivatives **27a** and **27b** from pyridine nitriles **26a** and **26b**, respectively. Condensation of pyridine-2-carboxamidine derivatives with acetylacetaldehyde dimethylacetal (**28**) in ethanol afforded ligands **29a** and **29b** in 50% and 80% yields, respectively (Scheme 1).

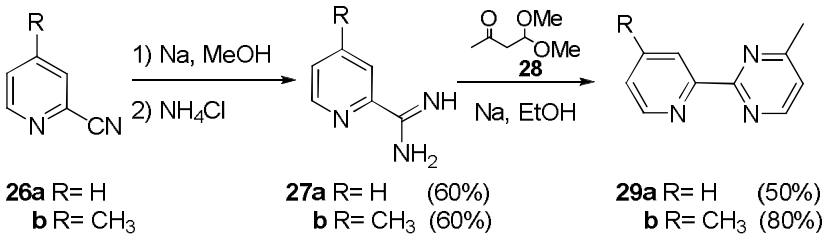

Scheme 1. Synthetic route to ligands **29a** and **29b**.

3.10.2. Synthesis of substituted 4-(pyrid-2'-yl)pyrimidine

Acylation of the 4-substituted pyridine derivative in position 2 was carried out with pyruvic acid, $AgNO_3$, H_2SO_4, and $NH_4S_2O_8$ in H_2O-CH_2Cl_2 to give **30b** and **30c**.

Compound **30a** is commercially available. Condensation of 2-acetylpyridine derivatives with ethyl acetate gives compounds **31a-c** and ethyl pivalate gives compounds **32a-b**.

Ligands **34a-c** and **35a-b** were prepared in moderate yields by the condensation of the pyridine-2-carboxamidine derivatives **31a-c** and **32a-b** with formamide (**33**). The synthetic route for preparation of substituted 4-(pyrid-2'-yl)pyrimidines is shown in Scheme 2.

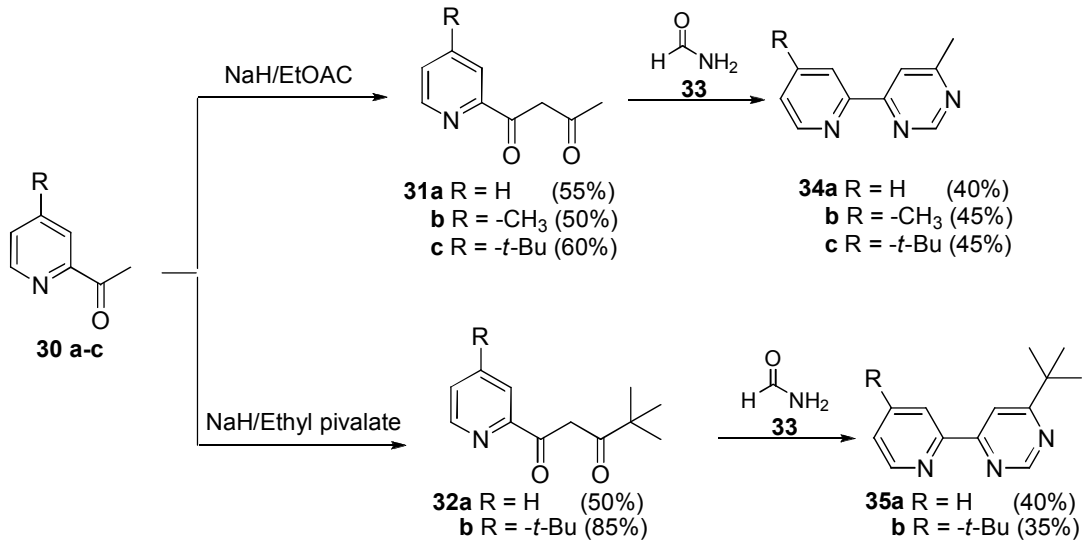

Scheme 2. Synthetic route to ligands **34a-c** and **35a-b**.

3.10.3. Synthesis of substituted 2-(pyrid-2'-yl)quinoxaline

Ligands **37a** and **37b** were prepared in good yields by condensation of benzene-1,2-diamine derivatives **36a** and **36b** with 2-acetylpyridine (**30a**) catalyzed by TsOH in methanol, respectively (Scheme 3).

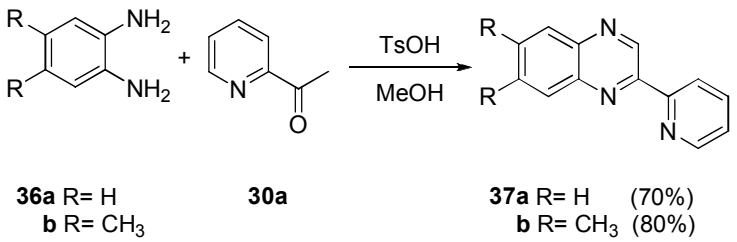

Scheme 3. Synthetic route to ligands **37a** and **37b**.

3.10.4. Synthesis of Ru(II) complexes of 39a-i

The synthesis of Ru(II) complexes of pyrimidine and quinoxaline derivatives involves the one pot reaction[74] of the ligands **29a-b**, **34a-c**, **35a-b**, and **37a-b** with Ru(*p*-cymene)Cl_2 (**38**) in DMF in a 2:1 fashion followed by adding of dcbpy (**13**) then treating with excess of ammonium thiocyanate (Scheme 4). The reaction mixture was evaporated under vacuum. Then 5 mL of water was added to remove the excess NH_4NCS. A brown precipitate appeared, and it was collected by filtration on a sintered glass funnel. Purification of the **39a-i** was carried on a LH-20 Sephadex column using MeOH as eluent.

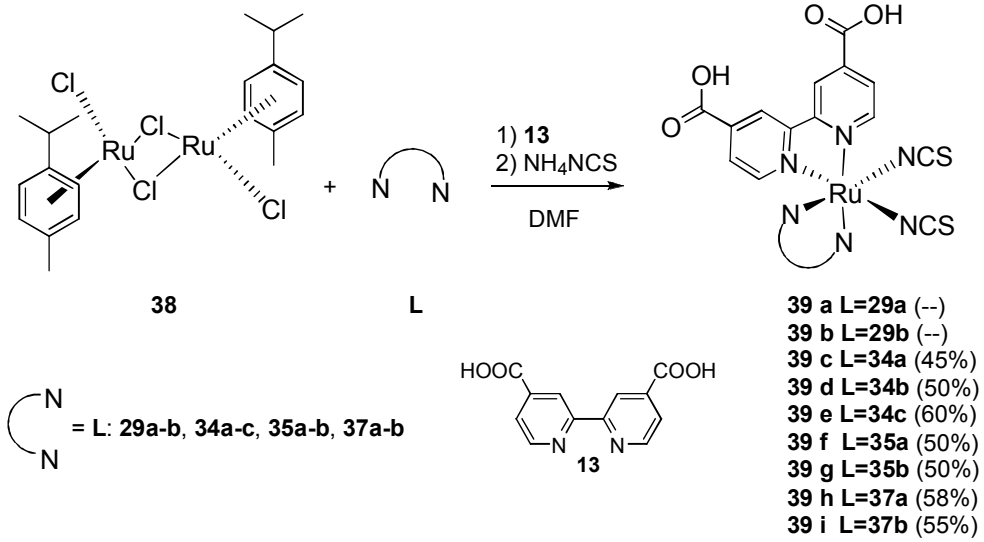

Scheme 4. Preparation of the dye complexes [Ru(**L**)(**13**)$(NCS)_2$].

3.10.5. Synthesis of compound 48 and its Ru complex 51 as black dye analog

The reaction of 2-aminopyridine (**40**) with trimethylacetyl chloride (**41**) proceeds smoothly to provide **42** in 70% yield. This species may then be *ortho*-metalated specifically at the 3-position by using 2 equivalents of *n*-BuLi. Reaction of the **42** with diethyl oxalate (**43**) incorporates the α-ketoester moiety (**44**). Condensation of methyl isonicotinate (**45**) and pyruvic acid (**46**) under acidic conditions resulted in methyl 2,6-diacetylisonicotinate (**47**). Reaction of the diacetyl moiety with **44** gave bis-(1',8'-naphthyrid-2'-yl)pyridine carboxylic acid **48** as a brown solid in 90% yield. Esterification of **48** in a sealed tube in an EtOH-H_2SO_4 mixture afforded **49** as a yellow solid in 60% yield (Scheme 5).

To get **51**, the ester analogue of the ligand was used because of solubility problems with **48** having three carboxylic acid groups. The reaction of **49** and $RuCl_3.3H_2O$ in EtOH under argon afforded complex **50** as a brown solid in 80% yield. The black dye analogue was synthesized by refluxing a mixture of NH_4NCS and **50** in DMF for 4 h. Then triethylamine and H_2O were added, and the solution was refluxed for a further 24 h to hydrolyze the ester groups on the tridentate ligand. The solvent volume was reduced under vacuum, and then ~20 mL of H_2O was added to the solution. The resulting precipitate was filtered and dried. The isolated solid was purified on a LH-20 Sephadex column using methanol as eluent to afford **51** as a green solid in 40% yield (Scheme 6).

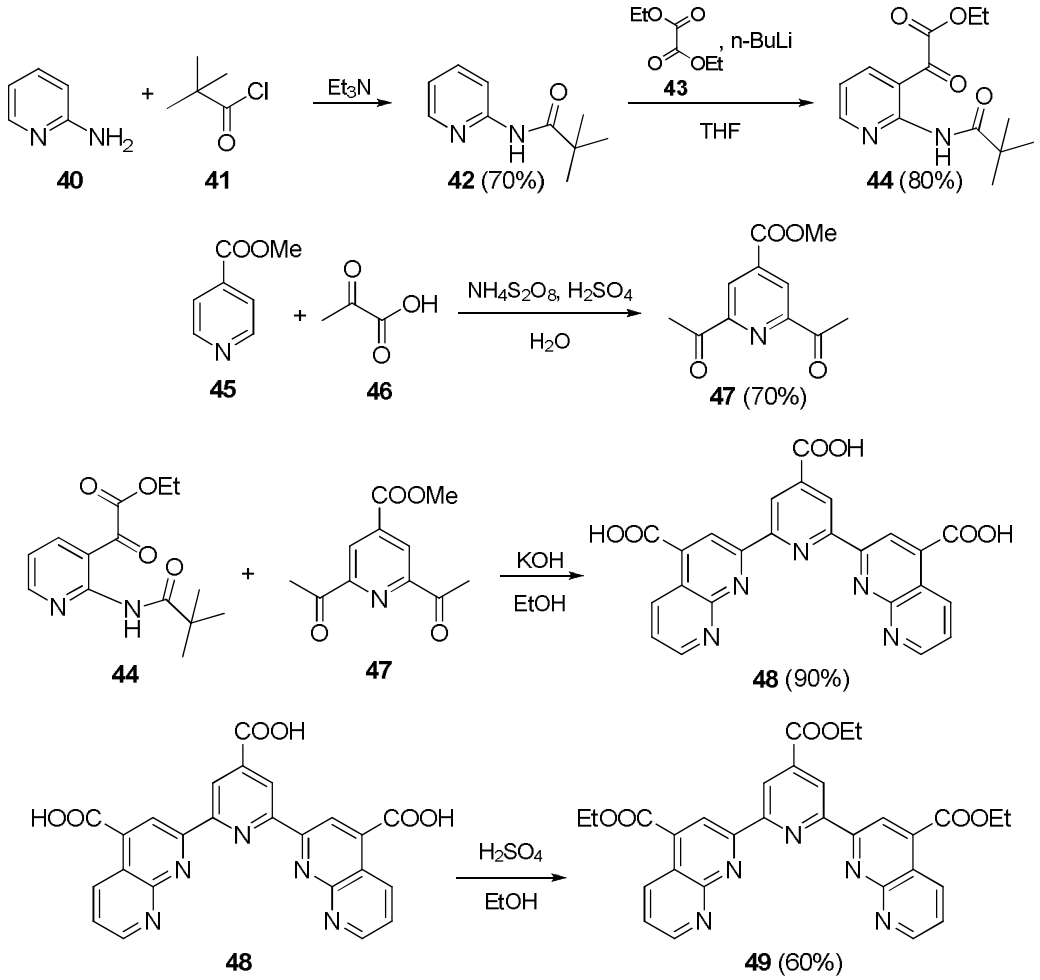

Scheme 5. Synthetic route to ligands **48** and **49**.

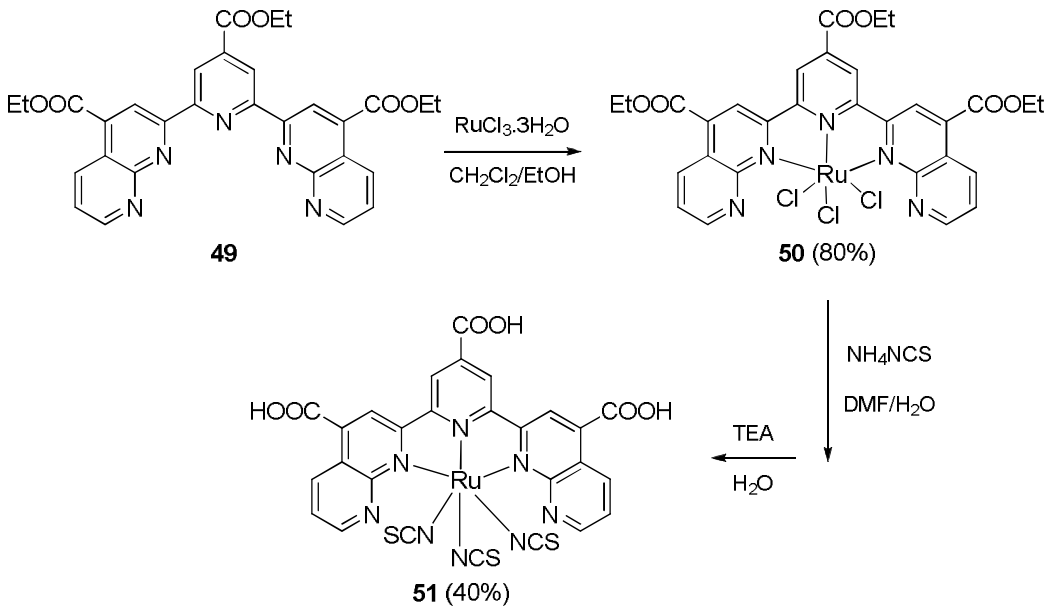

Scheme 6. Synthetic route to complex **51**.

3.10.6. Spectroscopic properties of the ligands and complexes

3.10.6.1. NMR spectra

Ligands **29a-b**, **34a-c**, **35a-b**, **37a-b**, **48**, and **49** were characterized by ^{1}H and ^{13}C NMR, IR and elemental analysis. The ^{1}H NMR chemical shift data for pyridine-pyrimidine and pyridine-quinoxaline ligands are summarized in Tables 2-4. The ^{1}H NMR chemical shift data for ligands **48** and **49** is summarized in Table 5. All the protons could be readily identified due to their characteristic coupling patterns aided by the use of 2D homonuclear chemical shift correlated ^{1}H NMR (COSY) for ligands and chemical shifts.

The ^{1}H NMR chemical shift data for ligands **29a** and **29b** are summarized in Table 2 and their downfield region spectrum is shown in Figure 39. The pyrimidine part is the same for both ligands so the chemical shift is the same for pyrimidine part for ligands **29a** and **29b**. The electron donating methyl group on the 4' position of the

pyridine part in ligand **29b** causes the chemical shifts of H3', H5' and H6' to move upfield 0.16-0.18 ppm.

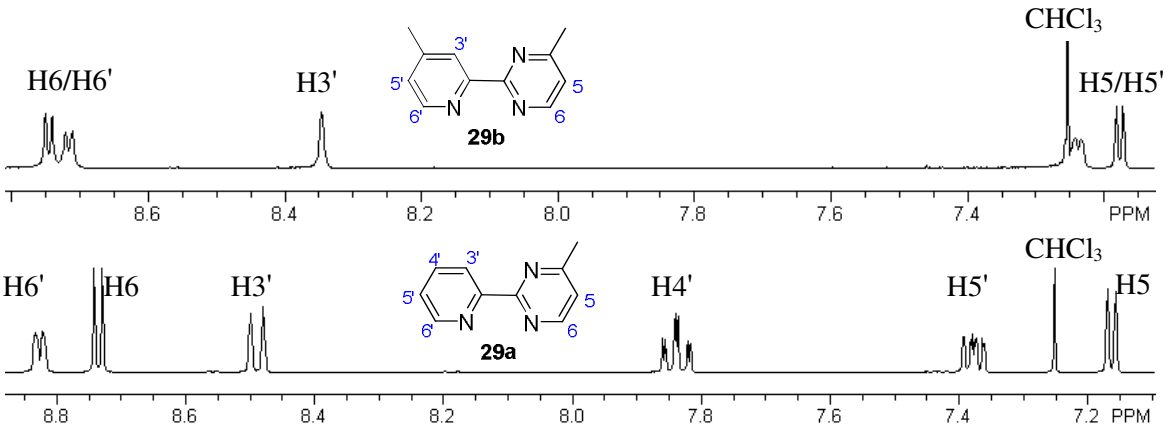

Figure 30. Downfield region of ^{1}H NMR spectrum of **29a** and **29b** in $CDCl_3$ (500 MHz, at rt).

Table 2. ^{1}H NMR chemical shift data[a] for ligands **29a-b**.

Ligand (**29a-b**)	H_5	H_6	H_3'	H_4'	H_5'	H_6'	$-CH_3$
29a	7.24	8.75	8.53	7.90	7.42	8.88	2.65
29b	7.24	8.75	8.35		7.24	8.72	2.67, 2.47

[a] Ligand spectra were recorded in $CDCl_3$.

The ^{1}H NMR chemical shift data for ligands **34a-c** and **35a-b** are summarized in Table 3 and the downfield region of their spectra are shown in Figure 31. The pyrimidine part is the same for ligands **34a-c** so the chemical shifts of H2 and H5 are almost unchanged. The electron donating methyl group on the 4' position of the pyridine part of ligand **34b** causes the chemical shifts of H3', H5' and H6' to move upfield 0.14-0.16 ppm. The weaker electron donating *t*-Bu group on ligand **34c** causes the chemical shifts of H3', H5' and H6' to move upfield 0.08-0.10 ppm.

The pyrimidine part is the same for ligands **35a** and **35b** so the chemical shifts of H2 and H5 are identical. The electron donating *t*-Bu group on the 4' position of the

pyridine part in ligand **35b** causes the chemical shifts of H3', H5' and H6' to move to upfield region by 0.8-0.1 ppm.

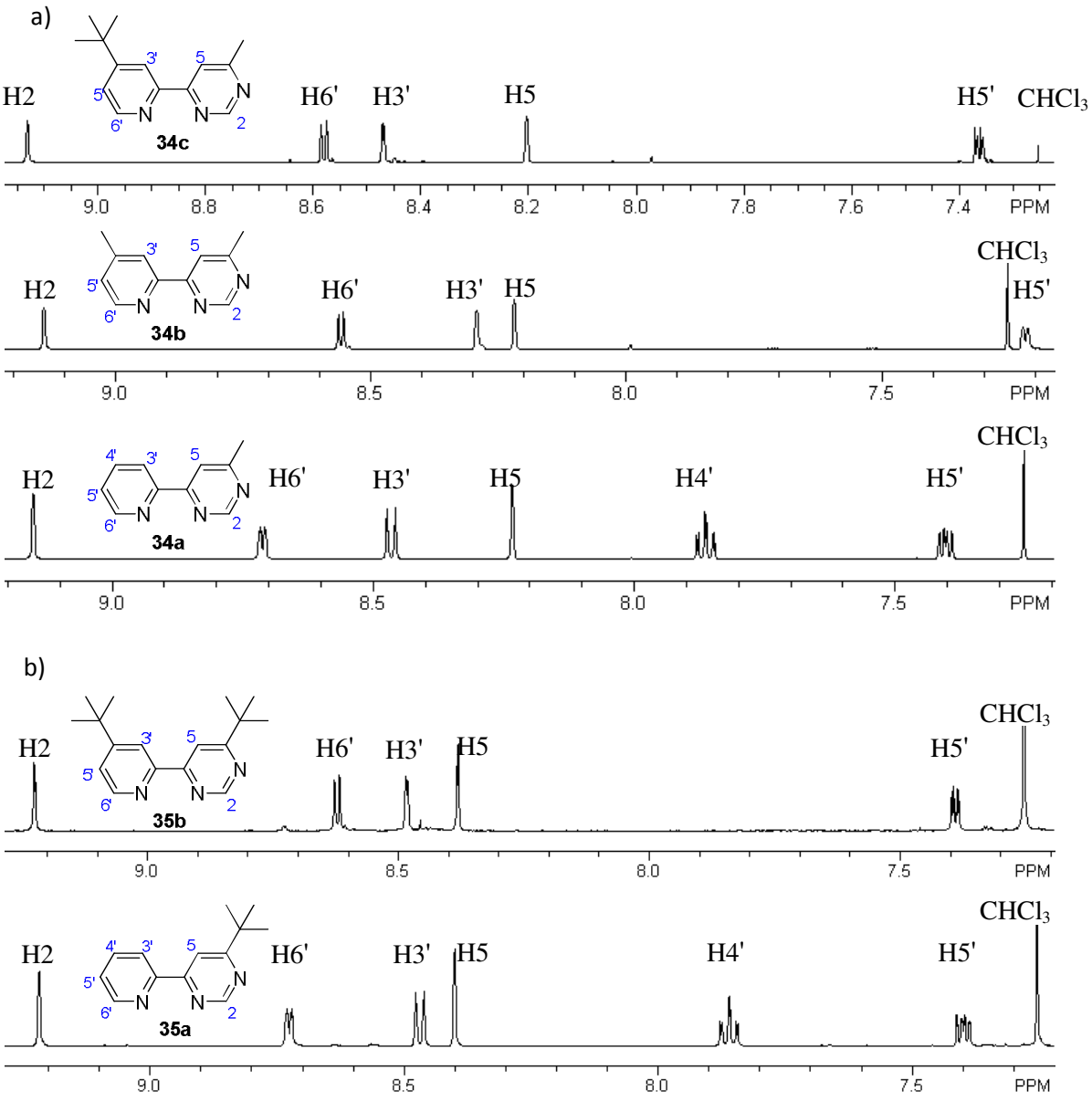

Figure 31. Downfield region of ^{1}H NMR spectrum of a) **34a-c** and b) **35a-b** in $CDCl_3$ (500 MHz, at rt).

Table 3. [1]H NMR chemical shift data[a] for ligands **34a-c** and **35a-b**.

Ligand (**34a-c**, **35a-b**)	H_2	H_5	H_3'	H_4'	H_5'	H_6'	$-CH_3$	$-t$-Bu
34a	9.12	8.21	8.45	7.84	7.38	8.68	2.62	
34b	9.14	8.22	8.29		7.22	8.54	2.61, 2.45	
34c	9.13	8.21	8.35		7.30	8.58	2.60	1.36
35a	9.23	8.40	8.47	7.85	7.40	8.73		1.43
35b	9.23	8.37	8.39		7.31	8.65		1.42, 1.39

[a] Ligand spectra were recorded in $CDCl_3$.

The [1]H NMR chemical shift data for ligands **37a** and **37b** are summarized in Table 4 and the downfield region of their spectra is shown in Figure 32. The pyridine part is the same for both ligands so the protons on this ring show very similar chemical shifts. The electron donating methyl groups at the 6' and 7' positions of the quinoxaline ring cause the positions of H5' and H8' to shift upfield by 0.2-0.3 ppm.

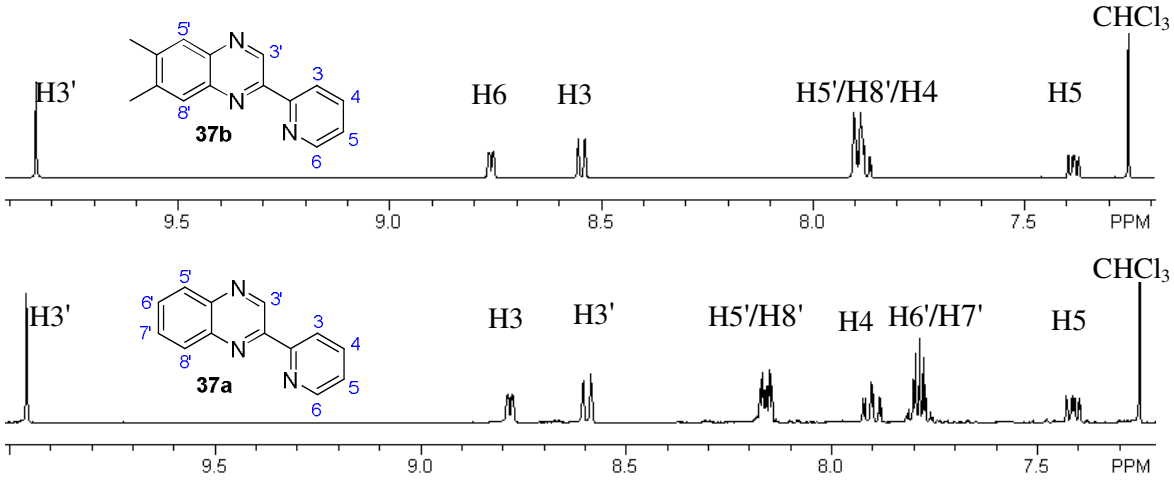

Figure 32. Downfield region of [1]H NMR spectrum of **37a** and **37b** in $CDCl_3$ (500 MHz, at rt).

Table 4. [1]H NMR chemical shift data[a] for ligands **37a-b**.

Ligand (**37a-b**)	H_3	H_4	H_5	H_6	H_3'	H_5'/ H_8'	H_6'/H_7'	$-CH_3$
37a	8.61	7.80	7.42	8.79	9.86	8.19-8.15	7.82-7.78	
37b	8.59	7.83	7.41	8.78	9.86	7.95-7.87		2.53

[a] Ligand spectra were recorded in $CDCl_3$.

The [1]H NMR chemical shift data for ligands **48** and **49** are summarized in Table 5 and the downfield region of their spectra is shown in Figure 33. Carboxylate and ester groups have a similar electron withdrawing effects so the chemical shifts of **48** and **49** are similar. The chemical shift for H3 and H3' were determined by comparison with **48** having carboxylate groups on the H4' and H4" positions.

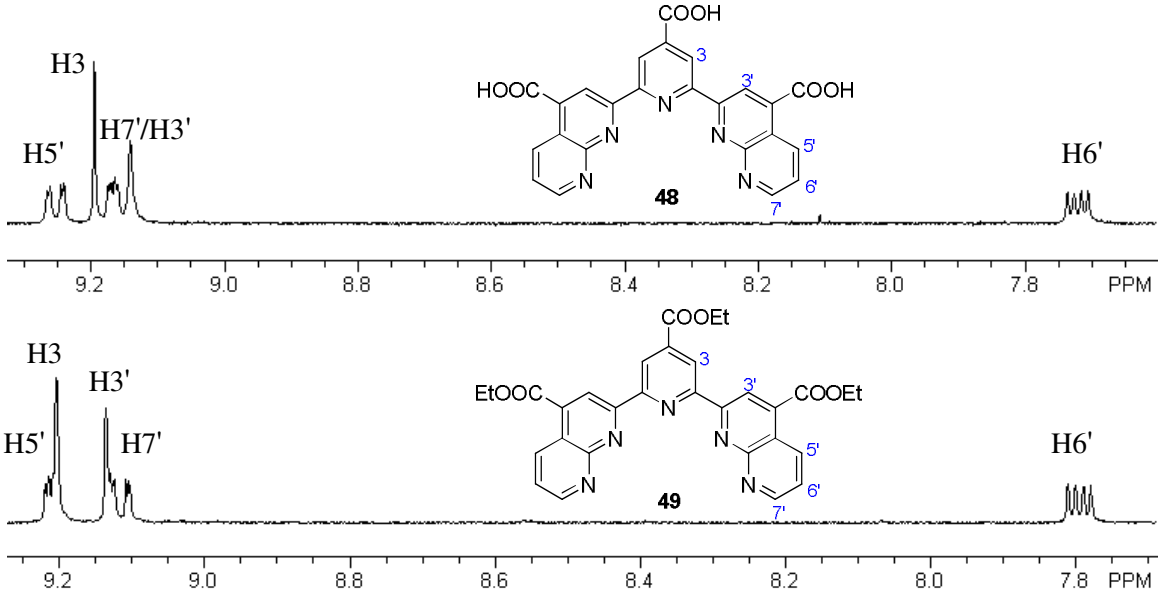

Figure 33. Downfield region of [1]H NMR spectrum of **48** and **49** in DMSO-*d6* (400 MHz, at rt).

Table 5. [1]H NMR chemical shift data[a] for ligands **48** and **49**.

Ligand	H_3	H_3'	H_5'	H_6'	H_7'	$-CH_2$	$-CH_3$
48	9.22	9.15	9.28	7.73	9.18		
49	9.20	9.14	9.21	7.80	9.21	4.52, 4.48	1.47, 1.44

[a] Ligand spectra were recorded in DMSO-*d6*.

Complexes **39a** and **39b** each may have 4 different isomers. The downfield region of the spectrum of **39a** is shown in Figure 34. In one isomer the pyridine part of the complex is *cis* to NCS, in the other isomer the pyrimidine part is *cis* to the NCS group. Chelate ring formation may occur using either N1 or N3 on the pyrimidine ring of ligand **29a-b** leading to two geometric isomers **39a-b 1** or **39a-b 2**. The possible two isomers: the pyridine part of the complex is *cis* to NCS, or the pyrimidine part is *cis* to NCS group. Possible 4 isomers for complex **39a** are shown in Scheme 7. The ^{1}H NMR of these complexes was poorly resolved so that a good proton inventory was not evident and the complexes were difficult to characterize.

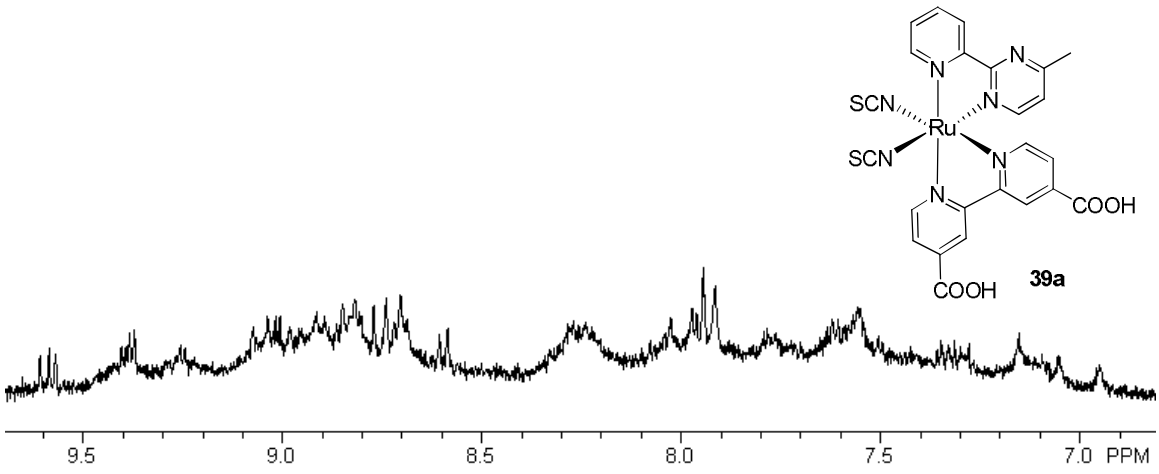

Figure 34. Downfield region of ^{1}H NMR spectrum of **39a** in DMSO-*d6* (500 MHz, at rt).

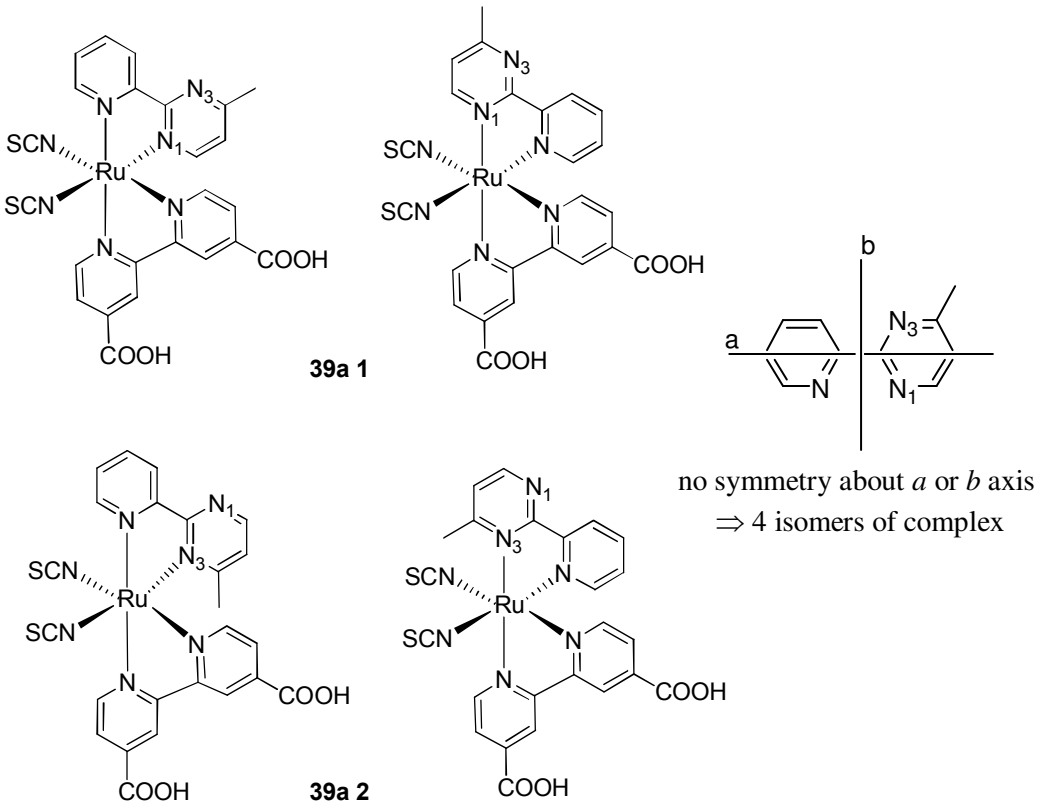

Scheme 7. Possible 4 isomers for complex **39a**.

Complexes **39c-i** were obtained and isolated as a mixture of isomers. The downfield region spectrum of **39e** is shown in Figure 35. In one isomer the pyridine part of the complex is *cis* to NCS, in the other isomer either the pyrimidine or quinoxaline part is *cis* to NCS group. The mixture of isomers was not separated. The ^{1}H NMR of each complex shows 2 sets of peaks accounting for both isomers.

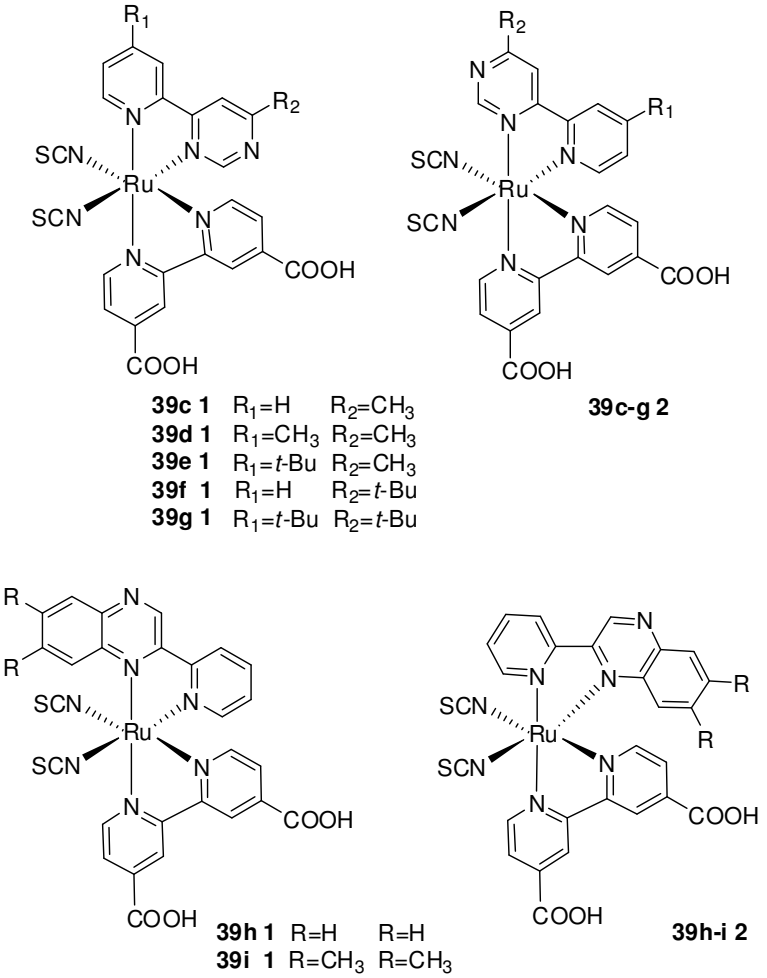

Scheme 8. Isomers for complexes **39c-i**.

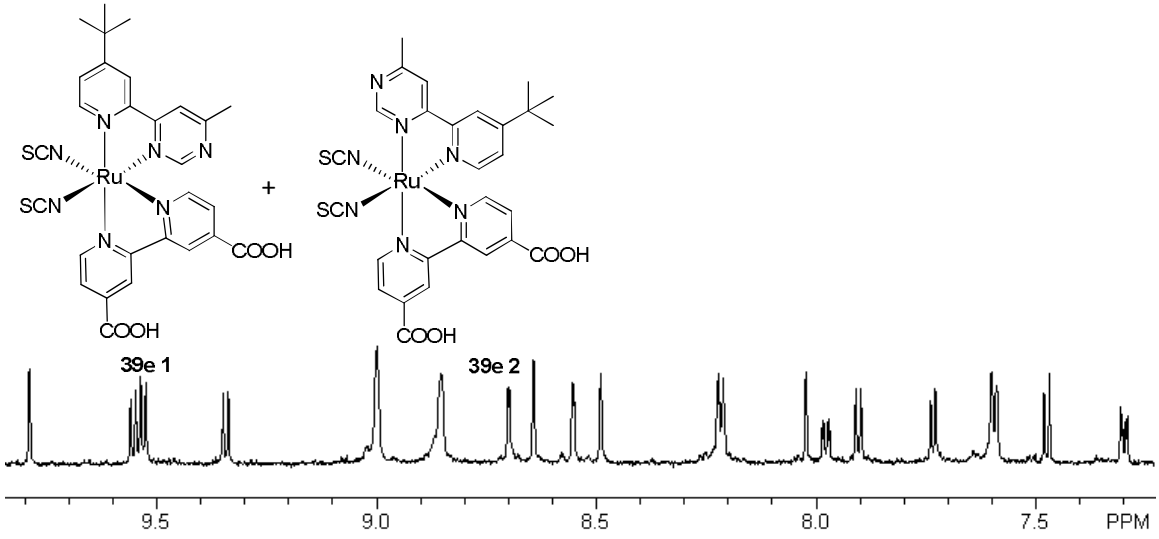

Figure 35. Downfield region of ^{1}H NMR spectrum of **39e** in methanol-*d4* (500 MHz, at rt).

Table 6 lists the chemical shifts of protons in the upfield region of the ^{1}H NMR spectra of complexes **39c-i**. Complex **39c** has a methyl group on the pyrimidine ring at 2.63 and 2.83 ppm. Complex **39d** has 4 signals that each integrates for 3 protons at 2.58 and 2.44 ppm for the methyl group on pyridine and, 2.87 and 2.71 ppm for the methyl group on pyrimidine. Complex **39e** has two methyl groups at 2.68 and 2.60 ppm each of which integrate for 3 protons on the pyrimidine and two -*t*-Bu groups at 1.55 and 1.32 ppm each of which integrate for 9 protons on the pyridine. Complex **39f** has two -*t*-Bu groups at 1.58 and 1.34 ppm each of which integrates for 9 protons on the pyrimidine. Complex **39g** has two -*t*-Bu groups at 1.56 and 1.33 ppm each of which integrate for 9 protons on the pyridine and two -*t*-Bu groups at 1.58 and 1.34 ppm each of which integrate for 9 protons on the pyrimidine.

Table 6. List of the chemical shifts of the protons in the upfield region of the ^{1}H NMR spectra for complexes **39c-i**.

Complex	pyridine		pyrimidine		pyridine		pyrimidine		quinoxaline
(**39c-i**)	-CH_3	-CH_3	-CH_3	-CH_3	-*t*-Bu	-*t*-Bu	-*t*-Bu	-*t*-Bu	-CH_3
39c			2.83	2.63					
39d	2.58	2.44	2.87	2.71					
39e			2.68	2.60	1.55	1.32			
39f							1.58	1.34	
39g					1.56	1.33	1.58	1.34	
39i									2.55, 2.54

Complex **51** appears to be paramagnetic and its ^{1}H NMR is shown in Figure 36. The spectrum does not show well resolved peaks. The addition of ascorbic acid to reduce Ru(III) to Ru(II) did not help to resolve the peaks. Complex **51** was only characterized by UV and mass spectrometry.

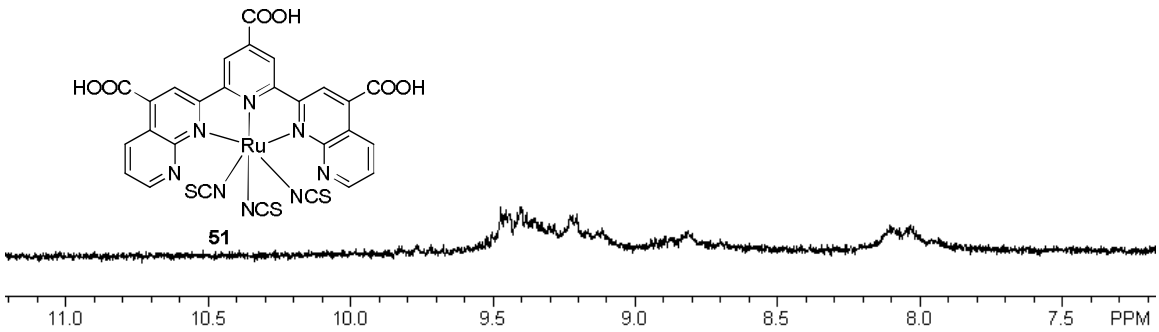

Figure 36. Downfield region of ^{1}H NMR spectrum of **51** in DMSO-*d*6 (500 MHz, at rt).

3.10.6.2. Electronic spectra

The electronic absorption spectra of complexes **39c-i** and **N3** were obtained in methanol at room temperature and the data have been summarized in Table 7. The spectra consist of two well-defined regions as illustrated in Figure 37. A relatively intense absorption is observed at shorter wavelengths, 200-350 nm. This absorption is attributed to ligand-centered $\pi - \pi^*$ transitions associated with the aromatic rings and the carbonyl groups of the ligands. The less intense absorption bands at longer wavelength in the region of 350-650 nm are assigned as MLCT and are due to the promotion of an electron from a metal d-orbital to a π^* orbital of the most electronegative ligand. Polypyridyl Ru(II) complexes are often characterized by a broad MLCT band in the visible region of the electromagnetic spectrum.

Figure 37a shows the electronic absorption spectra of complexes **39c-g** in methanol. The band shapes of these complexes are similar to the **N3** dye. Complexes **39c-e** and **39g** are slightly red shifted relative to **N3** so that they absorb more of the low energy solar spectrum. For complexes **39c-e**, having an alkyl group on the pyrimidine ring, the molar extinction coefficient increases as the alkyl substituent on the pyridine

ring gets bulkier. The molar extinction coefficient of complexes **39f-g** with a *t*-Bu group on the pyrimidine ring decreases as the alkyl substituent on the pyridine ring gets bulkier. Compared with the 4-(pyrid-2'-yl)-pyrimidine complexes, the **N3** dye has the highest molar extinction coefficient (Figure 37a).

Figure 37b shows the electronic absorption of complexes **39h** and **39i** in methanol. The band shapes of the complexes are different from the **N3** dye. There is a shoulder at shorter wavelength for **39h** and **39i** where **N3** dye has a band in the high energy region of the spectrum. Complexes **39h-i** are more red-shifted than **N3** due to their extended π-system. The molar extinction coefficient of **39h** is higher than **39i** but lower than the **N3** dye.

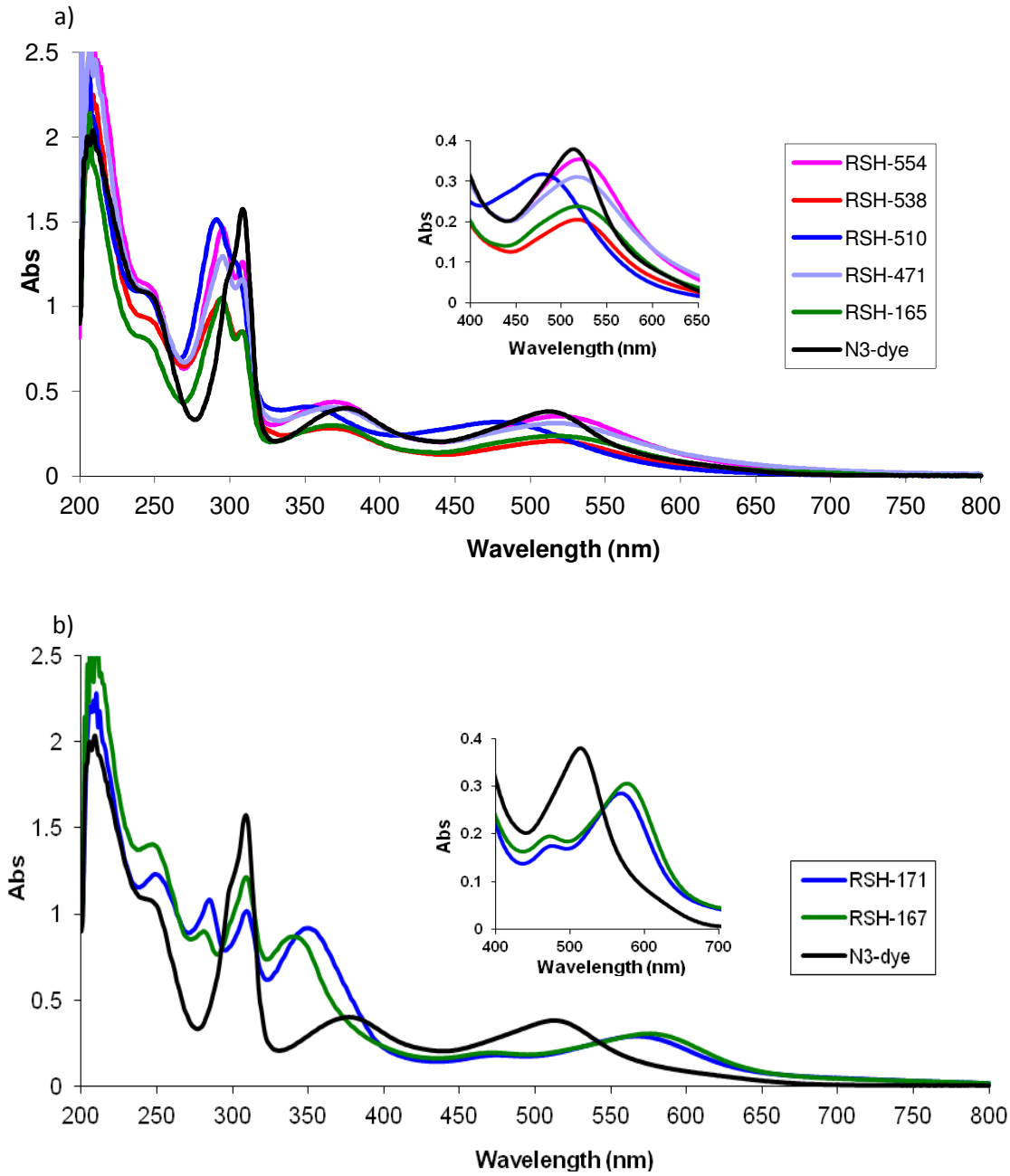

Figure 37. Electronic absorption spectra of a) **39c-g** and b) **39h-i**, $5x10^{-5}$ M in MeOH.

The electronic absorption spectra of complexes **39c-g** and **39h-i** anchored to a TiO_2 surface are illustrated in Figures 38a and 38b, respectively. In terms of electronic absorption, the molar extinction coefficients of the dye complexes **39c-i** and **N3** are different when they are in solution from when they are anchored to TiO_2. This difference

could be due to the anchoring carboxylate groups or to the amount of dye that is adsorbed on the TiO_2 surface. When the dye complexes are in solution, the carboxylate groups are free, but when the dye complexes are on the TiO_2 surface the carboxylate groups are not free but are anchored to the TiO_2. The concentration of the compounds in solution is certain and known. Since the thickness of the TiO_2 and the amount of the dye that is anchored to the surface is not known, the concentration of the anchored compound is not certain so the molar extinction coefficient of the complexes is different from solution to the anchored surface. For example, the molar extinction coefficient of **39e** is highest in solution ($5x10^{-5}$ M in MeOH), but lower when **39e** is anchored to the TiO_2 surface.

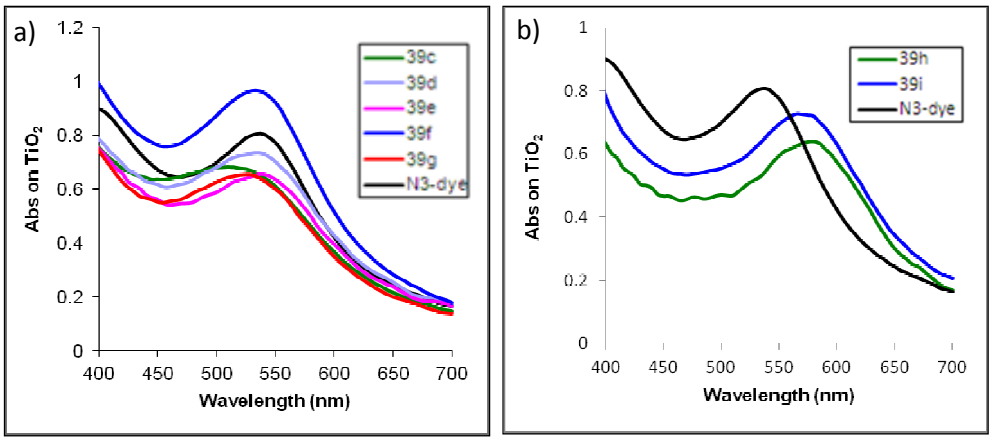

Figure 38. Electronic absorption spectra of a) **39c-g** and b) **39h-i** on TiO_2 surface.

We also prepared complex **51** which is an analog of the **black** dye. The electronic absorption spectrum of **51** in methanol is shown in Figure 39. Complex **51** has an absorption maximum at 663 nm. Among all the dye complexes that we have studied, **51** shows the lowest energy absorption. This bathochromic shift is due to the favoured stabilisation of the excited state by the anionic thiocyanato ligands as well as the conjugated terpyridine subunit ligand anchored to the ruthenium. The addition of the

fused pyrido group to the terminal pyridines of the tpy ligand, extends the π conjugation and causes the lower energy absorption by stabilizing the π* orbital of **51**, thus decreasing the energy gap between t_{2g} and π* orbitals.

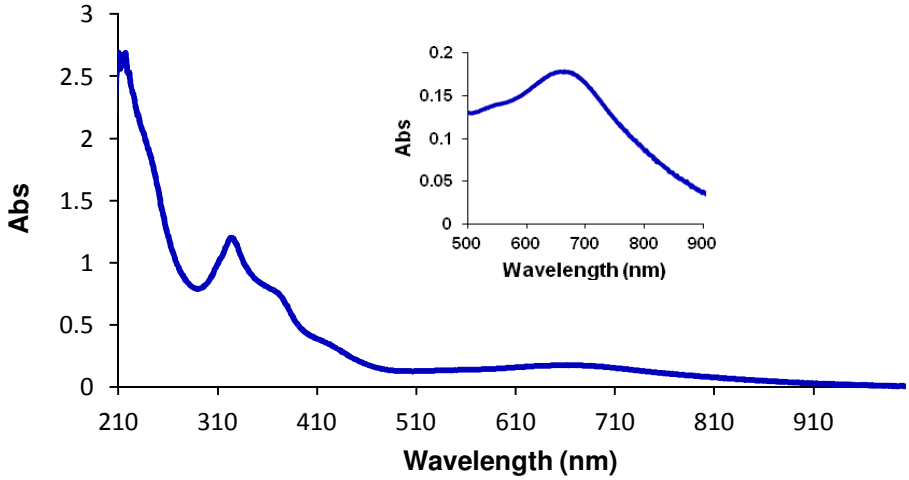

Figure 39. Electronic absorption spectra of **51**, $5x10^{-5}$ M in MeOH.

Table 7. Electronic absorption maxima and molar extinction coefficients for Ru(II) complexes **39 c-i**, **N3** and **black** dyes.

Compound	RSH-number	λ_{max}; nm (ε x 10^3 M^{-1} cm^{-1})[a]
[Ru(**34a**)(**13**)$(NCS)_2$] (**39c**)	RSH-165	518 (4.8), 369 (6.0), 308 (17.1)
[Ru(**34b**)(**13**)$(NCS)_2$] (**39d**)	RSH-471	515 (6.3), 369 (8.1), 308 (23.2)
[Ru(**34c**)(**13**)$(NCS)_2$] (**39e**)	RSH-554	518 (7.1), 369 (8.77), 309 (25.3)
[Ru(**35a**)(**13**)$(NCS)_2$] (**39f**)	RSH-510	479 (6.4), 353 (8.2), 291 (30.3)
[Ru(**35b**)(**13**)$(NCS)_2$] (**39g**)	RSH-538	518 (4.1), 368 (5.6), 308 (17.0)
[Ru(**37a**)(**13**)$(NCS)_2$] (**39h**)	RSH-167	576 (6.1), 471 (3.9), 340 (17.4)
[Ru(**37b**)(**13**)$(NCS)_2$] (**39i**)	RSH-171	569 (5.7), 476 (3.5), 349 (18.3)
N3 dye	--	513 (7.6), 377 (8.0), 309 (31.4)
[Ru(**48**)$(NCS)_3$] (**51**)	RSH-468	663 (3.6), 425 (sh), 371 (sh), 324 (24.1)
Black dye[140]	--	625, 556 (sh), 429

[a] Measured in MeOH ($5.0 x 10^{-5}$ M) at 298 K; sh = shoulder.

3.10.6.3. Infrared spectroscopy

The problem of determining the bonding modes of coordinated ambidentate ligands has been addressed by IR. The IR spectra of the complexes **39c-i** and **N3** were measured as a solid sample. The FT- IR spectrum of **N3** is shown in Figure 40.

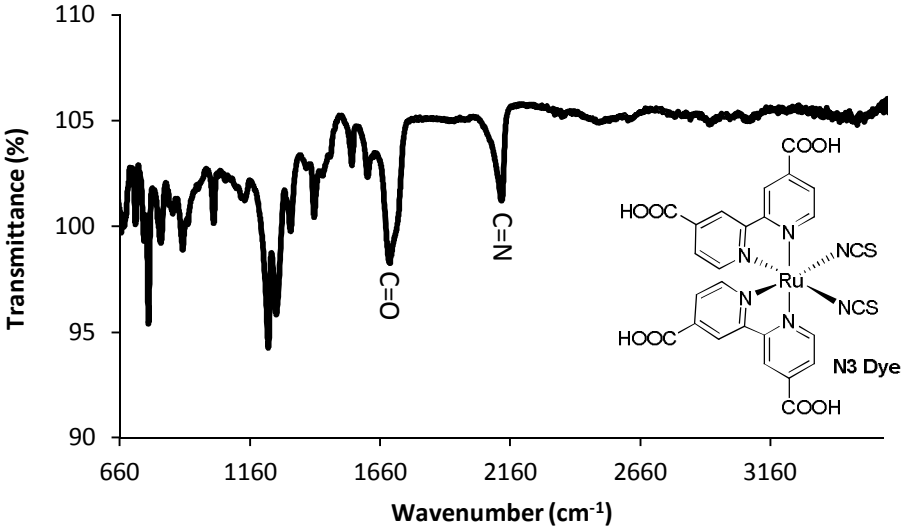

Figure 40. FT-IR spectrum of the **N3** dye.

The peaks at 3320-3330 cm^{-1} are assigned to the hydroxyl group. The NCS group had one characteristic mode υ_{CN} that has been frequently considered as diagnostic. Kohle *et al.*[154] showed by using a sample containing both isomers with N:S ratio of 79% : 21% that the υ_{CN} band of the S-bonded isomer is shifted to lower energy, relative to those of the N-bonded species (Figure 41b).

The strong stretching band at 2101-2105 cm^{-1} is assigned to the NCS stretching of the N-coordinated NCS ligand. Figure 41c shows a portion of the IR spectrum of **39g**. The band shape of the spectrum is consistent with N-coordinated of thiocyanate ligand

for all complexes **39c-i** and **51**. Another indication of thiocyanate ligand coordination to the metal is the stretching band at 1998 cm^{-1}. No peak for S-coordinated SCN at 1998 cm^{-1} was observed. The bands at 1720-1726 cm^{-1} are assigned to the carbonyl (C=O) stretching mode of the carboxylic acid (Table 8). Bands between 600 and 1000 cm^{-1} are due to C=S stretching and C–H bending modes.

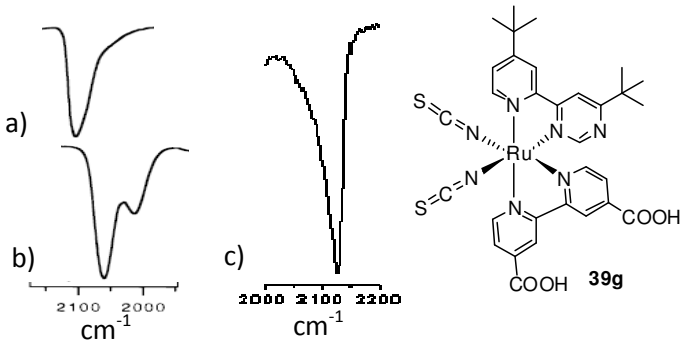

Figure 41. Portion of the IR spectrum of a) N-bound isothiocyanato (υ_{CN} = 2110 cm^{-1}) , b) a sample containing 21% S- and 79% N-bound forms of the same complex (S-bound complex: υ_{CN} = 2056 cm^{-1}), and c) complex **39g**.

Table 8. The IR data for free dye molecules.

Complex	IR (cm^{-1})
39c	3320, 2103, 1723
39d	3322, 2105, 1720
39e	3323, 2105, 1726
39f	3321, 2103, 1724
39g	3330, 2102, 1720
39h	3320, 2104, 1726
39i	3329, 2101, 1726
N3 dye	3464, 2131, 1698
51	3481, 2107, 1722
Black dye[155]	3478, 2100, 1701

3.10.6.4. Electrochemical studies

The cyclic voltammograms of complexes **39c-i** and **51** were recorded in methanol at room temperature and the electrochemical properties are summarized in Table 9. Figure 42a shows the oxidative wave for complex **39g** and Figure 42b shows the reductive wave. The oxidation of a Ru(II) complex involves the removal of one electron from the HOMO, which is a metal-centered d-orbital. The reduction of a Ru(II) complex is ligand-centered and involves the addition of one electron to the π* LUMO of the ligand.

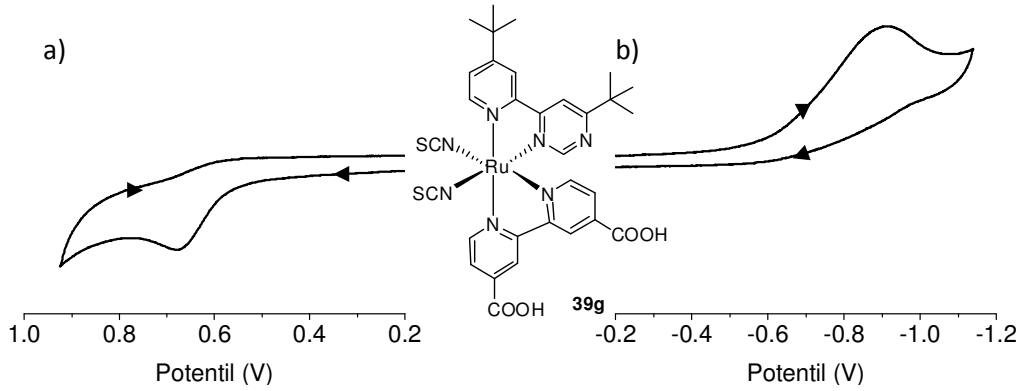

Figure 42. Cyclic voltammogram a) oxidation and b) reduction of **39g** vs SCE in methanol (0.1 M $TBAPF_6$, 100 mv/s, at rt).

The reduction waves attributed to the RuII/I redox couple and the oxidation waves attributed to the RuII/III redox couple show irreversible behavior which is due to carboxylic acid protons that are reduced on the surface of the glassy carbon electrode.[156]

There is one irreversible oxidation wave observed for the dye complexes **39c-i** and **51**. The oxidative waves for complexes **39c-g** are observed at +0.71 to +0.77 V, for complexes **39h-i** at +0.84 to +0.85 V, and for complex **51** at +0.81 V.

The oxidation potentials for pyridyl-pyrimidine complexes **39c-g** are smaller than the **N3** dye it means that **39c-g** complexes stabilize the oxidized species and oxidize easier than the **N3** dye. The quinoxaline derivatives **39h-i** have slightly higer oxidation potential than the **N3** dye which expresses **N3** dye can oxidize easier than the quinoxaline derivatives.

The reduction waves for complexes **39c-i** and **51** are also irreversible. The first reduction waves for complexes **39c-g** are observed at -0.88 to -1.30 V, for complexes **39h-i** at -0.89 V, and for complex **51** at -0.79 V.

The first reduction potential for complexes **39c-e** changes from -0.88 V to -1.30 V. Complexes **39c-e** stabilizes the reduced species in the order of: **39d** (-0.88 V) > **39c** (-0.90 V) > **39e** (-1.30 V). The first reduction potential of complexes **39f** and **39g** are -1.25 and -1.28 V, respectively. Quinoxaline derivatives **39h-i**, stabilize the reduced species in the same order since both have the same reduction potential at -0.89 V.

The oxidation and reduction potentials for complex **51** is at +0.81 V and at -0.79 V, respectively. Complex **51** with extended π conjugation compare to **black** dye has a higher oxidation potential that able to less stabilize the oxidized complex, and has a lower reduction potential than **black** dye.

Table 9. The redox data[a] (E) for Ru(II) complexes **39c-i**, **51**, **N3** and **black** dyes.

Compound	RSH-number	$E^{ox,ir}$ (V)	$E^{red,ir}$ (V)
[Ru(**34a**)(**13**)$(NCS)_2$] (**39c**)	RSH-165	+0.77	-0.90, -1.26
[Ru(**34b**)(**13**)$(NCS)_2$] (**39d**)	RSH-471	+0.75	-0.88, -1.28
[Ru(**34c**)(**13**)$(NCS)_2$] (**39e**)	RSH-554	+0.76	-1.30, -1.71
[Ru(**35a**)(**13**)$(NCS)_2$] (**39f**)	RSH-510	+ 0.74	-1.25, -1.73
[Ru(**35b**)(**13**)$(NCS)_2$] (**39g**)	RSH-538	+0.71	-1.28, -1.70
[Ru(**37a**)(**13**)$(NCS)_2$] (**39h**)	RSH-167	+0.85	-0.89
[Ru(**37b**)(**13**)$(NCS)_2$] (**39i**)	RSH-171	+0.84	-0.89
N3 dye	--	+0.80	-0.92, -1.75
[Ru(**48**)$(NCS)_3$] (**51**)	RSH-468	+0.81	-0.79, -1.01
Black dye[140]	--	+0.72	-1.10

[a] Measured relative to SCE in MeOH containing $TBAPF_6$ (0.1 M); ir = irreversible.

3.10.6.5. Mass Spectra

The MALDI-TOF mass spectra for complexes **39c-g** and **39i** showed a pattern corresponding to the loss of one NCS, one methyl and one hydrogen and the isotopic distribution is identical with the simulation of the parent complexes $C_xH_yN_6O_4RuS$. The MALDI-TOF mass spectrum for complex **39h** showed a pattern corresponding to the loss of one NCS and one hydrogen and the isotopic distribution is identical with the simulation of the parent complex $C_{26}H_{15}N_6O_4RuS$.

The MALDI-TOF mass spectrum of complex **51** showed a patern at *m/z* 682 and 624 corresponding to the loss of one and two NCS, respectively. The MALDI-TOF mass spectrum and the calculated mass distribution for $[M-(CH_3)-(NCS)-(H)]^+$ calculated for $C_{30}H_{30}N_6O_4RuS$ for complex **39g** is shown in Figure 43.

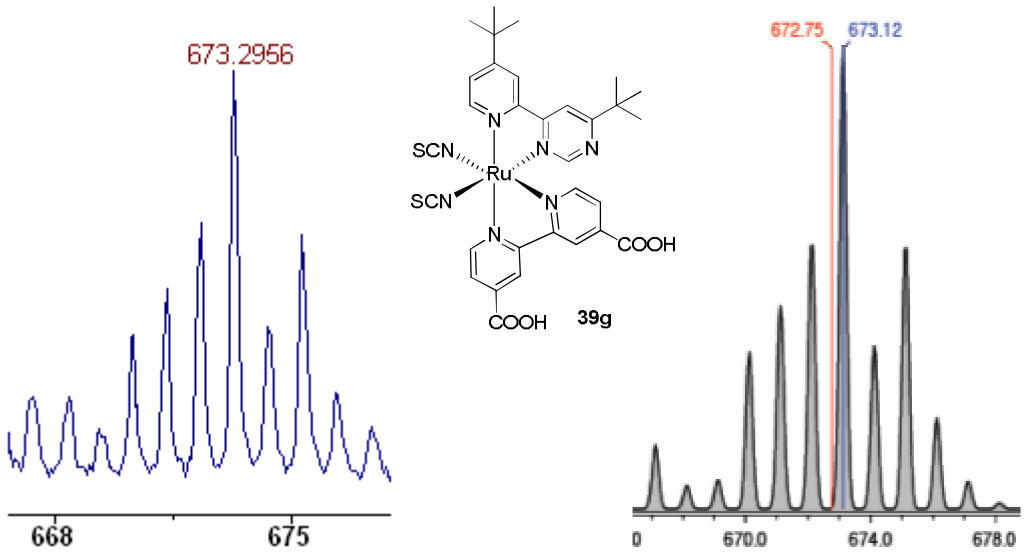

Figure 43. The MALDI-TOF mass spectrum of **39g** (left) and the calculated mass distribution (right) for $[M-(CH_3)-(NCS)-(H)]^+$ calculated for $C_{30}H_{30}N_6O_4RuS$.

3.10.6.6. Photovoltaic measurements

The photovoltaic performance of thin films of anatase TiO_2 impregnated with the dyes **39c-i** was evaluated by our collaborator Patrik Johansson in the Meyer Research Group at Johns Hopkins University. Solar cells were constructed from **39c-i** and **N3** dyes and irradiated over the region from 400 to 700 nm. The photocurrent action spectra were obtained in this manner and are shown in Figure 44. A solar cell for the **N3** dye was constructed and irradiated over the same region as dyes **39c-i** for comparison purposes.

The band shapes of the photocurrent action spectra closely parallel the absorption spectra for the dyes **39c-i** as shown in Figure 37. The low energy portion of the absorption bands extends into the near infrared and the IPCEs for the dyes **39c-g** at 550 nm varies from 25-56% (Figure 44a). For dyes **39h** and the **39i** IPCEs at 550 nm are 15% and 11%, respectively (Figure 44b). With regard to peak IPCE performance at 550 nm,

the **N3** dye shows the best efficiency at 65% while **39f** showing 56% and **39g** showing 54% are not far behind. The dyes **39d** and **39e** are respectable at 50% and 48%, respectively. The IPCE value for the **N3** dye is somewhat less than the best reported value but at least provides a standard to compare other compounds.

Sensitizers involving 4-(pyrid-2'-yl)-pyrimidine, show good IPCE indicating that the addition of an alkyl group, increases solar device efficiency. When the bulky *t*-Bu group is on the pyrimidine ring as in complexes **39f-g**, the IPCE value increases. The IPCE values for the quinoxaline derivatives with extended π conjugation are not high. The low IPCE values for the **39h-i** could be explained due to inefficient electron injection in the presence of I^-/I_3^- or to a fast disappearance of the oxidized dye by a very fast recombination with the injected electrons, or both. The IPCE data is tabulated in Table 10.

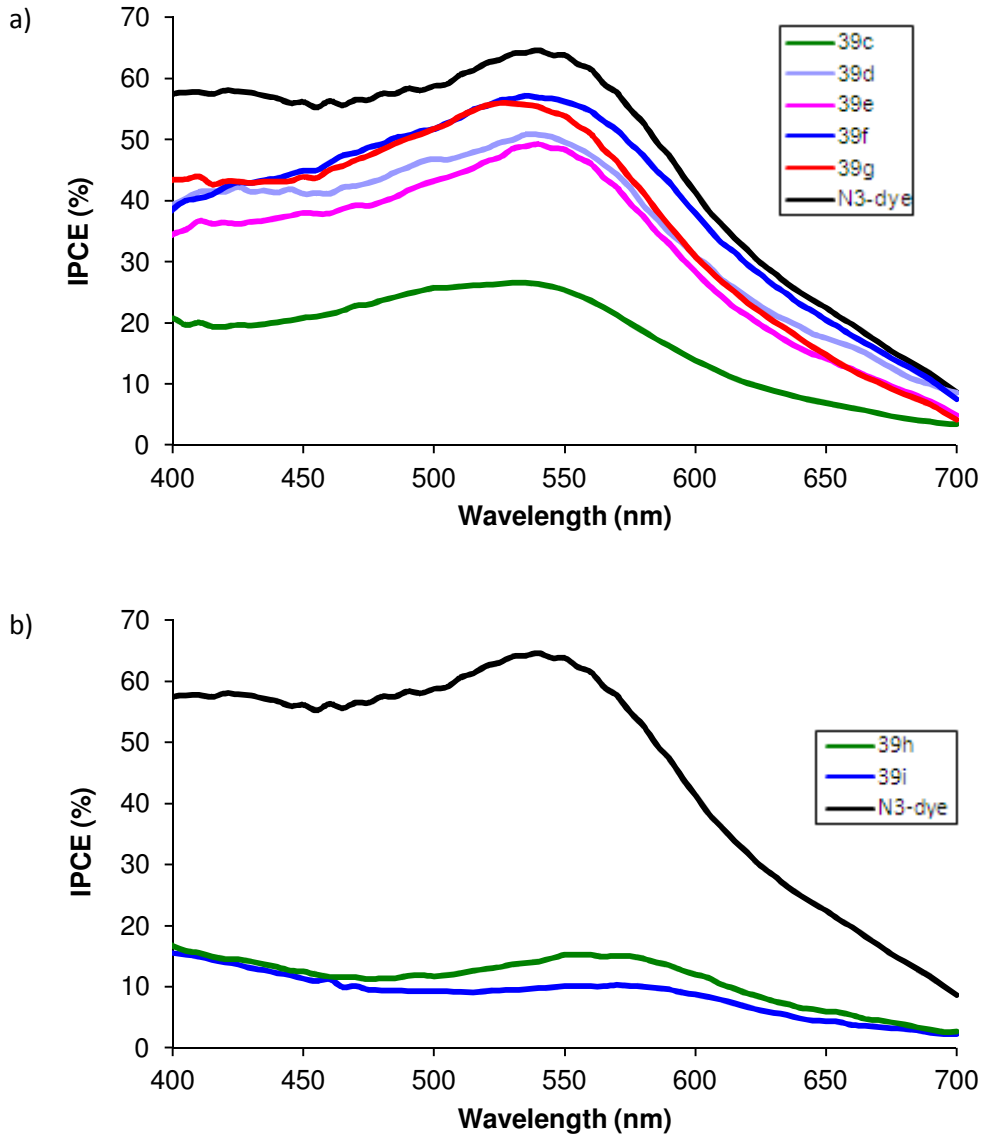

Figure 44. IPCE graphs for dye molecules: a) **39c-g** and b) **39h-i**.

Table 10. The IPCE data for dye complexes **39c-i** and **N3** at 550 nm.

Complex	IPCE
[Ru(**34a**)(**13**)$(NCS)_2$] (**39c**)	25%
[Ru(**34b**)(**13**)$(NCS)_2$] (**39d**)	50%
[Ru(**34c**)(**13**)$(NCS)_2$] (**39e**)	48%
[Ru(**35a**)(**13**)$(NCS)_2$] (**39f**)	56%
[Ru(**35b**)(**13**)$(NCS)_2$] (**39g**)	54%
[Ru(**37a**)(**13**)$(NCS)_2$] (**39h**)	15%
[Ru(**37b**)(**13**)$(NCS)_2$] (**39i**)	11%
N3 dye	63%

3.11. Summary of Results

The results of this project are summarized as follows:

1. The 2-cyano-4-methyl pyridine (**3b**) in 33% yield, the pyridine-2-carboxamidines (**27a** and **27b**) in 60% yields, 4-alkyl substituted 2-acetyl pyridines (**30b** and **30c**) in 30-45% yields, pyridine-2-carboxamidine (**31a-c** and **32a-b**) derivatives in 50-85% yields, **42** in 70% yield, α-ketoester moiety **44** in 80% yield, 2,6-diacetylisonicotinate (**47**) in 70% yield were synthesized and characterized by ^{1}H and ^{13}C NMR and IR.
2. Ligands **29a-b** (50-80%), **34a-c** (40-45%), **35a-b** (35-40%), **37a-b** (70-80%), **48** (90%) and **49** (60%) were synthesized and characterized by ^{1}H and ^{13}C NMR, IR, and elemental analysis.

3. Substitution of the alkyl group on the pyrimidine, pyridine, or quinoxaline rings causes a change in the ^{1}H chemical shifts. The bulkier electron donating *t*-Bu group has less effect than the smaller electron donating CH_3 group.
4. The Ru(II) complexes **39a-i** (45-60%) and **51** (40%) were synthesized in DMF and characterized by ^{1}H NMR, IR, UV-vis spectroscopy, CV and mass spectrometry.
5. The Ru(II) complexes **39a-b** could not be purified due to the formation of 4 isomers.
6. The Ru(II) complexes **39c-i** were isolated as a pair of isomers.
7. The Ru(II) complex **51** was isolated as a single product.
8. The NCS groups in the Ru(II) complexes **39c-i** and **51** are N-coordinated.
9. The MALDI-TOF mass spectra for complexes **39c-g** and **39i** showed a pattern corresponding to the loss of one NCS, one methyl and one hydrogen with $C_xH_yN_6O_4RuS$ isotopic distribution. Complex **39h** showed a pattern corresponding to the loss of one NCS and one hydrogen with $C_{26}H_{15}N_6O_4RuS$ isotopic distribution.
10. With regard to peak IPCE performance at 550 nm, the **N3** dye shows the best efficiency at 65% while **39f** at 56% and **39g** at 54% are respectable, as are **39d** and **39e** at 50% and 48%, respectively. The IPCE values for the quinoxaline derivatives with extended π-conjugation are low.
11. We have demonstrated that for the design and synthesis of heteroleptic Ru complexes the presence of substituents on one of the aromatic ligands coordinated

to the ruthenium atom has an influence on the spectroscopic and electrochemical properties, and device performance.

3.12. Perspective and Future Work

Ru complexes have shown good photovoltaic properties with a broad absorption spectrum, suitable excited and ground state energy levels, relatively long excited-state lifetime, and good (electro)chemical stability.

Many efforts have been made to optimize the ligands of Ru photosensitizers complexes. Several Ru complexes used in DSSCs have reached more than 10% solar cell efficiency under standard measurement conditions. A challenging but realizable goal for the present DSSC technology is to achieve efficiencies above 15%. The design of new ligands leading to the preparation of new Ru sensitizers is a convenient and versatile new route to achieve high efficiencies. Further work will be targeted at extending the conjugated system of the ligand. Employing a slightly longer hydrocarbon chain might be advantageous and could lead to even higher efficiencies.

4. RUTHENIUM (II) COMPLEXES INVOLVING BI-4-AZAACRIDINE

4.1. Introduction

As mentioned in the earlier chapter, fossil fuels will not last forever. Alternative energy sources must be developed based not only on practical, economic considerations but also from an environmental standpoint. Solar energy represents the best ultimate solution to these long term energy needs. From earliest times nature has recognized this unavoidable mandate and thus photosynthesis is the principle source of biochemical energy.

Molecular hydrogen is a clean burning, high energy fuel free of CO_2 emission. Hydrogen can be derived from the most pervasive and inexpensive substance on earth: water. Thus the photochemical decomposition of water into its elements may represent a long range solution to solve the current energy problem.[157]

Conceptually, the process is deceptively simple. Light-driven water decomposition mimics the process of photosynthesis.[11,12] Decomposition of water into hydrogen and oxygen requires a molecular catalyst to facilitate the bond breaking and bond making steps. Sunlight will supply the required energy to an appropriate photoredox catalyst which will utilize this energy to convert water into hydrogen and oxygen.[158]

The overall water decomposition involves the transfer of four electrons (Eq. 4.1). The exact mechanism for this process is not well understood but several features are clear. The bond breaking step will be cleavage of the O-H bond and the bond forming

steps will be H-H and O=O formation. The reduction of protons to hydrogen atoms and their subsequent combination to form molecular hydrogen is reasonably well understood.[159] The corresponding oxidation of hydroxide,[160] hydroperoxide,[161] or superoxide to dioxygen is much less understood.[162]

$$2H_2O + h\nu \rightarrow 4H^+ + 4e^- + O_2 \qquad \text{Eq. 4.1}$$

The key to this approach is clearly the photoredox catalyst which ideally would be an inexpensive, stable, water soluble substance which could effectively decompose water with high turn-over efficiency. The half-filled HOMO and LUMO orbitals of the catalyst's photoexcited state allow catalyst to undergo sequential oxidation and reduction (not necessarily in that order), ultimately regenerating the original catalyst.

The tris(2,2'-bipyridine)-ruthenium(II), $[Ru(bpy)_3]^{2+}$, has attracted considerable attention for many years due to its potential application as a photosensitizer for the visible light induced splitting of H_2O into its elements.[39,163] The important design features of an effective photocatalyst are the following:

1. Light absorption in the available region of the solar spectrum (400-700 nm).
2. Existence of an accessible and sufficiently long-lived excited state of appropriate energy to accomplish the desired redox chemistry.
3. High quantum yield for the population of the excited state and the absence of competing pathways for its decay.
4. An efficient mechanism for the desired redox reactions. The excited state energy must be sufficient for the required reduction and oxidation steps.

The $[Ru(bpy)_3]^{2+}$ complex meets the first two requirements and partially satisfies the third. $[Ru(bpy)_3]^{2+}$ has an absorption at 452 nm, emission at 607 nm and long lifetime excited state (1.10 μs). Irradiation of salts of $[Ru(bpy)_3]^{2+}$ dissolved in water produce neither hydrogen nor oxygen. Several systems have been designed involving additional species to help to complete the photocatalytic cycle.[164]

Our approach proposed to stay close to the $[Ru(bpy)_3]^{2+}$ prototype by merely replacing a pyridine ligand with a water molecule. A key feature of such a photocatalyst would be a coordinated water molecule can photooxidize to a metal-oxo species and liberate H_2. In this regard the $[Ru(bpy)(tpy)(H_2O)]^{2+}$ complex has been extensively studied by Meyer and others.[165]

Up to the present, efforts have focused on understanding the photochemistry and photophysics of the water decomposition problem, concentrating primarily on the inorganic chromophore (metal) and possible electronic relay systems designed to stabilize and utilize the photoexcited state.[166] Major efforts in the area of ligand design have addressed fine tuning of the photophysical properties of the complex[167] or immobilizing it onto an appropriate support.[168] Relatively little attention has been devoted to the design of supramolecular assemblies that will promote the necessary bond breaking and forming steps required for water decomposition.

In designing ruthenium polypyridine complexes that have specific electronic and photophysical properties, the choice and function of the ligands plays a dominant role. The fundamental pyridine moiety found in bpy and tpy can be replaced with a wide

variety of other azaaromatic ring systems that, in turn, can be used to tune and modulate the properties of the resulting metal complex. Two types of structural variation can be exploited in this regard. Additional heteroatoms can be introduced into the ligand system. For example, pyridine can be substituted with pyrimidine, pyrazine, or pyridazine.[169] These aza-analogues of pyridine cause the heteroaromatic ring to be more electronegative and also provide a potential second binding site leading to a wide variety of bridging ligands.

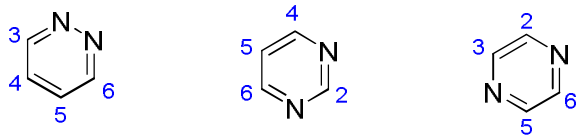

A second important effect involves the fusion of an additional aromatic ring onto pyridine that will extend the π–system and create a more delocalized ligand. Both of these effects, increasing electronegativity or delocalization, will have a similar effect on the electronic properties of the ligand and its resulting metal complexes. The energy of the π*–state will be lowered and hence the energy required for a photoinduced metal-to-ligand charge transfer will diminish and this electronic absorption will occur at lower energy or become "red-shifted" (Figure 45).

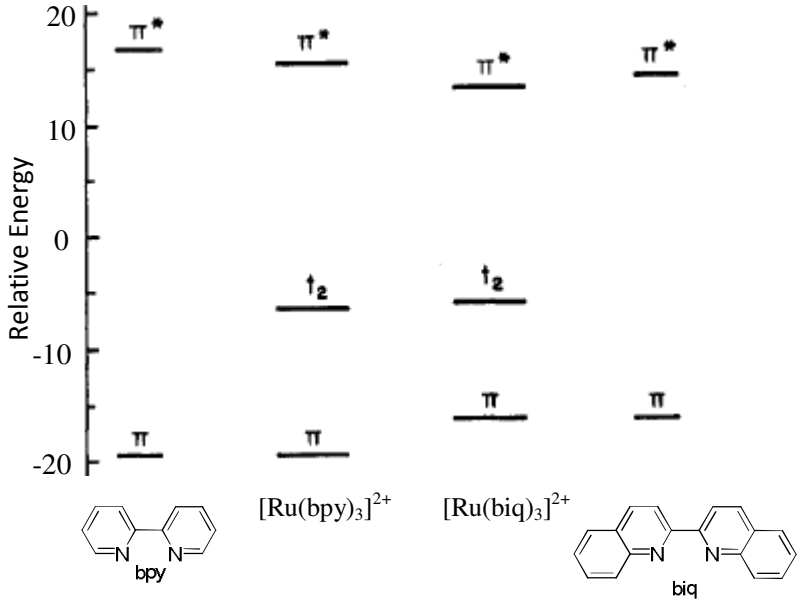

Figure 45. Relative orbital energies of 2,2'-bipyridine (bpy) and 2,2'-biquinoline (biq) ligands and their tris homoleptic Ru(II) complexes.

A series of heteroaromatic nuclei that exhibit this combination of effects might include pyridine, quinoline, 1,8-naphthyridine, and 4-azaacridine. The 1,8-naphthyridine might be considered as an 8-azaquinoline. Locating the second nitrogen at the 8-position of quinoline provides the maximum electronegativity effect on N1 that is most often the metal binding site. Chances for bridging are also diminished simply due to congestion that would result from simultaneous N1 and N8 binding to two different metal-centers. The fusion of a benzo-ring onto 1,8-naphthyridine results in the formation of 4-azaacridine where both increased electronegativity and increased delocalization effects should be apparent.

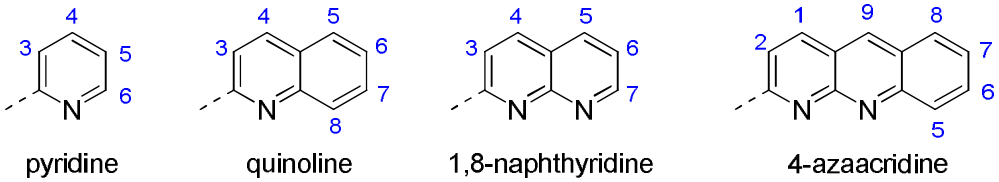

There has been considerable recent interest in the study of macrocycles containing polypyridyl subunits and their metal complexes. Polyaza-cavity-shaped molecules are well designed for interaction with metals.[170] Naphthyridines and their derivatives are of great importance because of their broad applications in biological activity and organic chemistry.[171] Cyclic systems are quite effective in chelating a single metal atom, and they do not lend themselves to the incorporation of more than one metal in a stereocontrolled fashion.[172]

4.2. Polypyridine Ligands and their Ru(II) Complexes

Based on the properties of $[Ru(bpy)_3]^{2+}$ in photosensitized electron transfer processes, modifications of the bipyridine ligands have been investigated. In this regard, Ru (II) complexes of 2,2'-biquinoline and 2,2'-binaphthyridine ligands are of interest.[173]

4.2.1. Quinolines

The fusion of a benzo ring onto pyridine provides quinolines. The condensation of 2-aminobenzaldehyde with 2-acetyl pyridine gives 2-(pyrid-2'-yl) quinoline (pq). The condensation of 2-aminobenzaldehyde with 2,3-butanedione gives 2,2'-biquinoline (biq).[174] The biq can be considered as a dibenzo derivative of 2,2'-bipyridine. The investigation was prompted by the steric requirements of this ligand.[175] Due to the position of the fused benzo rings with hydrogen atoms at 8 and 8' positions, the biquinoline is a more sterically demanding ligand than bipyridine.[176,177]

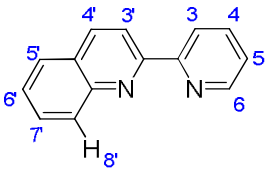

pyridyl quinoline

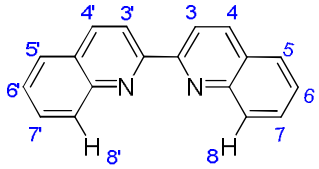

2,2'-biquinoline

4.2.2. Naphthyridines

The addition of a nitrogen atom at the 8-position of quinoline provides 1,8-naphthyridines. The condensation of 2-aminonicotinaldehyde with 2-acetyl pyridine gives 2-(pyrid-2'-yl) naphthyridine (pynap). The condensation of 2-aminonicotinaldehyde with 2,3-butanedione gives 2,2'-bi-[1,8]-naphthyridine (binap).[178,181] Due to the fused pyrido rings with nitrogen atoms at 8 and 8' positions, binaphthyridine is a more red-shifted ligand than bipyridine and biquinoline.

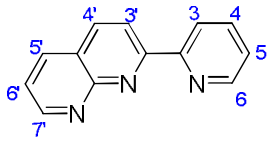

pyridyl naphthyridine

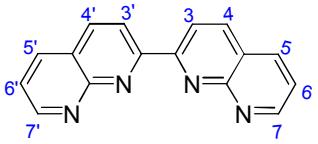

2,2'-binaphthyridine

4.2.3. Ru(II) complexes of quinolines and naphthyridines

Rebek and co-workers have bridged 2,2'-bipyridine at the 3 and 3' positions, with ethylenedioxy units, to create macrocycles capable of demonstrating an allosteric effect by site-specific metal binding.[179]

For several years chemists have been interested in the effects of annelation on aromaticity and have prepared and studied a series of mono- and bis-annelated pyridines

to establish the effects of annelating four- and five-membered rings to the pyridine nucleus.[180]

Thummel and co-workers reported the preparation and properties of a series of 3,3'-annelated derivatives of 2,2'-bipyridine, **96a-d**, and their conversion of 1,l'-ethano-bridged diquaternary salts, **97a-d**. The diquaternary salts **97a-d** were readily prepared by heating **96a-d** in 1,2-dibromoethane for 2 h during which time the desired material precipitated from solution.

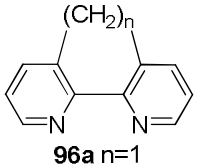

96a n=1
b n=2
c n=3
d n=4

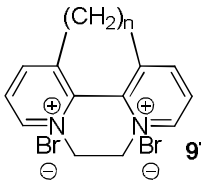

97a n=1
b n=2
c n=3
d n=4

Thummel and coworkers also prepared a series of 3,3'-annelated 2,2'-biquinolines[174] and 3,3'-annelated 2,2'-binaphthyridines[178] in which the length of the annelating bridge controls the relative orientation and dihedral angle of the two rings and thus influences the shape of the chelating bite.[181] The length of the annelated bridge varies from one to four methylene units. As the length of the aliphatic bridge is increased, the non-coplanarity of the system becomes more pronounced. The lowest energy conformation is nonplanar when the 3,3'-bridge contains two or more methylene units. The dihedral angle between the two covalently bonded aromatic rings is estimated to be 20^{o} for n = 2, 55^{o} for n = 3, and 80^{o} for n = 4. If effective coordination requires these two rings to become approximately coplanar, the bridging methylene units will experience

substantial torsional strain and nonbonded interactions as they are also forced closer to planarity. Some relief of this strain may be achieved by distortion of the 2,2'-bond connecting the aromatic rings in such a way as to bring the two rings closer to one another.

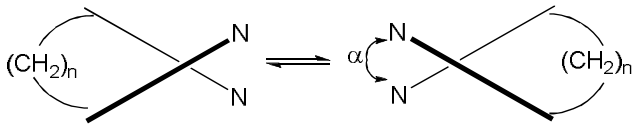

Thummel and coworkers prepared and examined $[Ru(\mathbf{57})_3]^{2+}$, $[Ru(\mathbf{58})_3]^{2+}$, $[Ru(\mathbf{59})_3]^{2+}$ and $[Ru(\mathbf{60})_3]^{2+}$, where three identical ligands are coordinated to the metal, and mixed ligand complexes $[Ru(\mathbf{57\text{-}60})(bpy)_2]^{2+}$ where one pq, pynap, biq, or binap ligand is coordinated along with two bipyridines to the metal. The replacement of bpy ligands with **57**, **58**, **59**, and **60** has yielded new complexes with modified properties that further increase the range of donor energies available for photosensitization processes.

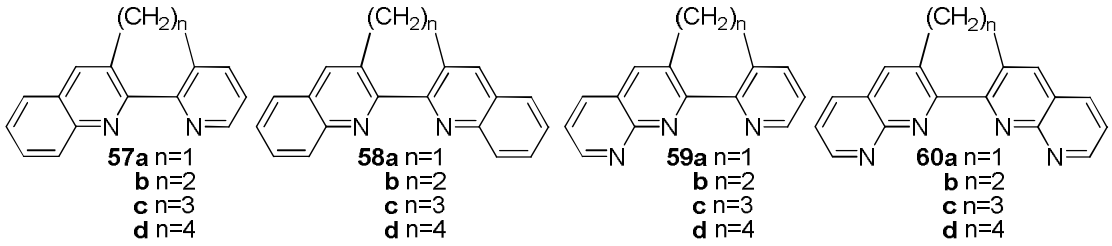

The MLCT absorption bands and emission bands of $[Ru(\mathbf{59})_3]^{2+}$ and $[Ru(\mathbf{60})_3]^{2+}$ occur at much lower energies than those of $[Ru(bpy)_3]^{2+}$ which is indicative of the effect of pyrido-substitution on the bpy ligand. The electronic absorption data for homoleptic Ru complexes of bpy, biq, binap, **58b**, and **60b** are tabulated in Table 11.

Table 11. Electronic absorption data for Ru complexes.[181]

Complex	λ_{max}/nm (εx10^3 M^{-1} cm^{-1})[a]
$[Ru(bpy)_3]^{2+}$	450 (14), 284 (80)
$[Ru(biq)_3]^{2+}$	524 (9), 485 (6.6), 512 (7.5), 380 (41)
$[Ru(\mathbf{58b})_3]^{2+}$	540 (8.1), 498 (5.8), 396 (34)
$[Ru(binap)_3]^{2+}$	596 (3.9), 572 (4.5), 550 (3.9), 342 (60)
$[Ru(\mathbf{60b})_3]^{2+}$	582 (10), 560 (7.8), 388 (33)

[a] Measured in CH_3CN.

The interest in the Ru complexes of biq and binap derives from the ease of reduction. These ligands ensure that photoexcitation of the complex results in the formation of a radical anion on the binap ligand as part of the MLCT excited state.[182] If the ligands could be doubly reduced, it is necessary that the first and the second reductions of their complexes are localized on the biq and binap ligands. So, they could act as a potent reducing agent. The ability of the ligand to store charge may also be mediated by the degree of planarity of the ligand.

Thummel[183] and Mayer[184] have studied a series of $[Ru(binap)(tpy)(H_2O)]^{2+}$ complexes (**61a-d**) as potential photooxidation mediators. The motivation behind studying these complexes is to have a free basic site that could mediate the proton transfer steps that accompany photo-induced electron transfers. The excited state properties of **61a-d** were studied, looking for increased basicity of the nap moiety in the excited state that might assist in the deprotonation of a metal-bound water and thus lead to photooxidation (**63**). This step involves the formation of a nap radical anion in the excited state (**62** → **63**) that could in turn act as an internal base to abstract a proton from the metal bound water leading to a Ru(III)-hydroxide (**64**).[184,185] The second proton

coupled electron transfer (PCET) step (**64** → **65**) is more difficult to envision. One possibility might be the coupling of two **64** radicals to give dimer **66** followed by disproportionation. A possible mechanism for PCET involving the 1,8-naphthyridine unit is given in Scheme 9. PCET is an an electrochemical reaction mechanism in which one electron and one proton simultaneously move in a concerted mechanism.

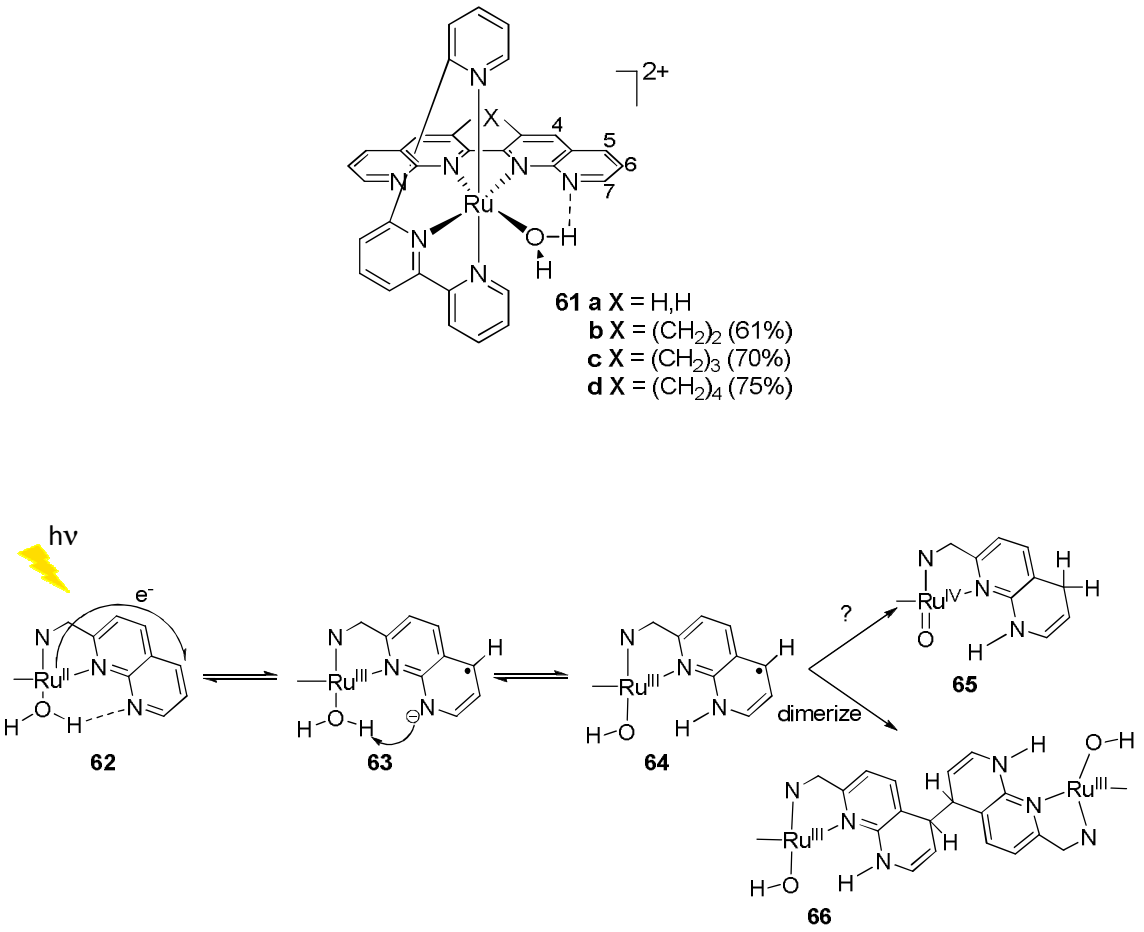

Scheme 9. Mechanism of proton coupled electron transfer (PCET) involving a 1,8-naphthyridine unit.

Photooxidation, evidenced by bleaching of the system, did not occur because the intermediate radical anion **63** is too unstable and the back electron transfer to the ground state occurs. Complexes **61a-d** were investigated using time resolved spectroscopy.[183] It

was found that the transient absorption signal from **61d** was considerably long lived than the corresponding signal from **61b**. The more distorted tetramethylene bridged binap ligand may somewhat inhibit the reverse PCET back to the starting **61d**.

Mayer and co-workers[184] reported that oxidation of the Ru in $[Ru(binap)(tpy)(H_2O)]^{2+}$ (**61a**) does not appear to result in proton transfer (**68**). The compound is most likely the Ru^{III}–aquo complex (**67**) and not the hydroxy-binap isomer (**68**). Thus this oxidation is not a coupled electron/proton transfer (Scheme 10). A more basic pendent ligand is needed.

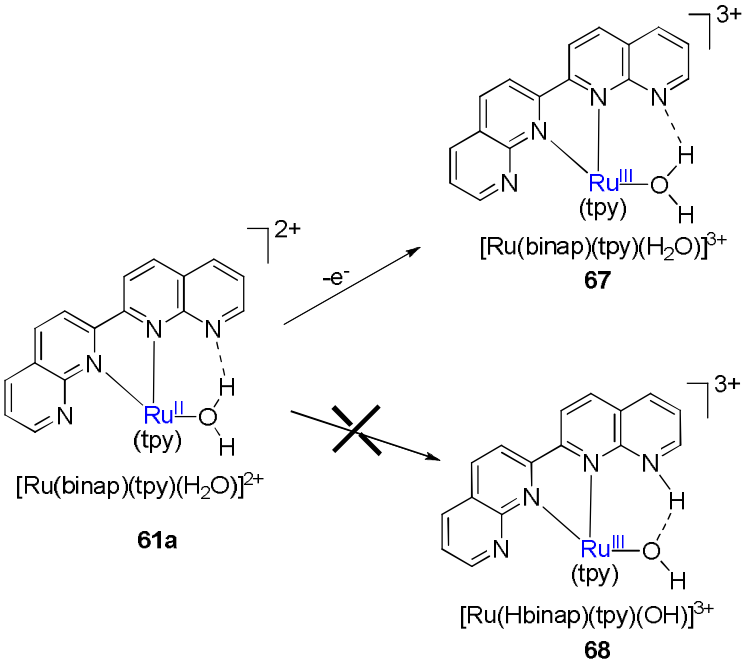

Scheme 10. Oxidation of $[Ru(binap)(tpy)(H_2O)]^{2+}$ (**61a**).

Zelewski and Balzani studied complexes of a series of 4,4'-dimethyl 3,3'-annelated biquinolines (**69**) where the annelating bridge contained one to three methylene units.[186] In a subsequent study, they elucidated the photophysical and electron-transfer

properties of $[Ru(\mathbf{69b})_n(bpy)_{3-n}]^{2+}$, where n=0-3.[187] Their results indicated that $[Ru(\mathbf{69b})(bpy)_2]^{2+}$ is expected to be a more efficient mediator than $[Ru(bpy)_3]^{2+}$ in the water splitting reaction. Such a mixed-ligand complex provides the basis for a new series of photochemically stable Ru-polypyridyl chromophores. The substitution of one or more of the bpy ligands in $[Ru(bpy)_3]^{2+}$ by larger, more sterically rigid, but electronically similar groups brings about increased decoupling of both absorption and emission states. $[Ru(\mathbf{69b})(bpy)_2]^{2+}$ has an absorption at 528 and 448 nm, emission at 730 nm and shorter lifetime excited state (0.38 μs). Indeed, **69a-c** has a much higher electron affinity than bpy and the absorption spectrum of $[Ru(\mathbf{69b})(bpy)_2]^{2+}$ shows higher intensity bands lying at lower energies than those of $[Ru(bpy)_3]^{2+}$. The shorter life time might be due to a smaller energy gap between the emitting state and the upper lying metal-centered excited state.

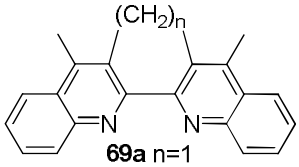

69a n=1
b n=2
c n=3

4.3. Objective of this Work

The goal is to build a molecule system that oxidation of the metal could mediate the proton transfer steps to accompany electron transfer steps. An additional benzo ring fused to the 6,7-position of the nap unit should help stabilize the intermediate radical anion **63**. For this reason a family of bidentate and tridentate ligands involving the 4-azaacridine nucleus were synthesized by the Friedländer condensation of 2-aminonicotinaldehyde (**74**) with appropriate diketones in KOH-EtOH solution. Bi-4-azaacridine may be considered as a biquinoline-fused analogue of bpy, which is both more delocalized and more electronegative, making it a much better charge acceptor.[188] This difference is evidenced by the absorption maxima of the free ligands, where the bpy long wavelength absorption is at 284 nm[189] and the bi-4-azaacridines absorption are at 321-362 nm. We have varied the conformation of the biaryl system by connecting the 3,3'-positions with a polymethylene bridge. It is noteworthy that the more planar system, profiting from better delocalization, has the lowest-energy absorption.

The bidentate bi-4-azaacridine ligands **76a-d** will in turn be used to prepare series of mixed-ligand complexes of the type $[Ru(\mathbf{76a\text{-}d})(bpy)_2]^{2+}$ and metal bound aquo $[Ru(\mathbf{76a\text{-}d})(tpy)(H_2O)]^{2+}$. $[Ru(\mathbf{76a\text{-}d})(bpy)_2]^{2+}$ were prepared to confirm that steric interaction associated with the bulky $Ru(bpy)_2$ moiety avoids the radical–radical coupling. This type of systems would allow investigating excited-state PCET reactions with a number of quenchers that can provide protons.[190] The photophysical, electrochemical, and structural properties of these systems will be examined.

4.4. Results and Discussion

4.4.1. Synthesis of 3,3'-annelated 2,2'-bi-4-azaacridines

The synthesis of the ligands **76a-d** starts with the preparation of the 2-aminoquinoline-3-carbaldehyde (**74**) (Scheme 11) and cyclic α-diketones (**75a-d**). Cyclization of acetanilide (**70**) with DMF-$POCl_3$ mixture afforded 2-chloro-3-quinolinecarbaldehyde (**71**) in 82% yield. Since direct aminolysis of 2-chloroquinoline-3-carbaldehyde (**71**)[191] with liquid or gaseous ammonia was not successful, the aldehyde group was protected with ethylene glycol to give **72** in 95% yield. The reaction of **72** with acetamide (**73**) in the presence of K_2CO_3,[192] followed by deprotection under acidic conditions afforded **74** in 50% yield (Scheme 11).

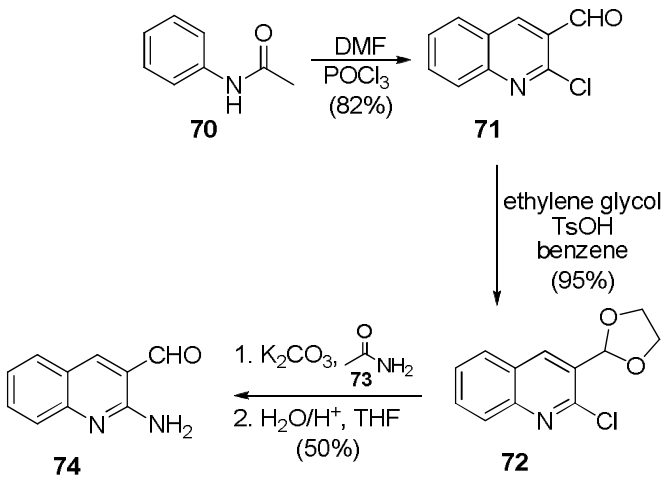

Scheme 11. Synthesis of 2-aminoquinoline-3-carbaldehyde (**74**).

The α-diketones 2,3-butanedione (**75a**) and 1,2-cyclohexanedione (**75b**) are commercially available. The cyclic α-diketones 1,2-cycloheptanedione (**75c**) and 1,2-

cyclooctanedione (**75d**) were prepared by the oxidation of cycloheptanone and cyclooctanone with selenium dioxide in ethanol in 90% yield, respectively.

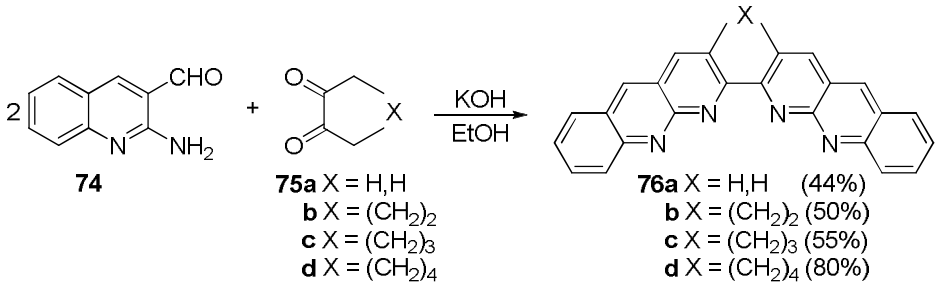

Scheme 12. Synthetic route to ligands **76a-d**.

Ligands **76a-d** were synthesized by the Friedländer condensation of two equivalents of **74** in ethanolic KOH with one equivalent of 2,3-butanedione (**75a**) at 50 ^{o}C to afford 3,3'-bi-4-azaacridine (**76a**) in 44% yield, one equivalent of 1,2-cyclohexanedione (**75b**) at reflux to afford 2,2'-dimethylene 3,3'-bi-4-azaacridine (**76b**) in 50% yield, one equivalent of 1,2-cycloheptanedione (**75c**) at room temperature to afford 2,2'-trimethylene-3,3'-bi-4-azaacridine (**76c**) in 55% yield, and one equivalent of 1,2-cyclooctanedione (**75d**) at room temperature to afford 2,2'-tetramethylene-3,3'-bi-4-azaacridine (**76d**) in 81% yield. The synthetic route to ligands **76a-d** is presented in Scheme 12.

4.4.2. Synthesis of $[Ru(76a\text{-}d)(tpy)(H_2O)]^{2+}$ complexes

The complex $[Ru(tpy)Cl_3]$ (**77**) was synthesized from $RuCl_3{\cdot}3H_2O$ using the method of Stoessel *et al.*[193] The synthesis of the $[Ru(\mathbf{76a\text{-}d})(tpy)(H_2O)]^{2+}$ complexes involved treating ligands **76a-d** with **77** in aq EtOH in the presence of triethylamine and precipitating the complexes as their hexafluorophosphate salts. This approach resulted in

low yields (<10%) for [Ru(**76a-c**)(tpy)(H_2O)]$^{2+}$ and did not work for [Ru(**76d**)(tpy)(H_2O)]$^{2+}$. So instead of using [Ru(tpy)Cl_3] which is poorly soluble in ethanol we used [Ru(tpy)(CH_3CN)Cl_2] (**78**) with good solubility in ethanol.

The complex [Ru(tpy)(CH_3CN)Cl_2] (**78**) was synthesized from [Ru(tpy)Cl_3] in chloroform-triethylamine-acetonitrile mixture using the method of Suen *et al.*[194] The complexes [Ru(**76a-d**)(tpy)(H_2O)](PF_6)$_2$ were prepared by treating one equivalent of the ligands **76a-d** with one equivalent of **78** in aq EtOH and precipitated as their hexafluorophosphate salts (Scheme 13). Purification was effected by the chromatography on alumina eluting with CH_2Cl_2/acetone (1:1). Since bi-4-azaacridine ligands have C_2-symmetry, a single isomer of the product is formed.

For the parent system, [Ru(bpy)(tpy)(H_2O)]$^{2+}$, the initially formed species is the chloro complex. For [Ru(bpy)(tpy)(Cl)]$^{+}$, the chloride can be exchanged for water only by heating the complex in acetone in the presence of Ag(I) to assist in ionizing the Ru-Cl bond.[165] The binap[183] and bi-4-azaacridine systems, however, hydrate spontaneously under the reaction conditions, promoted by anchimeric assistance from the uncomplexed N8 and N10, respectively. This assistance is manifested both by electrostatic repulsion between N8 (or N10) and the chloride leaving group and by stabilization of the incoming water through hydrogen bonding with N8 (or N10). Spec and co-workers have examined the structure of a similar [Ru(biq)(tpy)Cl]$^{+}$ system involving biq in place of binap.[195] Using the same preparative procedure, they do not obtain the aquo complex. Using binap, we get only the aquo complex and are unable to isolate the chloro complex.

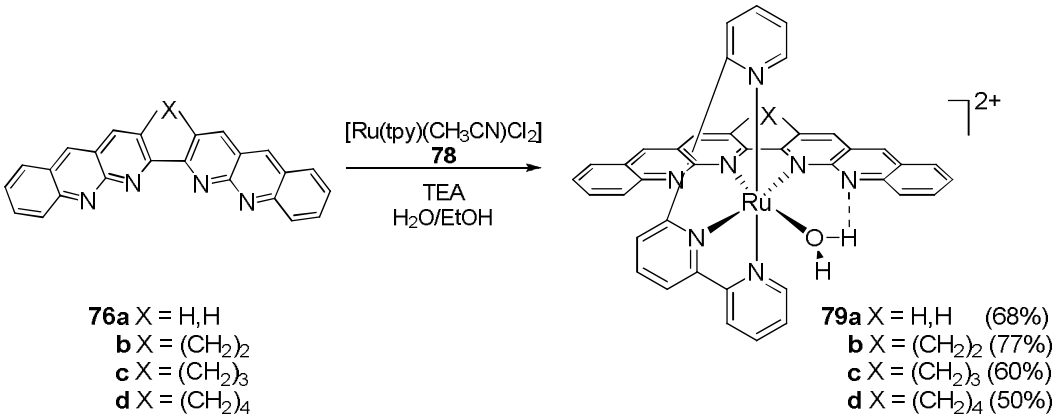

Scheme 13. Synthetic route to [Ru(**76a-d**)(tpy)(H_2O)]$^{2+}$ (**79a-d**) complexes.

4.4.3. Synthesis of [Ru(76a-d)(bpy)$_2$]$^{2+}$ complexes

The complex *cis*-[Ru(bpy)$_2$Cl$_2$]·2H_2O (**80**) was synthesized from $RuCl_3$·3H_2O using the method of Sullivan *et al.*[196] The mixed ligand complexes [Ru(**76a-d**)(bpy)$_2$]$^{2+}$ were prepared by treating one equivalent of the ligands **76a-d** with one equivalent of **80** in ethylene glycol in a microwave (MW) oven for 10 min. After cooling to room temperature, these complexes were precipitated as their hexafluorophosphate salts (Scheme 14). Purification was effected by the chromatography on alumina eluting with CH_2Cl_2/acetone (1:1). Since bi-4-azaacridine ligands have C_2-symmetry, a single isomer of product is formed.

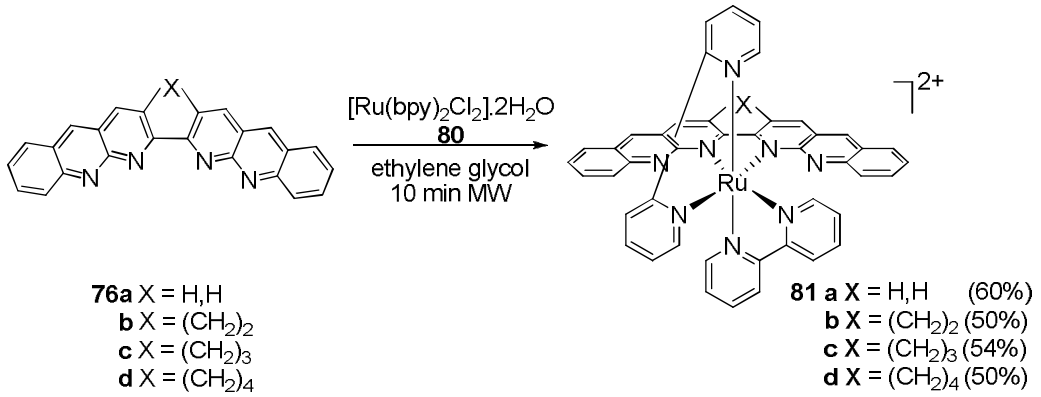

Scheme 14. Synthetic route to [Ru(**76a-d**)(bpy)$_2$]$^{2+}$ (**81a-d**) complexes.

4.4.4. Attempted synthesis of [Ru(76a-d)$_3$]$^{2+}$ complexes

Preparation of the homoleptic complexes [Ru(**76a-d**)$_3$]$^{2+}$ was attempted by treating 3.1 equivalents of the ligands **76a-d** with one equivalent of $RuCl_3 \cdot 3H_2O$ in ethylene glycol in a microwave (MW) oven for 10 min. After cooling to room temperature, the obtained complexes were extracted with CH_2Cl_2 (3 x 20 mL), dried over $MgSO_4$, and evaporated under vacuum. Purification was effected by the chromatography on alumina eluting with CH_2Cl_2/acetone (1:1). Even when 4 equivalents of the ligands **76a-d** were employed with longer reaction time, only [Ru(**76a-d**)$_2$Cl$_2$] complexes were obtained in 10-15% yields. The structures were confirmed by MALDI-TOF mass spectrometry.

4.4.5. Spectroscopic properties of the ligands

4.4.5.1. NMR spectra

The ^{1}H NMR spectrum of **76a** in $CDCl_3$ is shown in Figure 46. Compound **76a** is symmetric about the 2,2'-bond. The singlet at 8.92 ppm is assigned to H9. The downfield

AB doublets at 9.32 and 8.61 ppm are assigned to H2 and H1, respectively. This assignment was made based on the chemical shift of H1 in **76b**. H1 is singlet in **76b** and doublet in **76a**. Compound **76a** may exist in two planar conformations: *anti* and *syn*. Calculations using MM2 and mopac have revealed that the *anti* form is preferred in the solid state to avoid H-H and N-N interactions, but it is through the *syn* form that bidentate chelating occurs.

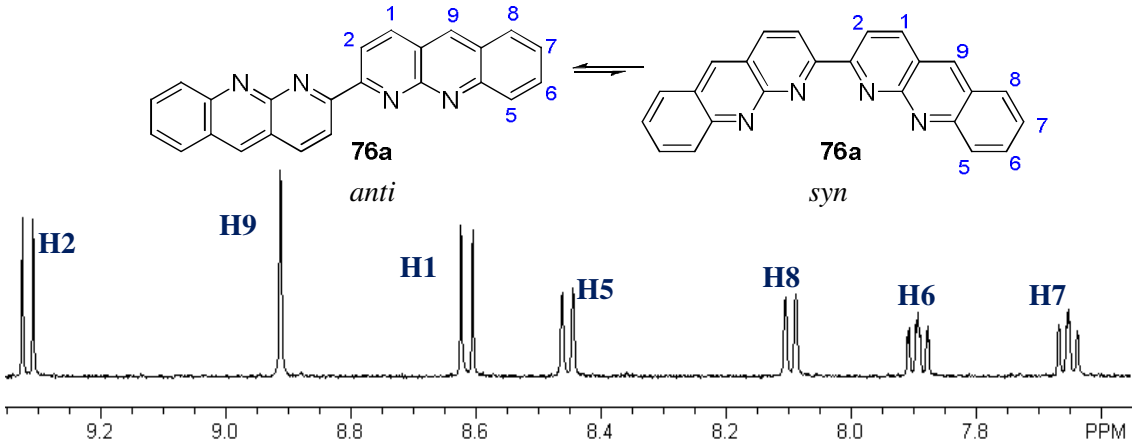

Figure 46. Downfield region of ^{1}H NMR spectrum of **76a** in $CDCl_3$ (400 MHz, at rt).

It has been reported by earlier workers[174,197] that the linear fusion of benzo-type rings to the parent bipyridine serve to sterically congest the coordinating pocket of the molecule in its *syn* conformation and limit the types of complexation which can occur. A way to lock the molecule into a *syn*-conformation would be to incorporate a polymethylene bridge at the 3,3'-positions. The length of the bridge controls the dihedral angle between the aromatic rings and thus the orientation of the unbound nitrogen with its unshared electron pairs that could influence the chemistry that might occur.

The ^{1}H NMR spectrum of **76b** in $CDCl_3$ is shown in Figure 47 and the energy minimized conformation obtained using Chem-3D is shown in Figure 51a. Compound

76b is symmetric about the 2,2'-bond. The 2 singlets at 8.75 and 8.27 ppm could be assigned to H9 and H1, respectively. This assignment is based on H9 of compound **76a** which is the only singlet. A sharp four-proton singlet at 3.39 ppm is assigned to the methylene group. The upfield region of ^{1}H NMR spectrum of **76b** in $CDCl_3$ is shown in Figure 50a.

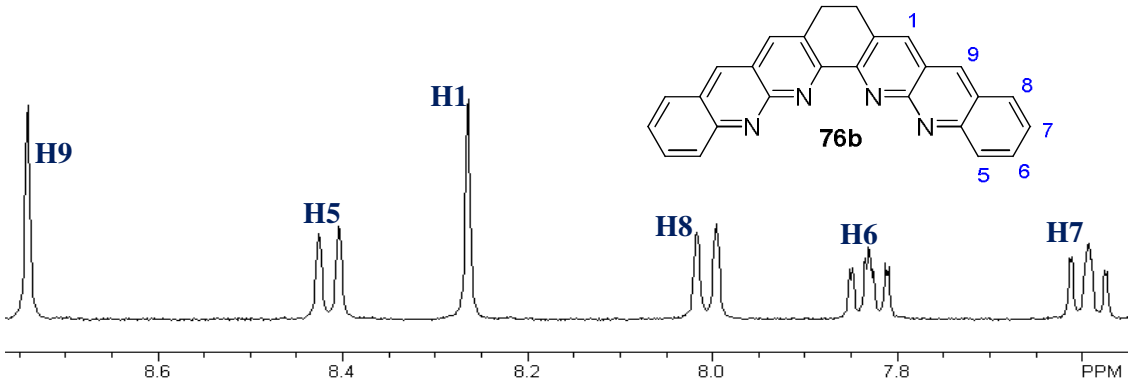

Figure 47. Downfield region of ^{1}H NMR spectrum of **76b** in $CDCl_3$ (400 MHz, at rt).

The ^{1}H NMR spectrum of **76c** in $CDCl_3$ is shown in Figure 48 and the energy minimized conformation obtained using Chem-3D is shown in Figure 51b. Compound **76c** is symmetric about the 2,2'-bond. The 2 singlets at 8.81 and 8.22 ppm could be assigned to H9 and H1, respectively. This assignment is done based on the H9 of compound **76a** which is the only singlet. A triplet at 2.90 ppm is assigned to the four benzylic methylene protons and the two quintet protons centered at 2.28 ppm is assigned to the central methylene protons. The upfield region of ^{1}H NMR spectrum of **76c** in $CDCl_3$ is shown in Figure 50b.

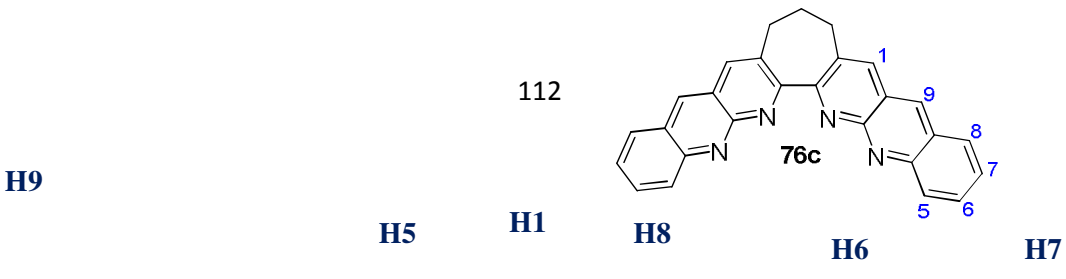

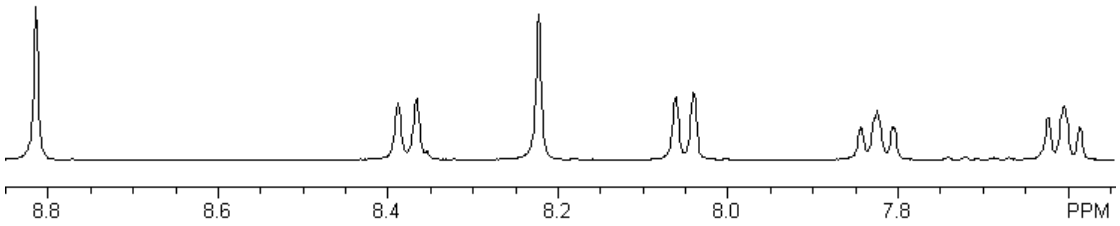

Figure 48. Downfield region of ^{1}H NMR spectrum of **76c** in $CDCl_3$ (400 MHz, at rt).

The ^{1}H NMR spectrum of **76d** in $CDCl_3$ is shown in Figure 49 and the energy minimized conformation obtained using Chem-3D is shown in Figure 51c. Compound **76d** is symmetric about the 2,2'-bond, but the methylene protons (Ha, Ha', Hb, and Hb') of the 3,3'-tetramethylene bridge are not equivalent. There are four distinct signals of equal intensity in the aliphatic region at 3.07, 2.52, 2.32, and 1.74 ppm assigned to these methylene protons. One of the α-methylene protons lies nearly in the plane of the adjacent aromatic ring and is thus substantially deshielded, resonating at 3.07 ppm. On the other hand the other α-methylene proton is oriented towards the shielding region of the 4-azaacridine ring and thus resonates at higher field at 2.52 ppm. The upfield peaks at 2.32 and 1.74 ppm are assigned to the nonbenzylic protons which are directed toward the shielding region of the further removed aromatic ring. The two singlets at 8.83 and 8.27 ppm could be assigned to H9 and H1, respectively. The upfield region of ^{1}H NMR spectrum of **76d** in $CDCl_3$ is shown in Figure 50c. The ^{13}C NMR spectrum of **76d** shows two clear upfield carbon resonances at 31.7, 31.3 ppm, verifying that **76d** has a C_2-symmetry axis.

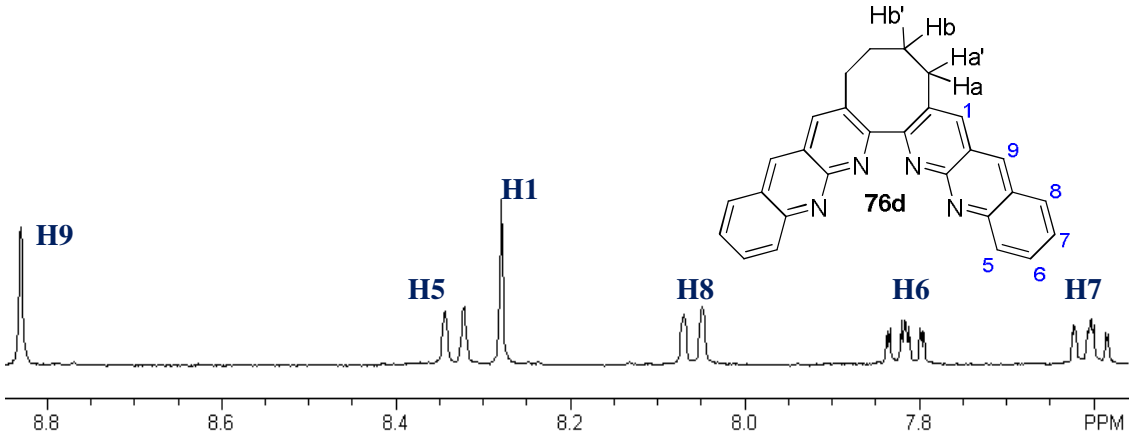

Figure 49. Downfield region of ^{1}H NMR spectrum of **76d** in $CDCl_3$ (400 MHz, at rt).

Similar behavior has been observed in the tetramethylene-bridged derivatives of 2,2'-biquinoline[174] and 2,2'-bi-1,8-naphthyridine[178].

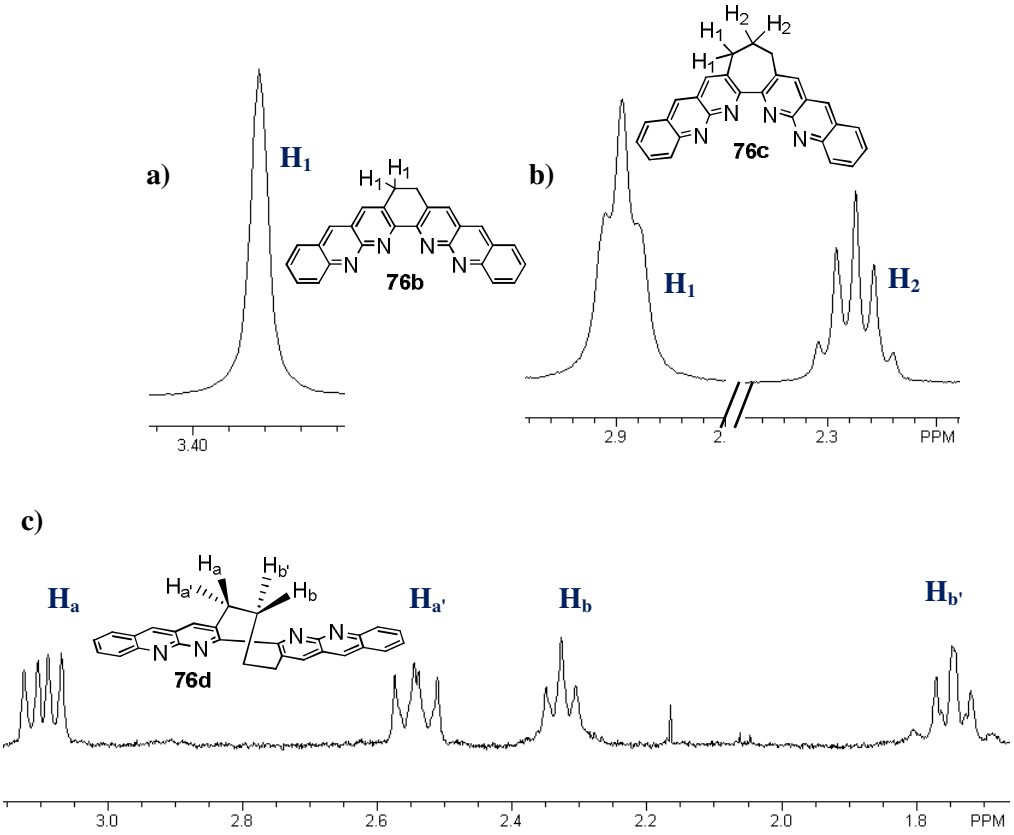

Figure 50. Upfield region of ^{1}H NMR spectrum of a) **76b**, b) **76c**, and c) **76d** in $CDCl_3$ (400 MHz, at rt).

a)

b)

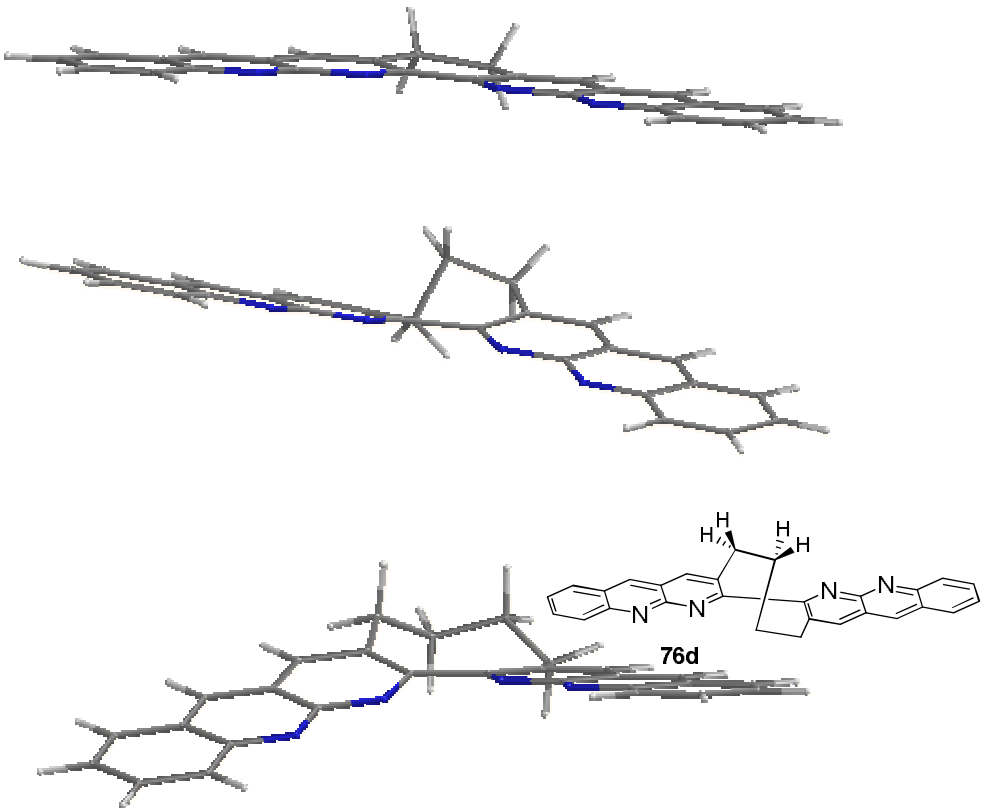

Figure 51. Compounds a) **76b**, b) **76c**, and c) **76d** in their energy minimized conformations obtained using Chem-3D.

A complete ^{1}H NMR analysis of ligands **76a-d** is reported in Table 12. All the protons could be readily identified due to their characteristic coupling patterns aided by the use of 2D homonuclear chemical shift correlated ^{1}H NMR (COSY) spectra.

Table 12. 1H NMR chemical shift data of the ligands **76a-d** recorded in $CDCl_3$ at rt.

Compound	H1	H2	H5	H6	H7	H8	H9	methylene
76a	8.61	9.32	8.47	7.89	7.65	8.09	8.92	--
76b	8.27	--	8.42	7.84	7.60	8.01	8.75	3.39
76c	8.22	--	8.39	7.84	7.61	8.05	8.81	2.90, 2.28
76d	8.27	--	8.34	7.82	7.60	8.06	8.83	3.07, 2.52, 2.32, 1.74

To determine the structural feature such as dihedral angles and distances of bi-4-azaacridines **76a-d** as a function of the length of the annelating bridge, molecular modeling calculations were carried out using the Mopac 2009 program. For the non-bridged bi-4-azaacridine (**76a**), the lowest energy conformation is almost planar. The lowest energy conformation for the 3,3'-bridged bi-4-azaacridines (**76b-d**) is nonplanar. The dihedral angle between the two covalently bonded aromatic rings is estimated to be 8^o for X = H,H, 28^o for X = $(CH_2)_2$, 59^o for X = $(CH_2)_3$, and 74^o for X = $(CH_2)_4$ (Table 13). During complexation the two rings may become more coplanar, the interatomic distance between N4-N4' gets smaller between 0.10-0.44 Å, and the bridging methylene units experience substantial torsional strain.

Table 13. Estimated[a] dihedral angles (^{o}) and N-N'interatomic distances (Å) for ligands **76a-d** and complexes **79a-d** and **81a-d**.

Ligands	Dihedral angle ^{o}	N4-N4'	Complexes	Dihedral angle ^{o}	N4-N4'	Complexes	Dihedral angle ^{o}	N4-N4'
76a	8	2.78	**79a**	0.04	2.61	**81a**	1	2.69
76b	28	2.85	**79b**	5	2.57	**81b**	10	2.70
76c	59	2.98	**79c**	14	2.54	**81c**	27	2.71
76d	74	3.03	**79d**	30	2.62	**81d**	32	2.67

[a] using the Mopac 2009 program

The chemical shift of the H5 is sensitive to the dihedral angle between the two 4-azaacridine rings. As the dihedral angel between the two covalently bonded aromatic rings becomes close to zero, the H5 becomes more deshielded and resonates at a lower field. The estimated dihedral angles were plotted versus the chemical shift of H5 for the ligands **76a-d**. The plot gave a nearly straight line (Figure 52).

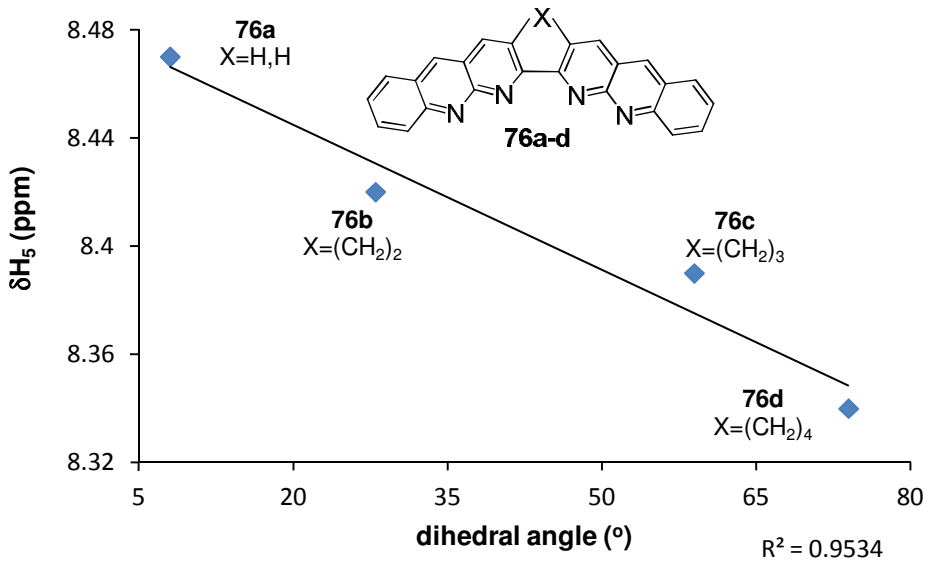

Figure 52. Relationship between the chemical shift of the H5 of bi-4-azaacridine systems and their estimated dihedral angles in $CDCl_3$ at rt.

4.4.5.2. Electronic spectra of the ligands

The electronic absorption spectra of ligands **76a-d** were obtained in ethanol at room temperature and the absorption maxima and extinction coefficients are summarized in Table 14. The correlation between UV absorptions and dihedral angle is relevant. As the 3,3'-bridge is increased from two to four carbons, there is a shift to higher energy, less intense absorptions. This observation is explained by the concurrent decrease in the conjugative interaction between the two 4-azaacridine rings with the increase in the biaryl dihedral angle.

The same effect is also observed for biquinolines (**58b-d**) and bi-1,8-naphthyridines (**60b-d**). The absorption maxima and extinction coefficients for ligands **58b-d** and **60b-d** are summarized in Table 14. Bi-4-azaacridine derivatives (**76a-d**) absorb at longer wavelength than the biquinoline and bi-1,8-naphthyridine derivatives.

Because of the extended π-conjugation the π*–levels of these bridge molecules lie at lower energy and have a greater electron affinity.

Table 14. Electronic absorption maxima and molar extinction coefficients for ligands **58b-d**, **60b-d**, and **76a-d**.

Compounds	λ_{max}/nm (εx10^3 M^{-1} cm^{-1})[a]
58b	360 (27), 344 (23)
58c	330 (15), 320 (15)
58d	325 (12), 310 (13)
60b	347 (37)
60c	349 (21)
60d	325 (13)
76a	386 (19), 307 (18)
76b	404 (18), 351 (11)
76c	372 (9), 274 (11)
76d	367 (8), 249 (26)

[a] Measured in 95% ethanol (5.0 x 10^{-5} M) at 298 K.

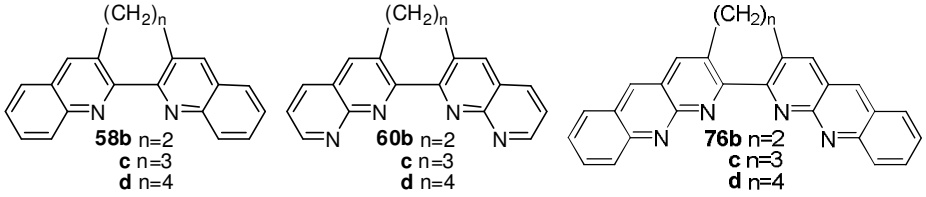

4.4.5.3. Conformational effects

The most important property of the 3,3'-bridged azabiaryl systems is the relationship between bridge length and conformation of the molecule. This relationship is best analyzed by careful consideration of the ^{1}H NMR spectra of these systems.

The upfield region of ^{1}H NMR spectrum of **76b**, [Ru(**76b**)(tpy)(H_2O)]$^{2+}$ (**79b**) and [Ru(**76b**)$(bpy)_2$]$^{2+}$ (**81b**) are shown in Figures 50a, 54a, and 55a, respectively. At room

temperature in $CDCl_3$ solution, the free dimethylene bridged ligand shows a sharp singlet for the bridge protons.

The five-membered ring metallocycle portion of the complexes **79b** and **81b** imposes greater constraints on conformational mobility. In **79b** the singlet at 3.39 ppm becomes two triplets centered at 3.82 and 3.66 ppm for the two nonequivalent methylene protons at room temperature in acetone-*d6* solution (Figure 54a). In the symmetric complex **81b** the singlet at 3.39 ppm becomes a doublet of doublets centered at 3.71 ppm for the two methylene protons at room temperature in acetone-*d6* solution (Figure 55a).

The upfield region of ^1H NMR spectrum of **76c**, [Ru(**76c**)(tpy)(H_2O)]$^{2+}$ (**79c**) and [Ru(**76c**)(bpy)$_2$]$^{2+}$ (**81c**) are shown in Figures 50b, 54b, and 55b, respectively. At room temperature in $CDCl_3$ solution, the trimethylene bridged for the free ligand shows a downfield triplet for the benzylic protons and an upfield quintet for the non-benzylic methylene.

The five-membered ring metallocycle portion of the complex imposes greater constraints on conformational mobility. This pattern becomes complex in **79c** and **81c**. In **79c** there are two triplets centered at 3.34 and 3.30 ppm for the two non-equivalent α-methylene protons and a quintet at 2.69 ppm for the two β-methylene protons (Figure 54b). In **81c** we observe multiplets between 3.33-3.17 ppm for the two non-equivalent α-methylene protons and a multiplet centered at 2.64 ppm for the two β-methylene protons (Figure 55b).

The upfield region of ^{1}H NMR spectrum of **76d**, [Ru(**76d**)(tpy)(H_2O)]$^{2+}$ (**79d**) and [Ru(**76d**)$(bpy)_2]^{2+}$ (**81d**) are shown in Figures 50c, 54c, and 55c, respectively. The tetramethylene bridged system behaves differently in free ligand. At room temperature in $CDCl_3$ solution, the symmetrical free ligand **76d** exhibits four distinct resonances in the aliphatic region of the NMR spectra (Figure 50c). Examination of a molecular model shows that, in its most favorable conformation, one of the benzylic protons is held over the shielding region of the opposite 4-azaacridine ring while the other benzylic proton is deshielded by the adjacent 4-azaacridine ring. One of the two non-benzylic methylene protons also experiences considerable shielding due to the closer pyridine ring.

The five-membered ring metallocycle portion of the complex imposes greater constraints on conformational mobility. This pattern becomes complex in **79d** and **81d**. Due to the conformational mobility of ligand **76d**, complexes **79d** and **81d** only became well-resolved at temperatures below -20 ^oC. At -80 ^oC, there are seven distinct signals of equal intensity in the aliphatic region at 3.43, 3.20, 3.11, 2.87, 2.46, 2.39, and 2.27 ppm assigned to the methylene protons for complex **79d** (Figure 54c). One of the signals is hidden under the solvent peak. For the symmetrical complex **81d** at -80 ^oC, there are four distinct signals of equal intensity in the aliphatic region at 3.23, 2.98, 2.41, and 2.12 ppm assigned to the methylene protons (Figure 55c).

4.4.6. Spectroscopic properties of the complexes 79a-d

*4.4.6.1. NMR spectra of the complexes **79a-d***

Initial attempts to measure the NMR spectra of complexes **79a-d** in CD_3CN showed that the spectra changed with time, indicating solvolysis of the bound water which was being replaced by acetonitrile. The change of the spectrum with time for **79c** is shown in Figure 53. Figure 53b shows the downfield region of ^1H NMR spectrum of **79c** in CD_3CN and Figure 53a shows the downfield region of ^1H NMR spectrum of **79c** in acetone-*d6* + 20 µL CD_3CN. The most obvious change upon addition of CD_3CN to the acetone-*d6* solution of **79c** is the singlet at 9.64 ppm and the broad H_2O peak at 8.84 ppm disappear and the singlet at 9.41 ppm increases.

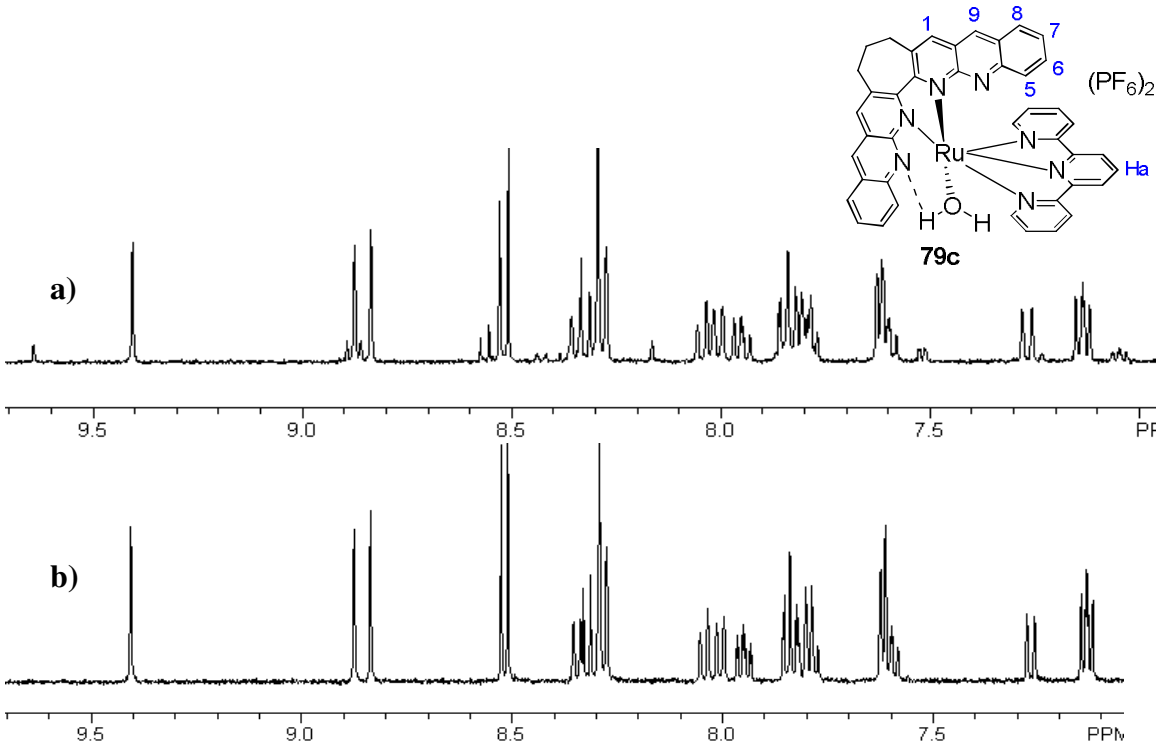

Figure 53. Downfield region of ^1H NMR spectrum of **79c** measured in a) acetone-*d6* + 20 µL CD_3CN and b) CD_3CN (500 MHz, at rt). Addition of CD_3CN to the NMR sample causes changing of spectrum with time and solvolysis of the bound water.

The complexes **79a-d** are characterized by their ^{1}H NMR spectra in acetone-*d6*, which show signals that are both well-resolved and dispersed for the complexes of [Ru(**76a-c**)(tpy)(H_2O)](PF_6)$_2$ at room temperature. Due to the conformational mobility of ligand **76d**, complex [Ru(**76d**)(tpy)(H_2O)](PF_6)$_2$ became well-resolved below -50 ^oC.

The values and intensities of the chemical shifts indicate that both ligands **76a-d** and tpy are bound to the metal atom in a 1:1 molar ratio. The complexes exhibit symmetry with respect to the tpy ligand so that all of the tpy signals, except the central Ha, integrate for two protons. The bi-4-azaacridine ligand is unsymmetrically bound with one half of the molecule being held closer to the orthogonal tpy ligand. The protons are assigned by a consideration of shielding effects and analysis of their 2D-COSY spectra. The signals are assigned on the NMR spectra.

The downfield regions of ^{1}H NMR spectra of complexes **79a-d** in acetone-*d*6 are shown in Figures 78-81, respectively. There are two different singlets for H9 and H9' for the bi-4-azaacridine in **79a** and four different singlets for H1, H1', H9, and H9' for the bi-4-azaacridine in **79b-d**. The H5 proton points toward the face of the central pyridine ring of the orthogonal tpy ligand, causing it to be shielded and shifted upfield by 0.2-0.45 ppm. This effect is somewhat diminished for the more remote protons. The remaining protons experience downfield coordination-induced chemical shifts due to the electronic depletion resulting from complexation and hydrogen bonding with the coordinated water.

The broad singlets observed at 8.94, 8.92, 8.84, and 9.00 ppm for complexes [Ru(**76a-d**)(tpy)(H_2O)]$^{2+}$ disappear upon the addition of 20 μL D_2O to the NMR sample,

identifying them as belonging to the coordinated water. Addition of D_2O to the NMR sample also makes a slight change both in resolution and chemical shifts for some peaks.

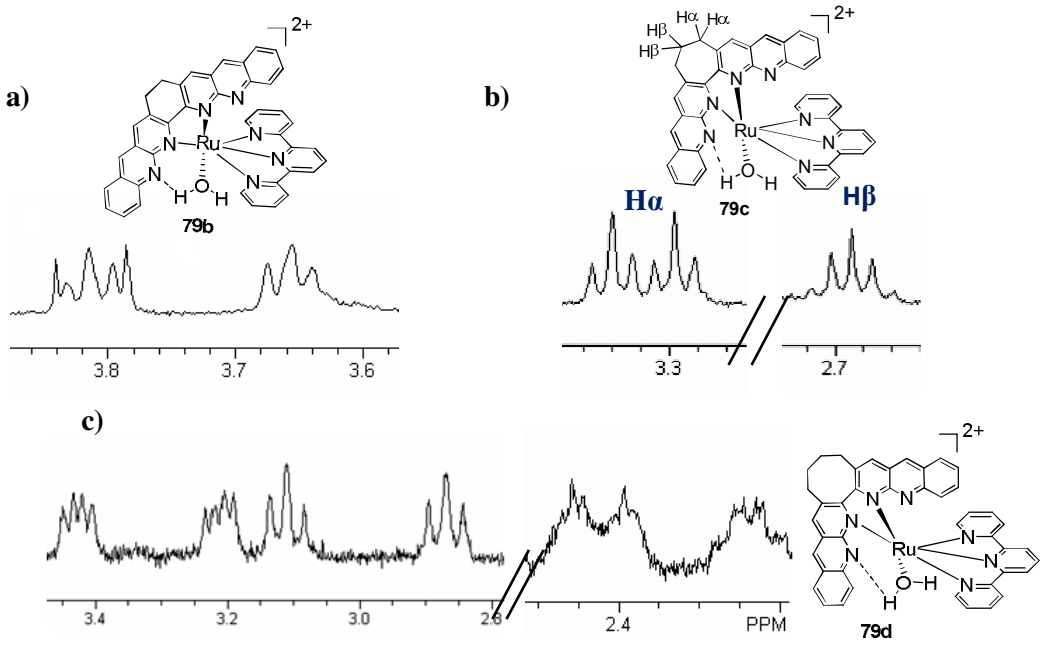

Figure 54. Upfield region of ^{1}H NMR spectrum of a) [Ru(**76b**)(tpy)(H_2O)]$^{2+}$ (**79b**) at rt, b) [Ru(**76c**)(tpy)(H_2O)]$^{2+}$ (**79c**) at rt, and c) [Ru(**76d**)(tpy)(H_2O)]$^{2+}$ (**79d**) at -80 ^{o}C in acetone-*d6* (500 MHz).

*4.4.6.2. NMR spectra of the complexes **81a-d***

The complexes **81a-d** are characterized by their ^{1}H NMR spectra in acetone-*d6*, which show signals that are both well-resolved and dispersed for the complexes of [Ru(**76a-c**)$(bpy)_2$]$(PF_6)_2$ at room temperature. Due to the conformational mobility of ligand **76d**, complex [Ru(**76d**)$(bpy)_2$]$(PF_6)_2$ became well-resolved below -50 ^{o}C.

The values and intensities of the chemical shifts indicate that the ligands **76a-d** and bpy are bound to the metal atom in a 1:2 molar ratio. The resultant complexes **81a-d** have a symmetric geometry so that all of the signals integrate for two protons. The

protons are assigned by a consideration of shielding effects and analysis of their 2D-COSY spectra. The signals are assigned on the NMR spectra.

The downfield region of ^{1}H NMR spectra of complexes **81a-d** in acetone-*d*6 is shown in Figures 82-85. ^{1}H NMR analysis of the 4-azaacridine part for complexes **81a-d** is reported in Table 15. There is one singlet for H9 for the bi-4-azaacridine in **81a** and there are 2 singlets for H9 and H1 for the bi-4-azaacridine in **81b-d**.

Table 15. ^{1}H NMR chemical shift data of the 4-azaacridine part for **81a-d** recorded in acetone-*d6* at rt.

Compound	H1	H5	H6	H7	H8	H9	methylene
81a	--	8.21	7.64	7.79	7.32	9.38	--
81b	8.81	8.25	7.65	7.77	7.21	9.28	3.71
81c	8.76	8.44	7.66	7.78	7.16	9.26	3.25, 2.64
81d[a]	8.85	8.57	7.68	7.81	7.13	9.29	3.23, 2.98, 2.41, 2.11

[a] ^{1}H NMR recorded in acetone-*d6* at -80 °C.

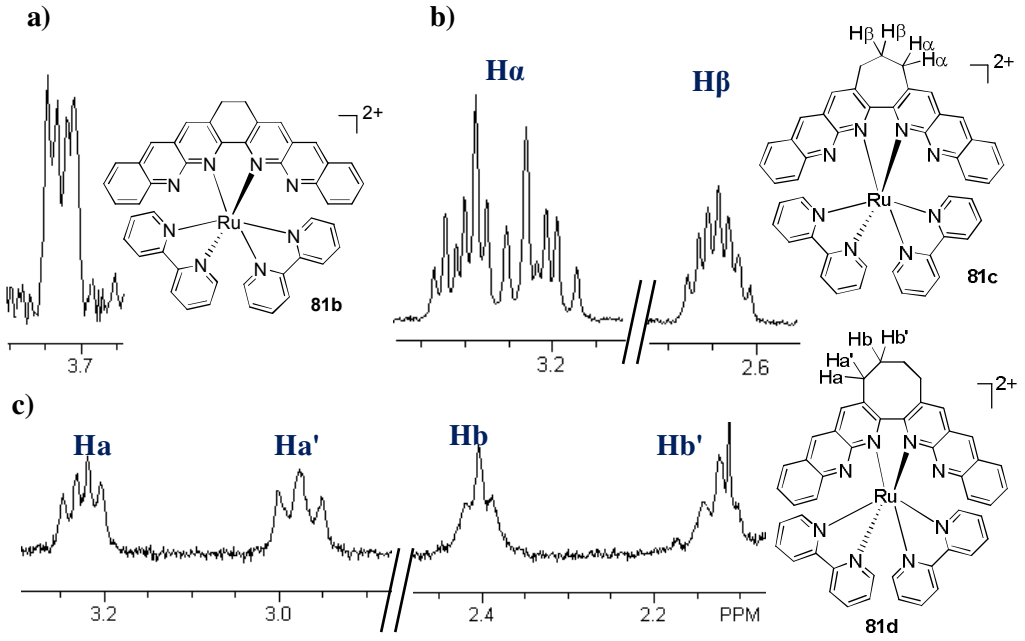

Figure 55. Upfield region of ^{1}H NMR spectrum of a) [Ru(**76b**)(bpy)$_2$]$^{2+}$ (**81b**) at rt, b) [Ru(**76c**)(bpy)$_2$]$^{2+}$ (**81c**) at rt, and c) [Ru(**76d**)(bpy)$_2$]$^{2+}$ (**81d**) at -80 °C in acetone-*d6* (500 MHz).

To determine the structural feature such as dihedral angles and distances of bi-4-azaacridines **81a-d** as a function of the length of the annelating bridge, molecular modeling calculations were carried out using the Mopac 2009 program. For the non-bridged bi-4-azaacridine $Ru(bpy)_2$ complex **81a**, the lowest energy conformation is almost planar. The lowest energy conformation for the annulated 3,3'-bridged bi-4-azaacridine $Ru(bpy)_2$ complexes (**81b-d**) is nonplanar. The dihedral angle between the two covalently bonded aromatic rings in complexes $[Ru(\mathbf{76a\text{-}d})(bpy)_2]^{2+}$ is estimated to be 1^o for X = H,H, 10^o for X = $(CH_2)_2$, 27^o for X = $(CH_2)_3$, and 32^o for X = $(CH_2)_4$ (Table 13). During complexation two rings may become approximately coplanar, the interatomic distance between N4-N4' gets smaller between 0.09-0.36 Å, and the bridging methylene units experience substantial torsional strain.

The chemical shift of the H5 is sensitive to the dihedral angle between the two 4-azaacridine rings. As the dihedral angel between the two covalently bonded aromatic rings becomes close to zero, the H5 becomes more shielded and resonates at a higher field. The estimated dihedral angles were plotted versus the chemical shift of H5 for the complexes **81a-d**. The plot gave a nearly straight line (Figure 56).

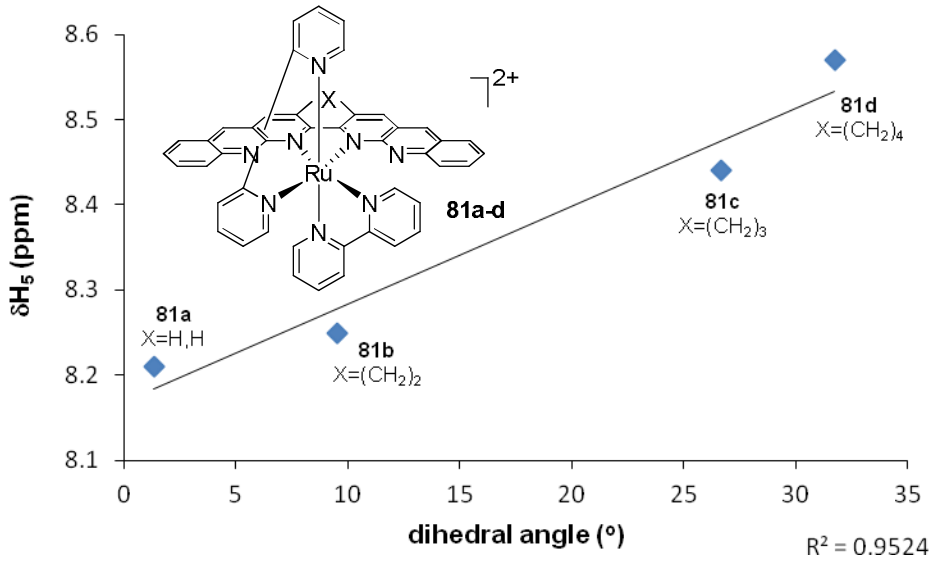

Figure 56. Relationship between the chemical shift of the H5 of [Ru(**76a-d**)(bpy)$_2$]$^{2+}$ (**81a-d**) complexes and their estimated dihedral angles in acetone-*d6*.

*4.4.6.3. Variable temperature NMR spectra for complexes **79d** and **81d***

The tetramethylene bridged derivatives **58d**, **60d**, and **76d** are respectively bis-quinolino, bis-1,8-naphthyridino, and bis-4-azaacridino fused derivatives of *cis*,*cis*-1,3-cyclooctadiene. The conformation of the central eight-member ring of these three systems is expected to be similar to the conformation of the diene. Anet and Yavari[198] have studied the conformation of *cis*,*cis*-1,3-cyclooctadiene by dynamic nuclear magnetic resonance spectroscopy and iterative force field calculations. Their calculation showed the twist-boat-chair form with C_{2v}-symmetry to be the most stable, having a dihedral angle of 54 ^{o} between the double bonds. The ΔG value for the conformation inversion process was estimated to be about 10 Kcal/mol.

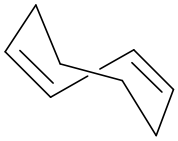

twist-boat-chair form of *cis*,*cis*-1,3-cyclooctadiene

Due to the conformational mobility of ligand **76d**, complex **79d** does not give a well-resolved NMR spectrum at room temperature. By slowly cooling **79d** dissolved in acetone-*d6* to -80 °C (193 K) and recording the 500 MHz ^{1}H NMR spectra as a function of temperature, we were able to get a well-resolved NMR spectrum. As the temperature decreases from +20 °C to -80 °C, the broad peaks got sharper and the overlapped peaks separated (Figure 57).

Most of the proton resonances shift slightly downfield with decreasing temperature. The tpy H4' shows a triplet at 8.51 ppm at +20 °C, 8.52 ppm at 0 °C, 8.53 ppm at -20 °C, 8.54 ppm at -40 °C, 8.56 ppm at -60 °C, and 8.58 ppm at -80 °C.

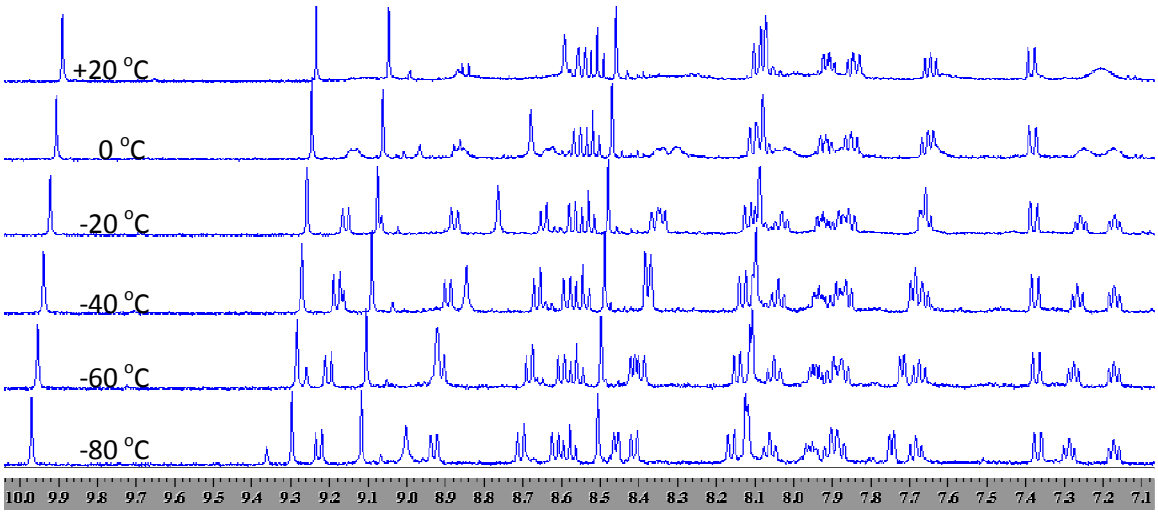

Figure 57. Downfield region of ^{1}H NMR spectrum of **79d** in acetone-*d6* (500 MHz, from -80 °C to +20 °C).

Due to the conformational mobility of ligand **76d**, complex **81d** does not give well-resolved NMR at room temperature. By slowly cooling the sample of **81d** dissolved in acetone-*d6* up to -80 °C (193 K) and recording the 500 MHz ^{1}H NMR spectra as a function of temperature, we were able to get a well-resolved NMR spectrum. As the temperature decreases from +20 °C to -80 °C, the broad peaks got sharper and the overlapped peaks separated (Figure 58).

The proton resonances shift slightly downfield with decreasing the temperature. The most downfield peak of the complex is a singlet at 9.23 ppm at +20 °C, 9.24 ppm at 0 °C, 9.25 ppm at -20 °C, 9.26 ppm at -40 °C, 9.28 ppm at -60 °C, and 9.29 ppm at -80 °C.

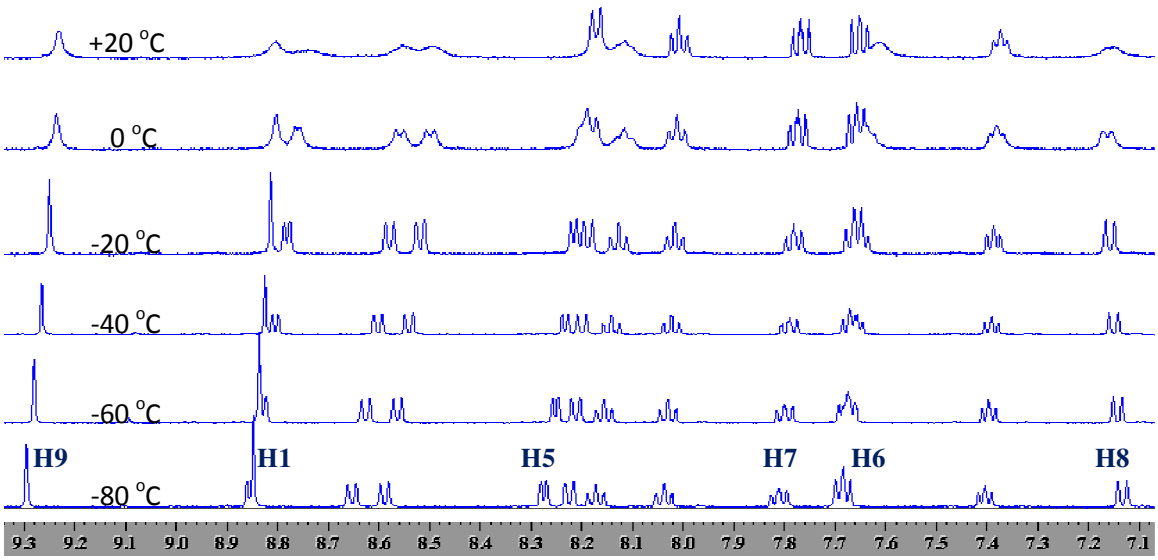

Figure 58. Downfield region of ^{1}H NMR spectrum of **81d** in acetone-*d6* (500 MHz, from -80 °C to +20 °C).

By slowly cooling **81d** in acetone-*d6*, the broad upfield peaks at 3.25, 2.99, 2.41, and 2.12 ppm were gradually sharpened (Figure 59). Takeda and Stejskal[199] have

described a method based on line broadening for the evaluation of rate constant for an equally populated two site case. We applied this method to our system **81d** by considering signals of Ha and Ha' at 3.25 and 2.99 ppm. The rate constant is given by the Eq. 4.2

$$k = \frac{\pi \, \delta\nu^2 \, (w^* + w_o) \sqrt{[1+2\left(\frac{w^*}{\delta\nu}\right)^2 - \left(\frac{w^*}{\delta\nu}\right)^4}}{2 \, (w^{*2} - w_o^2)} \qquad \text{Eq. 4.2}$$

where, w^* is the width at half maximum intensity of the broad signal, w_o is the width at half maximum intensity of the sharpened signal, and $\delta\nu$ is the frequency difference between sites undergoing exchange. For **81d** we have:

at +20 ^oC (293 K) w^* = 0.084 ppm

at -20 ^oC (253 K) w_o = 0.046 ppm

$\delta\nu = \delta a - \delta a'$ = 3.25 - 2.99 = 0.258 ppm

and the rate is k = 1716 s^{-1}

the k value is approximate because the line broadening is complicated by the fact that the coalescing signals are coupled to one another as well as to the adjacent methylene protons.[200] An approximate free energy of activation (ΔG) can then be determined by using the Eyrig equation[199] (Eq. 4.3)

$$k = \kappa \, \frac{k_B \, .T}{h} \, e^{-\Delta G^*/RT} \qquad \text{Eq. 4.3}$$

with κ = transmission coefficient (≈ 1), k_B = Boltzman's constant (3.30×10^{-21} Kcal.K^{-1}), and *h* = Planck's constant (1.58×10^{-31} Kcal.s) we derive the Eq. 4.4 for ΔG^*.

$$\Delta G^* = 4.575 \times 10^{-3} . T \left[10.319 + \log\left(\frac{T}{k}\right)\right] \quad \text{Eq. 4.4}$$

Here *k* = rate constant and T = coalescence temperature. At T = 253 K and *k* = 1716 s^{-1} we obtain the free energy of activation ΔG = 11 Kcal/mol for complex **81d**. Similar experiments were carried out for **58d** and **60d** with heating the ligands in *o*-xylene-*d10*. At T = 400 K, the free energy of activation is obtained for **60d** as ΔG = 17 Kcal/mol with rate constant of *k* = 42635 s^{-1} and for **58d** as ΔG = 17.5 Kcal/mol with rate constant of *k* = 3764 s^{-1}.

In conclusion, the rates of conformational inversion of the tetramethylene bridge derivatives **58d**, **60d**, **76d**, and **81d** are slow enough to observe four upfield signals on the NMR scale.

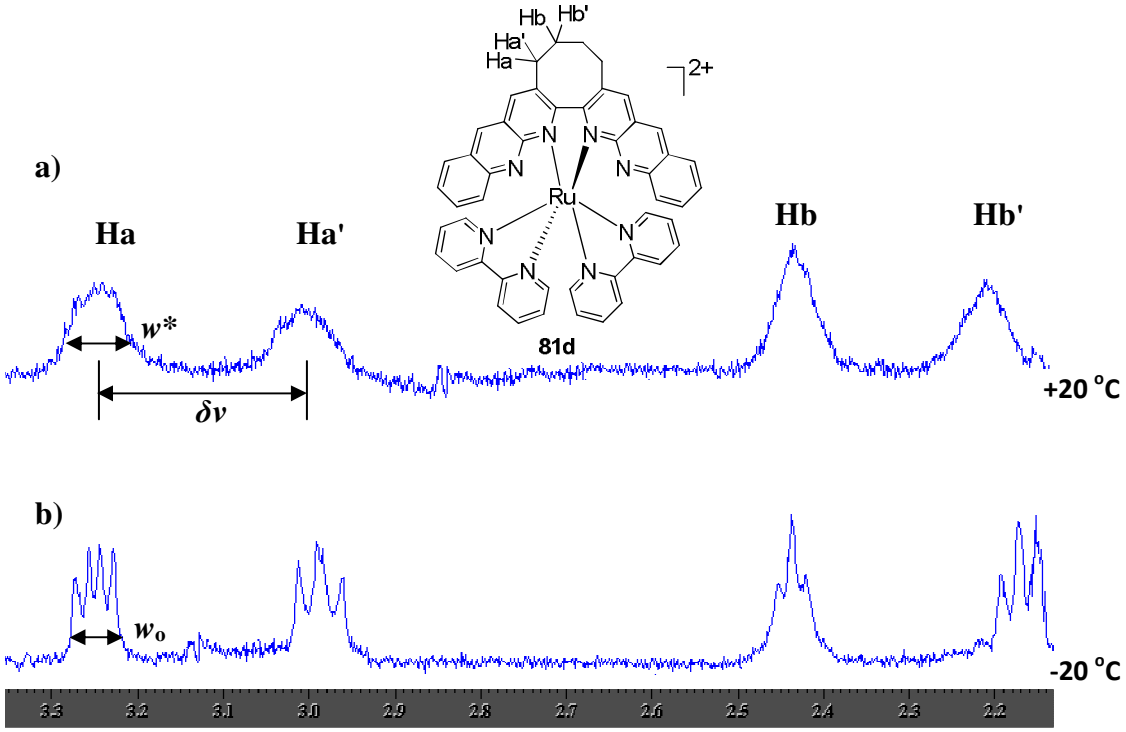

Figure 59. Upfield region of ^{1}H NMR spectrum of [Ru(**76d**)(bpy)$_2$]$^{2+}$ (**81d**) in acetone-*d6* a) at +20 ^{o}C and b) at -20 ^{o}C (500 MHz).

*4.4.6.4. Electronic spectra of the complexes **79a-d***

The electronic absorption maxima (λ_{max}) and molar extinction coefficients (ε) of the Ru(II) complexes **79a-d** were recorded in dichloromethane at room temperature and the data have been summarized in Table 16. The spectra consist of two well-defined regions as illustrated in Figure 60. A relatively intense absorption is observed at shorter wavelengths, 200-350 nm. This absorption is attributed to ligand-centered π–π* transitions associated with the aromatic rings of the ligands. The less intense absorption bands at longer wavelength in the region of 350-800 nm are assigned as MLCT and are due to the promotion of an electron from a metal d-orbital to a π* orbital of the most

electronegative ligand. Polypyridyl Ru(II) complexes are often characterized by a broad MLCT band in the visible region of the electromagnetic spectrum.

For the complexes [Ru(**76a-d**)(tpy)(H_2O)]$^{2+}$, the bpy ligand of the complex [Ru(bpy)(tpy)(H_2O)]$^{2+}$ has been replaced by a bi-4-azaacridine. Bi-4-azaacridine may be considered as a biquinoline-fused analogue of bpy, which is more delocalized and more electronegative, making it a much better charge acceptor.[188]

Bi-4-azaacridine derivatives **79a-d** have the same band shape as the bi-1,8-naphthyridine derivatives **61b-d** and are more red-shifted than them because of the further extension of the π-conjugation with additional benzo ring fused to the nap units. The π*–levels of bi-4-azaacridine bridged molecules lie at lower energy and have a greater electron affinity.[189]

The shape of the bands remains almost invarient for the complexes **79a-d** in the visible region (Figure 60). The correlation between UV absorptions and dihedral angle is relevant. As the 3,3'-bridge is increased from two to four carbons, there is a shift to higher energy and less intense absorptions. This observation is explained by the concurrent decrease in the conjugative interaction between the two 4-azaacridine rings with the increase in the biaryl dihedral angle. It is noteworthy that the more planar system, profiting from better delocalization, has the lowest-energy absorption. The same effect is also observed for bi-1,8-naphthyridines (**61b-d**). The absorption maxima and extinction coefficients complexes **61b-d** are summarized in Table 16. For the parent

system, the bpy component dominates with a strong absorption band at 509 nm and only a very small shoulder for tpy at ~450 nm.

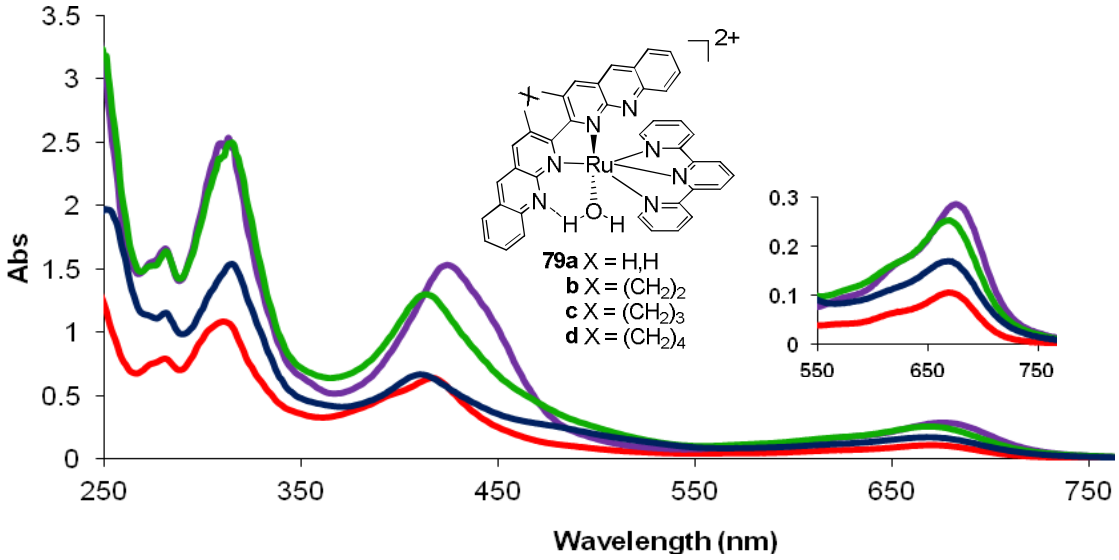

Figure 60. Electronic absorption spectra of the complexes **79a-d**, 5 x 10^{-5} M in CH_2Cl_2: **79a** (red), **79b** (purple), **79c** (green), **79d** (blue).

Table 16. Electronic absorption maxima and molar extinction coefficients for $[Ru(bpy)(tpy)(H_2O)]^{2+}$, **79a-d**, and **61b-d**.

Compounds	λ_{max}/nm ($\varepsilon x10^3$ M^{-1} cm^{-1})[a]
$[Ru(bpy)(tpy)(H_2O)](PF_6)_2$	509 (11.2)
[Ru(**76a**)(tpy)(H_2O)](PF_6)$_2$ (**79a**)	670 (2.1), 618 (sh), 417 (12.8)
[Ru(**76b**)(tpy)(H_2O)](PF_6)$_2$ (**79b**)	676 (5.7), 424 (30.6)
[Ru(**76c**)(tpy)(H_2O)](PF_6)$_2$ (**79c**)	674 (5.1), 414 (26.0)
[Ru(**76d**)(tpy)(H_2O)](PF_6)$_2$ (**79d**)	670 (3.4), 411 (13.3)
[Ru(**60b**)(tpy)(H_2O)](PF_6)$_2$ (**61b**)	601 (10.7), 426 (5.6)
[Ru(**60c**)(tpy)(H_2O)](PF_6)$_2$ (**61c**)	597 (9.6), 426 (8.1)
[Ru(**60d**)(tpy)(H_2O)](PF_6)$_2$ (**61d**)	593 (8.5), 435 (9.6)

[a] Measured in CH_2Cl_2 (5.0 x 10^{-5} M) at 298 K, sh=shoulder.

The electronic absorption of the Ru(II) complexes **79a-d** were recorded in 5x10^{-5} M acetone + 10 µL acetonitrile at room temperature. When an acetone solution of

[Ru(**76a-d**)(tpy)(H_2O)]$^{2+}$ is exposed to added acetonitrile, the absorption spectrum changes with time. The peak at ~670 nm decreases and the peak about 620 nm increases in intensity. The Ru-OH_2 complexes **79a-d** were converted into Ru-MeCN in about 3 h that the intensity of the absorption band does not change with time. Although initially there is change in the UV-Vis spectra, the color of the samples looked identical by eye before and after the addition of acetonitrile. The change in the absorption is indicating solvolysis of the bound water which was being replaced by acetonitrile. Electronic absorption spectrum of [Ru(**76c**)(tpy)(H_2O)]$^{2+}$ with added acetonitrile recorded as a function of time is shown in Figure 61. The absorption coefficient at 670 nm for **79c** decreases from 10.6 x 10^3 M^{-1} cm^{-1} to 9.6 x 10^3 M^{-1} cm^{-1}. The data have been summarized in Table 17.

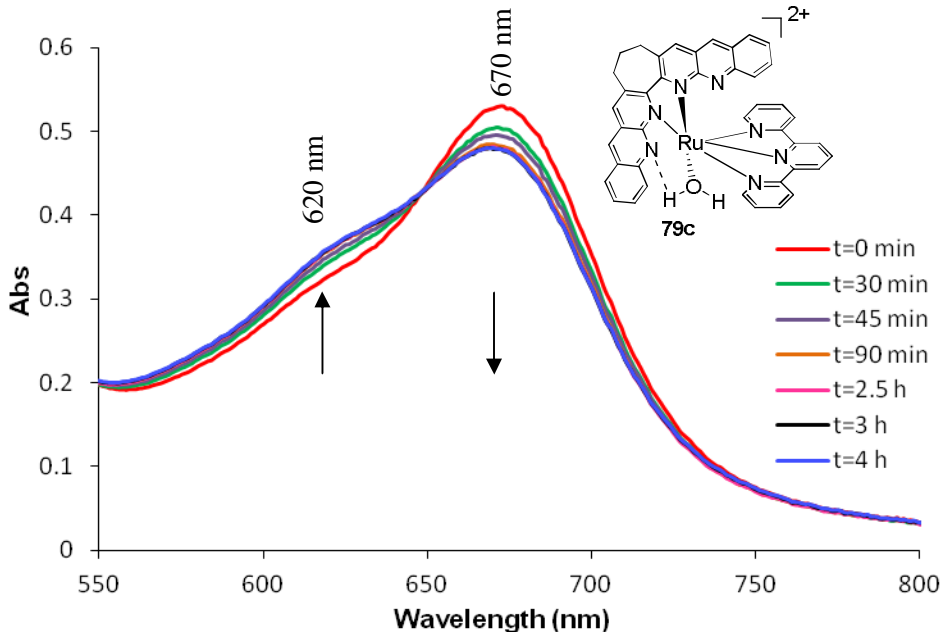

Figure 61. Electronic absorption spectrum of [Ru(**76c**)(tpy)(H_2O)]$^{2+}$ (**79c**) (5x10^{-5} M in acetone) with added acrtonitrile (10 µL) recorded as a function of time.

Table 17. Absorbance of [Ru(**76c**)(tpy)(H_2O)]$^{2+}$ (**79c**) at 670 nm in 5x10^{-5} M in acetone + 10 μL acetonitrile.

time (min)	ε (x10^3 M^{-1} cm^{-1})
0	10.6
30	10.1
45	9.9
90	9.7
150	9.65
180	9.6
240	9.6

The emission spectra of complexes **79a-d** were recorded in CH_2Cl_2 at room temperature. The complexes were excited at the maximum of their MLCT absorption band. None of the compounds showed any appreciable emission at room temperature.

*4.4.6.5. Electronic spectra of the complexes **81a-d***

The electronic absorption maxima (λ_{max}) and molar extinction coefficients (ε) of the Ru(II) complexes **81a-d** were recorded in dichloromethane at room temperature and the data have been summarized in Table 18. The spectra consist of two well-defined regions as illustrated in Figure 63. A relatively intense absorption is observed at shorter wavelengths, 250-350 nm. This absorption is attributed to ligand-centered π–π* transitions associated with the aromatic rings of the ligands. The less intense absorption bands at longer wavelength in the region of 350-800 nm are assigned as MLCT and are due to the promotion of an electron from a metal d-orbital to a π* orbital of the most electronegative ligand.

For the complexes [Ru(**76a-d**)$(bpy)_2]^{2+}$, one bpy ligand of the complex $[Ru(bpy)_3]^{2+}$ has been replaced by a bi-4-azaacridine. Bi-4-azaacridine may be considered as a benzo ring fused to the 6,7-position of the 1,8-naphthyridine, which is more delocalized and more electronegative, making it a much better charge acceptor.[188]

The MLCT band for the $[Ru(L)(bpy)_2]^{2+}$ complexes shows two components for the complexes $[Ru(bpy)_3]^{2+}$, [Ru(**58b**$)(bpy)_2]^{2+}$, [Ru(**60b**$)(bpy)_2]^{2+}$, and [Ru(**76a-d**$)(bpy)_2]^{2+}$ (Figure 62). One component, centered at 420-441 nm, is associated with MLCT into the bipyridine ligands. The longer wavelength component is due to charge transfer into the biquinoline, binaphthyridine, or bi-4-azaacridine ligand.[186,201]

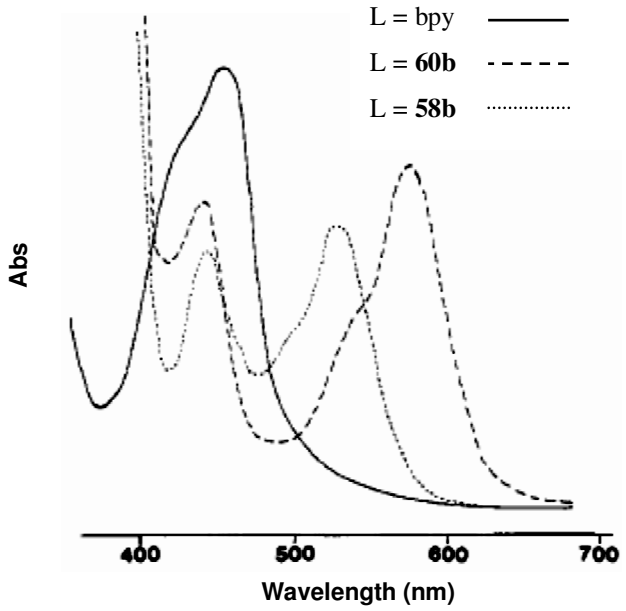

Figure 62. Variation in the electronic absorption spectra of $[Ru(L)(bpy)_2](PF_6)_2$ as a function of the delocalizing ability of the ligand L (5×10^{-5} M in CH_3CN).

Thummel *et al*. reported the biquinoline-centered absorptions at 506-528 nm and the binaphthyridine ones at 562-576 nm. We observe the bi-4-azaacridine-centered complexes absorb at 630-646 nm. Because of the further extension of the π-conjugation with additional benzo ring fused to the bpy the absorptions are more red-shifted from bpy to bi-4-azaacridine-centered compounds.[189] The π*–levels of bi-4-azaacridine bridged molecules lie at lower energy and have a greater electron affinity.

It is now well accepted that these transitions are associated with the promotion of an electron from a ruthenium *d* orbital to a ligand π* orbital.[202] The decrease in energy of this transition on progressing from bipyridine to biquinoline to binaphthyridine to bi-4-azaacridine can thus be correlated with a lowering of the energy of the π* orbital concomitant with the increasing delocalizing ability of these ligands.

The shape of the bands remains almost invarient for the complexes **81a-d** at visible region (Figure 63) while the intensity of MLCT absorption is also dependent upon the strength of the coordinative bond. The bridged bi-4-azaacridine complexes show a steady decrease in the intensity of the long wavelength band as the 3,3'-bridge increases in length from two carbons to four and the bi-4-azaacridine ligand becomes less planar. The weakest long wavelength absorption is thus observed for $[Ru(\mathbf{76d})(bpy)_2]^{2+}$, in which the highly distorted **76d**, by formation of the weakest coordinative bonds of this series, is the least efficient charge transfer acceptor. It is noteworthy that the more planar system, profiting from better delocalization, has the lowest energy absorption (Figure 63). The same effect is observed for the binaphthyridine series $[Ru(\mathbf{60b\text{-}d})(bpy)_2]^{2+}$, as the 3,3'-bridge increases in length in **60b-d** from two carbons to four significantly diminishes

MLCT into the binaphthyridine (Figure 64, Table 19). For the $[Ru(bpy)_3]^{2+}$, the bpy component dominates with a strong absorption band at 453 nm with a higher extinction coefficient.

In the $[Ru(\mathbf{76b\text{-}d})(bpy)_2]^{2+}$ series, there also appears to be a reasonable correlation between the energy of the MLCT absorption and the length of the annelating bridge in **76b-d**. As the bridge is lengthened from two carbons to four, this absorption shifts to shorter wavelengths or higher energy (Figure 63), indicating that as **76** becomes less planar, its ability to delocalize charge diminishes and the energy of its π* orbital increases. The same effect is observed for the binaphthyridine series $[Ru(\mathbf{60b\text{-}d})(bpy)_2]^{2+}$, as the 3,3'-bridge increases in length in **60b-d** from two carbons to four absorption shifts to shorter wavelengths (Figure 64, Table 19).

Within certain limitations, therefore, it may be possible to utilize conformational properties of the ligands to control both the position and intensity of MLCT absorptions associated with Ru(II) complexes.

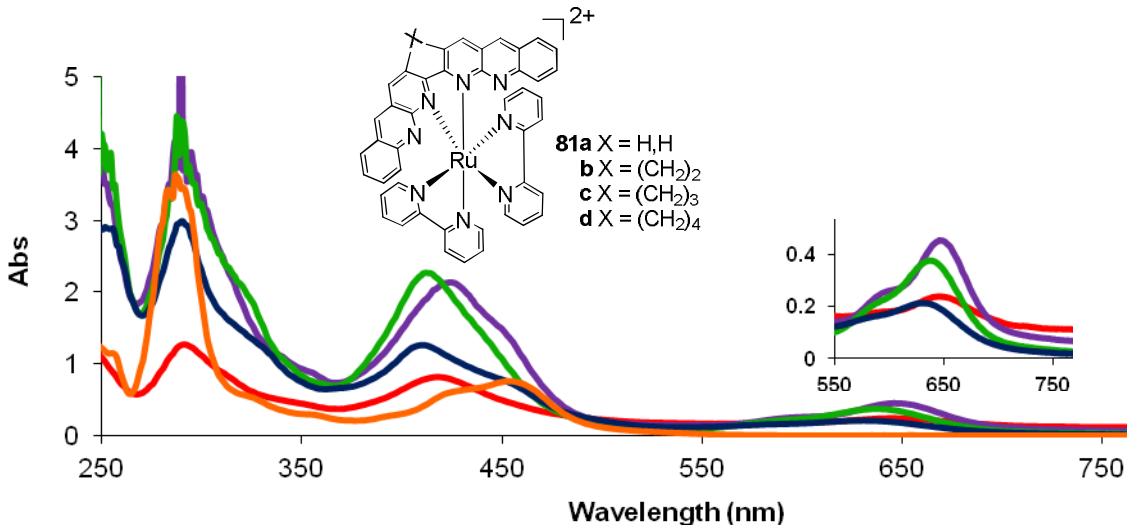

Figure 63. Electronic absorption spectra of the complexes **81a-d** and $[Ru(bpy)_3]^{2+}$, 5 x 10^{-5} M in CH_2Cl_2: **81a** (red), **81b** (purple), **81c** (green), **81d** (blue), and $[Ru(bpy)_3]^{2+}$ (orange).

Table 18. Electronic absorption maxima and molar extinction coefficients for $[Ru(bpy)_3]^{2+}$ and **81a-d**.

Compounds	λ_{max}/nm (εx10^3 M^{-1} cm^{-1})[a]
$[Ru(bpy)_3]^{2+}$	453 (15.2), 393 (sh)
[Ru(**76a**)(bpy)$_2$](PF$_6$)$_2$ (**81a**)	646 (4.8), 590 (sh), 417 (16.3)
[Ru(**76b**)(bpy)$_2$](PF$_6$)$_2$ (**81b**)	645 (9.1), 593 (sh), 450 (sh), 424 (42. 9)
[Ru(**76c**)(bpy)$_2$](PF$_6$)$_2$ (**81c**)	636 (7.5), 586 (sh), 412 (45.5)
[Ru(**76d**)(bpy)$_2$](PF$_6$)$_2$ (**81d**)	630 (4.3), 455 (sh), 410 (25.3)

[a] Measured in CH_2Cl_2 (5.0 x 10^{-5} M) at 298 K, sh=shoulder.

Table 19. Electronic absorption maxima and molar extinction coefficients for Ru complexes.[181]

Compounds	λ_{max}/nm (εx10^3 M^{-1} cm^{-1})[a]
$[Ru(\mathbf{biq})(bpy)_2]^{2+}$	525 (7.3), 420 (7.5), 375 (14.9), 320 (26.2)
$[Ru(\mathbf{58b})(bpy)_2]^{2+}$	528 (7.1), 440 (6.2), 395 (22.4), 373 (14.9)
$[Ru(\mathbf{binap})(bpy)_2]^{2+}$	574 (10.8), 436 (10.8), 346 (37.4)
$[Ru(\mathbf{60b})(bpy)_2]^{2+}$	576 (9.3), 440 (8.4), 394 (24.3), 369 (31.8)
$[Ru(\mathbf{60c})(bpy)_2]^{2+}$	568 (6.8), 441 (9.3), 361 (26.2), 325 (22.4)
$[Ru(\mathbf{60d})(bpy)_2]^{2+}$	562 (5.6), 443 (10.3), 367 (18.7), 324 (18.7)

[a] Measured in CH_3CN

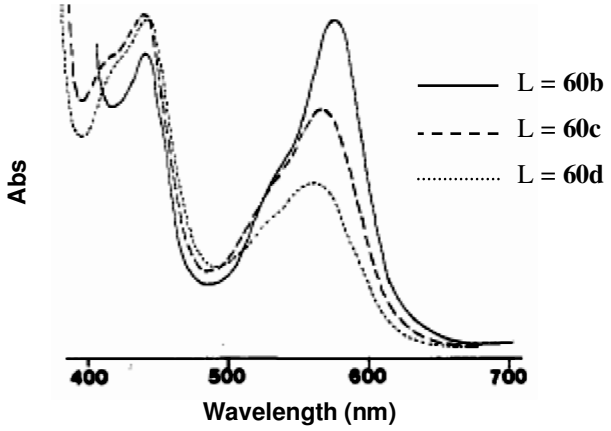

Figure 64. Variation in the electronic absorption spectra of $[Ru(\mathbf{60b\text{-}d})(bpy)_2](PF_6)_2$ as a function of bridge length ($5x10^{-5}$ M in CH_3CN).

The emission spectra of complexes **81a-d** were recorded in CH_2Cl_2 at room temperature. The complexes were excited at the maximum of their MLCT absorption band. None of the complexes showed any appreciable emission at room temperature.

*4.4.6.6. Electrochemical studies of the complexes **79a-d***

The cyclic voltammograms of complexes **79a-d** were recorded in dichloromethane to avoid the solvolysis of the bound water which is replaced by acetonitrile at room temperature and the electrochemical properties are summarized in

Table 20. Figure 65a shows the oxidative wave for complex **79b** and Figure 65b shows the reductive wave. The oxidation of a Ru(II) complex involves the removal of one electron from the HOMO, which is a metal-centered d-orbital. The reduction of a Ru(II) complex is ligand-centered and involves the addition of one electron to the π* LUMO of the most electronegative ligand. The reduction waves are attributed to the RuII/I redox couple and the oxidation waves are attributed to the RuII/III redox couple.

There is one reversible oxidation wave observed for the complexes **79a-d**. The oxidative wave for complexes **79a-d** is observed at +0.98 to +1.19 V. When one tpy ligand in $[Ru(tpy)_2]^{2+}$ is substituted with bpy to afford $[Ru(bpy)(tpy)(H_2O)]^{2+}$, the oxidation potential decreases from +1.30 V to +0.82 V. The bound water molecule facilitates oxidation by 0.48 V, indicating that the coordinated water helps to stabilize the Ru(II) state. The substitution of either binap or biazaacridine for bpy raises the potential to >1 V, reflecting the influence of the more electronegative ligand, which should destabilize Ru(III). As the ligand becomes more twisted in progressing from **76b** to **76d**, this effect is less strongly felt and the potential decreases by 220 mV.

There are two reversible reduction waves observed for the complexes **79a-d**. The first reduction of $[Ru(\mathbf{76b\text{-}d})(tpy)(H_2O)]^{2+}$ complexes exhibits a steady decrease from -0.40 V to -0.56 V as the ligand **76b-d** becomes less planar and less delocalized. The second reductions occur in the range of -0.76 V to -1.15 V as the ligand becomes less planar.

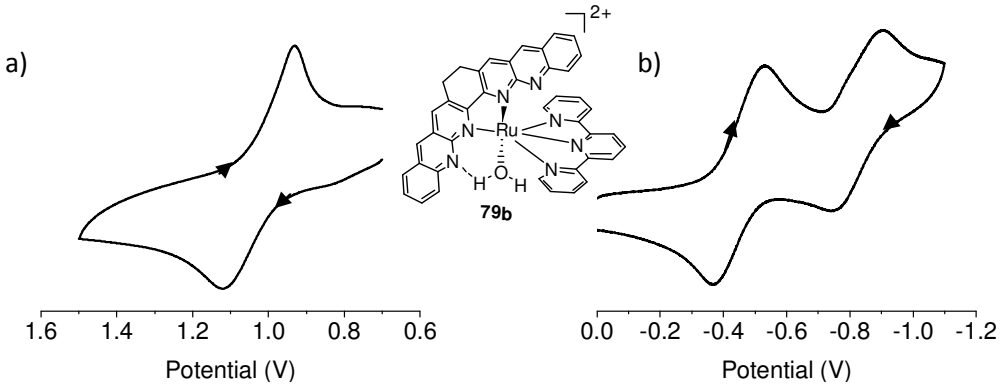

Figure 65. Cyclic voltammogram a) oxidation and b) reduction of **79b** vs SCE in CH_2Cl_2 (0.1 M $TBAPF_6$, 100 mv/s, at rt).

Table 20. Redox data ($E_{1/2}$ and ΔE) for $[Ru(bpy)(tpy)(H_2O)]^{2+}$, **79a-d** and **61a-c**.

Compounds	$E_{1/2}^{ox}(\Delta E)$ [a]	$E_{1/2}^{red}(\Delta E)$ [a]
$[Ru(tpy)_2]^{2+}$	+1.30 (187)	-1.27 (110), -1.60 (147)
$[Ru(bpy)(tpy)(H_2O)]^{2+}$	+0.82 (123)	-1.51 (130)
$[Ru(\mathbf{76a})(tpy)(H_2O)]^{2+}$ (**79a**)	+1.19 (83)	-0.48 (60), -0.81 (52)
$[Ru(\mathbf{76b})(tpy)(H_2O)]^{2+}$ (**79b**)	+1.20 (52)	-0.40 (77), -0.76 (46)
$[Ru(\mathbf{76c})(tpy)(H_2O)]^{2+}$ (**79c**)	+1.02 (189)	-0.45 (165), -0.82 (160)
$[Ru(\mathbf{76d})(tpy)(H_2O)]^{2+}$ (**79d**)	+0.98 (126)	-0.56 (102), -1.15 (117)
$[Ru(\mathbf{60b})(tpy)(H_2O)]^{2+}$ (**61b**)	+1.08 (80)	-0.72 (86), -1.16 (87)
$[Ru(\mathbf{60c})(tpy)(H_2O)]^{2+}$ (**61c**)	+1.04 (90)	-0.78 (92), -1.21 (100)
$[Ru(\mathbf{60d})(tpy)(H_2O)]^{2+}$ (**61d**)	+1.01 (89)	-0.83 (87), -1.22 (93)

[a] Measured relative to SCE in CH_2Cl_2 containing Bu_4NPF_6 (0.1 M); $E_{1/2} = (E_{pa} + E_{pc})/2$ in V, $\Delta E = (E_{pa} - E_{pc})$ in mV.

*4.4.6.7. Electrochemical studies of the complexes **81a-d***

The cyclic voltammograms of complexes **81a-d** were recorded in dichloromethane at room temperature and the electrochemical properties are summarized in Table 21. Figure 66a shows the oxidative wave for complex **81a** and Figure 66b shows the reductive wave.

There is one reversible oxidation wave observed for the complexes of [Ru(**58a-b**)$(bpy)_2]^{2+}$, [Ru(**60b-d**)$(bpy)_2]^{2+}$, and [Ru(**76b-d**)$(bpy)_2]^{2+}$. The mixed ligand biquinoline, binaphthyridine, and bi-4-azaacridine complexes show variation in the conformation of the bridged ligands and the oxidation potentials vary in a less defined pattern from +1.34 to +1.37 V (Table 22), +1.18 to +1.42 V (Table 22), and +1.25 to +1.38 V (Table 21), respectively. As the 3,3'-bridge increases in length the oxidation potential for biquinoline complexes decreases by 30 mV, and for binaphthyridine and bi-4-azaacridine complexes increases by 240 mV and 130 mV, respectively.

There are two reversible reduction waves observed for the complexes **81a-d**. The first reduction of [Ru(**76b-d**)$(bpy)_2]^{2+}$ complexes exhibits a steady decrease from -0.43 V to -0.54 V by 110 mV as the ligand **76b-d** becomes less planar and less delocalized. The second reductions occur in the range of -0.89 V to -1.01 V as the ligand becomes more planar (Table 21). The first reduction of the biquinoline, binaphthyridine, and bi-4-azaacridine complexes gets more negative as the 3,3'-bridge increases in length.

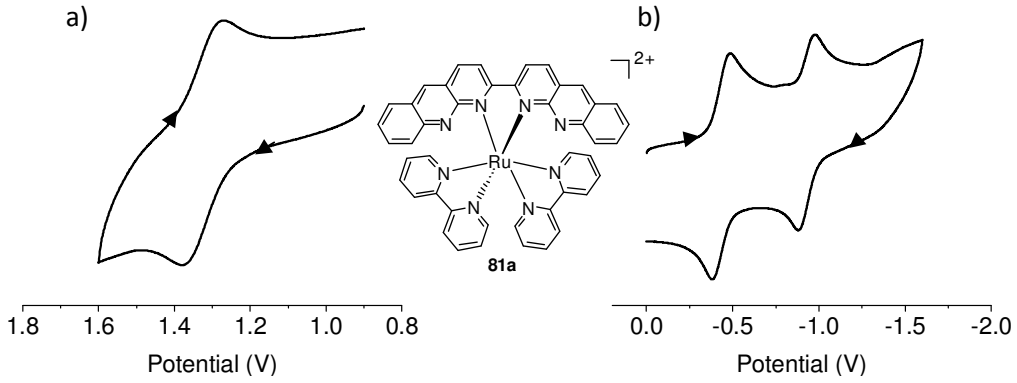

Figure 66. Cyclic voltammogram a) oxidation and b) reduction of **81a** vs SCE in CH_2Cl_2 (0.1 M $TBAPF_6$, 100 mv/s, at rt).

Table 21. Redox data ($E_{1/2}$ and ΔE) for $[Ru(bpy)_3]^{2+}$ and complexes **81a-d**.[a]

Compounds	$E_{1/2}^{ox}(\Delta E)$	$E_{1/2}^{red}(\Delta E)$
$[Ru(bpy)_3]^{2+}$	+1.33 (208)	-1.32 (133), -1.59 (160)
[Ru(**76a**)$(bpy)_2$]$(PF_6)_2$ (**81a**)	+1.34 (117)	-0.43 (97), -0.95 (98)
[Ru(**76b**)$(bpy)_2$]$(PF_6)_2$ (**81b**)	+1.25 (148)	-0.51 (114), -1.01 (119)
[Ru(**76c**)$(bpy)_2$]$(PF_6)_2$ (**81c**)	+1.26 (126)	-0.52 (98), -0.98 (96)
[Ru(**76d**)$(bpy)_2$]$(PF_6)_2$ (**81d**)	+1.38 (122)	-0.54 (103), -0.89 (101)

[a] Measured relative to SCE in CH_2Cl_2 containing Bu_4NPF_6 (0.1 M); $E_{1/2} = (E_{pa} + E_{pc})/2$ in V, $\Delta E = (E_{pa} - E_{pc})$ in mV.

Table 22. Half-wave potentials for derivatives of biq and binap Ru(II) complexes.[a]

Compounds	$E_{1/2}^{ox}$	$E_{1/2}^{red}$
$[Ru(biq)(bpy)_2](PF_6)_2$	+1.37	-0.89, -1.36
[Ru(**58a**)$(bpy)_2$]$(PF_6)_2$	+1.36	-0.90, -1.43
[Ru(**58b**)$(bpy)_2$]$(PF_6)_2$	+1.34	-0.90, -1.37
$[Ru(binap)(bpy)_2](PF_6)_2$	+1.42	-0.53, -1.00
[Ru(**60b**)$(bpy)_2$]$(PF_6)_2$	+1.18	-0.76, -1.26
[Ru(**60c**)$(bpy)_2$]$(PF_6)_2$	+1.18	-0.80, -1.26
[Ru(**60d**)$(bpy)_2$]$(PF_6)_2$	+1.33	-0.70, -1.08

[a] Measured relative to SCE in CH_3CN containing Bu_4NPF_6 (0.1 M); $E_{1/2} = (E_{pa} + E_{pc})/2$ in V at room temperature.

*4.4.6.8. Mass spectra for complexes **79a-d***

Complexes **79a-d** showed a pattern corresponding to the loss of two PF_6 and one H_2O with $C_xH_yN_7Ru$ isotopic distribution. The positive ion MALDI-TOF mass spectrum (Figure 67, left) showed a pattern at *m/z* 693 $[M-(H_2O)-2(PF_6)]^+$ similar to the simulated isotopic distribution for $C_{39}H_{25}N_7Ru$ (Figure 67, right) confirming the formation of the complex [Ru(**76a**)(tpy)(H_2O)]$^{2+}$.

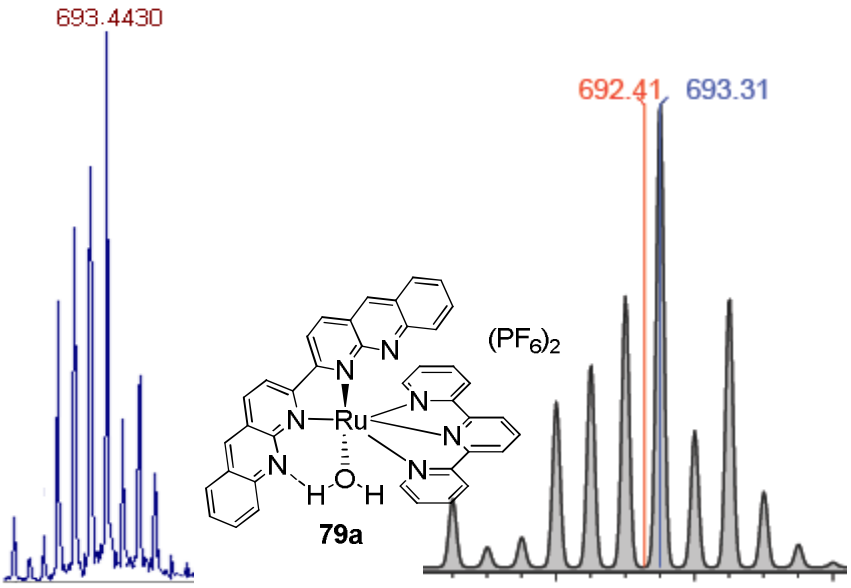

Figure 67. The MALDI-TOF mass spectrum of **79a** (left) and the calculated mass distribution (right) for $C_{39}H_{25}N_7Ru$.

*4.4.6.9. Mass spectra for complexes **81a-d***

Complexes **81a-d** showed a pattern corresponding to the loss of two PF_6 with $C_xH_yN_8Ru$ isotopic distribution. The positive ion MALDI-TOF mass spectrum (Figure 68, left) showed a pattern at *m/z* 826 $[M\text{-}2(PF_6)]^+$ similar to the simulated isotopic distribution for $C_{48}H_{36}N_8Ru$ (Figure 68, right) confirming the formation of the complex $[Ru(\mathbf{76d})(bpy)]^{2+}$.

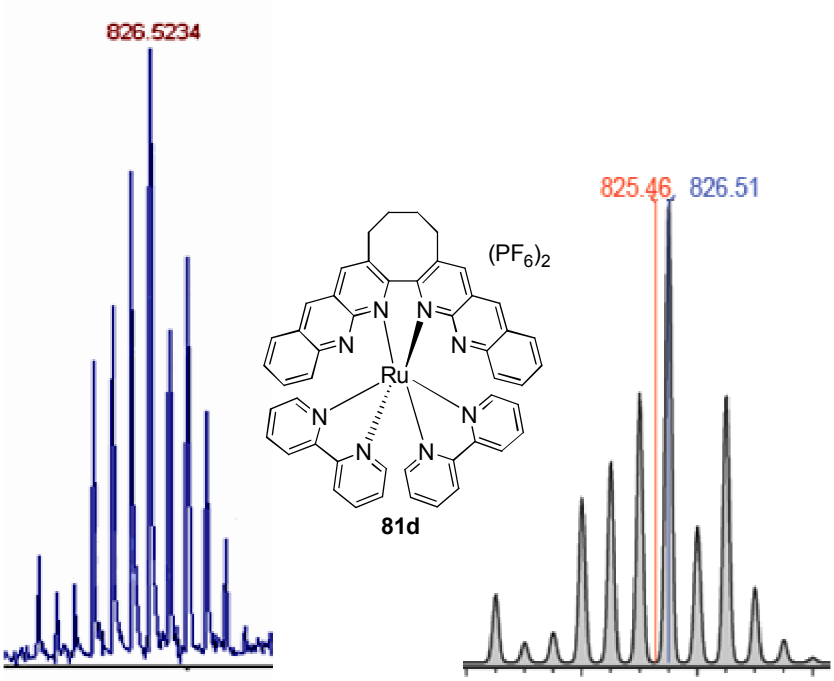

Figure 68. The MALDI-TOF mass spectrum of **81d** (left) and the calculated mass distribution (right) for $C_{48}H_{36}N_8Ru$.

*4.4.6.10. X-Ray determination of [Ru(**76d**)(bpy)$_2$](PF$_6$)$_2$· ½ acetone*

To help better understand the conformational demands of octahedral coordination on the geometry of bi-4-azaacridine ligands, we undertook a single crystal X-ray analysis of the complex [Ru(**76d**)(bpy)$_2$](PF$_6$)$_2$.

The measurements were made with a Siemens SMART platform diffractometer equipped with a 4K CCD APEX II detector. A hemisphere of data (1271 frames at 6 cm detector distance) was collected using a narrow-frame algorithm with scan widths of 0.3% in omega and an exposure time of 40 s/frame. The data were integrated using the Bruker-Nonius SAINT program, with the corrected intensities. Some of the pertinent geometric data are summarized in Table 23.

The complex [Ru(**76d**)$(bpy)_2$]$(PF_6)_2$ was crystallized in 1:1 acetone/H_2O solution to afforded a dark green plate, having the approximate dimensions of 0.40 x 0.25 x 0.10 mm^3. The asymmetric unit consists of one cation, two PF_6 anions, and one-half molecule of acetone solvent situated on an inversion center. The ORTEP plot for [Ru(**76d**)$(bpy)_2$]$^{2+}$ cation is illustrated in Figures 69-70.

For the tetramethylene-bridged free ligand **76d**, we have estimated a dihedral angle of about 74 ^{o} between the two azaacridine halves of the molecule (Table 13). Due to the constraints of the five-membered chelate ring, the ligand flattens considerably in the complex. Taking the average of the interior (N30–C31–C32–N1) and exterior (C18–C31–C32–C13) torsion angles for the estimated structure and the crystal structure, we find a dihedral angle of 31.7 ^{o} and find the dihedral angle of 28.1 ^{o}, respectively (Figure 69, Table 24). The dihedral angle between the estimated and the crystal structure differ only by 3.6 ^{o}. The Ru–N1 and Ru–N30 bond lengths are relatively short at ~2.096 Å. The bond angle between N30–C31–C32 (114.24 ^{o}) and N1–C32–C31 (113.86 ^{o}) is similar to each other. The C–C bond lengths in the four carbon bridge vary from 1.509 to 1.538 Å. The Ru–N bond lengths in complex **81d** vary from 2.043 to 2.098 Å. Among the Ru–N bond lengths, Ru–N33 is the shortest and the Ru–N30 is the longest. The ligand **76d** is significantly nonplanar. Therefore, Ru–N1 (2.096 Å) and Ru–N30 (2.098 Å) which are the bond lengths between the ligand **76d** and the Ru metal are longer than the Ru–N bond lengths between the bpy and the Ru metal (2.066 to 2.043 Å).

Table 23. Data collection and parameters for [Ru(**76d**)$(bpy)_2$]$(PF_6)_2$·1/2 acetone.

Compound	[Ru(**76d**)$(bpy)_2$]$(PF_6)_2$·1/2 acetone

Molecular Formula	$C_{48}H_{36}F_{12}N_8P_2Ru \cdot 1/2$ acetone
Molecular Weight	1144.90
Space group	$P2_1/n$ (Monoclinic)
Cell constants	a = 18.4482(13) Å α = 90 °
	b = 12.5148(9) Å β = 109 °
	c = 21.8850(16) Å γ = 90 °
Formula units per cell	Z = 4
Volume	4765.5(6) Å^3
Crystal color and shape	Very dark green plate
Crystal size	0.40 x 0.25 x 0.10 mm
Density	ρ = 1.596 g/cm^3
Absorption coefficient	μ = 0.491 mm^{-1}
Temperature	T = 223(2) K
Radiation	λ = 0.71073 Å
Collection range	1.26 ° $\leq \theta \leq$ 25.07 °
R1	0.0514
*wR*2	0.1252

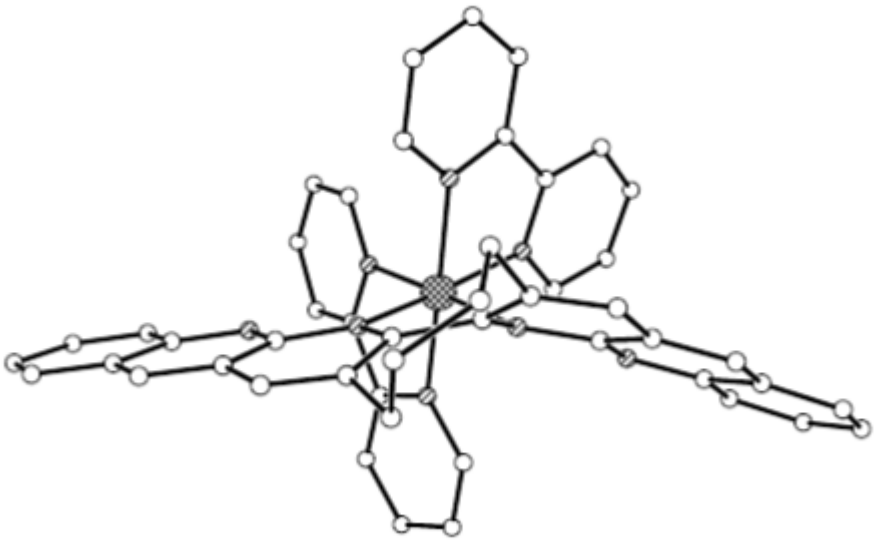

Figure 69. Isotropic view showing the configuration of the main ligand in [Ru(**76d**)(bpy)$_2$](PF$_6$)$_2$.

Table 24. Selected geometric parameters for [Ru(**76d**)(bpy)$_2$](PF$_6$)$_2$·1/2 acetone.

Bond lengths (Å)			
Ru–N1	2.096 (3)	C31–C32	1.471 (5)
Ru–N30	2.098 (3)	C13–C14	1.522 (5)
Ru–N33	2.043 (3)	C14–C15	1.519 (6)
Ru–N44	2.066 (3)	C15–C16	1.509 (6)
Ru–N45	2.059(3)	C16–C17	1.538 (5)
Ru–N56	2.050 (3)	C17–C18	1.520 (5)
N1–C2	1.383 (4)	C18–C31	1.438 (5)
N1–C32	1.340 (4)	N30–C31	1.347 (4)
C32–C13	1.429 (5)	N30–C29	1.389 (4)
Bond angles (^{o})			
N30–Ru–N1	77.26 (11)	C17–C16–C15	112.51 (33)
N30–C31–C32	114.24 (29)	C16–C15–C14	112.12 (34)
N1–C32–C31	113.86 (29)	C15–C14–C13	115.77 (33)
C31–C18–C17	124.52 (32)	C14–C13–C32	122.72 (33)
C18–C17–C16	116.23 (32)		
Dihedral angles (^{o})			
N30–C31–C32–N1	24.5 (4)	C14–C15 –C16–C17	53.2 (5)
C18–C31–C32–C13	31.8 (5)	C15–C16 –C17–C18	90.9 (4)
C32–C13–C14–C15	110.1 (4)	C16–C17–C18–C19	86.8 (4)
C13–C14–C15–C16	82.7 (4)	C16–C17–C18–C31	100.7 (4)

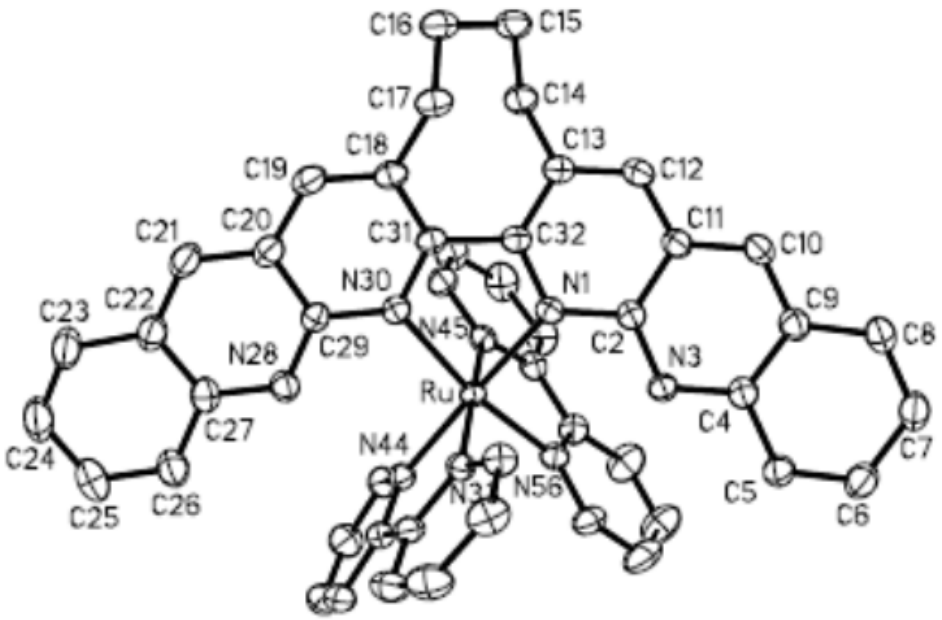

Figure 70. X-ray crystal structure of the cation of [Ru(**76d**)(bpy)$_2$](PF$_6$)$_2$·1/2 acetone with the atom numbering scheme, hydrogen atoms are omitted for clarity.

4.4.6.11. Photophysical measurements

Photooxidation and associated proton transfer steps are under investigation by the Damrauer Research Group at University of Colorado.

4.5. Summary of Results

The results of this project are summarized as follows:

1. The 2-chloro-3-quinolinecarbaldehyde (**71**) in 82% yield, 2-chloro-3-(1',3'-dioxolan-2'-yl)quinoline (**72**) in 95% yield, 2-aminoquinoline-3-carbaldehyde (**74**) in 50% yield, 1,2-cycloheptanedione (**75c**) in 90% yield, and 1,2-cyclooctanedione (**75d**) in 90% yield were synthesized and characterized by ^{1}H and ^{13}C NMR and IR.

12. Ligands **76a-d** (44-80%) were synthesized and characterized by ^{1}H and ^{13}C NMR, mass spectrometry, and elemental analysis.
13. As the 3,3'-bridge increases in length and the ligand becomes less planar, more twisted, and less delocalized.
14. The length of the anelating bridge controls the dihedral angle between the aromatic rings and thus the orientation of the unbound nitrogen with unshared electron pairs that could influence chemistry at the metal-center. The more sterically hindered annulated 3,3'-polymethylene bridged compounds **(76b-d**) are less planar than the unsubstituted system **(76a**).
15. The Ru(II) complexes **79a-d** (50-77%) and **81a-d** (50-60%) were synthesized in aq ethanol and ethylene glycol in a microwave oven, respectively and characterized by ^{1}H NMR, UV-vis spectroscopy, CV, mass spectrometry, and elemental analysis.
16. Complexes **79a-d** and **81a-d** show a decrease in the intensity of the long wavelength absorption band as the 3,3'-bridge increases in length and the ligand becomes less planar and less delocalized.
17. With regard to the UV-vis absorption spectra, complexes **79a-d** are ~70 nm more red-shifted than the binap analogs **61b-d** because of the extended π-conjugation.
18. The $[Ru(bpy)(tpy)(H_2O)]^{2+}$ has an electronic absorption at shorter wavelength with a larger absorption coefficient as compared to complexes **61b-d**. Complexes **79a-d** have an electronic absorption at longer wavelength with a smaller absorption coefficient as compared to complexes **61b-d**. As the number of

aromatic rings fused to the bpy increases, the resultant compound has an absorption at longer wavelength with a lower absorption coefficient.

19. The same argument is true for the $[Ru(bpy)_3]^{2+}$ and **81a-d** complexes.
20. The complexes **79a-d** and **81a-d** were excited at the maximum of their MLCT absorption band. These complexes do not show any appreciable emission at room temperature.
21. The H_2O group in the Ru(II) complexes **79a-d** is exchangeable with D_2O and acetonitrile.
22. The MALDI-TOF mass spectra for complexes **79a-d** showed a pattern corresponding to the loss of two PF_6 and one H_2O with $C_xH_yN_7Ru$ isotopic distribution. Complexes **81a-d** showed a pattern corresponding to the loss of two PF_6 with $C_xH_yN_8Ru$ isotopic distribution.

5. RUTHENIUM (II) COMPLEXES INVOLVING 2,6-DI(1',8'-NAPHTHYRID-2'-YL)4-*t*-BUTYLPYRIDINE DERIVATIVES

5.1. Introduction

Ruthenium complexes containing ring-substituted polypyridine ligands and related structures are known to catalyze water oxidation.[203] One such system is the "blue dimer" *cis*,*cis*-[{Ru(bpy)$_2$(H$_2$O)}$_2$O](ClO$_4$)$_4$ having [Ru(bpy)$_2$(H$_2$O)] subunits linked by a μ-oxo bridge which tends to cleave, thus limiting the lifetime of the catalyst.[42] This problem has been addressed by the design of ligands that bridge the two metal-centers and thus increase the stability of the catalyst.[204]

Zong and Thummel[44] have synthesized a new family of mono-nuclear Ru complexes for water oxidation. The structure of the ligands often dictates such critical features as absorption energy and intensity, redox properties, and excited state lifetimes.[205] Zong and Thummel have discovered that the use of 1,8-naphthyridine (nap) as a ligand component can show some distinct advantages over the more traditional pyridine or quinoline moieties.[142] Since nap is more electronegative and more delocalized than pyridine, transition metal complexes involving this moiety show longer wavelength and lower energy absorptions than their pyridine counterparts.[206]

Investigations with 1,10-phenanthroline have demonstrated that substituents in the *ortho*-positions have a stabilizing effect on the metal oxidation states. Studies by McMillin[207] and Karpishin[208] have methodically investigated this effect for a variety of different size substituents. Electronic effects can also play an important role such that

more electronically delocalizing or electronegative ligands can provide a lower energy π^* state and thus decrease the energy of the MLCT transition, allowing the chromophore to harvest more visible light.[209]

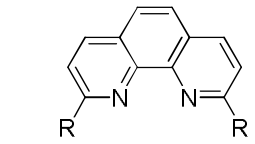

R=-phenyl, $-CH_2(CH_2)_2CH_3$, $-CH(CH_3)(C_2H_5)$, $-CH_3$

5.2. Objective of this Work

In this chapter Ru(II) complexes involving tridentate ligands 2,6-di(1',8'-naphthyrid-2'-yl)-4-*t*-butyl pyridine (**84**), 2,6-di(4'-azaacrid-3'-yl)-4-*t*-butylpyridine (**85**), 2-(1',10'-phenanthrolin-2'-yl)1,8-naphthyridine (**102**), and 3-(1',10'-phenanthrolin-2'-yl)4-azaacridine (**103**) are studied as catalysts for water oxidation.

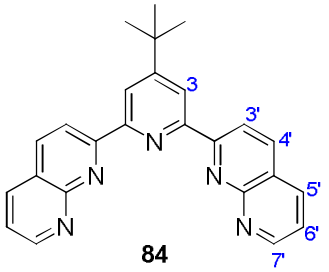

84

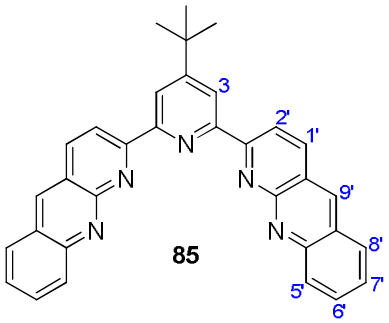

85

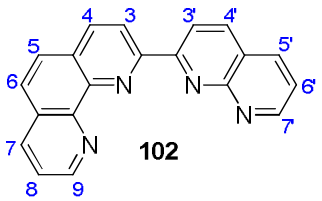

102

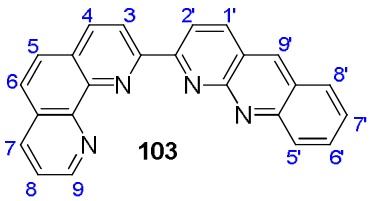

103

5.3. Results and Discussion

5.3.1. Synthesis of ligands 84 and 85

The Friedländer condensation of two equivalents of **83** in ethanolic KOH with one equivalent of 4-*t*-butyl-2,6-diacetyl pyridine (**82**) at 90 ^{o}C afforded 2,6-di(1',8'-naphthyrid-2'-yl)-4-*t*-butyl pyridine (**84**) in 87% yield and the Friedländer condensation of two equivalents of **74** in ethanolic KOH with one equivalent of **82** at 90 ^{o}C afforded 2,6-di(4'-azaacrid-3'-yl)-4-*t*-butylpyridine (**85**) in 90% yield. The synthetic route to ligands **84** and **85** is presented in Scheme 15.

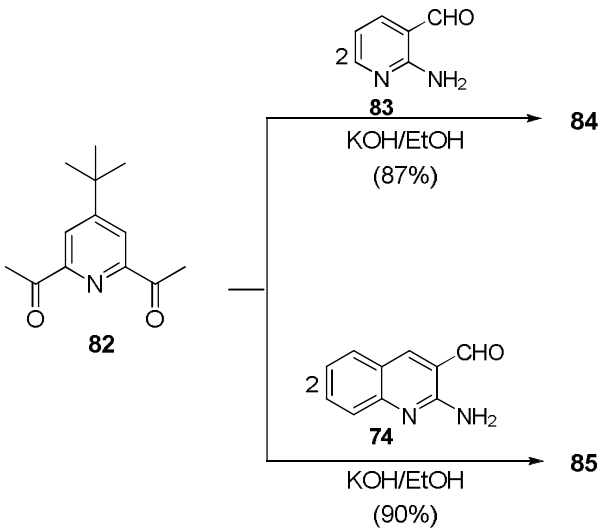

Scheme 15. Synthetic route to ligands **84** and **85**.

5.3.2. Synthesis of ligands 102 and 103

The synthesis of the ligands **102** and **103** starts with the preparation of the 2-acetyl-1,10-phenanthroline (**101**) (Scheme 16). The N-oxide **99** was prepared by treating 1,10-phenanthroline (**98**) with glacial acetic acid in 30% hydrogen peroxide in 85% yield.

Treatment of **99** with benzoyl chloride and KCN afforded 2-cyano-1,10-phenanthroline (**100**) in 87% yield. The N-oxide allows the introduction of a cyano group into the 2-position of the phenanthroline ring system. The cyano compound **100** was converted into 2-acetyl-1,10-phenanthroline (**101**) by treatment with CH_3MgBr in 60% yield (Scheme 16).

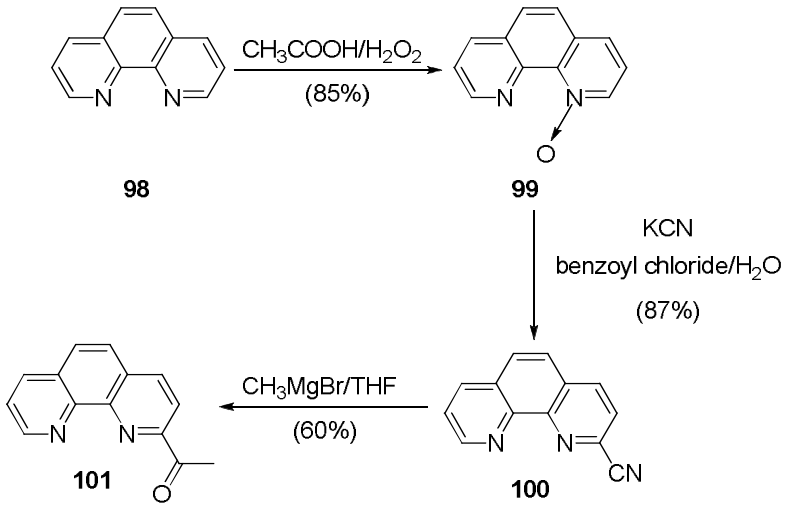

Scheme 16. Synthesis of 2-acetyl-1,10-phenanthroline (**101**).

The Friedländer condensation of one equivalent of **83** in ethanolic KOH with one equivalent of 2-acetyl-1,10-phenanthroline (**101**) at reflux afforded 2-(1',10'-phenanthrolin-2'-yl)1,8-naphthyridine (**102**), in 83% yield and the Friedländer condensation of one equivalent of **74** in ethanolic KOH with one equivalent of **101** at reflux afforded 3-(1',10'-phenanthrolin-2'-yl)4-azaacridine (**103**) in 65% yield. The synthetic route to ligands **102** and **103** is presented in Scheme 17.

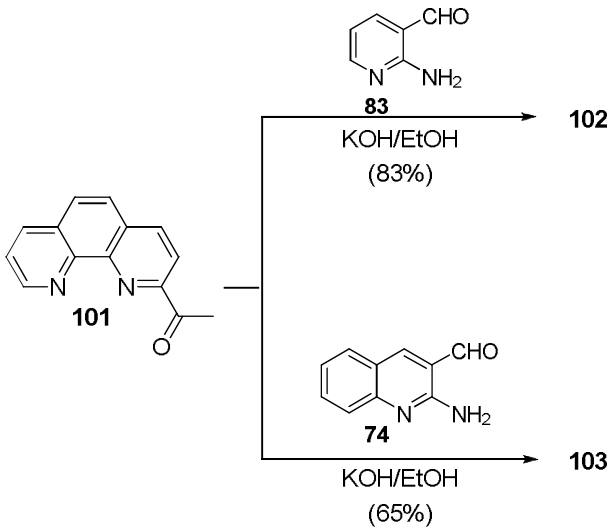

Scheme 17. Synthetic route to ligands **102** and **103**.

5.3.3. Synthesis of Ru(II) complexes of 84 and 85

The complex [Ru(tpy)Cl_3] (**77**) was synthesized from $RuCl_3 \cdot 3H_2O$ using the method of Stoessel *et al.*[193] The synthesis of the [Ru(**84-85**)(tpy)]$^{2+}$ complexes involved treating one equivalent of ligands **84** and **85** with one equivalent of **77** in 2-methoxy ethanol in the presence of triethylamine and precipitating the complexes as their hexafluorophosphate salts to afford complex **86** as a purple solid in 40% yield and complex **87** as a purple solid in 50% yield. The synthetic route to complexes **86** and **87** is presented in Scheme 18.

The complex [Ru(bpy)$(DMSO)_2Cl_2$] (**89**) was synthesized from [Ru$(DMSO)_4Cl_2$][210] (**88**) using the method of Ware *et al.*[211] The synthesis of the [Ru(**84-85**)(bpy)Cl]$^+$ complexes involved treating one equivalent of ligands **84** and **85** with one equivalent of **89** in aq ethanol in the presence of triethylamine and precipitating the complexes as their hexafluorophosphate salts to afford complex **90** as a green solid in

35% yield and complex **91** as a deep blue solid in 36% yield. The synthetic route to complexes **90** and **91** is presented in Scheme 18.

The synthesis of the [Ru(**84-85**)(bpy)(H_2O)]$^{2+}$ complexes involved treating one equivalent of ligands **84** and **85** with ten equivalents of $AgBF_4$ in acetone and H_2O and precipitating the complexes as their hexafluorophosphate salts to afford complex **92** as a a blue solid in 70% yield and complex **93** as a purple solid in 100% yield. Complex **92** and **93** are the aquo analogue of complex **90** and **91**, respectively. The synthetic route to complexes **92** and **93** is presented in Scheme 19.

The synthesis of the [Ru(**84-85**)(4-pic)$_2$(H_2O)]$^{2+}$ complexes involved treating one equivalent of ligands **84** and **85** with 1.1 equivalent of $RuCl_3 \cdot 3H_2O$ in ethanol, followed by the addition of 2.2 equivalent of 4-picoline, H_2O and triethylamine and precipitating the complexes as their hexafluorophosphate salts to afford complex **94** as a dark blue solid in 50% yield and complex **95** as a deep blue solid in 50% yield. Complex **95** was prepared by Zong[44] and the tabulated data are taken from the literature. The synthetic route to complexes **94** and **95** is presented in Scheme 18.

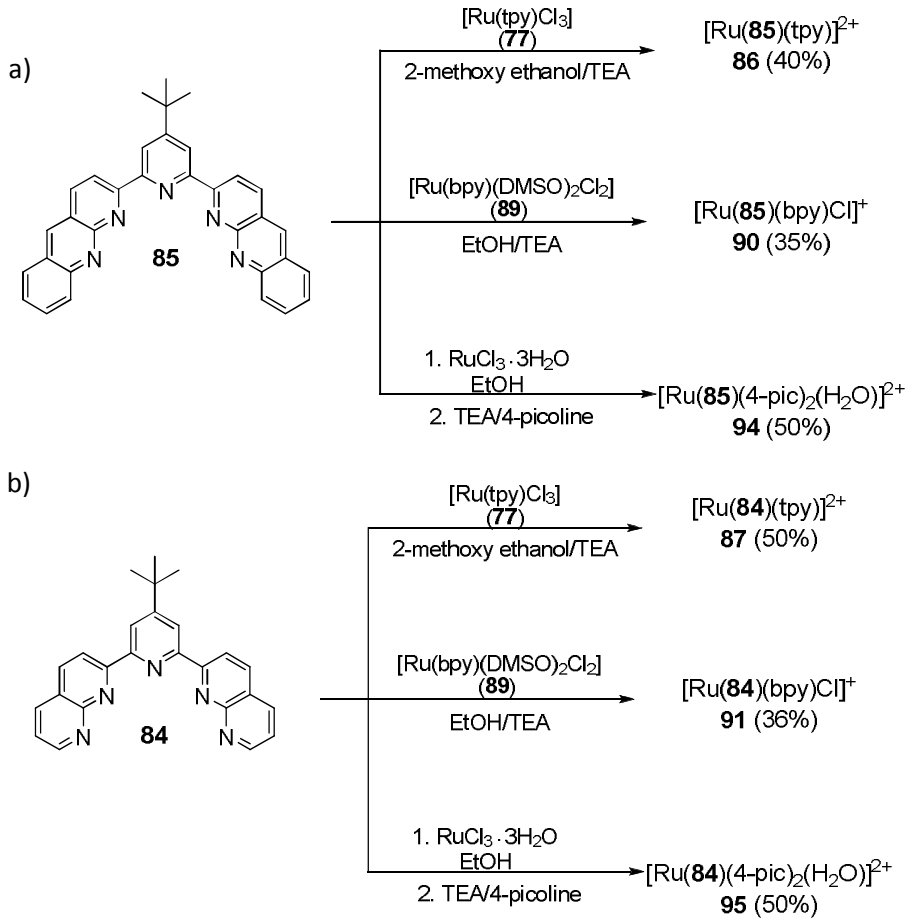

Scheme 18. Preparation of the Ru(II) complexes of a) 2,6-di(4'-azaacrid-3'-yl)-4-*t*-butylpyridine and b) 2,6-di(1',8'-naphthyrid-2'-yl)-4-*t*-butylpyridine.

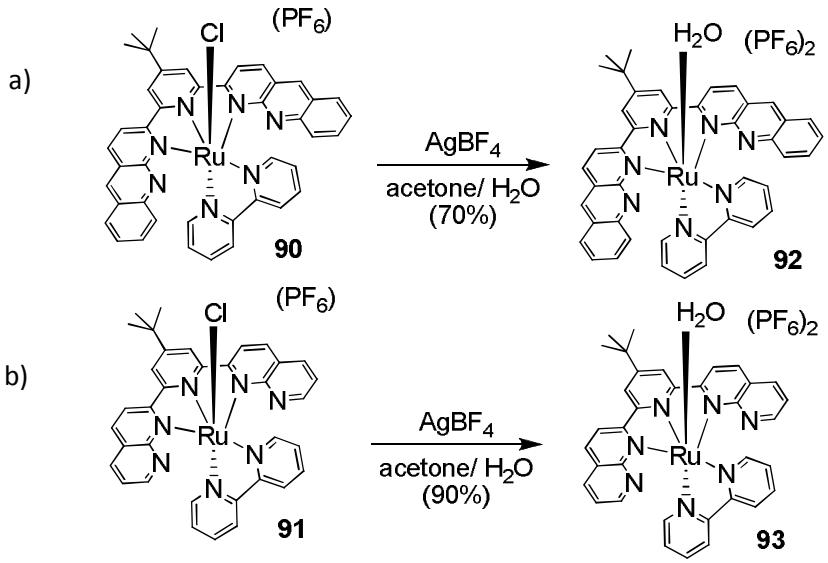

Scheme 19. Conversion of –Cl to H_2O in complexes of a) **90** and b) **91**.

5.3.4. Synthesis of Ru(II) complexes of 102 and 103

The complex $[Ru(DMSO)_2(4\text{-pic})_2Cl_2]$ (**104**)[212] was synthesized from $[Ru(DMSO)_4Cl_2]$[210] (**88**) using the method of Silva *et al*. The synthesis of the $[Ru(\mathbf{102})(4\text{-picoline})_2(H_2O)]^{2+}$ involved treating one equivalent of ligand **102** with one equivalent of **104** in aq EtOH and precipitating as hexafluorophosphate salt to afford complex **105** as a green solid in 10% yield. The synthesis of the $[Ru(\mathbf{102\text{-}103})(bpy)Cl]^+$ complexes involved treating one equivalent of ligands **102** and **103** with 1.2 equivalent $RuCl_3{\cdot}3H_2O$ in ethanol, followed by the addition of 1.1 equivalent of bpy, H_2O and triethylamine and precipitating the complexes as their hexafluorophosphate salts to afford complexes **106** and **107** as a green solid in 10% and 20% yield, respectively. The synthetic route to complexes **105-107** is presented in Scheme 20.

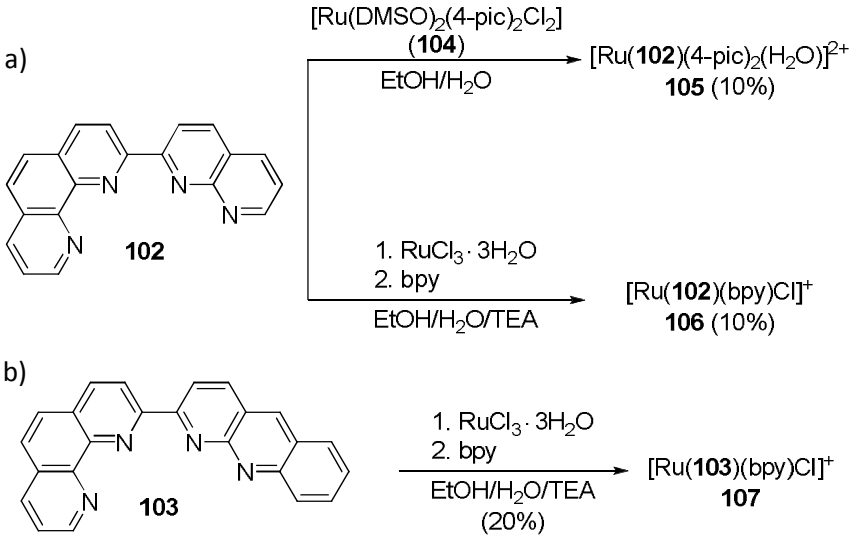

Scheme 20. Preparation of the Ru(II) complexes of a) **105** and **106** and b) **107**.

Several synthetic approaches were attempted to prepare $[Ru(\mathbf{103})(4\text{-pic})_2(H_2O)]^{2+}$ involving the treatment of one equivalent of ligand **103** (i) with one equivalent of **104** in

aq EtOH, (ii) with 2.2 equivalents of 4-picoline and one equivalent of $RuCl_3 \cdot 3H_2O$ in EtOH, (iii) with one equivalent of $RuCl_3 \cdot 3H_2O$ in 4-picoline. As a result instead of desired product we recovered the starting material or got $[Ru(\mathbf{103})(4\text{-pic})_3]^{2+}$.

5.3.5. Spectroscopic properties of the ligands

5.3.5.1. NMR spectra

The ^1H NMR spectrum of **85** in $CDCl_3$ is shown in Figure 71. Compound **85** is symmetric about the central pyridine. The two singlets at 9.13 and 8.89 ppm could be assigned to H3 and H9', respectively. This assignment was made based on the chemical shift of H3 in **84**. The downfield AB doublets at 9.05 and 8.56 ppm are assigned to H2' and H1', respectively. The singlet at 1.58 ppm is assigned to the *t*-butyl group.

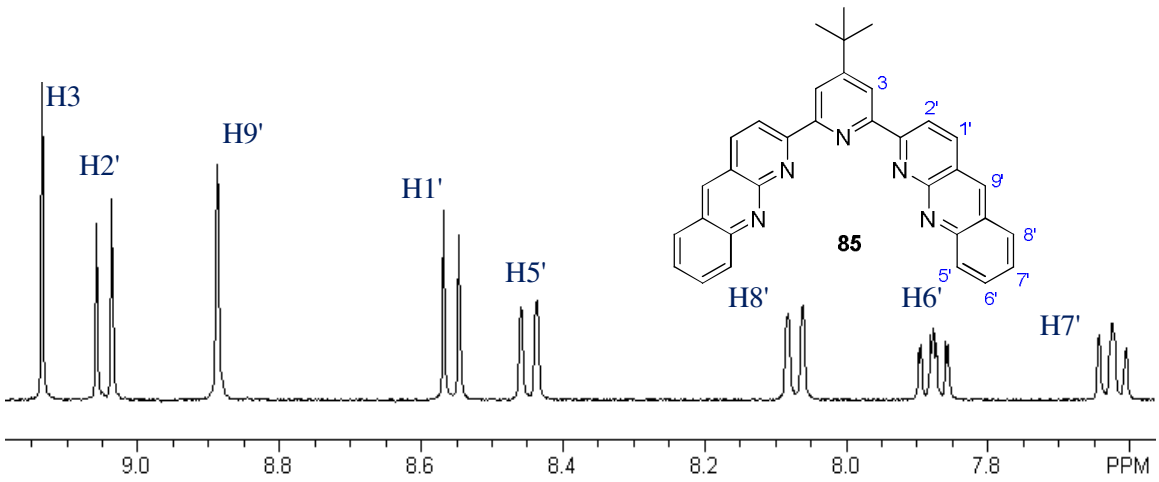

Figure 71. Downfield region of ^1H NMR spectrum of **85** in $CDCl_3$ (400 MHz, at rt).

A complete ^{1}H NMR analysis of ligands **84** and **85** is reported in Table 25. All the protons could be readily identified due to their characteristic coupling patterns aided by the use of 2D homonuclear chemical shift correlated ^{1}H NMR (COSY) spectra.

Table 25. 1H NMR chemical shift data of the ligands **84** and **85** recorded in $CDCl_3$ at rt.

Compound	H3	H1'	H2'	H3'	H4'	H5'	H6'	H7'	H8'	H9'	*t*-butyl
85	9.13	8.56	9.05	--	--	8.45	7.89	7.63	8.08	8.89	1.58
84	9.00	--	--	9.02	8.38	8.28	7.54	9.19	--	--	1.53

The downfield region of ^{1}H NMR spectra of ligands **102-103** in $CDCl_3$ are shown in Figures 94-95.

5.3.6. Spectroscopic properties of the complexes

5.3.6.1. NMR spectra

The complexes **86-87**, **90-95**, and **105-107** are characterized by their ^{1}H NMR spectra in acetone-*d6*, which show signals that are both well-resolved and dispersed for the complexes at room temperature. The values and intensities of the chemical shifts indicate that the complexation between ligand and metal atom occurred in a 1:1 molar ratio. Protons could be readily identified due to their characteristic coupling patterns aided by the use of 2D homonuclear chemical shift correlated ^{1}H NMR (COSY) spectra. The signals for complexes **86-87** and **90-95** are assigned on the NMR spectra and tabulated in Table 26. The downfield regions of the ^{1}H NMR spectra of ruthenium complexes of ligands **84** and **85** in acetone-*d*6 are shown in Figures 86-93.

The downfield region of ^{1}H NMR spectrum of **86** in acetone-*d*6 is shown in Figure 86. The two singlets in complex **86** corresponding to H3 and H9' are observed at 9.61 and 9.14 ppm with an integration of two protons each, explaining that the ligand **85** is symmetric. The downfield AB doublets at 9.34 and 8.87 ppm are assigned to H2' and H1' of **85**. The triplet at 9.16 ppm is the characteristic Ha triplet of tpy with an integration of one proton. The singlet at 1.88 ppm is assigned to the *t*-butyl group.

The downfield region of ^{1}H NMR spectrum of **87** in acetone-*d*6 is shown in Figure 87. There is one singlet at 9.48 ppm assigned to H3 with an integration of two protons explaining the ligand **84** is symmetric. The downfield AB doublets at 9.21 and 8.70 ppm are assigned to H3' and H4' of **84**. The triplet at 8.65 ppm is the characteristic Ha triplet of tpy with an integration of one proton. The singlet at 1.80 ppm is assigned to the *t*-butyl group.

The downfield region of ^{1}H NMR spectrum of **90** in acetone-*d*6 is shown in Figure 88. The two singlets in complex **90** corresponding to H3 and H9' are observed at 9.27 and 9.11 ppm with an integration of two protons each, explaining that the ligand **85** is symmetric. However, H6" and H6' of bpy appear at 10.71 and 7.57 ppm, respectively, indicating that the bpy is unsymmetric in this complex. The downfield AB doublets at 8.99 and 8.78 ppm are assigned to H2' and H1' of **85**. The singlet at 1.78 ppm is assigned to the *t*-butyl group.

The downfield region of ^{1}H NMR spectrum of **91** in acetone-*d*6 is shown in Figure 89. The singlet in complex **91** corresponding to H3 is observed at 9.14 ppm,

integrating for two protons, explaining that ligand **84** is symmetric. However, H6" and H6' of bpy appear at 10.48 and 7.56 ppm, respectively, indicating that bpy is unsymmetric in this complex. The downfield AB doublets at 8.99 and 8.60 ppm are assigned to H3' and H4' of **84**. The singlet at 1.73 ppm is assigned to *t*-butyl group.

Complexes **92** and **93** are the aquo analogue of complexes **90** and **91**. The downfield region of the ^{1}H NMR spectrum of **92** and **93** in acetone-*d*6 are shown in Figures 90 and 91, respectively. The downfield doublet for H6" in **90** is shifted from 10.71 ppm to 10.26 ppm for **92** and the downfield doublet for H6" in **91** is shifted from 10.48 ppm to 9.96 ppm for **93** because –Cl is more electronegative than H_2O. As the electron density decreases around the proton, the chemical shift of the proton shifts downfield.

The downfield region of ^{1}H NMR spectrum of **94** in acetone-*d*6 is shown in Figure 92. The two singlets in complex **94** corresponding to H3 and H9' are observed at 9.62 and 9.29 ppm with an integration of two protons each, indicating that ligand **85** is symmetric. The two doublets at 7.97 and 6.70 ppm, integrating for four protons each, are assigned respectively to Ha and Hb for 4-picoline. The downfield AB quartet at 9.20-9.13 ppm is assigned to H1' and H2' of **85**. The singlet at 1.96 ppm is assigned to the methyl group and the singlet at 1.68 ppm is assigned to the *t*-butyl group. The peak for bound H_2O was not observed in the ^{1}H NMR spectrum.

The downfield region of ^{1}H NMR spectrum of **95** in acetone-*d*6 is shown in Figure 93. The singlet in complex **95** corresponding to H3 is observed at 9.17 ppm,

integrating for two protons, indicating that ligand **84** is symmetric. The downfield AB quartet at 9.16-8.94 ppm is assigned to H3' and H4' of **84**. The singlet at 2.83 ppm is assigned to the methyl group and the singlet at 1.64 ppm is assigned to the *t*-butyl group. The two doublets at 7.89 and 6.78 ppm, integrating for four protons each, are assigned respectively to Ha and Hb for 4-picoline. As it is reported, the chloro complex is not isolated and only the H-bonded aquo species is produced.[44]

Table 26. ^{1}H NMR chemical shift data of the ligand part for the Ru(II) complexes recorded in acetone-*d6* at rt.

Compound	H3	H9'	H1'	H2'	H5'	H6'	H7'	H8'	*t*-butyl
[Ru(**85**)(tpy)]$^{2+}$ (**86**)	9.61	9.14	8.88	9.23	8.11	7.73	7.65	7.64	1.88
[Ru(**85**)(bpy)Cl]$^{+}$ (**90**)	9.27	9.11	8.78	8.99	8.11	7.65	7.85	7.19	1.78
[Ru(**85**)(bpy)(H_2O)]$^{2+}$ (**92**)	9.41	9.20	8.95	9.14	8.17	7.72	7.93	7.25	1.79
[Ru(**85**)(4-pic)$_2$(H_2O)]$^{2+}$ (**94**)	9.62	9.29	9.15	9.15	8.79	8.26	7.93	8.44	1.68
Compound	H3	H3'	H4'	H5'	H6'	H7'	*t*-butyl		
[Ru(**84**)(tpy)]$^{2+}$ (**87**)	9.48	9.21	8.70	8.37	7.56	8.40	1.80		
[Ru(**84**)(bpy)Cl]$^{+}$ (**91**)	9.14	8.99	8.60	8.22	7.52	8.36	1.73		
[Ru(**84**)(bpy)(H_2O)]$^{2+}$ (**93**)	9.24	9.09	8.72	8.31	7.59	8.45	1.72		
[Ru(**84**)(4-pic)$_2$(H_2O)]$^{2+}$ (**95**)	9.17	9.16	8.94	8.83	8.05	9.44	1.64		

5.3.6.2. Electronic spectra

The electronic absorption maxima (λ_{max}) and molar extinction coefficients (ε) of complexes **86-87**, **90-95**, and **105-107** were recorded in acetone at room temperature and are listed in Table 27. The long wavelength region of the absorption spectra of the complexes **86-87** and **90-95** are illustrated in Figures 72-74. The spectra consist of two well-defined regions. A relatively intense absorption is observed at shorter wavelengths, 200-350 nm. This absorption is attributed to ligand-centered π–π^* transitions associated

with the aromatic rings of the ligands. The less intense absorption bands at longer wavelength in the region of 350-800 nm are assigned as MLCT and are due to the promotion of an electron from a metal d-orbital to a π* orbital of the most electronegative ligand. Polypyridyl Ru(II) complexes are often characterized by a broad MLCT band in the visible region of the electromagnetic spectrum.

The 4-azaacridine Ru(II) complexes **86**, **90**, **92**, **94**, and **107** are more red-shifted than their 1,8-naphthyridine analogues **87**, **91**, **93**, **95**, and **106** due to the further extension of π-conjugation resulting from a benzo ring being fused to the nap units. The π*–levels of 4-azaacridine molecule lies at lower energy than nap and have a greater electron affinity.

The shape of the bands remains almost invarient for both bi-4-azaacridine and bi-naphthyridine systems. The bi-4-azaacridine complexes **90** and **94** have higher absorbance than the bi-naphthyridine analogs **91** and **95**, respectively. However, for the [Ru(tpy)] system the naphthyridine analogue **87** has a higher absorbance than the bi-4-azaacridine analogue **86** (Figures 72-74). All UV-Vis absorbance measurements were repeated in duplicate under the same conditions and the same results were obtained.

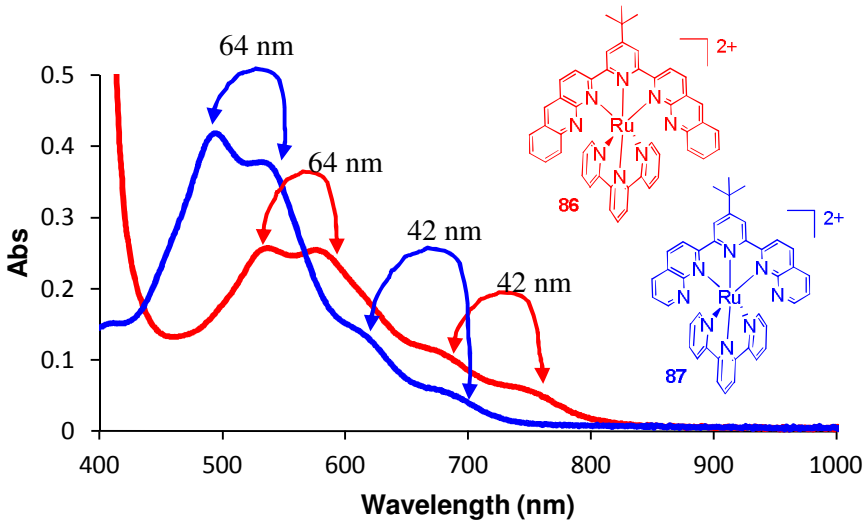

Figure 72. Visible spectra of **86** and **87** recorded in acetone (5.0×10^{-5} M): **86** (red) and **87** (blue).

The vibrational difference at lower wavelength for $[Ru(\mathbf{85})(tpy)]^{2+}$ (**86**) is 64 nm and the vibrational difference at longer wavelength is 42 nm. These differences are the same for $[Ru(\mathbf{84})(tpy)]^{2+}$ (**87**) (Figure 72).

Complexes $[Ru(\mathbf{85})(bpy)Cl]^{+}$ (**90**) and $[Ru(\mathbf{84})(bpy)Cl]^{+}$ (**91**) show less vibrational structure in comparison with complexes **86** and **87**. Complex **90** has an unusual absorption at 930 nm (Figure 73).

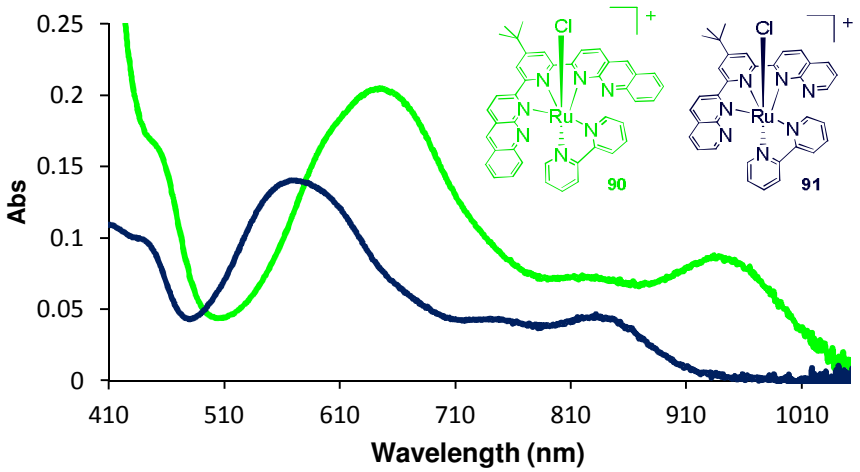

Figure 73. Visible spectra of **90** and **91** recorded in acetone (5.0 x 10^{-5} M): **90** (green) and **91** (blue).

Complexes [Ru(**85**)(4-pic)(H_2O)]$^{2+}$ (**94**) and [Ru(**84**)(4-pic)(H_2O)]$^{2+}$ (**95**) show less vibrational structure in comparison with other Ru complexes in this study (Figure 74).

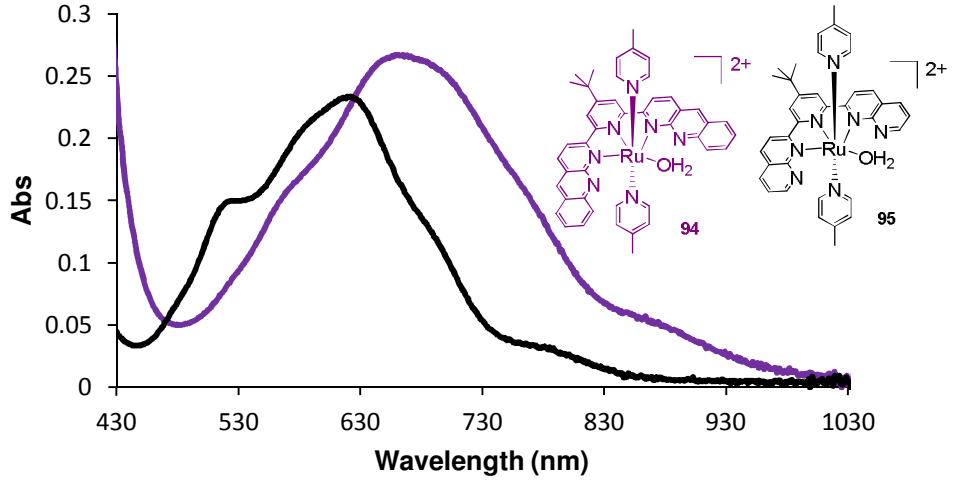

Figure 74. Visible spectra of **94** and **95** recorded in acetone (5.0 x 10^{-5} M): **94** (purple) and **95** (black).

Among the [Ru(**85**)] complexes, [Ru(**85**)(bpy)Cl]$^{+}$ (**90**) has the lowest energy absorption. The –Cl analogue of [Ru(**85**)(bpy)] has an absorption at longer wavelength than the aquo analogue. For the naphthyridine system, [Ru(**84**)(bpy)Cl]$^{+}$ (**91**) has the

lowest energy absorption. The –Cl analogue of [Ru(**84**)(bpy)] has an absorption at longer wavelength than the aquo analogue.

The electronic absorption of $5x10^{-5}$ M Ru(II) aquo complexes **92-95** were recorded in acetone + 2 mL acetonitrile at room temperature. When an acetone solution of complexes **92-95** is exposed to added acetonitrile, the absorption spectrum of these complexes changes with time. The Ru-OH_2 complexes **92-95** were converted into Ru-MeCN in about 1 h after which the intensity of the absorption band did not change with time. The change in the absorption indicates that bound water is being replaced by acetonitrile. Electronic absorption spectrum of $[Ru(\mathbf{85})(4\text{-pic})(H_2O)]^{2+}$ (**94**) with added acetonitrile recorded as a function of time is show in Figure 75. The band at ~661 decreases and the band at 597 nm increases in intensity.

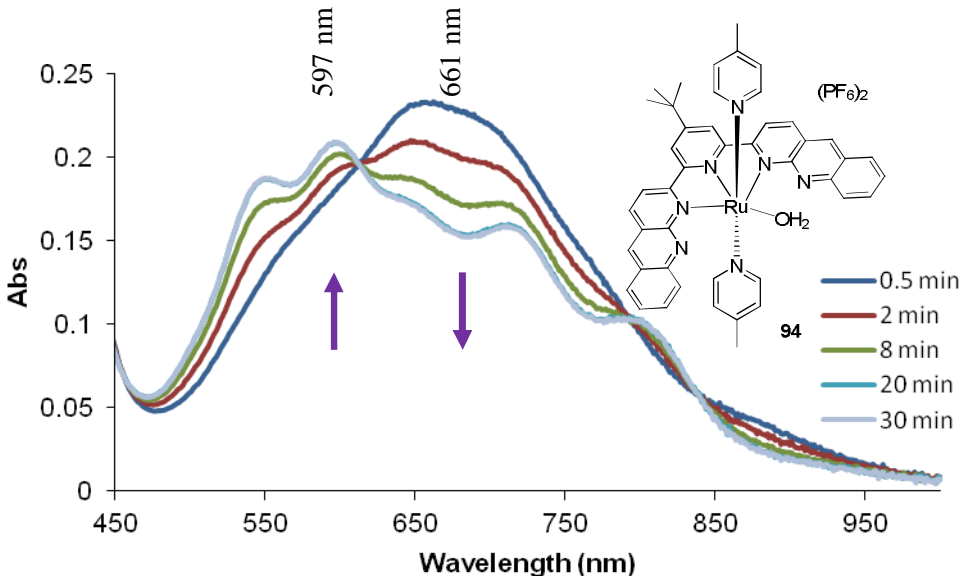

Figure 75. Electronic absorption spectrum of $[Ru(\mathbf{85})(4\text{-pic})_2H_2O]^{+2}$ (**94**) (7.5×10^{-5}M, 4 mL of acetone) with added CH_3CN (2 mL) recorded as a function of time.

The emission spectra of complexes **86-87** and **90-95** were recorded in acetone at room temperature. The complexes were excited at the maximum of their MLCT absorption band. None of the compounds showed any appreciable emission at room temperature.

Table 27. Electronic absorption maxima and molar extinction coefficients for Ru(II) complexes **86-87**, **90-95**, and **105-107**.

Compound	λ_{max}/nm (ε x 10^3 M^{-1} cm^{-1})[a]
[Ru(**85**)(tpy)]$^{2+}$ (**86**)	751 (sh), 677 (sh), 581 (5.08), 536 (5.14), 401 (16.56)
[Ru(**85**)(bpy)Cl]$^{+}$ (**90**)	940 (1.73), 837 (sh), 647 (4.06), 456 (sh), 403 (17.92)
[Ru(**85**)(bpy)(H_2O)]$^{2+}$ (**92**)	834 (sh), 609 (2.68), 546 (5.24), 403 (12.7)
[Ru(**85**)(4-pic)$_2$(H_2O)]$^{2+}$ (**94**)	861 (sh), 670 (5.30), 568 (sh)
[Ru(**84**)(tpy)]$^{2+}$ (**87**)	681 (sh), 615 (sh), 537 (7.50), 494 (8.38)
[Ru(**84**)(bpy)Cl]$^{+}$ (**91**)	835 (0.93), 740 (sh), 574 (2.77)
[Ru(**84**)(bpy)(H_2O)]$^{2+}$ (**93**)	751 (sh), 589 (2.63), 509 (sh)
[Ru(**84**)(4-pic)$_2$(H_2O)]$^{2+}$ (**95**)	778 (sh), 622 (4.62), 517 (2.96)
[Ru(**102**)(4-pic)$_2$(H_2O)]$^{2+}$ (**105**)	603 (3.0), 367 (22.5)
[Ru(**102**)(bpy)Cl]$^{+}$ (**106**)	630 (3.4), 494 (sh), 415 (5.3), 367 (20.2)
[Ru(**103**)(bpy)Cl]$^{+}$ (**107**)	673 (5.5), 494 (sh), 440 (sh), 392 (38.1)

[a] Measured in acetone (5.0 x 10^{-5} M) at 298 K; sh = shoulder.

5.3.6.3. Electrochemical studies

The cyclic voltammograms of **86-87**, **90-95**, and **105-107** were recorded in dichloromethane to avoid solvolysis. Initial attempts to measure the CV of complexes **92-95** in CH_3CN showed that the CV changes with time, indicating solvolysis of the bound water which was being replaced by CH_3CN. The electrochemical properties of these complexes are summarized in Table 28. Figure 76a shows the oxidative wave for complex **86** and Figure 76b shows the reductive wave. The oxidation of a Ru(II) complex

involves the removal of one electron from the HOMO, which is a metal-centered d-orbital. The reduction of a Ru(II) complex is ligand-centered and involves the addition of one electron to the π* LUMO of the most electronegative ligand. The reduction waves attributed to the RuII/I redox couple and the oxidation waves attributed to the RuII/III redox couple.

There is one reversible oxidation wave observed for the complexes **86-87** and **90-95**. The oxidative wave for complexes **86-87** and **90-95** is observed at +0.76 to +1.24 V. Except [Ru(**84**)(4-pic)$_2$H$_2$O](PF$_6$)$_2$ (**95**), the azaacridine Ru complexes show higher oxidation potential in comparison with the naphthyridine Ru complexes. Electrochemical properties of **95** were taken from the literature.[44] The oxidation potential of Ru(bpy)Cl complexes **90** and **91** show the lowest oxidation potential. According to the oxidation potential, the easiest complex that could be oxidized is complex **91**. The azaacridine Ru complexes show lower oxidation potential in comparison with the naphthyridine Ru complexes. The first reductions for complexes **86-87** and **90-95** were observed at -0.67 to -1.11 V.

Among the [Ru(**85**)] complexes, [Ru(**85**)(tpy)]$^{2+}$ (**90**) and [Ru(**85**)(4-pic)$_2$(H$_2$O)]$^{2+}$ (**94**) have similar oxidation potentials. The –Cl analogue of [Ru(**85**)(bpy)] has a lower oxidation potential than the aquo analogue. It means that the –Cl analogue is oxidized easier than the aquo analogue. For the naphthyridine system, [Ru(**84**)(bpy)Cl]$^{+}$ (**91**) has a higher oxidation potential than the aquo analogue. It means that the aquo analogue is oxidized easier than the –Cl analogue so can thus more easily stabilize the oxidized species.

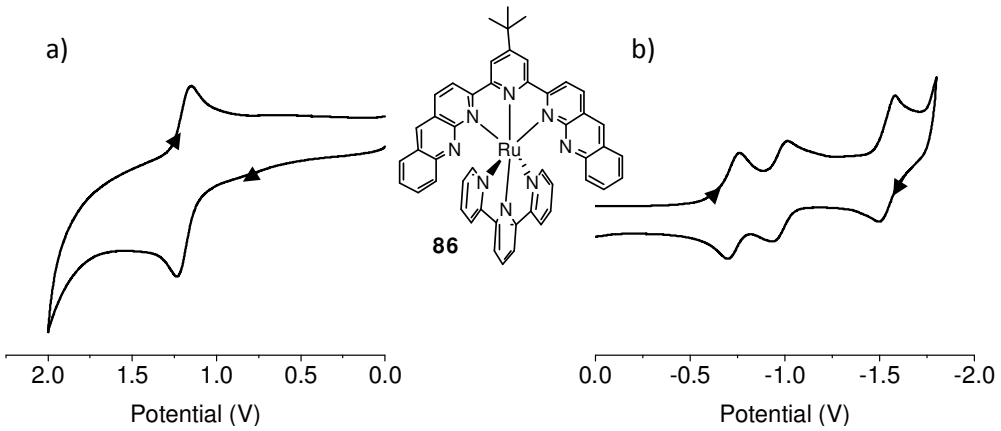

Figure 76. Cyclic voltammogram a) oxidation and b) reduction of **86** vs SCE in CH_3CN (0.1 M $TBAPF_6$, 100 mv/s, at rt).

Table 28. Redox data ($E_{1/2}$ and ΔE) for Ru(II) complexes **86-87**, **90-95**, and **105-107**.

Compound [a]	$E_{1/2}^{ox}(\Delta E)$	$E_{1/2}^{red}(\Delta E)$
$[Ru(\mathbf{85})(tpy)]^{2+}$ (**86**)	+ 1.19 (86)	-0.73 (62), -0.97 (85), -1.54 (87)
$[Ru(\mathbf{85})(bpy)Cl]^{+}$ (**90**)	+ 0.79 (113)	-0.92 (97), -1.20 (38), -1.72^{ir}
$[Ru(\mathbf{85})(bpy)(H_2O)]^{2+}$ (**92**)	+ 0.89 (102)	-1.13^{ir}, -1.45 (114)
$[Ru(\mathbf{85})(4\text{-pic})_2(H_2O)]^{2+}$ (**94**)	+ 1.18 (103)	-0.67 (65), -0.93 (151), -1.51 (236)
$[Ru(\mathbf{84})(tpy)]^{2+}$ (**87**)	+ 1.15 (115)	-0.99 (69), -1.31 (83), -1.95^{ir}
$[Ru(\mathbf{84})(bpy)Cl]^{+}$ (**91**)	+ 0.76 (97)	-1.11^{ir}, -1.37^{ir}, -1.78^{ir}
$[Ru(\mathbf{84})(bpy)(H_2O)]^{2+}$ (**93**)	+ 0.71 (95)	-1.12^{ir}, -1.40^{ir}
$[Ru(\mathbf{84})(4\text{-pic})_2(H_2O)]^{2+}$ (**95**)	+ 1.24 (89)	-0.87 (70), -1.26 (99)
$[Ru(\mathbf{102})(4\text{-pic})_2(H_2O)]^{2+}$ (**105**)	+ 1.10 (122)	-0.92 (106)
$[Ru(\mathbf{102})(bpy)Cl]^{+}$ (**106**)	+ 0.82 (192)	-0.91 (177)
$[Ru(\mathbf{103})(bpy)Cl]^{+}$ (**107**)	+ 0.81 (98)	-0.88 (103)

[a] Measured relative to SCE in CH_2Cl_2 containing Bu_4NPF_6 (0.1 M); $E_{1/2} = (E_{pa} + E_{pc})/2$ in V, $\Delta E = (E_{pa} - E_{pc})$ in mV; ir = irreversible.

5.3.6.4. Mass spectra

Complexes **86** and **87** showed a pattern corresponding to the loss of two PF_6 with $C_xH_yN_8Ru$ isotopic distribution. The positive ion MALDI-TOF mass spectrum (Figure

77, left) showed a pattern at *m/z* 726 $[M\text{-}2(PF_6)]^+$ similar to the simulated isotopic distribution for $C_{40}H_{32}N_8Ru$ (Figure 77, right) confirming the formation of the complex $[Ru(\mathbf{84})(tpy)]^{2+}$. Complexes **90**, **91**, and **106-107** showed a pattern corresponding to the loss of one PF_6 and one –Cl with $C_xH_yN_zRu$ isotopic distribution. The positive ion MALDI-TOF mass spectrum of the complex $[Ru(\mathbf{85})(bpy)(Cl)]^+$ showed a pattern at *m/z* 749 $[M\text{-}2(PF_6)\text{-}Cl]^+$ for $C_{43}H_{33}N_7Ru$. Complexes **92** and **93** showed a pattern corresponding to the loss of two PF_6 and one H_2O with $C_xH_yN_7Ru$ isotopic distribution. The positive ion MALDI-TOF mass spectrum of the complex $[Ru(\mathbf{84})(bpy)(H_2O)]^{2+}$ showed a pattern at *m/z* 649 $[M\text{-}2(PF_6)\text{-}(H_2O)]^+$ for $C_{35}H_{29}N_7Ru$. Complexes **94**, **95**, and **105** showed a pattern corresponding to the loss of two PF_6, two 4-picoline, and one H_2O with $C_xH_yN_zRu$ isotopic distribution.

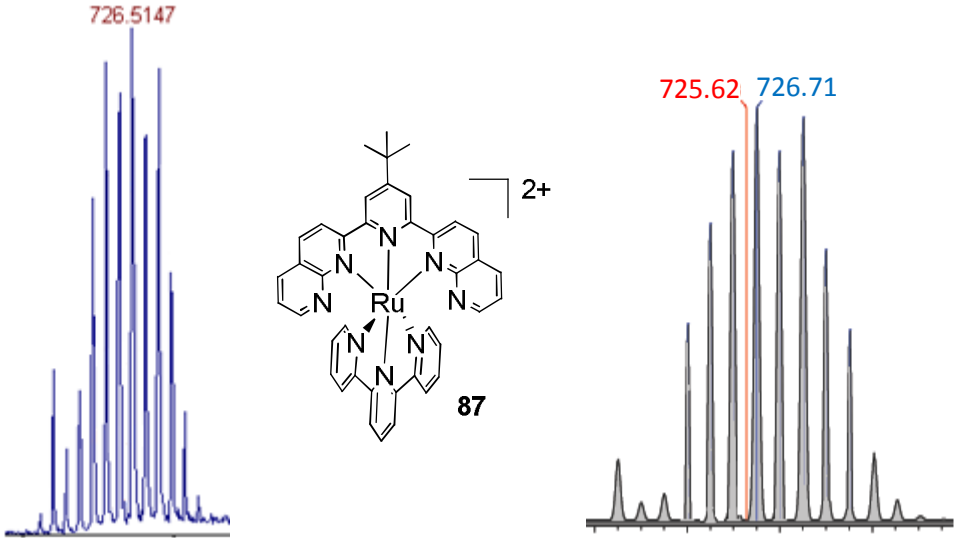

Figure 77. The MALDI-TOF mass spectrum of **87** (left) and the calculated mass distribution (right) for $C_{40}H_{32}N_8Ru$.

5.3.6.5. Water oxidation

The catalytic activity of **90-95** and **105-107** toward water oxidation was evaluated by adding a CH_3CN solution (50 μL) of the catalyst (0.2 mmol) to 3 mL of an aqueous Ce(IV)-CF_3SO_3H solution (pH = 1.0) at room temperature and measuring the amount of oxygen formed after 24 h. The generated O_2 was measured by GC. The turnover number (TN) of the complexes is given in Tables 29-30.

Catalysts **90-93** possess two different structural domains: the equatorial tridentate ligand and the axial monodentate ligand. The remaining coordination site is bpy. The equatorial ligand for **90** and **92** is 2,6-di(4'-azaacrid-3'-yl)-4-*t*-butylpyridine (**85**) and for **91** and **93** is 2,6-di(1',8'-naphthyrid-2'-yl)-4-*t*-butyl pyridine (**84**). The monodentate ligand is –Cl for **90-91** and H_2O for **92-93**. Catalysts **90-93** do not show catalytic activity (Table 29).

Catalysts **106-107** possess the same axial ligand with different equatorial tridentate ligands. The equatorial tridentate ligand for **106** is 2-(1',10'-Phenanthrolin-2'-yl)1,8-naphthyridine (**102**) and for **107** is 3-(1',10'-Phenanthrolin-2'-yl)4-azaacridine (**103**). The remaining coordination sites are bpy and –Cl. Catalysts **106-107** do not show catalytic activity (Table 30).

When 4-picoline was employed as the axial ligand for three different equatorial tridentate ligands **84**, **85**, and **102**; complexes **94**, **95**, and **105** show catalytic activity. TN for [Ru(**85**)(4-pic)$_2$(H_2O)](PF_6)$_2$ (**94**) is 391, TN for [Ru(**84**)(4-pic)$_2$(H_2O)](PF_6)$_2$ (**95**) is 260, and TN for [Ru(**102**)(4-pic)$_2$(H_2O)](PF_6)$_2$ (**105**) is 173.

Table 29. Water oxidation data for **86-87** and **90-95**.

Complex	TN[a]	Complex	TN[a]
[Ru(**85**)(tpy)]$^{2+}$ (**86**)	0	[Ru(**84**)(tpy)]$^{2+}$ (**87**)	0
[Ru(**85**)(bpy)Cl]$^{+}$ (**90**)	<20	[Ru(**84**)(bpy)Cl]$^{+}$ (**91**)	<20
[Ru(**85**)(bpy)(H_2O)]$^{2+}$ (**92**)	<20	[Ru(**84**)(bpy)(H_2O)]$^{2+}$ (**93**)	<20
[Ru(**85**)(4-pic)$_2$(H_2O)]$^{2+}$ (**94**)	391	[Ru(**84**)(4-pic)$_2$(H_2O)]$^{2+}$ (**95**)	260

[a] TN = turnover number (mol O_2 evolved per mol catalyst within 24 h).

Table 30. Water oxidation data for **105-107**.

Complex	TN[a]
[Ru(**102**)(bpy)Cl]$^{+}$ (**106**)	<20
[Ru(**103**)(bpy)(Cl)]$^{+}$ (**107**)	<20
[Ru(**102**)(4-pic)$_2$(H_2O)]$^{2+}$ (**105**)	173

[a] TN = turnover number (mol O_2 evolved per mol catalyst within 24 h).

5.4. Summary of Results

The results of this project are summarized as follows:

1. Ligands **84-85** and **102-103** were synthesized in 87%-90% and 65%-83% yields, respectively and characterized by ^{1}H and ^{13}C NMR.
2. The [Ru(**85**)] complexes **86**, **90** and **94** (35-50%), [Ru(**84**)] complexes **87**, **91** and **95** (36-50%), [Ru(**102**)] complexes (10%), and [Ru(**103**)(bpy)Cl]$^{+}$ (20%) were synthesized in aq ethanol and characterized by ^{1}H NMR, UV-vis spectroscopy, CV, mass spectrometry, and elemental analysis.
3. Complexes [Ru(**85**)(bpy)Cl]$^{+}$ (**90**) and [Ru(**84**)(bpy)Cl]$^{+}$ (**91**) were treated with $AgBF_4$ in acetone to convert –Cl to H_2O. [Ru(**85**)(bpy)(H_2O)]$^{2+}$ (**92**) and [Ru(**84**)(bpy)(H_2O)]$^{2+}$ (**93**) were synthesized in 70% and 90% yields, respectively.

4. With regard to the UV-vis the bi-4-azaacridine complexes **86**, **90**, **92**, and **94** are ~90 nm more red shifted than the binap analogs **87**, **91**, **93**, and **95** because of the extended π-conjugation.
5. The shape of the absotption bands remains almost invarient for both bi-4-azaacridine and bi-naphthyridine systems.
6. The complexes **86-87** and **90-95** were excited at the maximum of their MLCT absorption band. These complexes do not showed any appreciable emission at room temperature.
7. The H_2O group in the Ru(II) complexes **90-95** can be replaced by acetonitrile.
8. Complexes **86** and **87** showed a pattern corresponding to the loss of two PF_6, complexes **90**, **91**, and **106-107** showed a pattern corresponding to the loss of one PF_6 and one –Cl, complexes **92** and **93** showed a pattern corresponding to the loss of two PF_6 and one H_2O, and complexes **94**, **95**, and **105** showed a pattern corresponding to the loss of two PF_6, two 4-picoline, and one H_2O with $C_xH_yN_zRu$ isotopic distribution.
9. [Ru(**85**)(4-pic)$_2$(H_2O)](PF_6)$_2$ (**94**), [Ru(**84**)(4-pic)$_2$(H_2O)](PF_6)$_2$ (**95**), and [Ru(**102**)(4-pic)$_2$(H_2O)](PF_6)$_2$ (**105**) have catalytic activity with the TN 391, 260, and 173, respectively.

5.5. Perspective and Future Work

Future studies will look at the effect of structural changes in both the axial and equatorial ligands as well as the mechanistic aspects of the oxidation. Also studies will be done on the detailed characterization of water oxidation intermediates with the Ru(II)

polypyridyl complexes [Ru(**84-85, 102**)(4-pic)$_2$(H_2O)](PF_6)$_2$ in aqueous and non-aqueous solutions and comparing the physiochemical properties.

6. EXPERIMENTAL SECTION

The ^{1}H NMR spectra were recorded at room temperature on General Electric QE-300, JEOL ECX-400, and ECX-500 spectrometers operating at 300, 400, and 500 MHz for ^{1}H NMR, 75, 100, and 125 MHz for ^{13}C NMR, respectively. Chemical shifts are reported in parts per million (ppm) referenced to the residual solvent peak. The *J* values are ± 0.5 Hz. Electronic absorption spectra were recorded with a VARIAN Cary-50 UV-visible spectrophotometer and were corrected for the background spectrum of the solvent. Emission spectra were obtained on a Perkin Elmer LS-50B luminescence spectrometer equipped with a Hamamatsu R928HA photomultiplier tube. Electrochemical measurements were carried out using a BAS Epsilon electroanalytical system. Cyclic voltammetry experiments were performed at room temperature in a one-compartment cell equipped with a glassy carbon working electrode, a saturated calomel reference electrode (SCE), and a Pt wire as the auxiliary electrode in dichloromethane (CH_2Cl_2) containing tetrabutylammonium hexafluorophosphate (0.1 M) at a scan rate of 100 mV S^{-1}. Mass spectra were obtained on a Voyager-DE-STR MALDI-TOF mass spectrometer using α-cyano-4-hydroxycinnamic acid as the matrix. Melting points were determined with a Thomas Hoover capillary melting-point apparatus and were uncorrected. Infrared spectra were recorded on a Thermo Nicolet AVATAR 370 FT-IR spectrometer. The microwave reactions were carried out in a household microwave oven modified according to a published description.[213] The turnover number (TON) was determined using an Ocean Optics (FOXY-OR125-G) oxygen sensor and the 24 h endpoint reading verified by a GC measurement according to a procedure that has been previously described.[203]

Elemental analyses were performed by QTI, P.O. Box 470, Whitehouse, NJ 08888. All reagents and solvents were purchased from commercial sources and were used as received except the $[Ru(tpy)Cl_3]$ (**77**),[193] $[Ru(tpy)(CH_3CN)Cl_2]$ (**78**),[194] $[Ru(bpy)_2Cl_2]\cdot 2H_2O$ (**80**),[196] $[Ru(DMSO)_4Cl_2]$ (**88**),[210] $[Ru(bpy)(DMSO)_2Cl_2]$ (**89**),[211] 2-aminonicotinaldehyde (**83**),[214] $[Ru(\mathbf{84})(4\text{-pic})_2(H_2O)]^{2+}$ (**95**),[44] and $[Ru(DMSO)_2(4\text{-pic})_2Cl_2]$ (**104**)[212] that were prepared according to published procedures.

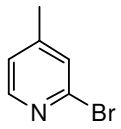

53

2-Bromo-4-methyl pyridine (53, RSH-28):[215]

To an ice-cooled solution of 2-amino-4-methyl pyridine (**52**, 15 g, 0.14 mol) in HBr (48%, 60 mL), bromine (24 mL, 3 mol) and a solution of $NaNO_2$ (27.5 g, 0.4 mol) in H_2O (40 mL) were added dropwise and the mixture was stirred for 30 min at 0 ^oC. The mixture was neutralized with NaOH (0.1 M) and extracted with Et_2O. The organic phase was separated, dried over $MgSO_4$ and evaporated under vacuum. The crude product was distilled under reduced pressure to afford **53** as a colorless oil (18 g, 74%): bp 88 ^oC/10 mmHg; ^1H NMR ($CDCl_3$, 500 MHz) δ 8.21 (d, J = 4.5 Hz, 1H), 7.33 (s, 1H), 7.07 (d, J = 4.4 Hz, 1H), 2.34 (s, 3H); ^{13}C NMR ($CDCl_3$, 125 MHz) δ 150.1, 149.5, 142.0, 128.4, 123.8, 20.6.

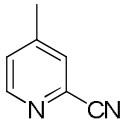

26b **2-Cyano-4-methyl pyridine (26b, RSH-58)**:[216]

A solution of **53** (1.6 g, 8 mmol) and anhyd CuCN (0.72 g, 8 mmol) in DMSO (15 mL) was irradiated in a microwave oven for 4 min. After cooling, the reaction mixture was dissolved in water (30 mL) and extracted with EtOAc (2 × 30 mL). The organic phase was separated, dried over $MgSO_4$ and evaporated under vacuum. The residue was purified by chromatography on alumina eluting with CH_2Cl_2 to provide **26b** as a white solid (0.3 g, 33%): mp 82-84 ^oC; ^1H NMR ($CDCl_3$, 500 MHz) δ 8.57 (d, J = 4.4 Hz, 1H), 7.52 (s, 1H), 7.34 (d, J = 4.3 Hz, 1H), 2.44 (s, 3H); ^{13}C NMR ($CDCl_3$, 125 MHz) δ 150.9, 148.8, 133.9, 129.5, 127.9, 117.5, 21.0; IR (ATR) ν 2238 cm^{-1}.

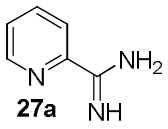

27a **Pyridine-2-carboxamidine (27a, RSH-52)**:[217]

To a solution of Na (1.5 g, 60 mmol) in MeOH (40 mL), 2-cyanopyridine (**26a**, 5 g, 48 mmol) was added and the mixture was stirred for 10 h at rt. NH_4Cl (3.5 g, 60 mmol) was then added to the solution and the mixture was stirred for an additional 6 h. The unreacted NH_4Cl was filtered and the filtrate was evaporated. The solid residue was triturated with Et_2O to remove unreacted cyanopyridine, filtered, and crystallized from EtOH to afford **27a** as a white precipitate (3.5 g, 60%): mp 133-135 ^oC; ^1H NMR (D_2O, 500 MHz) δ 8.72 (d, J = 4.2 Hz, 1H), 8.06 (dd, J = 2.1, 0.9 Hz, 1H), 8.02 (d, J = 7.5 Hz,

1H), 7.73 (ddd, *J* = 6.9, 5.1, 1.5 Hz, 1H); ^{13}C NMR ($CDCl_3$, 125 MHz) δ 163.0, 150.1, 143.8, 138.8, 128.8, 123.4; IR (ATR) *v* 3252, 3070 cm^{-1}.

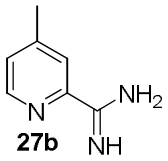

27b **4-Methyl-pyridine-2-carboxamidine (27b, RSH-64)**:

Compound **27b** was synthesized by following the same procedure as for **27a**, using Na (1.5 g, 60 mmol), 2-cyano-4-methyl pyridine (**26b,** 5 g, 42 mmol), MeOH (40 mL) and NH_4Cl (3.5 g, 60 mmol) to give **27b** as a white solid (3.4 g, 60%): mp 213-215 ^oC; ^1H NMR (D_2O, 500 MHz) δ 8.47 (d, *J* = 5.1 Hz, 1H), 7.87 (s, 1H), 7.31 (d, *J* = 4.5 Hz, 1H), 2.55 (s, 3H); ^{13}C NMR ($CDCl_3$, 125 MHz) δ 162.8, 151.1, 144.3, 140.5, 128.8, 124.1, 21.5; IR (ATR) *v* 3462, 3117 cm^{-1}.

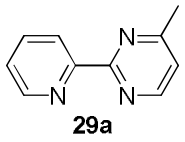

29a **4-Methyl-2-(pyrid-2'-yl)pyrimidine (29a, RSH-47)**:[217]

To a solution of Na (500 mg, 22 mmol) in EtOH (60 mL), pyridine-2-carboxamidine hydrochloride (**27a**, 1 g, 6.34 mmol) was added followed by acetylacetaldehyde dimethylacetal (**28**, 0.84 mL, 6.34 mmol) and the reaction mixture was refluxed for 4 h and then stirred overnight at rt. The solution was acidified with acetic acid (pH~6) and concentrated under vacuum. The yellow residue was purified by chromatography on alumina eluting with CH_2Cl_2/EtOAc (1:1) to give **29a** as a light yellow solid (0.5 g, 50%): mp 58-60 ^oC; ^1H NMR ($CDCl_3$, 400 MHz) δ 8.88 (d, *J* = 4.2 Hz, 1H), 8.75 (d, *J* =

5.1 Hz, 1H), 8.53 (dd, *J* = 5.0, 1.0 Hz, 1H), 7.90 (dd, *J* = 5.0, 1.0 Hz, 1H), 7.42 (m, 1H), 7.24 (d, *J* = 5.1 Hz, 1H), 2.65 (s, 3H); ^{13}C NMR ($CDCl_3$, 100 MHz) δ 268.1, 163.4, 157.3, 155.0, 150.2, 137.0, 124.9, 123.7, 120.1, 24.7.

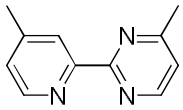

29b **4-Methyl-2-(4'-methyl-pyrid-2'-yl)pyrimidine (29b, RSH-121)**:

Compound **29b** was synthesized by following the same procedure as for **29a**, using Na (0.17 g, 7.5 mmol), 4-methyl-pyridine-2-carboxamidine hydrochloride (**27b**, 0.43 g, 2.5 mmol) and acetylacetaldehyde dimethylacetal (**28**, 0.33 mL, 2.5 mmol) to give **29b** as a light yellow solid (0.37 g, 80%): mp 74-77 ^{o}C; ^{1}H NMR ($CDCl_3$, 500 MHz) δ 8.75 (d, *J* = 5.1 Hz, 1H), 8.72 (d, *J* = 4.6 Hz, 1H), 8.35 (s, 1H), 7.24 (d, *J* = 4.6, 1H), 7.18 (d, *J* = 5.1 Hz, 1H), 2.67 (s, 3H), 2.47 (s, 3H); ^{13}C NMR ($CDCl_3$, 125 MHz) δ 167.9, 163.5, 157.1, 154.7, 149.9, 148.2, 125.3, 124.4, 119.4.

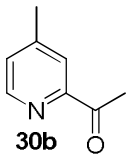

30b **2-Acetyl-4-methyl-pyridine (30b, RSH-1)**:

To the mixture of 4-methyl-pyridine (**54a**, 5 g, 0.05 mol), pyruvic acid (**46**, 14 g, 0.16 mol), $AgNO_3$ (0.73 g, 4.3 mmol), H_2SO_4 (2 mL) in H_2O (50 mL) and CH_2Cl_2 (20 mL), $NH_4S_2O_8$ (17 g, 0.08 mol) was added portion-wise. The mixture was stirred for 2 h at 40 ^{o}C. The aqueous phase was separated and made basic with sat NaOH solution. The basic aqueous solution was extracted with CH_2Cl_2 (3 x 25 mL). The organic layers were

combined, dried over $MgSO_4$ and evaporated under vacuum. The oily residue was purified by chromatography on alumina eluting with EtOAC/hexane (1:100) to afford **30b** as a yellow oil (3 g, 45%): ^{1}H NMR ($CDCl_3$, 500 MHz) δ 8.53 (d, *J* = 5.04 Hz, 1H), 7.86 (s, 1H), 7.28 (d, *J* = 5.50 Hz, 1H), 2.71 (s, 3H), 2.40 (s, 3H); ^{13}C NMR ($CDCl_3$, 125 MHz) δ 200.4, 153.4, 148.8, 148.2, 128.0, 122.5, 25.9, 21.0.

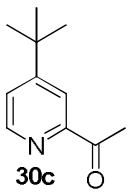

30c **2-Acetyl-4-*t*-butyl-pyridine (30c, RSH-500)**:

Compound **30c** was synthesized by following the same procedure as for **30b**, using 4-*t*-butyl-pyridine (**54b**, 5 g, 0.04 mol), pyruvic acid (**46**, 8 g, 0.07 mol), $AgNO_3$ (0.5 g, 3 mmol), $NH_4S_2O_8$ (12 g, 0.06 mol), H_2SO_4 (2 mL), H_2O (50 mL) and CH_2Cl_2 (20 mL) to give **30c** as a colorless oil (2.0 g, 30%): ^{1}H NMR ($CDCl_3$, 500 MHz) δ 8.54 (d, *J* = 5.04 Hz, 1H), 8.03 (dd, *J* = 1.37 Hz, 1H), 7.42 (dd, *J* = 5.50, 1.83 Hz, 1H), 2.68 (s, 3H), 1.30 (s, 3H); ^{13}C NMR ($CDCl_3$, 125 MHz) δ 200.4, 161.1, 153.5, 149.0, 124.1, 118.6, 34.9, 30.4, 25.9.

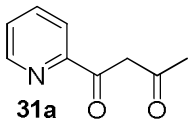

31a **1-(Pyrid-2′-yl)-1,3-butanedione (31a, RSH-127)**:[218]

To an ice cooled mixture of NaH (0.25 g, 6 mmol) in EtOAc (15 mL), 2-acetylpyridine (**30a**, 0.36 g, 3 mmol) in EtOAc (10 mL) was added dropwise. The mixture was stirred for 30 min at rt and then refluxed for 3 h. The mixture was cooled to rt and neutralized

with H_2O (25 mL). The organic layer was separated, dried over $MgSO_4$ and evaporated under vacuum. The oily residue was purified by chromatography on alumina eluting with CH_2Cl_2 to afford **31a** as a brown oil (0.27 g, 55%): ^{1}H NMR ($CDCl_3$, 500 MHz) δ 8.63 (d, *J* = 4.01 Hz, 1H), 8.04 (d, *J* = 8.02Hz, 1H), 7.80 (dt, *J* = 7.45, 1.72 Hz, 1H), 7.38 (dd, *J* = 5.73, 1.15 Hz, 1H), 6.79 (s, 1H, C-H enol), 2.21 (s, 3H); ^{13}C NMR ($CDCl_3$, 125 MHz) δ 195.2, 180.9, 152.2, 149.3, 137.1, 126.3, 122.2, 97.3, 26.2.

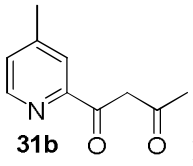

31b **1-(4'-Methyl-pyrid-2'-yl)-1,3-butanedione (31b, RSH-158)**:

Compound **31b** was synthesized by following the same procedure as for **31a**, using NaH (0.25 g, 6 mmol) in EtOAc (15 mL), 2-acetyl-4-methyl-pyridine (**30b**, 0.40 g, 3 mmol) in EtOAc (10 mL) to give **31b** as a brown oil (0.27 g, 50%): ^{1}H NMR ($CDCl_3$, 500 MHz) δ 8.47 (d, *J* = 5.24 Hz, 1H), 7.86 (s, 1H), 7.19 (d, *J* = 5.50 Hz, 1H), 6.76 (s, 1H, C-H enol), 2.38 (s, 3H), 2.19 (s, 3H); ^{13}C NMR ($CDCl_3$, 125 MHz) δ 195.1, 180.9, 153.1, 149.2, 146.8, 129.4, 127.3, 97.6, 26.4, 23.2.

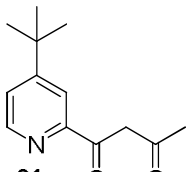

31c **1-(4'-*t*-Butyl-pyrid-2'-yl)-1,3-butanedione (31c, RSH-552)**:

Compound **31c** was synthesized by following the same procedure as for **31a**, using NaH (0.25 g, 6 mmol) in EtOAc (15 mL), 2-acetyl-4-*t*-butyl-pyridine (**30c**, 0.53 g, 3 mmol) in EtOAc (10 mL) to give **31c** as a brown oil (0.40 g, 60%): ^{1}H NMR ($CDCl_3$, 500 MHz) δ

8.52 (d, *J* = 4.58 Hz, 1H), 8.06 (d, *J* = 1.72 Hz, 1H), 7.36 (dd, *J* = 5.15, 1.72 Hz, 1H), 6.79 (s, 1H, C-H enol), 2.19 (s, 3H), 1.31 (s, 9H); ^{13}C NMR ($CDCl_3$, 125 MHz) δ. 195.4, 180.8, 161.1, 153.4, 146.8, 123.2, 119.1, 98.1, 35.1, 31.5, 23.6.

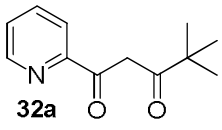

32a **1-(Pyrid-2'-yl)-4,4-dimethyl-1,3-pentanedione (32a, RSH-498)**:

Compound **32a** was synthesized by following the same procedure as for **31a**, using NaH (0.25 g, 6 mmol) in ethyl pivalate (15 mL), 2-acetyl-pyridine (**30a**, 0.36 g, 3 mmol) in ethyl pivalate (10 mL) to give **32a** as a brown oil (0.31 g, 50%): ^{1}H NMR ($CDCl_3$, 500 MHz) δ 8.62 (dd, *J* = 4.58, 1.15 Hz, 1H), 8.03 (d, *J* = 8.02 Hz, 1H), 7.77 (dt, *J* = 7.45, 1.72 Hz, 1H), 7.35 (dd, *J* = 5.73, 1.15 Hz, 1H), 6.95 (s, 1H, C-H enol), 1.23 (s, 9H); ^{13}C NMR ($CDCl_3$, 125 MHz) δ 204.1, 198.6, 152.4, 148.9, 137.1, 126.4, 122.6, 93.1, 30.6, 27.5.

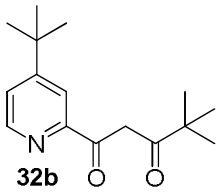

32b **1-(4'-*t*-Butyl-pyrid-2'-yl)-4,4-dimethyl-1,3-pentanedione (32b, RSH-532)**:

Compound **32b** was synthesized by following the same procedure as for **31a**, using NaH (0.25 g, 6 mmol) in ethyl pivalate (15 mL), 2-acetyl-4-*t*-butyl-pyridine (**30c**, 0.5 g, 3 mmol) in ethyl pivalate (10 mL) to give **32b** as a brown oil (0.66 g, 85%): ^{1}H NMR ($CDCl_3$, 500 MHz) δ 8.56 (d, *J* = 5.15 Hz, 1H), 8.09 (d, *J* = 1.72 Hz, 1H), 7.39 (dd, *J* =

5.15, 2.29 Hz, 1H), 6.97 (s, 1H, C-H enol), 1.34 (s, 9H), 1.26 (s, 9H); ^{13}C NMR ($CDCl_3$, 125 MHz) δ 204.1, 201.6, 183.0, 161.4, 149.3, 123.2, 119.2, 92.9, 30.7, 30.6, 27.5, 27.4.

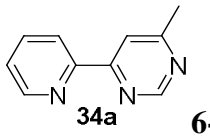

6-Methyl-4-(pyrid-2'-yl)-pyrimidine (34a, RSH-129):[218]

A mixture of 1-(pyrid-2'-yl)-1,3-butanedione (**31a,** 0.5 g, 3 mmol) and formamide (**33**, 10 mL) was gently refluxed for 5 h. After cooling, the residue was extracted with CH_2Cl_2 and washed with water and brine. The combined extracts were dried with anhyd $MgSO_4$, and the solvent was evaporated. The crude product was purified by chromatography on alumina eluting with hexane/EtOAc (2:1) to provide **34a** as a light yellow solid (0.20 g, 40%): mp 39-42 ^{o}C; ^{1}H NMR ($CDCl_3$, 500 MHz) δ 9.12 (d, *J* =0.9 Hz, 1H), 8.68 (d, *J* = 3.6 Hz, 1H), 8.45 (d, *J* = 7.8 Hz, 1H), 8.21 (s, 1H), 7.84 (td, *J* =7.8, 1.8 Hz, 1H), 7.38 (ddd, *J* = 7.8, 4.8, 1.2 Hz, 1H), 2.62 (s, 3H); ^{13}C NMR ($CDCl_3$, 125 MHz) δ 168.4, 162.5, 158.5, 154.1, 149.6, 137.3, 125.4, 121.9, 116.9, 24.5.

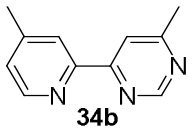

6-Methyl-4-(4'-methyl-pyrid-2'-yl)-pyrimidine (34b, RSH-137):

Compound **34b** was synthesized by following the same procedure as for **34a**, using 1-(4'-methyl-pyrid-2'-yl)-1,3-butanedione (**31b**, 0.53 g, 3 mmol) and formamide (**33**, 10 mL) to give **34b** as a yellow solid (0.25 g, 45%): mp 72-75 ^{o}C;^{1}H NMR ($CDCl_3$, 400 MHz) δ 9.14 (d, *J* =0.92 Hz, 1H), 8.54 (d, *J* = 5.04 Hz, 1H), 8.29 (s, 1H), 8.22 (s, 1H), 7.22 (d, *J*

=5.50 Hz, 1H), 2.61 (s, 3H), 2.45 (s, 3H); ^{13}C NMR ($CDCl_3$, 100 MHz) δ 168.3, 162.6, 158.4, 153.9, 149.4, 148.7, 126.4, 122.8, 117.1, 24.5, 21.3.

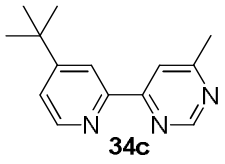

34c

6-Methyl-4-(4'-*t*-butyl-pyrid-2'-yl)-pyrimidine (34c, RSH-508):

Compound **34c** was synthesized by following the same procedure as for **34a**, using 1-(4'-*t*-butyl-pyrid-2'-yl)-1,3-butanedione (**31**, 0.66 g, 3 mmol) and formamide (**33**, 10 mL) to give **34c** as a yellow solid (0.31 g, 45%): mp 80-82 ^{o}C; ^{1}H NMR ($CDCl_3$, 500 MHz) δ 9.13 (d, J = 1.15 Hz, 1H), 8.58 (d, J = 5.15 Hz, 1H), 8.35 (d, J = 1.72 Hz, 1H), 8.21 (s, 1H), 7.30 (dd, J = 5.15, 1.72 Hz, 1H), 2.60 (s, 3H), 1.36 (s, 9H); ^{13}C NMR ($CDCl_3$, 125 MHz) δ 168.1, 162.8, 161.5, 158.3, 153.8, 149.5, 122.5, 118.9, 117.1, 35.1, 31.8, 24.4.

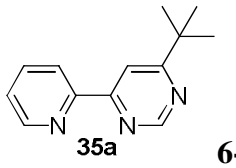

35a

6-*t*-Butyl-4-(pyrid-2'-yl)-pyrimidine (35a, RSH-499):

Compound **35a** was synthesized by following the same procedure as for **34a**, using 1-(pyrid-2'-yl)-4,4-dimethyl-1,3-pentanedione (**32a**, 0.62 g, 3 mmol) and formamide (**33**, 10 mL) to give **35a** as a yellow solid (0.26 g, 40%): mp 91-92 ^{o}C; ^{1}H NMR ($CDCl_3$, 400 MHz) δ 9.23 (d, *J* = 1.72 Hz, 1H), 8.73 (dt, *J* = 4.58, 2.29 Hz, 1H), 8.47 (d, *J* = 8.02 Hz, 1H), 8.40 (d, *J* = 1.15 Hz, 1H), 7.85 (td, *J* =7.45, 1.72 Hz, 1H), 7.40 (ddd, *J* = 7.45, 4.58, 1.15 Hz, 1H), 1.43 (s, 9H); ^{13}C NMR ($CDCl_3$, 100 MHz) δ 179.1, 162.8, 158.1, 154.5, 149.6, 137.2, 125.3, 121.9, 112.8, 37.9, 29.8.

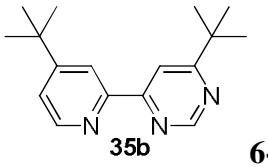

35b

6-*t*-Butyl-4-(4'-*t*-butyl-pyrid-2'-yl)-pyrimidine (35b, RSH-533):

Compound **35b** was synthesized by following the same procedure as for **34a**, using 1-(4'-*t*-butyl-pyrid-2'-yl)-4,4-dimethyl-1,3-pentanedione (**32b**, 0.78 g, 3 mmol) and formamide (**33**, 10 mL) to give **35b** as a yellow solid (0.30 g, 35%): mp 119-121 ^{o}C; ^{1}H NMR ($CDCl_3$, 500 MHz) δ 9.23 (s, 1H), 8.65 (d, *J* = 5.15 Hz, 1H), 8.37 (d, *J* = 1.72 Hz, 1H), 8.39 (s, 1H), 7.31 (d, *J* = 5.15, 1.72 Hz, 1H), 1.42 (s, 9H), 1.39 (s, 9H); ^{13}C NMR ($CDCl_3$, 125 MHz) δ 179.0, 163.2, 161.6, 158.1, 154.4, 149.5, 122.4, 119.0, 113.1, 37.9, 35.2, 30.7, 29.6.

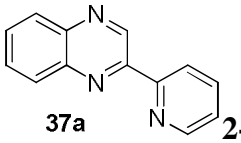

37a

2-(Pyrid-2'-yl)quinoxaline (37a, RSH-40):[219]

A mixture of benzene-1,2-diamine (**36a**, 0.43 g, 4 mmol), 2-acetylpyridine (**30a**, 0.53 g, 4.4 mmol) and *p*-TsOH (35 mg, 0.2 mmol) in MeOH (20 mL) was stirred at 50-60 ^{o}C for 10 h. The mixture was cooled to rt. The solvent was evaporated under vacuum and the crude product was purified by chromatography on silica eluting with CH_2Cl_2/EtOAc (1:1) to provide **37a** as a light yellow solid (0.58 g, 70%): mp 100-102 ^{o}C; ^{1}H NMR ($CDCl_3$, 500 MHz) δ 9.86 (s, 1H), 8.80 (d, *J* = 4.5 Hz, 1H), 8.61 (d, *J* = 8.4 Hz, 1H), 8.19-8.15 (m, 2H), 7.79 (dt, *J* = 7.8, 1.8 Hz, 1H), 7.82-7.78 (m, 2H), 7.42 (ddd, *J* = 7.2, 5.1, 1.2 Hz, 1H); ^{13}C NMR ($CDCl_3$, 125 MHz) δ 149.6, 144.2, 137.3, 130.3, 130.2, 129.8, 129.4, 124.7, 122.2, 120.4, 116.8.

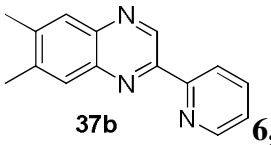

37b **6,7-Dimethyl-2-(pyrid-2'-yl)quinoxaline (37b, RSH-41)**:

Compound **37b** was synthesized by following the same procedure as for **37a**, using 4,5-dimethyl benzene-1,2-diamine (**36b**, 0.54 g, 4 mmol), 2-acetylpyridine (**30a**, 0.53 g, 4.4 mmol), *p*-TsOH (35 mg, 0.2 mmol) in MeOH (20 mL) to give **37b** as a light yellow solid (0.75 g, 80%): mp 144-146 ^{o}C; ^{1}H NMR ($CDCl_3$, 500 MHz) δ 9.86 (s, 1H), 8.78 (d, *J* = 4.0 Hz, 1H), 8.59 (d, *J* = 7.0 Hz, 1H), 7.95-7.87 (m, 3H), 7.41 (ddd, *J* = 6.3, 5.1, 1.2 Hz, 1H), 2.53 (s, 6H); ^{13}C NMR ($CDCl_3$, 125 MHz) δ 155.0, 149.5, 143.3, 141.6, 140.9, 140.8, 137.2, 128.8, 128.4, 124.4, 121.9, 20.5.

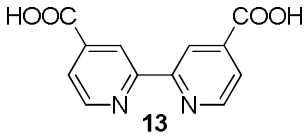

13 **2,2'-Bipyridine-4,4'-dicarboxylic acid (13, RSH-172)**:[220]

To a stirring solution of 4,4'-dimethyl-2,2'-bipyridine (**55**, 1.5 g, 8 mmol) in conc H_2SO_4 (45 mL), $K_2Cr_2O_7$ (9 g, 30 mmol) was added in small portions. After all of the dichromate had been added, the reaction mixture was stirred until the color of the mixture changed from dark red to green. The green mixture was poured into 2 L of ice-water. The precipitate was filtered and washed with water. The solid was refluxed in 50% HNO_3 (60 mL) for 5 h. The solution was poured into ice-water. After cooling to rt, the precipitate was filtered, washed with water and ether and dried under vacuum to give **13** as a white solid (1.8 g, 90%): mp > 260 ^{o}C; ^{1}H-NMR (DMSO-*d*6, 400 MHz) δ 8.88 (d, *J* = 4.4 Hz, 1H), 8.80 (s, 1H), 7.87 (d, *J* = 4.4 Hz, 1H).

[Ru(29a)(13)(NCS)$_2$] (39a, RSH-562):[74]

In a three necked round bottomed flask completely covered with Al foil, dichloro(*p*-cymene)ruthenium(II) (**56**, 122 mg, 0.2 mmol) was dissolved in DMF (30 mL). The flask was purged with Ar for 15 min. To this solution 4-methyl-2-(pyrid-2'-yl)pyrimidine (**29a**, 68 mg, 0.4 mmol) was added with stirring. The reaction mixture was heated at 80 ^{o}C for 2 h. After this time 2,2'-bipyridine-4,4'-dicarboxylic acid (**13**, 98 mg, 0.4 mmol) was added, and the reaction mixture was heated at 160 ^{o}C for 4 h under Ar and in the absence of light to avoid cis to trans isomerization. Then ammonium thiocyanate (0.99 g, 13 mmol) was added, and the reaction mixture was maintained at 130 ^{o}C for 5 h. After the reaction mixture was cooled to rt and the solvent was evaporated under vacuum. Then 5 mL of water was added to remove the ammonium thiocyanate excess. A brown precipitate appeared, and it was collected by filtration with a sintered glass funnel. The product was washed three times with water and Et_2O. The crude product was purified by size exclusion chromatography. The product was dissolved in a mixture of 2.5 mL of MeOH and 0.5 mL of tetrabutylammonium hydroxide (40% by weight) to form the tetrabutylammonium salt of the ruthenium complex. This solution was purified on an LH-20 Sephadex column (2.5 × 30 cm) using MeOH as the eluent. The main dark purple band was collected, and the solvent was evaporated under vacuum. A few drops of 0.01 M HNO_3 was added to the resulting semisolid product until a purple precipitate appeared. It was collected with a sintered glass funnel and dried under vacuum to give **39a** as a red solid. Since compound **39a** has 4 different isomers, it could not be characterized by ^{1}H NMR.

[Ru(29b)(13)(NCS)$_2$] (20b, RSH-561):

Compound **39b** was synthesized by following the same procedure as for **39a**, using dichloro(*p*-cymene)ruthenium(II) (**56**, 122 mg, 0.2 mmol), DMF (30 mL), 4-methyl-2-(4'-methyl-pyrid-2'-yl)pyrimidine (**29b**, 74 mg, 0.4 mmol), 2,2'-bipyridine-4,4'-dicarboxylic acid (**13**, 98 mg, 0.4 mmol) and ammonium thiocyanate (0.99 g, 13 mmol) to give **39b** as a red solid. Since compound **39b** has 4 different isomers, it could not be characterized by ^{1}H NMR.

[Ru(34a)(13)(NCS)$_2$] (39c, RSH-165):

Compound **39c** was synthesized by following the same procedure as for **39a**, using dichloro(*p*-cymene)ruthenium(II) (**56**, 122 mg, 0.2 mmol), DMF (30 mL), 6-methyl-4-(pyrid-2'-yl)-pyrimidine (**34a**, 68 mg, 0.4 mmol), 2,2'-bipyridine-4,4'-dicarboxylic acid (**13**, 98 mg, 0.4 mmol) and ammonium thiocyanate (0.99 g, 13 mmol) to give **39c** as a dark red solid (58 mg, 45%): ^{1}H NMR (DMSO-*d6*, 500 MHz) δ 9.59 (s, 1H), 9.38 (d, J = 5.73 Hz, 1H), 9.36 (d, J = 5.73 Hz, 1H), 9.27 (d, *J* = 5.15 Hz, 1H), 9.11-9.07 (m, 2H), 8.95-8.92 (m, 2H), 8.85 (d, *J* = 8.02 Hz, 1H), 8.77 (s, 1H), 8.71 (d, *J* = 8.02 Hz, 1H), 8.60 (s, 1H), 8.32 (dt, *J* = 8.02, 1.15 Hz, 1H), 8.27 (dd, J = 5.73, 1.15 Hz, 1H), 8.24 (dd, J = 6.30, 1.72 Hz, 1H), 8.05 (dt, *J* = 6.87, 1.15 Hz, 1H), 8.02-8.01 (m, 2H), 7.95 (dt, *J* = 8.02, 1.15 Hz, 1H), 7.74 (d, *J* = 5.73 Hz, 1H), 7.58-7.53 (m, 3H), 7.29 (dt, *J* = 7.45, 1.15 Hz, 1H), 2.83 (s, 3H), 2.63 (s, 3H); IR (ATR) *v* 3320, 2103, 1723 cm^{-1}; MS (MALDI-TOF): m/z 575 [M-(NCS)]$^+$, 559 [M-(NCS)-(CH_3)]$^+$, 517 [M-2(NCS)]$^+$.

[Ru(34b)(13)(NCS)$_2$] (39d, RSH-471):

Compound **39d** was synthesized by following the same procedure as for **39a**, using dichloro(*p*-cymene)ruthenium(II) (**56**, 122 mg, 0.2 mmol), DMF (30 mL), 6-methyl-4-(4'-methyl-pyrid-2'-yl)-pyrimidine (**34b**, 74 mg, 0.4 mmol), 2,2'-bipyridine-4,4'-dicarboxylic acid (**13**, 98 mg, 0.4 mmol) and ammonium thiocyanate (0.99 g, 13 mmol) to give **39d** as a dark red solid (66 mg, 50%): ^{1}H NMR (CD_3OD, 500 MHz) δ 9.77 (s, 1H), 9.60 (d, *J* = 5.73 Hz, 1H), 9.58 (d, *J* = 5.73 Hz, 1H), 9.27 (d, *J* = 5.73 Hz, 1H), 9.02-9.01 (m, 2H), 8.88-8.87 (m, 2H), 8.58 (s, 1H), 8.49 (s, 1H), 8.44 (s, 1H), 8.34 (s, 1H), 8.25-8.24 (m, 2H), 8.03 (s, 1H), 7.98 (d, *J* = 6.30 Hz, 1H), 7.81 (d, *J* = 5.73 Hz, 1H), 7.79 (d, *J* = 5.15 Hz, 1H), 7.64-7.61 (m, 2H), 7.41 (d, *J* = 5.73 Hz, 1H), 7.10 (d, *J* = 4.58 Hz, 1H), 2.87 (s, 3H), 2.71 (s, 3H), 2.58 (s, 3H), 2.44 (s, 3H); IR (ATR) *v* 3322, 2105, 1720 cm^{-1}; MS (MALDI-TOF): m/z 589 [M-(NCS)]$^+$, 557 [M-(NCS)-2(CH_3)]$^+$, 530 [M-2(NCS)]$^+$.

[Ru(34c)(13)(NCS)$_2$] (39e, RSH-554):

Compound **39e** was synthesized by following the same procedure as for **39a**, using dichloro(*p*-cymene)ruthenium(II) (**56**, 122 mg, 0.2 mmol), DMF (30 mL), 6-methyl-4-(4'-*t*-butyl-pyrid-2'-yl)-pyrimidine (**34c**, 90 mg, 0.4 mmol), 2,2'-bipyridine-4,4'-dicarboxylic acid (**13**, 98 mg, 0.4 mmol) and ammonium thiocyanate (0.99 g, 13 mmol) to give **39e** as a dark red solid (84 mg, 60%): ^{1}H NMR (CD_3OD, 500 MHz) δ 9.79 (s, 1H), 9.56 (d, *J* = 5.73 Hz, 1H), 9.53 (d, *J* = 5.73 Hz, 1H), 9.34 (d, *J* = 5.73 Hz, 1H), 9.0 (br s, 2H), 8.85 (br s, 2H), 8.70 (d, *J* = 1.72 Hz, 1H), 8.64 (s, 1H), 8.56 (d, *J* = 1.72 Hz,

1H), 8.49 (s, 1H), 8.22-8.21 (m, 2H), 8.02 (s, 1H), 7.98, (dd, *J* = 5.73, 1.72 Hz, 1H), 7.91 (d, *J* = 6.30 Hz, 1H), 7.73 (d, *J* = 5.73 Hz, 1H), 7.60-7.59 (m, 2H), 7.48 (d, *J* = 6.30 Hz, 1H), 7.30 (dd, *J* = 6.30, 1.80 Hz, 1H), 2.68 (s, 3H), 2.60 (s, 3H), 1.55 (s, 9H), 1.32 (s, 9H); IR (ATR) *v* 3323, 2105, 1726 cm^{-1}; MS (MALDI-TOF): m/z 631 $[M-(NCS)]^+$, 616 $[M-(NCS)-(CH_3)]^+$, 573 $[M-2(NCS)]^+$.

[Ru(35a)(18)(NCS)$_2$] (39f, RSH-510):

Compound **39f** was synthesized by following the same procedure as for **39a**, using dichloro(*p*-cymene)ruthenium(II) (**56**, 122 mg, 0.2 mmol), DMF (30 mL), 6-*t*-butyl-4-(pyrid-2'-yl)-pyrimidine (**35a**, 85 mg, 0.4 mmol), 2,2'-bipyridine-4,4'-dicarboxylic acid (**13**, 98 mg, 0.4 mmol) and ammonium thiocyanate (0.99 g, 13 mmol) to give **39f** as a red solid (69 mg, 50%): ^{1}H NMR (CD_3OD, 400 MHz) δ 9.84 (s, 1H), 9.64 (d, *J* = 5.95 Hz, 1H), 9.61 (d, *J* = 5.50 Hz, 1H), 9.48 (d, *J* = 5.04 Hz, 1H), 9.06-9.04 (m, 2H), 8.91-8.90 (m, 2H), 8.86 (d, *J* = 8.24 Hz, 1H), 8.72 (d, *J* = 7.79 Hz, 1H), 8.57 (s, 1H), 8.42 (s, 1H), 8.30-8.28 (m, 2H), 8.25 (dt, *J* = 8.24, 1.37 Hz, 1H), 8.11 (s, 1H), 8.02 (d, *J* = 5.95 Hz, 1H), 7.96-7.86 (m, 3H), 7.68-7.66 (m, 2H), 7.63 (d, *J* = 5.04 Hz, 1H), 7.26 (dt, *J* = 6.87, 0.92 Hz, 1H), 1.58 (s, 9H), 1.34 (s, 9H); IR (ATR) *v* 3321, 2103, 1724 cm^{-1}; MS (MALDI-TOF): m/z 617 $[M-(NCS)]^+$, 585 $[M-(NCS)-2(CH_3)]^+$, 559 $[M-2(NCS)]^+$.

[Ru(35b)(13)(NCS)$_2$] (39g, RSH-538):

Compound **39g** was synthesized by following the same procedure as for **39a**, using dichloro(*p*-cymene)ruthenium(II) (**56**, 122 mg, 0.2 mmol), DMF (30 mL), 6-*t*-butyl-4-(4'-*t*-butyl-pyrid-2'-yl)-pyrimidine (**35b**, 0.11 g, 0.4 mmol), 2,2'-bipyridine-4,4'-dicarboxylic

acid (**13**, 98 mg, 0.4 mmol) and ammonium thiocyanate (0.99 g, 13 mmol) to give **39g** as a dark red solid (74 mg, 50%): ^{1}H NMR (CD_3OD, 500 MHz) δ 9.86 (d, *J* = 0.86 Hz, 1H), 9.47 (d, *J* = 5.73 Hz, 1H), 9.45 (d, *J* = 5.73 Hz, 1H), 9.38 (d, *J* = 5.73 Hz, 1H), 8.97-8.96 (m, 2H), 8.81-8.80 (m, 2H), 8.79 (d, *J* = 2.29 Hz, 1H), 8.64 (d, *J* = 2.29 Hz, 1H), 8.63 (d, *J* = 1.15 Hz, 1H), 8.47 (d, *J* = 1.15 Hz, 1H), 8.17 (d, *J* = 1.72 Hz, 1H), 8.16 (d, *J* = 1.72 Hz, 1H), 8.05 (d, *J* = 1.15 Hz, 1H), 7.96 (dd, *J* = 5.73, 1.72 Hz, 1H), 7.78 (d, *J* = 5.73 Hz, 1H), 7.63 (d, *J* = 5.73 Hz, 1H), 7.55-7.53 (m, 2H), 7.48 (d, *J* = 6.30 Hz, 1H), 7.30 (dd, *J* = 6.30, 2.29 Hz, 1H), 1.59 (s, 9H), 1.56 (s, 9H), 1.34 (s, 9H), 1.33 (s, 9H); IR (ATR) *v* 3330, 2102, 1720 cm^{-1}; MS (MALDI-TOF): m/z 673 $[M-(NCS)]^+$, 643 $[M-(NCS)-2(CH_3)]^+$, 615 $[M-2(NCS)]^+$, 558 $[M-2(NCS)-2(CCH_3)]^+$.

[Ru(37a)(13)(NCS)$_2$] (39h, RSH-167):

Compound **39h** was synthesized by following the same procedure as for **39a**, using dichloro(*p*-cymene)ruthenium(II) (**56**, 122 mg, 0.2 mmol), DMF (30 mL), 2-(pyrid-2'-yl)quinoxaline (**37a**, 83 mg, 0.4 mmol), 2,2'-bipyridine-4,4'-dicarboxylic acid (**13**, 98 mg, 0.4 mmol) and ammonium thiocyanate (0.99 g, 13 mmol) to give **39h** as a purple solid (80 mg, 58%): ^{1}H NMR (DMSO-*d6*, 500 MHz) δ 10.06, (s, 1H), 9.97 (s, 1H), 9.42 (d, *J* = 5.73 Hz, 1H), 9.32 (d, *J* = 5.15 Hz, 1H), 9.29 (d, *J* = 5.73 Hz, 1H), 9.24 (d, *J* = 8.59 Hz, 1H), 9.22-9.20 (m, 3H), 9.04 (s, 1H), 9.02-9.0 (m, 2H), 8.41-8.35 (m, 4H), 8.09-8.07 (m, 2H), 8.05-8.0 (m, 3H), 7.95 (t, *J* = 8.02 Hz, 1H), 7.73 (t, *J* = 7.45 Hz, 1H), 7.66-7.64 (m, 2H), 7.57 (d, *J* = 6.30 Hz, 1H), 7.47 (d, *J* = 5.73 Hz, 1H), 7.38 (t, *J* = 8.02 Hz, 1H), 7.33 (t, *J* = 6.87 Hz, 1H), 6.84 (d, *J* = 8.59 Hz, 1H); IR (ATR) *v* 3320, 2104, 1726 cm^{-1}; MS (MALDI-TOF): m/z 611 $[M-(NCS)]^+$, 552 $[M-2(NCS)]^+$.

[Ru(37b)(13)(NCS)$_2$] (39i, RSH-171):

Compound **39i** was synthesized by following the same procedure as for **39a**, using dichloro(*p*-cymene)ruthenium(II) (**56**, 122 mg, 0.2 mmol), DMF (30 mL), 6,7-dimethyl-2-(pyrid-2'-yl)quinoxaline (**37b**, 94 mg, 0.4 mmol), 2,2'-bipyridine-4,4'-dicarboxylic acid (**13**, 98 mg, 0.4 mmol) and ammonium thiocyanate (0.99 g, 13 mmol) to give **39i** as a purple solid (78mg, 55%): ^{1}H NMR (DMSO-*d6*, 500 MHz) δ 9.94 (s, 1H), 9.85 (s, 1H), 9.46 (d, *J* = 5.95 Hz, 1H), 9.33 (d, *J* = 5.04 Hz, 1H), 9.28 (d, *J* = 5.50 Hz, 1H), 9.25 (s, 1H), 9.19 (s, 1H), 9.15-9.13 (m, 2H), 8.97-8.92 (m, 3H), 8.38-8.35 (m, 2H), 8.32 (d, *J* = 8.24 Hz, 1H), 8.12 (s, 1H), 8.02-7.98 (m, 2H), 7.90 (d, *J* = 5.50 Hz, 1H), 7.83 (s, 1H), 7.60-7.58 (m, 2H), 7.54 (d, *J* = 7.33 Hz, 1H), 7.45 (d, *J* = 7.33 Hz, 1H), 7.29 (t, *J* = 7.56 Hz, 1H), 6.59 (s, 1H), 2.55 (s, 3H), 2.54 (s, 3H), 2.27 (s, 3H), 1.78 (s, 3H); IR (ATR) *v* 3329, 2101, 1726 cm^{-1}; MS (MALDI-TOF): m/z 639 [M-(NCS)]$^+$, 613 [M-(NCS)-(CH$_3$)]$^+$, 581 [M-2(NCS)]$^+$.

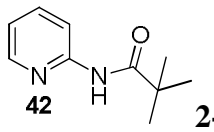

42

2-(Pivaloylamino)pyridine (42, RSH-32):[221]

A solution of trimethylacetyl chloride (**41**, 6.63 g, 55 mmol) in 10 mL of CH_2Cl_2 was slowly added to an ice cooled solution of 2-aminopyridine (**40**, 4.70 g, 50 mmol) and triethylamine (6.31 g, 62.5 mmol) in CH_2Cl_2 (75 mL). The resulting mixture was stirred in an ice bath for 15 min and then at rt for 2 h and then poured into water. The CH_2Cl_2 layer was washed with dilute $NaHCO_3$, dried over Na_2SO_4, and evaporated. Crystallization from hexane afforded **42** as white crystals (7.0 g, 70%): mp 71-73 ^{o}C; ^{1}H

NMR ($CDCl_3$, 300 MHz) δ 8.30-8.20 (m, 2H), 8.12 (br, 1H, NH), 7.7 (t, *J* = 5.04 Hz, 1H), 7.05 (t, *J* = 5.04 Hz, 1H), 1.32 (s, 9H); ^{13}C NMR ($CDCl_3$, 75 MHz) δ 176.8, 152.0, 145.6, 139.1, 124.3, 114.2, 39.4, 27.8; IR (ATR) *v* 3305, 3240, 2965, 1678 cm^{-1}.

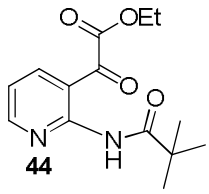

44

[2-(Pivaloylamino)pyrid-3-yl]oxoacetic Acid Ethyl Ester (44, RSH-33):

Compound **44** was prepared following the protocol developed by Turner[221] and Hewawasam.[222] The 2-(pivaloylamino) pyridine (**42**, 7.60 g, 42.7 mmol) in dry THF (100 mL) was treated with *n*-butyllithium (1.6 M in hexane, 53 mL, 84.8 mmol) at -70 °C for 1 h, yielding a light yellow solution. The mixture was allowed to warm to ice-bath temperature, and some precipitate was observed. The mixture was stirred at 0 °C for 3 h, and more precipitate formed. After the mixture was cooled to -70 °C, diethyl oxalate (**43**, 16 mL in 10 mL of dry THF) was added dropwise. The mixture was allowed to warm to rt and stirred for 20 min. The reaction mixture was quenched with acidic ice-water (1 mL of conc HCl and 100 mL of ice). The product was extracted with ether (3 x 50 mL) and dried over Na_2SO_4. Evaporation of the solvents gave a red oil (9.0 g) that was chromatogaphed on SiO_2 eluting with a mixture of 1:1 EtOAc and hexanes to provide **44** as light yellow crystals (6.0 g, 50%): mp 118-119 °C; ^1H NMR ($CDCl_3$, 400 MHz) δ 9.92 (br, 1H, NH), 8.61 (dd, *J* = 4.58, 1.72 Hz, 1H), 8.08 (dd, *J* = 8.02, 2.29 Hz, 1H), 7.17(dd, *J* = 8.02, 5.15 Hz, 1H), 4.41 (q, *J* = 6.87 Hz, 2H), 1.42 (t, *J* = 6.87 Hz, 3H), 1.33 (s, 9H);

^{13}C NMR ($CDCl_3$, 100 MHz) δ 185.0, 176.8, 161.5, 153.0, 150.5, 140.8, 118.7, 117.3, 62.8, 40.0, 27.3, 14.0; IR (ATR) *v* 1731, 1709, 1673 cm^{-1}. Anal. Calcd for $C_{14}H_{18}N_2O_4$: C, 60.42; H, 6.52; N, 10.07. Found: C, 60.43; H, 6.51; N, 10.04.

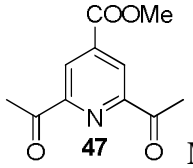

47 **Methyl 2,6-Diacetylisonicotinate (47, RSH-34)**:[223]

To the mixture of methyl isonicotinate (**45**, 5.50 g, 40 mmol), pyruvic acid (**46**, 14.1 g, 140 mmol), $AgNO_3$ (0.5 g, 3 mmol), H_2SO_4 (3 mL), in H_2O (50 mL) and CH_2Cl_2 (50 mL), $NH_4S_2O_8$ (30 g, 0.15 mol) was added portion-wise. The mixture was stirred for 2 h at 40 ^oC. The organic phase was separated and neutralized with sat NaOH solution. The organic layer was dried over $MgSO_4$ and evaporated under vacuum. Evaporation of the solvent gave **47** as a yellow solid (6.2 g, 70%): mp 131-132 °C; ^1H NMR ($CDCl_3$, 400 MHz) δ 8.73 (s, 2H), 4.01 (s, 3H), 2.83 (s, 6H); ^{13}C NMR ($CDCl_3$, 100 MHz) δ 198.4, 164.4, 153.7, 140.0, 124.0, 53.1, 25.7; IR (ATR) *v* 1727, 1701, 1250, 949, 770 cm^{-1}. Anal. Calcd for $C_{11}H_{11}NO_4$: C, 59.73; H, 5.01; N, 6.33. Found: C, 59.68; H, 4.87; N, 6.33.

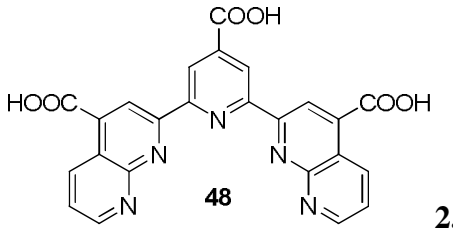

48

2,6-Di(4'-carboxy-1',8'-naphthyrid-2'-yl)pyridine-4-carboxylic Acid (48, RSH-35):

A mixture of **44** (278 mg, 1.0 mmol) and **47** (73 mg, 0.33 mmol) in EtOH (20 mL) was treated with KOH (200 mg, 3.57 mmol) under reflux for 24 h. The alcohol was removed and water (20 mL) was added to the residue to give a solution. The aqueous solution was extracted with CH_2Cl_2 (3 x 3 mL), acidified with HOAc (0.4 mL) to produce a white precipitate. The precipitate was collected, washed with water, EtOH, and ether, and dried to give **48** as a white solid (137 mg, 90%): mp > 260 ^oC;^1H NMR (DMSO-*d6*, 300 MHz) δ 9.28 (dd, *J* = 8.1, 1.5 Hz, 2H), 9.22 (s, 2H), 9.18 (dd *J* = 4.2, 1.5 Hz, 2H), 9.15 (s, 2H), 7.73 (dd, *J* = 8.7, 4.2 Hz, 2H); ^{13}C NMR ($D_2O/CD_3OD/KOH$, 75 MHz) δ 174.7, 173.6, 159.7, 156.5, 155.7, 155.3, 150.2, 148.5, 137.8, 124.4, 123.6, 120.7, 118.6; IR (ATR) *v* 1701, 1592 cm^{-1}. Anal. Calcd for $C_{24}H_{13}N_5O_6 \cdot 2H_2O$: C, 57.26; H, 3.40; N, 13.91. Found: C, 56.78; H, 2.80; N, 13.69.

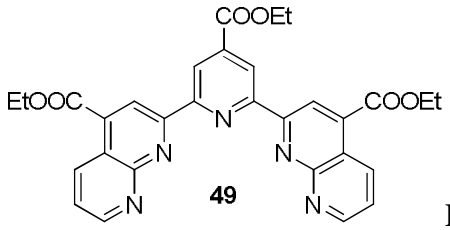

Ethyl 2,6-di(4'-ethoxycarbonyl-1',8'-naphthyrid-2'-yl)pyridine-4-carboxylate (49, RSH-218):

Mixture of compound **48** (2g, 4.28 mmol) and H_2SO_4 (1 mL) in EtOH (10 mL) were refluxed overnight in a sealed tube. The reaction mixture was cooled to rt, concentrated, and extracted with CH_2Cl_2 (3 x 15 mL). The extracts were combined, washed with brine, dried over $MgSO_4$ and the solvent was evaporated to afford **49** as a yellow solid (1.42 g, 60%): mp 157-159 ^oC; ^1H NMR ($CDCl_3$, 400 MHz) δ 9.53 (s, 2H), 9.47 (s, 2H), 9.28 (dd, *J* = 8.24, 1.83 Hz, 2H), 9.26 (dd, *J* = 4.12, 1.83 Hz, 2H), 7.66 (dd, *J* = 8.24, 4.12 Hz, 2H), 4.62 (q, *J* = 6.88 Hz, 4H), 4.53 (q, *J* = 6.88 Hz, 2H), 1.56 (t, *J* = 6.88 Hz, 6H), 1.49 (t, *J* = 6.88 Hz, 3H); ^{13}C NMR ($CDCl_3$, 100 MHz) δ 165.6, 158.2, 156.4, 155.4, 154.4, 137.5, 135.6, 123.6, 123.2, 121.7, 62.4, 62.2, 14.6, 14.4; IR (ATR) *v* 1720, 1280 cm^{-1}.

[Ru(49)Cl_3] (50, RSH-468a):

$RuCl_3.3H_2O$ (0.26 g, 1 mmol) and EtOH (50 mL) were stirred for 2 min, then a solution of the ligand **49** (0.40 g, 0.73 mmol) in 50 mL of CH_2Cl_2 was added. The reaction mixture was refluxed for 2 h under Ar. The solution was concentrated to 20 mL, and the reaction mixture was cooled to rt. The precipitated complex was collected on a sintered glass funnel and washed thoroughly with EtOH to remove unreacted $RuCl_3$. The air-dried product afforded **50** as a dark brown solid (0.44 g, 80%).

[Ru(48)(NCS)$_3$] (51, RSH-468b):

The complex **51** was synthesized in dark under Ar by refluxing a solution of **50** (0.5 g, 0.66 mmol) and NH_4NCS (2 g, 0.03 mol in 10 mL of H_2O) in DMF (50 mL) at 130 ^oC for 4 h. Then 20 mL of triethylamine in 10 mL of H_2O was added, and the solution was refluxed for a further 24 h to hydrolyze the ester groups on the ligand. The solution was concentrated to about 10 mL, and then the solution was added to 70 mL of H_2O. The resulting precipitate was filtered and dried. The isolated solid was purified on a Sephadex LH-20 column, using MeOH as eluent to afford **51** as a green solid (0.19 g, 40%).

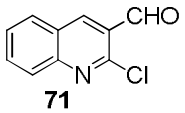

71

2-Chloro-3-quinolinecarboxaldehyde (71, RSH-181):

Following the literature procedure,[191] $POCl_3$ (32 mL, 350 mmol) was added dropwise to an ice-cold solution of DMF (12 mL, 150 mmol) and the mixture was stirred at 0 ^oC for 30 min. To the deep-red solution acetanilide (**70**, 6.75 g, 50 mmol) was added and the mixture was stirred at 0 ^oC for an additional 45 min, then the reaction mixture was heated at 75 ^oC for 16 h. The reaction mixture was cooled to rt, then poured into 250 mL of ice-water and stirred at 0-5 ^oC for 30 min. The solid was filtered, washed with water and dried to give **71** (8 g, 82%) as a light yellow solid: mp 140-141 ^oC (lit.[191] mp 147-149 ^oC); ^1H NMR ($CDCl_3$, 400 MHz) δ 10.56 (s, 1H), 8.76 (s, 1H), 8.07 (d, J = 9.50 Hz, 1H), 7.98 (d, J = 9.16 Hz, 1H), 7.88 (dt, J = 8.70, 1.37 Hz, 1H), 7.65 (dt, J = 8.59, 1.37 Hz, 1H); ^{13}C NMR ($CDCl_3$, 100 MHz) δ 189.3, 150.2, 149.7, 140.5, 133.8, 129.8, 128.7, 128.3, 126.6, 126.4; IR (ATR) ν 1686 cm^{-1}.

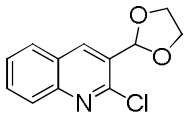

72

2-Chloro-3-(1',3'-dioxolan-2'-yl)quinoline (72, RSH-182):

Following the literature procedure,[224] a solution of 2-chloroquinoline-3-carbaldehyde (**71**, 6 g, 30 mmol), ethylene glycol (6 g, 90 mmol) and *p*-toluenesulfonic acid (0.26 g, 1.5 mmol) in benzene (100 mL) was heated at reflux under a Dean-Stark trap until TLC (Al_2O_3, CH_2Cl_2/hexanes 1:1) indicated completion of the reaction. The solution was cooled to rt and neutralized with sat aq $NaHCO_3$ solution (50 mL). The organic layer was washed with water (2 x 50 mL), dried over $MgSO_4$ and evaporated to afford **72** as a light-brown oil (7 g, 95%): ^{1}H NMR ($CDCl_3$, 400 MHz) δ 8.39 (s, 1H), 8.01 (d, *J* = 7.79 Hz, 1H), 7.85 (dd, *J* = 9.16, 1.37 Hz, 1H), 7.73 (dt, *J* = 8.24, 1.37 Hz, 1 H), 7.56 (dt, *J* = 8.24, 1.37 Hz, 1 H), 6.22 (s, 1H), 4.16-4.07 (m, 4H); ^{13}C NMR ($CDCl_3$, 100 MHz) δ 149.4, 147.8, 136.8, 131.1, 129.5, 128.4, 128.2, 127.4, 126.9, 100.5, 65.7.

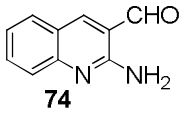

74

2-Aminoquinoline-3-carbaldehyde (74, RSH-186):

Following the literature procedure,[185c,192b] a mixture of 2-chloro-3-(1',3'-dioxolan-2'-yl)quinoline (**72**, 5.66 g, 24 mmol), K_2CO_3 (100 g, 724 mmol) and acetamide (**73**, 120 g, 2.03 mol) was stirred mechanically at 200 °C for 7 h. The mixture was cooled to rt, extracted with water (200 mL) and a mixture of $CHCl_3$–isopropanol (3:1, 3 x 60 mL). The combined organic phases were washed with brine (150 mL) and dried over $MgSO_4$. The solvents were evaporated under vacuum to give brownish oil (7.82 g). The obtained crude product was mixed with THF (100 mL), H_2O (50 mL) and conc HCl (5 mL). The

reaction mixture was refluxed for 1 h to deprotect the acetal, then cooled to rt and concentrated to produce a yellow precipitate. The precipitate was filtered and washed with H_2O. The filtrate was extracted with $CHCl_3$ (3 x 30 mL) and the aq phase was basified with sat aq K_2CO_3 solution to produce a yellow precipitate. The precipitate was collected, washed with H_2O and dried to afford **74** as a yellow solid (2.0 g, 50%): mp 193-194 ^oC (lit.[225] mp 196-197 ^oC); ^1H NMR ($CDCl_3$, 400 MHz) δ 10.03 (s, 1 H), 8.35 (s, 1 H), 7.73 (d, *J* = 7.79 Hz, 1H), 7.69 (dt, *J* = 8.70, 6.85, 1.37 Hz, 1H), 7.62 (d, *J* = 8.24 Hz, 1 H), 7.28 (dt, *J* = 7.79, 0.92 Hz, 1H), 6.63 (s, br, 2 H); ^{13}C NMR ($CDCl_3$, 125 MHz) δ 192.7, 155.4, 150.6, 148.4, 133.9, 129.3, 126.1, 123.2, 122.7, 117.4; IR (ATR) *v* 1676 cm^{-1}.

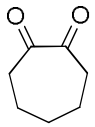

75c **1,2-Cycloheptanedione** (**75c, RSH-376**):[226]

Selenium dioxide (11 g, 0.1 mol) was added to a solution of cycloheptanone (10 g, 0.09 mol) in EtOH (50 mL). The mixture was refluxed for 8 h, then allowed to stand at rt for ~18 h, and then filtered. The mixture was concentrated and the residue was filtered again. The distillation of the mixture at reduced pressure afforded **75c** as a yellow oil (10.2 g, 90%): bp 107-109 °C/17 mmHg; ^1H NMR ($CDCl_3$, 500 MHz) δ 2.58-2.56 (m, 2H), 1.97-1.94 (m, 2H), 1.82-1.80 (m, 1H); ^{13}C NMR ($CDCl_3$, 125 MHz) δ 209.5, 40.0, 33.4, 27.8.

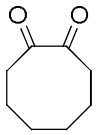

75d **1,2-Cyclooctanedione** (**75d**):

Compound **75d** was synthesized by following the same procedure as for **75c**, using cyclooctanone (10 g, 0.08 mol) and SeO_2 (11 g, 0.1 mol) in EtOH (50 mL) to give **75d** as a yellow oil (10 g, 90%): bp 118-120 °C/17 mmHg; ^{1}H NMR ($CDCl_3$, 500 MHz) δ 2.57-2.55 (m, 2H), 1.77-1.75 (m, 2H), 1.61-1.60 (m, 2H); ^{13}C NMR ($CDCl_3$, 125 MHz) δ 210.2, 40.1, 26.5, 21.3.

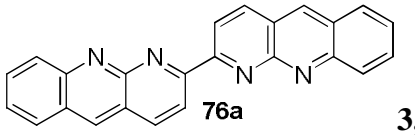

76a **3,3'-Bi-4-azaacridine** (**76a, RSH-353**):

A mixture of freshly distilled 2,3-butanedione (**75a**, 0.1 g, 1.16 mmol), 2-aminoquinoline-3-carbaldehyde (**74**, 0.4 g, 2.32 mmol), EtOH (15 mL) and KOH (4 mg) was heated at 50 ^{o}C overnight under Ar. The mixture was cooled to rt and filtered. The precipitate was washed with EtOH and dried to afford **76a** as a yellow solid (0.2 g, 44%), mp > 290 ^{o}C: ^{1}H NMR ($CDCl_3$, 400 MHz) δ 9.32 (d, J = 8.7 Hz, 1H), 8.92 (s, 1H), 8.61 (d, J = 8.7 Hz, 1H), 8.47 (d, J = 8.7 Hz, 1H), 8.09 (d, J = 8.3 Hz, 1H), 7.89 (t, J = 7.8 Hz, 1H), 7.65 (t, J = 7.8 Hz, 1H); ^{13}C NMR ($CDCl_3$, 100 MHz) δ 171.1, 163.3, 160.7, 133.3, 137.7, 131.6, 130.2, 128.2, 127.1, 121.8, 120.5; MS (MALDI-TOF): m/z 397 $[M+K]^+$, 360 $[M+2]^+$. Anal. Calcd for $C_{24}H_{14}N_4 \cdot 0.5\ H_2O$: C, 78.47; H, 3.95; N, 15.25. Found: C, 78.34; H, 3.70; N, 15.11.

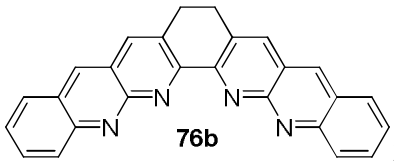

76b **2,2'-Dimethylene-3,3'-bi-4-azaacridine (76b, RSH-341)**:

A mixture of 1,2-cyclohexanedione (**75b**, 0.03 g, 0.3 mmol), 2-aminoquinoline-3-carbaldehyde (**74**, 0.1 g, 0.6 mmol), EtOH (8 mL) and KOH (2 mg) was heated at reflux for 30 min under Ar. The mixture was cooled to rt, concentrated, and extracted with CH_2Cl_2 (3 x 15 mL). The extracts were combined, washed with brine, dried over $MgSO_4$ and the solvent was evaporated. The crude product was purified by chromatography on alumina eluting with CH_2Cl_2/acetone/MeOH (30:25:2). Crystals collected from solution were dried to afford **76b** as a white solid (0.06 g, 50%), mp > 290 ^oC: ^1H NMR ($CDCl_3$, 400 MHz) δ 8.75 (s, 1H), 8.42 (d, *J* = 8.70 Hz, 1H), 8.27 (s, 1H), 8.01 (d, *J* = 8.24 Hz, 1H), 7.84 (dt, *J* = 8.47, 1.37 Hz, 1H), 7.60 (dt, *J* = 8.24, 0.92 Hz, 1H), 3.39 (s, 2H); ^{13}C NMR ($CDCl_3$, 100 MHz) δ 160.0, 156.1, 145.4, 136.9, 135.7, 133.2, 132.1, 131.4, 129.8, 128.1, 126.1, 121.3, 28. 9; MS (MALDI-TOF): m/z 385 $[M+1]^+$, 386 $[M+2]^+$. Anal. Calcd for $C_{26}H_{16}N_4 \cdot 0.5\ H_2O$: C, 79.39; H, 4.32; N, 14.25. Found: C, 79.34; H, 4.24; N, 14.11.

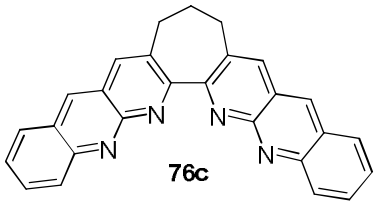

76c **2,2'-Trimethylene-3,3'-bi-4-azaacridine (76c, RSH-377)**:

A mixture of 1,2-cycloheptanedione (**75c**, 0.04 g, 0.35 mmol), 2-aminoquinoline-3-carbaldehyde (**74**, 0.12 g, 0.7 mmol), EtOH (10 mL) and KOH (3 mg) was stirred at rt

overnight. The reaction mixture was filtered and the precipitate was washed with EtOH and dried to afford **75c** as a yellow solid (0.08 g, 55%), mp > 290 °C: ^{1}H NMR ($CDCl_3$, 400 MHz) δ 8.81 (s, 1H), 8.39 (d, *J* = 9.16 Hz, 1H), 8.22 (s, 1H), 8.05 (d, *J* = 8.24 Hz, 1H), 7.84 (t, *J* = 8.24 Hz, 1H), 7.61 (dt, *J* = 7.79 Hz, 1H), 2.90 (m, 2H), 2.28 (p, *J* = 6.4 Hz, 1H); ^{13}C NMR ($CDCl_3$, 100 MHz) δ 163.6, 154.3, 151.0, 136.3, 135.4, 132.6, 130.8, 130.7, 127.8, 127.4, 126.8, 121.4, 29.8, 29.6; MS (MALDI-TOF): m/z 400 $[M+2]^+$. Anal. Calcd for $C_{27}H_{18}N_4 \cdot 2K$: C, 68.06; H, 3.78; N, 11.76. Found: C, 68.33; H, 3.51; N, 11.77.

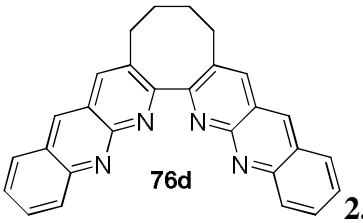

76d

2,2'-Tetramethylene-3,3'-bi-4-azaacridine (76d, RSH-263):

A mixture of 1,2-cyclooctanedione (**75d**, 0.04 g, 0.27 mmol) and 2-aminoquinoline-3-carbaldehyde (**74**, 0.1 g, 0.58 mmol), EtOH (15 mL) and KOH (4 mg) was stirred at rt overnight. The reaction mixture was concentrated, extracted with CH_2Cl_2 (3 x 15 mL). The extracts were combined, washed with brine, dried over $MgSO_4$ and the solvent was evaporated. The crude product was purified by chromatography on alumina, eluting with CH_2Cl_2/MeOH (50:1), to afford **76d** as a yellow solid (0.09 g, 80%), mp > 290 °C: ^{1}H NMR ($CDCl_3$, 400 MHz) δ 8.83 (s, 1H), 8.34 (d, *J* = 9.16 Hz, 1H), 8.27 (s, 1H), 8.06 (d, *J* = 8.24 Hz, 1H), 7.82 (dt, *J* = 1.37, 8.24 Hz, 1H), 7.60 (dt, *J* = 0.92, 8.24 Hz, 1H), 3.07 (dd, *J* = 5.95, 8.24 Hz, 2H), 2.52 (dt, *J* = 2.75, 10.9 Hz, 2H), 2.32 (t, *J* = 9.16 Hz, 2H), 1.74 (t, *J* = 10.53 Hz, 2H); ^{13}C NMR ($CDCl_3$, 100 MHz) δ 153.5, 150.9, 136.6, 136.3, 130.9, 130.4, 127.9, 127.3, 126.6, 121.4, 31.7, 31.3; MS (MALDI-TOF): m/z 414

$[M+2]^+$. Anal. Calcd for $C_{28}H_{20}N_4 \cdot 1.0\ H_2O$: C, 78.14; H, 5.17; N, 13.02. Found: C, 78.02; H, 4.61; N, 12.72.

[Ru(76a)(tpy)(H_2O)](PF_6)$_2$ (79a, RSH-392):

A mixture of **76a** (22 mg, 0.05 mmol), [Ru(tpy)(CH_3CN)Cl_2] (**78**, 18 mg, 0.05 mmol), EtOH (10 mL) and H_2O (3 mL) was refluxed for 3 h. The solution was concentrated to about 5 mL, and then NH_4PF_6 (140 mg, 0.78 mmol) in water (3 mL) was added. The solution was stirred for 30 min. The green precipitate was collected by filtration, washed with water, dried under vacuum and purified by chromatography on alumina eluting with CH_2Cl_2/acetone (1:1) to give **79a** as a green solid (34 mg, 68%): ^{1}H NMR (acetone-*d*6, 500 MHz) δ 9.97 (s, 1H), 9.43 (d, *J* = 9.16 Hz, 1H), 9.37 (d, *J* = 9.16 Hz, 1H), 9.17 (s, 1H), 9.08 (d, *J* = 8.70 Hz, 1H), 8.99 (d, *J* = 8.24 Hz, 2H), 8.94 (s, br, H_2O), 8.74-8.63 (m, 4H), 8.55 (d, *J* = 8.24 Hz, 1H), 8.14-8.09 (m, 3H), 7.96-7.88 (m, 6H), 7.69 (dt, *J* = 8.24, 0.92 Hz, 1H), 7.39 (d, *J* = 8.70 Hz, 1H), 7.16 (dt, *J* = 6.87, 1.26 Hz, 2H); MS (MALDI-TOF): m/z 693 $[M-(H_2O)-(PF_6)_2]^+$. Anal. Calcd for $C_{39}H_{27}N_7OP_2F_{12}Ru \cdot 0.5\ PF_6$: C, 43.61; H, 2.51; N, 9.13. Found: C, 43.50; H, 2.30; N, 8.96.

[Ru(76b)(tpy)(H_2O)](PF_6)$_2$ (79b, RSH-410):

Compound **79b** was synthesized by following the same procedure as for **79a**, using **76b** (20 mg, 0.05 mmol), **78** (25.5 mg, 0.057 mmol), EtOH (10 mL), H_2O (3 mL) and NH_4PF_6 (140 mg, 0.78 mmol) to afford **79b** as a green solid (40 mg, 77%): ^{1}H NMR (acetone-*d*6, 500 MHz) δ 9.86 (s, 1H), 9.09 (d, *J* = 12.82 Hz, 2H), 9.00 (d, *J* = 8.24 Hz, 2H), 8.92 (s, br, H_2O), 8.69-8.62 (m, 3H), 8.52 (d, *J* = 8.24 Hz, 1H), 8.45 (s, 1H), 8.11-

8.05 (m, 3H), 7.93-7.87 (m, 6H), 7.66 (dt, *J* = 8.24, 0.92 Hz, 1H), 7.33 (d, *J* = 9.62 Hz, 1H), 7.16 (dt, *J* = 6.87, 0.92 Hz, 2H), 3.82 (t, *J* = 9.62 Hz, 2H), 3.66 (t, *J* = 9.62 Hz, 2H); MS (MALDI-TOF): m/z 719 $[M-(H_2O)-(PF_6)_2]^+$, 734 $[M-(PF_6)_2]^+$. Anal. Calcd for $C_{41}H_{29}N_7OP_2F_{12}Ru \cdot 0.5\ PF_6$: C, 44.79; H, 2.64; N, 8.92. Found: C, 44.66; H, 2.87; N, 8.30.

[Ru(76c)(tpy)(H_2O)](PF_6)$_2$ (79c, RSH-445):

Compound **79c** was synthesized by following the same procedure as for **79a**, using **76c** (33 mg, 0.07 mmol), **78** (30 mg, 0.07 mmol), EtOH (10 mL), H_2O (3 mL) and NH_4PF_6 (140 mg, 0.78 mmol) to afford **79c** as a green solid (44 mg, 60%): ^{1}H NMR (acetone-*d*6, 500 MHz) δ 9.88 (s, 1H), 9.14 (s, 1H), 9.07 (s, 1H), 8.91 (d, *J* = 8.59 Hz, 2H), 8.84 (s, br, H_2O), 8.61-8.55 (m, 4H), 8.40 (s, 1H), 8.12-8.09 (m, 3H), 7.95-7.92 (m, 5H), 7.86 (dt, *J* = 8.59, 1.72 Hz, 1H), 7.67 (t, *J* = 6.87 Hz, 1H), 7.39 (d, *J* = 8.02 Hz, 2H), 7.18 (dt, *J* = 7.45, 1.15 Hz, 2H), 3.34 (t, *J* = 7.16 Hz, 2H), 3.30 (t, *J* = 7.16 Hz, 2H), 2.69 (t, *J* = 6.87 Hz, 2H); MS (MALDI-TOF): m/z 732 $[M-(H_2O)-(PF_6)_2]^+$, 751$[M-(PF_6)_2]^+$. Anal. Calcd for $C_{42}H_{31}N_7OP_2F_{12}Ru \cdot 0.5\ H_2O$: C, 48.05; H, 3.05; N, 9.34. Found: C, 47.90; H, 2.87; N, 8.99.

[Ru(76d)(tpy)(H_2O)](PF_6)$_2$ (79d, RSH-460):

Compound **79d** was synthesized by following the same procedure as for **79a**, using **76d** (20 mg, 0.05 mmol), **78** (25 mg, 0.056 mmol), EtOH (10 mL), H_2O (3 mL) and NH_4PF_6 (140 mg, 0.78 mmol) to afford **79d** as a green solid (21 mg, 40%): ^{1}H NMR (acetone-*d*6, 500 MHz at -80 ^{o}C) δ 9.97 (s, 1H), 9.30 (s, 1H), 9.23 (d, *J* = 8.59 Hz, 1H), 9.12 (s, 1H),

9.00 (br s, H_2O), 8.93 (d, *J* = 8.59 Hz, 1H), 8.70 (d, *J* = 8.02 Hz, 1H), 8.62 (d, *J* = 8.02 Hz, 1H), 8.58 (t, *J* = 8.02 Hz, 1H), 8.51 (s, 1H), 8.46 (d, *J* = 5.73 Hz, 1H), 8.41 (d, *J* = 8.02 Hz, 1H), 8.16 (d, *J* = 8.02 Hz, 1H), 8.13-8.12 (m, 2H), 8.06 (t, *J* = 7.17 Hz, 1H), 7.97-7.94 (m, 1H), 7.92-7.87 (m, 2H), 7.75 (d, *J* = 5.15 Hz, 1H), 7.68 (t, *J* = 7.45 Hz, 1H), 7.37 (d, *J* = 8.59 Hz, 1H), 7.29 (t, *J* = 6.30 Hz, 1H), 7.17 (t, *J* = 6.30 Hz, 1H), 3.45-3.41 (m, 1H), 3.23-3.19 (m, 1H), 3.11 (t, *J* = 12.60 Hz, 1H), 2.87 (t, *J* = 13.17 Hz, 1H), 2.48-2.37 (m, 2H), 2.26-2.29 (m, 1H); MS (MALDI-TOF): m/z 747 $[M-(H_2O)-(PF_6)_2]^+$, 765 $[M-(PF_6)_2]^+$. Anal. Calcd for $C_{43}H_{33}N_7OP_2F_{12}Ru$: C, 48.96; H, 3.13; N, 9.30. Found: C, 48.94; H, 3.11; N, 8.83.

$[Ru(76a)(bpy)_2](PF_6)_2$ (81a, RSH-360):

A mixture of **76a** (20 mg, 0.056 mmol), $[Ru(bpy)_2Cl_2]\cdot 2H_2O$ (**80**, 30 mg, 0.056 mmol) and ethylene glycol (6 mL) was irradiated in the MW oven for 10 min. The reaction mixture was cooled to rt, then NH_4PF_6 (140 mg, 0.78 mmol) in water (3 mL) was added. The solution was stirred for 30 min. The green precipitate was collected by filtration, washed with water, dried under vacuum and purified by chromatography on alumina eluting with CH_2Cl_2/acetone (1:1) to give **81a** as a green solid (35 mg, 60%): ^{1}H NMR (acetone-*d*6, 400 MHz) δ 9.38 (s, 1H), 9.16 (d, *J* = 8.70 Hz, 1H), 9.07 (d, *J* = 8.70 Hz, 1H), 8.75 (d, *J* = 7.79 Hz, 1H), 8.68 (d, *J* = 7.79 Hz, 1H), 8.23-8.19 (m, 3H), 8.05-8.03 (m, 2H), 7.79 (dt, *J* = 8.24, 1.27 Hz, 1H), 7.69 (dt, *J* = 7.79, 0.93 Hz, 1H), 7.64 (dt, *J* = 7.33, 1.37 Hz, 1H), 7.33-7.31 (m, 2H); MS (MALDI-TOF): m/z 916 $[M-(PF_6)]^+$, 772 $[M-(PF_6)_2]^+$, 615 $[M-(bpy)-(PF_6)_2]^+$. Anal. Calcd for $C_{44}H_{30}N_8P_2F_{12}Ru\cdot 1.0\ H_2O$: C, 48.90; H, 2.78; N, 10.37. Found: C, 48.85; H, 2.60; N, 10.09.

[Ru(76b)(bpy)$_2$](PF$_6$)$_2$ (81b, RSH-491):

Compound **81b** was synthesized by following the same procedure as for **81a**, using **76b** (22 mg, 0.06 mmol), **80** (30 mg, 0.06 mmol), ethylene glycol (6 mL) and NH_4PF_6 (140 mg, 0.78 mmol) in H_2O (3 mL) to afford **81b** as a green solid (30 mg, 50%): ^{1}H NMR (acetone-*d*6, 500 MHz) δ 9.28 (s, 1H), 8.81 (s, 1H), 8.77 (d, *J* = 8.02 Hz, 1H), 8.68 (d, *J* = 8.59 Hz, 1H), 8.24-8.17 (m, 3H), 8.06-8.01 (m, 2H), 7.77 (dt, *J* = 8.02, 1.15 Hz, 1H), 7.67-7.62 (m, 2H), 7.32 (dt, *J* = 7.45, 1.15 Hz, 1H), 7.21 (dd, *J* = 8.59, 1.15 Hz, 1H), 3.71 (dd, *J* = 5.15, 2.93 Hz, 2H); MS (MALDI-TOF): m/z 946 [M-(PF$_6$)]$^+$, 800 [M-(PF$_6$)$_2$]$^+$, 642 [M-(bpy)-(PF$_6$)$_2$], 490 [M-(bpy)$_2$-(PF$_6$)$_2$]. Anal. Calcd for $C_{46}H_{32}N_8P_2F_{12}Ru$·0.5 PF_6: C, 47.57; H, 2.76; N, 9.65. Found: C, 47.50; H, 2.87; N, 8.90.

[Ru(76c)(bpy)$_2$](PF$_6$)$_2$ (81c, RSH-383):

Compound **81c** was synthesized by following the same procedure as for **81a**, using **76c** (20 mg, 0.05 mmol), **80** (26 mg, 0.05 mmol), ethylene glycol (6 mL) and NH_4PF_6 (140 mg, 0.78 mmol) in H_2O (3 mL) to afford **81c** as a green solid (30 mg, 54%): ^{1}H NMR (acetone-*d*6, 400 MHz) δ 9.26 (s, 1H), 8.76 (s, 1H), 8.63 (d, *J* = 7.79 Hz, 1H), 8.56 (d, *J* = 8.24 Hz, 1H), 8.41 (d, *J* = 5.50 Hz, 1H), 8.20-8.13 (m, 3H), 8.01 (dt, *J* = 7.79, 1.37 Hz, 1H), 7.77 (dt, *J* = 8.24, 1.37 Hz, 1H), 7.68-7.60 (m, 2H), 7.35 (dt, *J* = 7.33, 1.37 Hz, 1H), 7.16 (d, *J* = 8.70 Hz, 1H), 3.33-3.17 (m, 2H), 2.68-2.60 (m, 1H); MS (MALDI-TOF): m/z 957 [M-(PF$_6$)]$^+$, 812 [M-(PF$_6$)$_2$]$^+$, 656 [M-(bpy)-(PF$_6$)$_2$]$^+$; Anal. Calcd for $C_{47}H_{34}F_{12}N_8P_2Ru$: C, 51.23; H, 3.09; N, 10.17. Found: C, 51.49; H, 3.18; N, 9.88.

[Ru(76d)(bpy)$_2$](PF$_6$)$_2$ (81d, RSH-364):

Compound **81d** was synthesized by following the same procedure as for **81a**, using **76d** (50 mg, 0.1 mmol), **80** (62 mg, 0.1 mmol), ethylene glycol (6 mL) and NH_4PF_6 (140 mg, 0.78 mmol) in H_2O (3 mL) to afford **81d** as a green solid (66 mg, 50%): ^{1}H NMR (acetone-*d*6, 500 MHz) δ 9.29 (s, 1H), 8.85 (d, *J* = 6.30 Hz, 1H), 8.85 (s, 1H), 8.65 (d, *J* = 8.59 Hz, 1H), 8.59 (d, *J* = 8.02 Hz, 1H), 8.27 (d, *J* = 5.15 Hz, 1H), 8.22 (d, *J* = 8.59 Hz, 1H), 8.17 (dt, *J* = 8.02, 1.15 Hz, 1H), 8.04 (dt, *J* = 8.02, 1.15 Hz, 1H), 7.81 (dt, *J* = 8.02, 1.15 Hz, 1H), 7.68 (t, *J* = 7.45 Hz, 2H), 7.40 (t, *J* = 6.30 Hz, 1H), 7.13 (d, *J* = 8.59 Hz, 1H), 3.25-3.21 (m, 1H), 2.98 (t, *J* = 12.03 Hz, 1H), 2.41 (t, *J* = 8.02 Hz, 1H), 2.13-2.10 (m, 1H); MS (MALDI-TOF): m/z 971 [M-(PF_6)]$^+$, 826 [M-(PF_6)$_2$]$^+$, 670 [M-(bpy)-(PF_6)$_2$]$^+$. Anal. Calcd for $C_{43}H_{33}N_7OP_2F_{12}Ru$: C, 51.66; H, 3.23; N, 10.05. Found: C, 51.57; H, 3.35; N, 9.57.

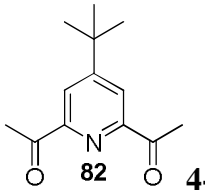

82

4-*t*-Butyl-2,6-diacetylpyridine (82, RSH-496):[223]

Compound **82** was synthesized by following the same procedure as for **47**, using 4-*t*-butyl-pyridine (**54b**, 5 g, 0.04 mol), pyruvic acid (**46**, 13 g, 0.15 mol), $AgNO_3$ (0.5 g, 3 mmol), $NH_4S_2O_8$ (30 g, 0.15 mol), H_2SO_4 (3 mL), H_2O (50 mL) and CH_2Cl_2 (50 mL) to give **82** as a white solid (3.3 g, 40 %): mp 44-45 ^{o}C; ^{1}H NMR ($CDCl_3$, 500 MHz) δ 8.21 (s, 2H), 2.78 (s, 6H), 1.35 (s, 9H); ^{13}C NMR ($CDCl_3$, 125 MHz) δ 200.1, 162.8, 152.9, 121.9, 35.5, 30.6, 25.8.

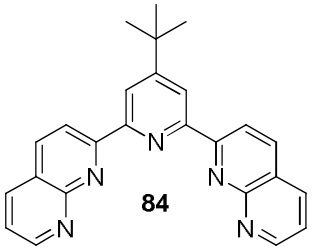

84

2,6-Di(1',8'-naphthyrid-2'-yl)-4-*t*-butylpyridine (84):[44]

A mixture of 2-aminonicotinaldehyde[214] (**83**, 0.26 g, 2.1 mmol), 4-*t*-butyl-2,6-diacetylpyridine (**82**, 2.25 g, 1.02 mmol) and KOH (0.05 g) in EtOH (25 mL) was refluxed at 95 °C for 6h under Ar and kept at room temperature overnight. Light yellow needles (100 mg) were collected and washed with absolute EtOH. The filtrate was concentrated to about 3 mL and cooled in a refrigerator. The precipitate was collected and washed with absolute EtOH (5 mL) to afford **84** as a light yellow powder (213 mg) for a total yield of 313 mg (87%), mp > 270 °C: ^{1}H NMR ($CDCl_3$, 500 MHz) δ 9.19 (dd, *J* = 3.72, 1.72 Hz, 2H), 9.02 (d, *J* = 8.59 Hz, 2H), 9.00 (s, 2H), 8.38 (d, *J* = 8.38 Hz, 2H), 8.28 (dd, *J* = 8.02, 1.72 Hz, 2H), 7.54 (dd, *J* = 8.02, 4.58 Hz, 2H), 1.53 (s, 9H); ^{13}C NMR ($CDCl_3$, 125 MHz) δ 162.4, 156.4, 155.6, 155.2, 153.0, 138.3, 135.2, 124.2, 121.6, 119.6, 117.6, 34.8, 31.3.

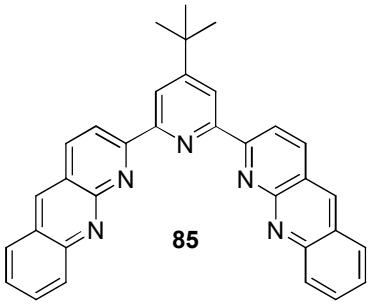

85

2,6-Di(4'-azaacrid-3'-yl)-4-*t*-butylpyridine (85, RSH-193):

A mixture of 2-aminoquinoline-3-carbaldehyde (**74**, 0.1 g, 600 mmol), 4-*t*-butyl-2,6-diacetylpyridine (**82**, 0.06 g, 300 mmol) and KOH (10 mg) in EtOH (10 mL) was refluxed at 95 °C overnight under Ar. The reaction mixture was cooled to rt and concentrated to produce a yellow precipitate which was filtered. The solid was washed with EtOH and dried to afford **85** as a yellow solid (0.13 g, 90%), mp > 290 ^{o}C: ^{1}H NMR ($CDCl_3$, 400 MHz) δ 9.13 (s, 2H), 9.05 (d, *J* = 8.70 Hz, 2H), 8.89 (s, 2H), 8.56 (d, *J* = 9.16 Hz, 2H), 8.45 (d, *J* = 9.62 Hz, 2H), 8.08 (d, *J* = 7.79 Hz, 2H), 7.89 (dt, *J* = 8.24, 1.72 Hz, 2H), 7.63 (t, *J* = 7.33 Hz, 2H), 1.58 (s, 9H); ^{13}C NMR ($CDCl_3$, 100 MHz) δ 162.4, 159.7, 155.3, 145.7, 136.8, 135.2, 133.2, 131.8, 130.0, 129.0, 127.1, 124.2, 121.0, 118.1, 115.6, 35.1, 31.3; MS (MALDI-TOF): m/z 493 $[M+2]^+$; Anal. Calcd. for $C_{33}H_{25}N_5 \cdot 1.2$ KOH: C, 70.92; H, 4.72; N, 12.53. Found: C, 71.09; H, 4.38; N, 12.27.

[Ru(85)(tpy)]$(PF_6)_2$ (86, RSH-282):

To a suspension of [Ru(tpy)Cl_3] (**77**, 22 mg, 0.05 mmol) and **85** (25 mg, 0.05 mmol) in 2-methoxyethanol (16 mL), Et_3N (10 μL) was added at rt. The resultant mixture was heated to reflux for 2 h under Ar. After cooling to rt, the deep purple solution was filtered and

the filtrate was concentrated to 3 mL under reduced pressure at 50 ºC. Then NH_4PF_6 (90 mg, 0.56 mmol) in a minimum amount of water was added and cooled to rt. The purple precipitate was collected by filtration, washed with water, dried under vacuum, and purified by chromatography on alumina eluting with CH_2Cl_2/acetone (1:1) to give **86** as a purple solid (22 mg, 40%): ^{1}H NMR (acetone-*d*6, 400 MHz) δ 9.61 (s, 2H), 9.35 (d, *J* = 8.02 Hz, 2H), 9.23 (d, *J* = 8.59 Hz, 2H), 9.16 (t, *J* = 8.02 Hz, 1H), 9.14 (s, 2H), 8.88 (d, *J* = 8.59 Hz, 2H), 8.61 (d, *J* = 8.02 Hz, 2H), 8.11 (d, *J* = 8.59 Hz, 2H), 7.95 (dt, *J* = 8.02, 1.15 Hz, 2H), 7.73 (dt, *J* = 9.16, 1.15 Hz, 2H), 7.71 (dt, *J* = 8.02, 1.15 Hz, 2H), 7.64 (d, *J* = 5.73 Hz, 2H), 7.45 (d, *J* = 9.16 Hz, 2H), 7.05 (dt, *J* = 6.87, 1.15 Hz, 2H), 1.88 (s, 9H); MS (MALDI-TOF): m/z 826 $[M\text{-}2PF_6]^+$; Anal. Calcd. for $C_{48}H_{36}N_8F_{12}P_2Ru$: C, 51.66; H, 3.23; N, 10.04. Found: C, 52.08; H, 3.63; N, 8.92.

[Ru(85)(bpy)Cl](PF$_6$) (90, RSH-456):

A mixture of **85** (50 mg, 0.1 mmol), [Ru(bpy)$(DMSO)_2Cl_2$] (**89**, 50 mg, 0.1 mmol), EtOH (10 mL), H_2O (4 mL) and Et_3N (20 µL) was heated to reflux for 24 h under Ar. After cooling to rt, the green solution was filtered and the filtrate was concentrated to 3 mL under reduced pressure at 50 ºC. Then NH_4PF_6 (40 mg, 0.24 mmol) in a minimum amount of water was added and cooled to rt. The green precipitate was collected by filtration, washed with water, dried under vacuum, and purified by chromatography on alumina eluting with CH_2Cl_2/acetone (1:1) to give **90** as a green solid (35 mg, 35%): ^{1}H NMR (acetone-*d*6, 500 MHz) δ 10.71 (d, *J* = 5.73 Hz, 1H), 9.27 (s, 2H), 9.15 (d, *J* = 8.02 Hz, 1H), 9.11 (s, 2H), 8.99 (d, *J* = 8.59 Hz, 2H), 8.86 (dt, *J* = 8.02, 1.72 Hz, 1H), 8.78 (d, *J* = 9.16 Hz, 2H), 8.41 (d, *J* = 8.02 Hz, 1H), 8.16 (d, *J* = 7.45 Hz, 1H), 8.11 (d, *J* = 8.59

Hz, 2H), 7.85 (dt, *J* = 8.02, 1.15 Hz, 2H), 7.65 (t, *J* = 6.87 Hz, 2H), 7.57 (d, *J* = 5.73 Hz, 1H), 7.49 (dt, *J* = 8.02, 1.72 Hz, 1H), 7.19 (d, *J* = 9.16 Hz, 2H), 6.81 (dt, *J* = 7.45, 1.15 Hz, 1H), 1.78 (s, 9H); MS (MALDI-TOF): m/z 784 $[M\text{-}PF_6]^+$; Anal. Calcd. for $C_{43}H_{33}N_7ClF_6PRu\cdot 1.0$ acetone: C, 55.90; H, 3.95; N, 9.82. Found: C, 55.85; H, 3.99; N, 9.18.

[Ru(85)(bpy)(H_2O)](PF_6)$_2$ (92, RSH-458):

To the mixture of **90** (40 mg, 0.04 mmol) in acetone (10 mL), $AgBF_4$ (87 mg, 0.4 mmol) in H_2O (5 mL) was added. The reaction mixture was heated at reflux for 5 h under Ar. The hot solution was filtered through celite and concentrated to 5 mL under reduced pressure at 50 ºC. Then NH_4PF_6 (20 mg, 0.12 mmol) in a minimum amount of water was added, and cooled to rt. The blue precipitate was collected by filtration, washed with water, dried under vacuum, and purified by chromatography on SiO_2 eluting with acetone to give **92** as a blue solid (30 mg, 70%): ^{1}H NMR (acetone-*d*6, 500 MHz) δ 10.26 (d, *J* = 5.15 Hz, 1H), 9.41 (s, 2H), 9.23 (s, 2H), 9.14 (d, *J* = 9.16 Hz, 3H), 8.97 (t, *J* = 4.01 Hz, 1H), 8.95 (d, *J* = 9.16 Hz, 2H), 8.44 (t, *J* = 5.73 Hz, 1H), 8.41 (d, *J* = 8.59 Hz, 1H), 8.17 (d, *J* = 8.59 Hz, 2H), 7.93 (dt, *J* = 10.31, 1.72 Hz, 2H), 7.72 (t, *J* = 8.02 Hz, 2H), 7.64 (d, *J* = 6.30 Hz, 1H), 7.54 (t, *J* = 6.87 Hz, 1H), 7.25 (d, *J* = 8.59 Hz, 2H), 6.88 (t, *J* = 6.30 Hz, 1H), 5.80 (br s, H_2O), 1.79 (s, 9H); MS (MALDI-TOF): m/z 766 $[M\text{-}2(PF_6)]^+$, 749 $[M\text{-}2(PF_6)\text{-}(H_2O)]^+$, 593 $[M\text{-}2(PF_6)\text{-}(H_2O)\text{-}(bpy)]^+$. Anal. Calcd. for $C_{43}H_{35}N_7OF_{12}P_2Ru\cdot 0.5\ PF_6$: C, 45.69; H, 3.10; N, 8.68. Found: C, 45.60; H, 2.90; N, 8.50.

[Ru(85)(4-pic)$_2$(H$_2$O)](PF$_6$)$_2$ (94, RSH-406):

A mixture of **85** (60 mg, 0.12 mmol), EtOH (10 mL), and an ethanolic solution (5 mL) of $RuCl_3 \cdot 3H_2O$ (34 mg, 0.13 mmol) was heated to reflux. The reaction continued for 3 h, then 4-picoline (**54a**, 0.3 mL, 0.26 mmol), Et_3N (20 µL), and H_2O (4 mL) were added. The color of the mixture changed from brown to green. The mixture was refluxed overnight under Ar. After cooling to rt, the green solution was filtered and the filtrate was concentrated to 5 mL under reduced pressure at 50 ºC. Then NH_4PF_6 (40 mg, 0.24 mmol) in a minimum amount of water was added, and the mixture was cooled to rt. The green precipitate was collected by filtration, washed with water, dried under vacuum, and purified by chromatography on alumina eluting with CH_2Cl_2/acetone (1:1) to give **94** as a blue solid (70 mg, 50%): ^{1}H NMR (acetone-*d*6, 400 MHz) δ 10.39 (s, H_2O), 9.62 (s, 2H), 9.29 (s, 2H), 9.15 (dd, *J* = 17.86, 9.16 Hz, 4H), 8.79 (d, *J* = 9.16 Hz, 2H), 8.44 (d, *J* = 8.24 Hz, 2H), 8.26 (dt, *J* = 10.07, 1.37 Hz, 2H), 7.97 (dd, *J* = 6.87, 3.43 Hz, 4H), 7.93 (t, *J* = 8.24 Hz, 2H), 6.70 (d, *J* = 6.41 Hz, 4H), 1.96 (s, 6H), 1.68 (s, 9H); MS (MALDI-TOF): m/z 1086 $[M]^+$, 1084 $[M\text{-}2]^+$, 593 $[M\text{-}2(4\text{-pic})\text{-}(H_2O)\text{-}2(PF_6)]^+$; Anal. Calcd. for $C_{45}H_{41}N_7OF_{12}P_2Ru$: C, 49.72; H, 3.77; N, 9.02. Found: C, 49.10; H, 3.77; N, 8.71.

[Ru(84)(tpy)](PF$_6$)$_2$ (87, RSH-448):

Compound **87** was synthesized by following the same procedure as for **86**, using [Ru(tpy)Cl_3] (**77**, 44 mg, 0.1 mmol), **84** (40 mg, 0.1 mmol), 2-methoxyethanol (30 mL), Et_3N (10 µL) and NH_4PF_6 (90 mg, 0.56 mmol) to afford **87** as a purple solid (50 mg, 50%): ^{1}H NMR (acetone-*d*6, 500 MHz) δ 9.48 (s, 2H), 9.21 (d, *J* = 8.59 Hz, 2H), 9.02 (d,

J = 8.02 Hz, 2H), 8.70 (d, *J* = 8.59 Hz, 2H), 8.65 (t, *J* = 8.59 Hz, 1H), 8.58 (d, *J* = 8.02 Hz, 2H), 8.40 (dd, *J* = 8.02, 1.72 Hz, 2H), 8.37 (dd, *J* = 4.58, 2.29 Hz, 2H), 7.81 (dt, *J* = 7.45, 1.15 Hz, 2H), 7.56-7.54 (m, 4H), 7.04 (dt, *J* = 7.45, 1.72 Hz, 2H), 1.80 (s, 9H); MS (MALDI-TOF): m/z 870 $[M-(PF_6)]^+$, 726 $[M-2(PF_6)]^+$, 493 $[M-2(PF_6)-(tpy)]^+$; Anal. Calcd. for $C_{43}H_{33}N_7ClF_6PRu \cdot 0.5\ KPF_6$: C, 43.36; H, 3.07; N, 10.12. Found: C, 43.35; H, 3.18; N, 9.04.

[Ru(84)(bpy)Cl](PF$_6$) (91, RSH-447):

Compound **91** was synthesized by following the same procedure as for **90**, using **84** (40 mg, 0.1 mmol), $[Ru(bpy)(DMSO)_2Cl_2]$ (**89**, 50 mg, 0.1 mmol), EtOH (10 mL), H_2O (4 mL), Et_3N (20 µL) and NH_4PF_6 (40 mg, 0.24 mmol) to afford **91** as a deep blue solid (30 mg, 36%): ^{1}H NMR (acetone-*d*6, 500 MHz) δ 10.48 (d, *J* = 5.73 Hz, 1H), 9.14 (s, 2H), 8.99 (d, *J* = 8.59 Hz, 2H), 8.78 (d, *J* = 8.02 Hz, 1H), 8.60 (d, *J* = 8.59 Hz, 2H), 8.38-8.35 (m, 2H), 8.40 (dd, *J* = 8.02, 1.72 Hz, 2H), 8.22 (dd, *J* = 4.01, 1.72 Hz, 2H), 7.88 (dt, *J* = 7.16, 1.15 Hz, 1H), 7.57-7.51 (m, 4H), 6.81 (dt, *J* = 6.87, 1.15 Hz, 1H), 1.73 (s, 9H); MS (MALDI-TOF): m/z 684 $[M-(PF_6)]^+$; Anal. Calcd. for $C_{35}H_{29}N_7ClPF_6Ru$: C, 50.66; H, 3.50; N, 11.87. Found: C, 50.87; H, 3.38; N, 11.12.

[Ru(84)(bpy)(H$_2$O)](PF$_6$)$_2$ (93, RSH-459):

Compound **93** was synthesized by following the same procedure as for **92**, using **91** (23 mg, 0.03 mmol) in acetone (15 mL), $AgBF_4$ (0.06 g, 0.3 mmol) in H_2O (5 mL) and NH_4PF_6 (40 mg, 0.24 mmol) to afford **93** as a purple solid (28 mg, 90%): ^{1}H NMR (acetone-*d*6, 500 MHz) δ 9.96 (d, *J* = 4.58 Hz, 1H), 9.24 (s, 2H), 9.09 (d, *J* = 8.59 Hz,

2H), 8.79 (d, *J* = 4.58 Hz, 1H), 8.72 (d, *J* = 8.59 Hz, 2H), 8.45 (dd, *J* = 8.02, 1.72 Hz, 2H), 8.35 (d, *J* = 8.02 Hz, 1H), 8.31 (d, *J* = 4.01, 1.72 Hz, 2H), 8.07 (dt, *J* = 7.45, 1.15 Hz, 1H), 7.59 (dd, *J* = 8.02, 4.58 Hz, 2H), 7.57 (dt, *J* = 8.02, 1.15 Hz, 1H), 7.50 (d, *J* = 5.73 Hz, 1H), 6.86 (dt, *J* = 7.45, 1.15 Hz, 1H), 5.64 (br s, H_2O), 1.72 (s, 9H); MS (MALDI-TOF): m/z 837 $[M\text{-}2(PF_6)\text{-}(H_2O)+matrix]^+$, 668 $[M\text{-}2(PF_6)+1]^+$, 837 $[M\text{-}2(PF_6)\text{-}(H_2O)]^+$, 492 $[M\text{-}2(PF_6)\text{-}(H_2O)\text{-}(bpy)]^+$. Anal. Calcd. for $C_{35}H_{31}N_7OF_{12}P_2Ru{\cdot}0.5\ PF_6$: C, 40.81; H, 3.01; N, 9.52. Found: C, 40.86; H, 2.99; N, 9.15.

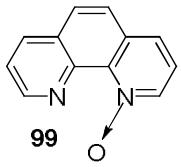

99

1,10-Phenanthroline-1-oxide (99, RSH-281)[227]

To a solution of 1,l0-phenanthroline monohydrate (**98**, 9.4 g, 0.05 mol) in glacial acetic acid (60 mL), 30% hydrogen peroxide (6 mL) was added. The temperature of the solution was maintained at 72-75 ^oC for 3 h after which an additional 6 mL of 30% hydrogen peroxide was added. Heating was continued for 3 h. The solution was concentrated to a volume of ~25 mL in vacuum, then 50 mL of water was added and evaporation in vacuum was continued to a volume of ~10 mL. The mixture was neutralized with a Na_2CO_3. The solid mass was extracted 7 x 25 mL portions of $CHCl_3$. The combined $CHCl_3$ extracts were stirred for 1 h with decolorizing charcoal and $MgSO_4$. After filtration and evaporation 1,10-phenanthroline-1-oxide (**99**) was obtained as a black-green solid (8.3 g, 85%): mp 180-184 ^oC (lit.[227] 178-180 ^oC).; ^1H NMR ($CDCl_3$, 400 MHz) δ 9.27 (dd, *J* = 4.5 Hz, 1.8 Hz, 1H), 8.64 (dd, *J* = 6.3 Hz, 1.5 Hz, 1H), 8.29 (dd, *J* = 8.3 Hz, 2.0 Hz, 1H), 7.82 (q, *J* = 25 Hz, 9.0 Hz, 2H), 7.76 (dd, *J* = 8.0 Hz, 1.4 Hz, 1H),

7.69 (dd, J = 8.3 Hz, 4.5 Hz, 1H), 7.47 (dd, J = 8.2 Hz, 4.5 Hz, 1H); ^{13}C NMR ($CDCl_3$, 100 MHz) δ 149.9, 148.1, 136.4, 135.4, 129.2, 128.6, 128.3, 127.0, 125.7, 126.9, 121.5, 121.0.

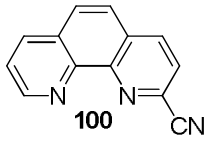

100 **2-Cyano-1,10-phenanthroline** (**100**)

To a solution of 1,10-phenanthroline-1-oxide (**99**, 2.5 g, 0.013 mol) and KCN (2.5 g, 0.038 mol) in H_2O (40 mL), benzoyl chloride (4 mL) was added dropwise under magnetic stirring. The total addition required 1 h, and the reaction mixture was stirred for an additional 2 h. The resulting precipitate was collected by suction filtration, washed with water, and dried as a brown solid to afford **100** as a white solid (2.3 g, 87%); mp 230-232 °C (lit.[227] 233-234 °C); ^{1}H NMR ($CDCl_3$, 400 MHz) δ 9.29 (dd, J = 4.5, 1.8 Hz, 1H), 8.41 (d, J = 8.2 Hz, 1H), 8.32 (dd, J = 7.8, 1.4 Hz, 1H), 7.98 (d, J = 6.8 Hz, 1H), 7.96 (d, J = 7.3 Hz, 1H), 7.85 (d, J = 8.7 Hz, 1H), 7.74 (dd, J = 8.2, 4.5 Hz, 1H); ^{13}C NMR ($CDCl_3$, 100 MHz) δ 155.7, 149.9, 137.4, 136.4, 135.2, 133.3, 129.8, 128.6, 128.3, 127.0, 123.3, 121.5, 117.1; IR (ATR) v 2218 cm^{-1}.

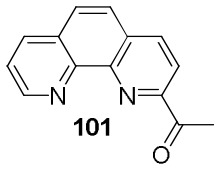

101 **2-Acetyl-1,10-phenanthroline (101, RSH-279)**

To a suspension of 2-cyano-1,10-phenanthroline (**100**, 2.6 g, 12 mmol) in dry THF (50 mL) was added dropwise a solution of CH_3MgBr (3M in Et_2O) (11 mL, 33 mol) in THF

(20 mL) at -78 °C. The reaction mixture was further stirred for 30 min at -78 °C and 1 h at rt. An aq saturated solution of NH_4Cl (50 mL) was added slowly to the mixture. The organic phase was separated. The aq phase was extracted with CH_2Cl_2 3 x 15 mL. Combined organic phases were concentrated, washed with brine (30 mL). The solvent was dried over $MgSO_4$ and evaporated under vacuum. The residue was purified by chromatography on alumina eluting with CH_2Cl_2/Et_2O (10:1) to afford **101** as a white solid (1.7 g, 60%): mp 152-154 °C; ^{1}H NMR ($CDCl_3$, 400 MHz) δ 9.26 (dd, *J* = 4.5, 1.5 Hz, 1H), 8.37 (s, 2H), 8.30 (dd, *J* = 8.4, 1.5 Hz, 1H), 7.80 (AB, 2H), 7.70 (dd, *J* = 8.4, 4.5 Hz, 1H), 3.08 (s, 3H); ^{13}C NMR ($CDCl_3$, 100 MHz) δ 197.7, 158.3, 155.7, 149.8, 136.4, 136.6, 135.2, 129.8, 128.6, 128.3, 127.0, 121.5, 119.4, 27.7; IR (ATR) *v* 1640 cm^{-1}.

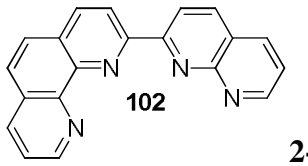

102

2-(1',10'-Phenanthrolin-2'-yl)1,8-naphthyridine (102, RSH-260)

A mixture of 2-acetyl-1,10-phenanthroline (**101**, 0.1 g, 0.4 mmol), 2-aminonicotinaldehyde (**83**, 0.05g, 0.4 mmol), EtOH (10 mL) and KOH (3 mg) was heated at reflux overnight under Ar. The mixture was cooled to rt, concentrated, and extracted with CH_2Cl_2 (3 x 15 mL). The extracts were combined, washed with brine, dried over $MgSO_4$ and the solvent was evaporated. The crude product was purified by chromatography on alumina eluting with CH_2Cl_2/acetone (30:25) to afford **102** as a yellow solid (0.1 g, 83%): mp 250-252 °C; ^{1}H NMR ($CDCl_3$, 400 MHz) δ 9.36 (d, *J* = 8.1 Hz, 1H), 9.30-9.26 (m, 2H), 9.18 (dd, *J* = 4.2, 1.5 Hz, 1H), 8.46 (d, *J* = 8.1 Hz, 1H),

8.42 (d, *J* = 9.0 Hz, 1H), 8.29 (m, 2H), 7.87 (AB, 2H), 7.68 (dd, *J* = 8.1, 3.9 Hz, 1H), 7.53 (dd, *J* = 8.1, 3.9 Hz, 1H); ^{13}C NMR ($CDCl_3$, 100 MHz) δ 158.7, 155.27, 154.8, 153.3, 149.9, 145.7, 144.9, 137.4, 136.7, 136.6, 135.8, 128.8, 128.5, 126.8, 126.1, 122.8, 122.6, 121.8, 121.4, 121.1; MS (MALDI-TOF): m/z 310 $[M+2]^+$.

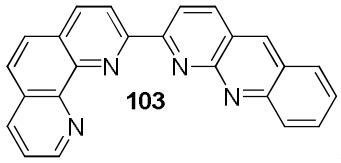

3-(1',10'-Phenanthrolin-2'-yl)4-azaacridine (103, RSH-259)

Compound **103** was synthesized by following the same procedure as for **102**, using 2-acetyl-1,10-phenanthroline (**101**, 0.1 g, 0.4 mmol), 2-aminoquinoline-3-carbaldehyde (**74**, 0.08g, 0.4 mmol), EtOH (10 mL) and KOH (3 mg) to afford **103** as a yellow solid (0.1 g, 65%): mp 260-262 °C; ^{1}H NMR ($CDCl_3$, 400 MHz) δ 9.42 (d, *J* = 8.24 Hz, 1H), 9.37 (d, *J* = 8.70 Hz, 1H), 9.29 (dd, *J* = 4.12, 1.37 Hz, 1H), 8.89 (s, 1H), 8.60 (d, *J* = 8.70 Hz, 1H), 8.49 (d, *J* = 8.70 Hz, 1H), 8.44 (d, *J* = 8.70 Hz, 1H), 8.32 (dd, *J* = 8.24, 1.83 Hz, 1H), 8.07 (d, *J* = 8.70 Hz, 1H), 7.89 (AB, 2H), 7.85 (dd, *J* = 8.24, 1.37 Hz, 1H), 7.70 (dd, *J* = 8.24, 4.58 Hz, 1H), 7.62 (dt, *J* = 7.70, 0.92 Hz, 1H); ^{13}C NMR ($CDCl_3$, 100 MHz) δ 159.7, 155.3, 154.3, 150.0, 149.9, 145.7, 136.8, 136.4, 135.2, 133.2, 131.8, 129.9, 129.8, 128.9, 128.3, 127.0, 126.9, 125.5, 124.2, 137.6, 136.8, 121.5, 120.8, 117.6; MS (MALDI-TOF): m/z 360 $[M+2]^+$.

$[Ru(102)(4\text{-pic})_2(H_2O)](PF_6)_2$ (105, RSH-467)

A mixture of **102** (0.2 g, 0.6 mmol), $[Ru(DMSO)_2Cl_2(4\text{-pic})_2]$ (**104**, 0.32 g, 0.6 mmol), EtOH (10 mL), and H_2O (1 mL) was heated to reflux for 4 h under Ar. After cooling to rt,

the solution was filtered and the filtrate was concentrated to 5 mL under reduced pressure. Then NH_4PF_6 (120 mg, 0.72 mmol) in a minimum amount of water was added. The green precipitate was collected by filtration, washed with water, dried under vacuum, and purified by chromatography on alumina eluting with CH_2Cl_2/acetone (1:1) to give **105** as a green solid (6 mg, 10%): ^{1}H NMR (acetone-*d*6, 500 MHz) δ 9.56 (d, *J* = 5.15 Hz, 1H), 9.46 (dd, *J* = 4.58, 2.45 Hz, 1H), 9.43 (s, br, H_2O), 9.22 (d, *J* = 8.59 Hz, 1H), 9.11 (d, *J* = 8.59 Hz, 1H), 9.00 (d, *J* = 8.59 Hz, 1H), 8.89 (dd, *J* = 8.59, 1.72 Hz, 1H), 8.84 (d, *J* = 7.45 Hz, 1H), 8.69 (d, *J* = 8.59 Hz, 1H), 8.41 (AB, 2H), 8.22 (dd, *J* = 8.02, 5.15 Hz, 1H), 8.08 (dd, *J* = 8.59, 4.58 Hz, 1H), 7.82 (d, *J* = 6.80 Hz, 4H), 6.83 (d, *J* = 6.30 Hz, 4H), 1.24 (s, 6H); MS (MALDI-TOF): m/z 632 $[M\text{-}2(PF_6)\text{-}2(4\text{-pic})]^+$, 410 $[M\text{-}2(PF_6)\text{-}(H_2O)\text{-}2(4\text{-pic})]^+$.

[Ru(102)(bpy)(Cl)](PF$_6$) (106, RSH-332)

A mixture of **102** (0.16 g, 0.5 mmol), $RuCl_3 \cdot 3H_2O$ (0.15 g, 0.6 mmol) in EtOH (20 mL) was heated to reflux. The reaction continued for 3 h, then 2,2'-bipyridine (86 mg, 0.55 mol), Et_3N (20 μL), and H_2O (1 mL) were added. The mixture was refluxed for 3 h under Ar. After cooling to rt, the green solution was filtered and the filtrate was concentrated to 5 mL under reduced pressure at 50 ºC. Then NH_4PF_6 (80 mg, 0.48 mmol) in a minimum amount of water was added, and the mixture was cooled to rt. The green precipitate was collected by filtration, washed with water, dried under vacuum, and purified by chromatography on alumina eluting with CH_2Cl_2/acetone (1:1) to give **106** as a green solid (37 mg, 10 %): ^{1}H NMR (acetone-*d*6, 400 MHz) δ 10.47 (dd, *J* = 5.5, 0.92 Hz, 1H), 9.21 (d, *J* = 58.7 Hz, 1H), 8.93 (d, *J* = 8.7 Hz, 1H), 8.89 (d, *J* = 8.24 Hz, 1H), 8.74 (d, *J* =

8.7 Hz, 1H), 8.65 (d, *J* = 8.7 Hz, 1H), 8.55 (dd, *J* = 8.24, 0.92 Hz, 1H), 8.51 (d, *J* = 7.79 Hz, 1H), 8.47-8.42 (m, 3H), 8.31 (d, *J* = 8.7 Hz, 1H), 8.29 (dd, *J* = 4.1, 1.8 Hz, 1H), 8.12 (dd, *J* = 5.5, 1.4 Hz, 1H), 8.06 (dt, *J* = 5.5, 0.92 Hz, 1H), 7.72 (dd, *J* = 8.2, 5.0 Hz, 1H), 7.65 (dt, *J* = 7.8, 1.4 Hz, 1H), 7.57 (dd, *J* = 8.2, 3.9 Hz, 1H), 7.43 (d, *J* = 5.0 Hz, 1H), 6.83 (dt, *J* = 5.5, 1.4 Hz, 1H); MS (MALDI-TOF): m/z 601 $[M-(PF_6)]^+$, 566 $[M-(PF_6)-(Cl)]^+$.

[Ru(103)(bpy)(Cl)](PF_6) (107, RSH-477)

Compound **107** was synthesized by following the same procedure as for **106**, using **103** (62 mg, 0.17 mmol), $RuCl_3 \cdot 3H_2O$ (0.50 mg, 0.2 mmol) in EtOH (20 mL), 2,2'-bipyridine (30 mg, 0.2 mmol), Et_3N (20 µL), and H_2O (1 mL) and NH_4PF_6 (80 mg, 0.48 mmol) in H_2O (3 mL) to afford **107** as a green solid (27 mg, 20%): ^{1}H NMR (acetone-*d*6, 400 MHz) δ 10.58 (dd, *J* = 4.6, 1.7 Hz, 1H), 9.29 (d, *J* = 8.6 Hz, 1H), 9.14 (s, 1H), 9.07 (d, *J* = 8.6 Hz, 1H), 8.89 (d, *J* = 8.6 Hz, 1H), 8.81 (d, *J* = 8.6 Hz, 1H), 8.77 (d, *J* = 8.6 Hz, 1H), 8.65 (dt, *J* = 8.02, 1.7 Hz, 1H), 8.57-8.53 (m, 2H), 8.45 (d, *J* = 9.2 Hz, 1H), 8.33 (d, *J* = 8.6 Hz, 1H), 8.22 (dt, *J* = 7.5, 1.1 Hz, 1H), 8.12 (d, *J* = 8.02 Hz, 1H), 8.01 (dd, *J* = 5.2, 1.15 Hz, 1H), 7.78 (dt, *J* = 8.02, 1.15 Hz, 1H), 7.73 (dd, *J* = 8.02, 5.2 Hz, 1H), 7.64-7.59 (m, 2H), 7.42 (d, *J* = 5.7 Hz, 1H), 6.93 (d, *J* = 8.6 Hz, 1H), 6.81 (dt, *J* = 7.5, 1.15 Hz, 1H); MS (MALDI-TOF): m/z 651 $[M-(PF_6)]^+$, 616 $[M-(PF_6)-(Cl)]^+$.

APPENDIX

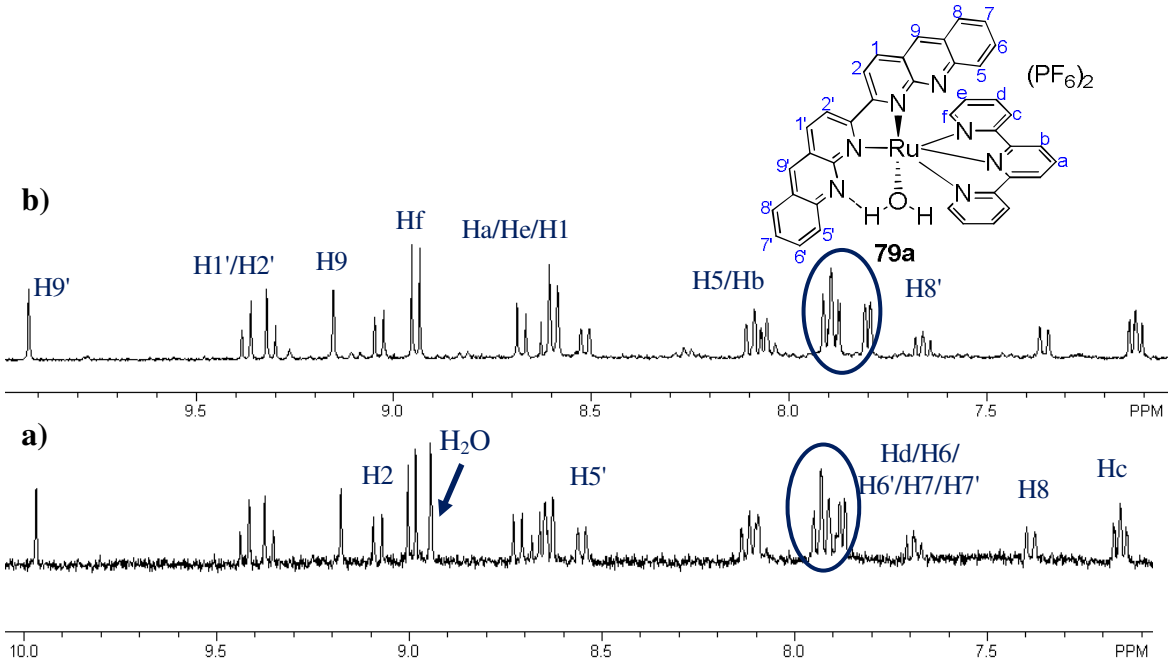

Figure 78. Downfield region of ^{1}H NMR spectrum of **79a** measured a) in acetone-*d6*, b) in acetone-*d6* + 20 µL D_2O (500 MHz, at rt). Addition of D_2O to the NMR sample causes the broad H_2O singlet to disappear and makes a slight change both in resolution and chemical shift which are shown with the circles.

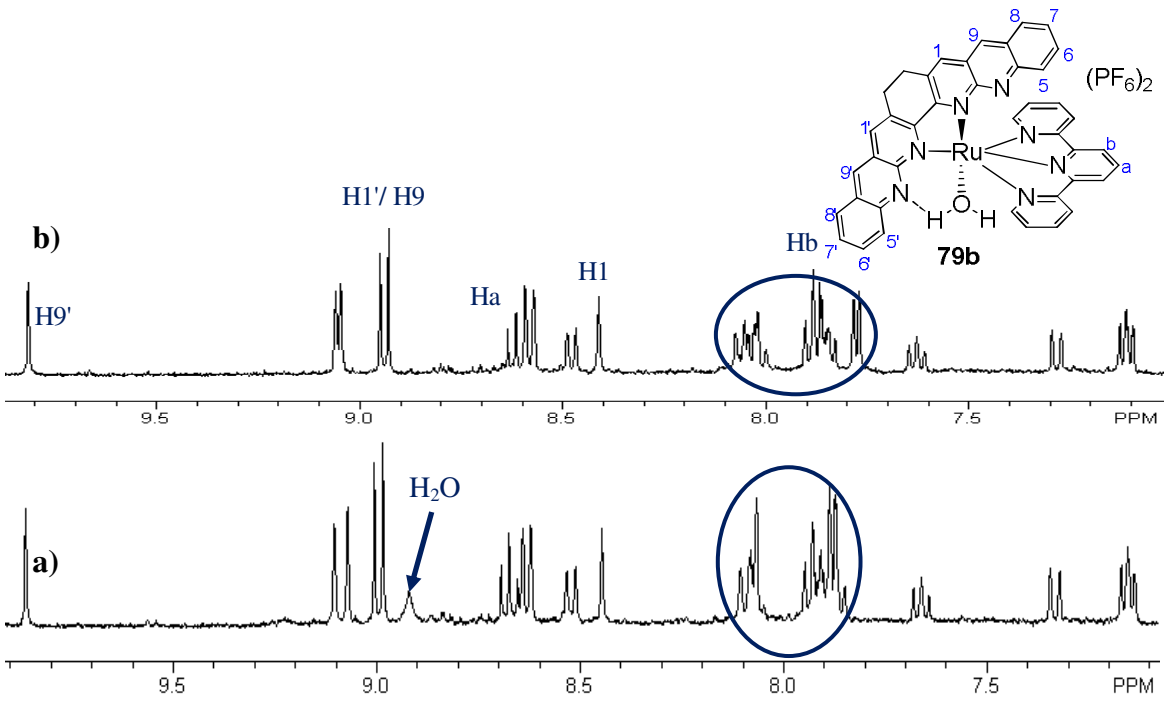

Figure 79. Downfield region of ^{1}H NMR spectrum of **79b** measured a) in acetone-*d6*, b) in acetone-*d6* + 20 µL D_2O (500 MHz, at rt). Addition of D_2O to the NMR sample causes the broad H_2O singlet to disappear and makes a slight change both in resolution and chemical shift which are shown with the circles.

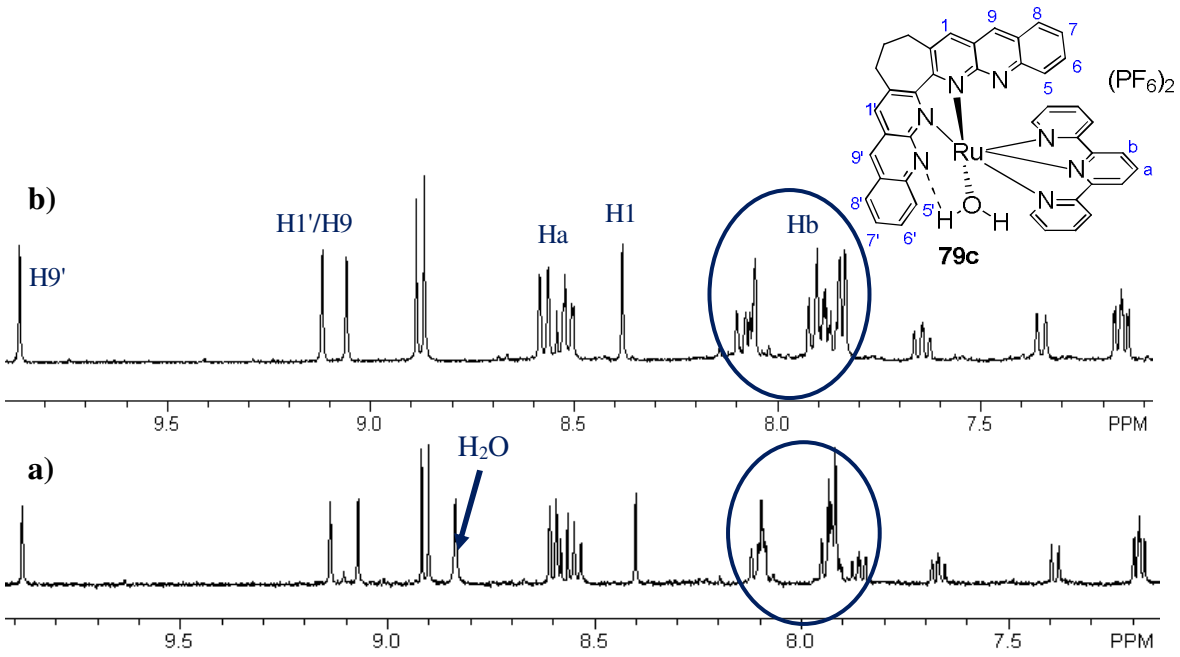

Figure 80. Downfield region of ^{1}H NMR spectrum of **79c** measured a) in acetone-*d6*, b) in acetone-*d6* + 20 µL D_2O (500 MHz, at rt). Addition of D_2O to the NMR sample causes the broad H_2O singlet to disappear and makes a slight change both in resolution and chemical shift which are shown with the circles.

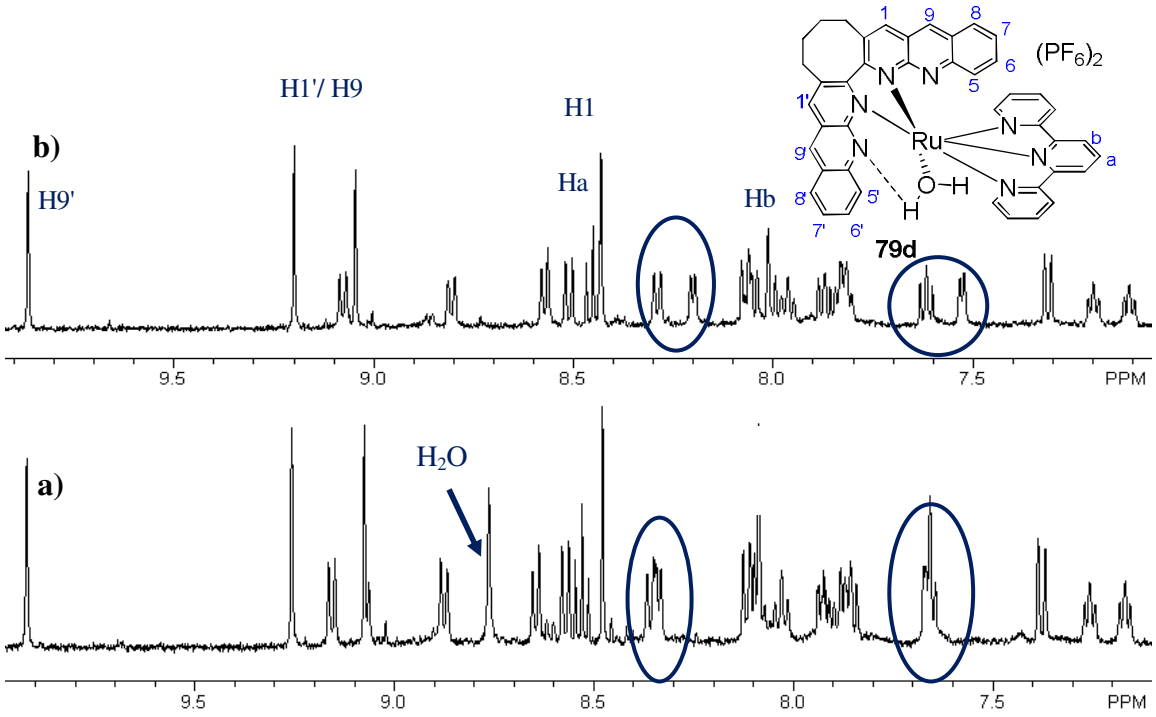

Figure 81. Downfield region of ^{1}H NMR spectrum of **79d** measured a) in acetone-*d6*, b) in acetone-*d6* + 20 µL D_2O (500 MHz, at -20 °C). Addition of D_2O to the NMR sample causes the broad H_2O singlet to disappear and makes a slight change both in resolution and chemical shift which are shown with the circles.

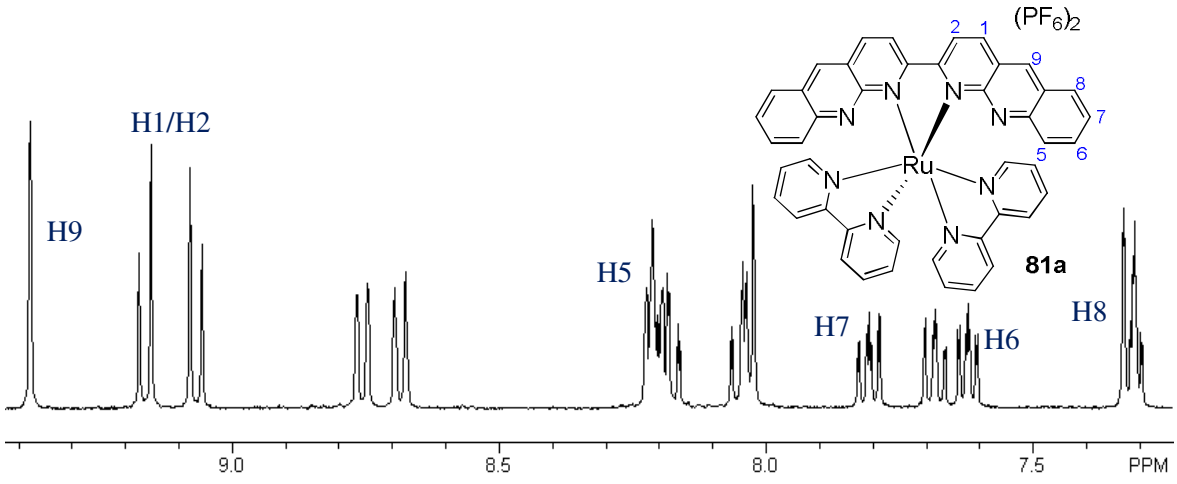

Figure 82. Downfield region of ^{1}H NMR spectrum of **81a** measured in acetone-*d6* (400 MHz, at rt).

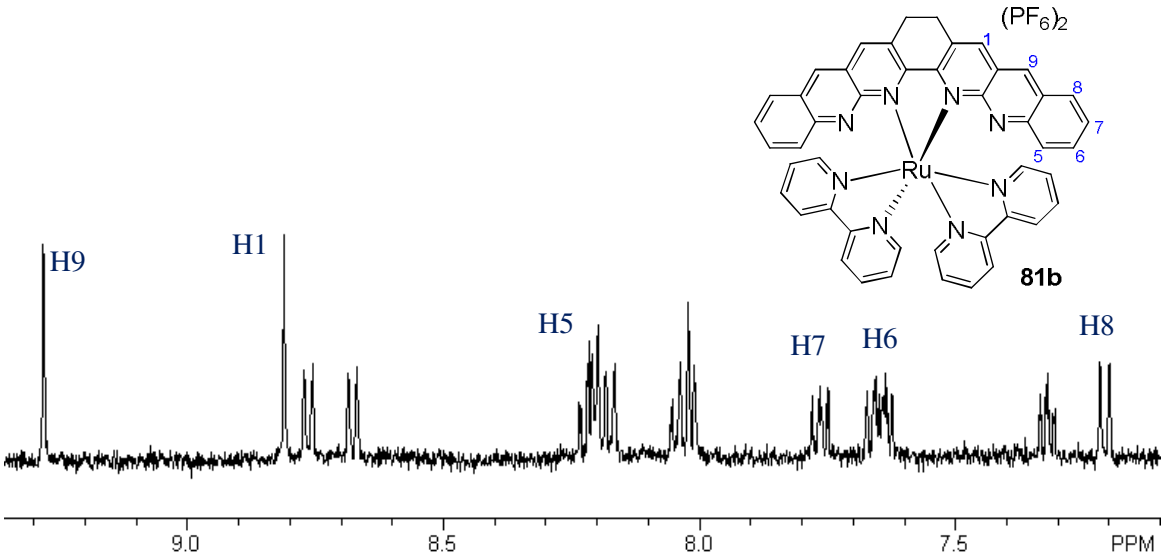

Figure 83. Downfield region of ^{1}H NMR spectrum of **81b** measured in acetone-*d6* (500 MHz, at rt).

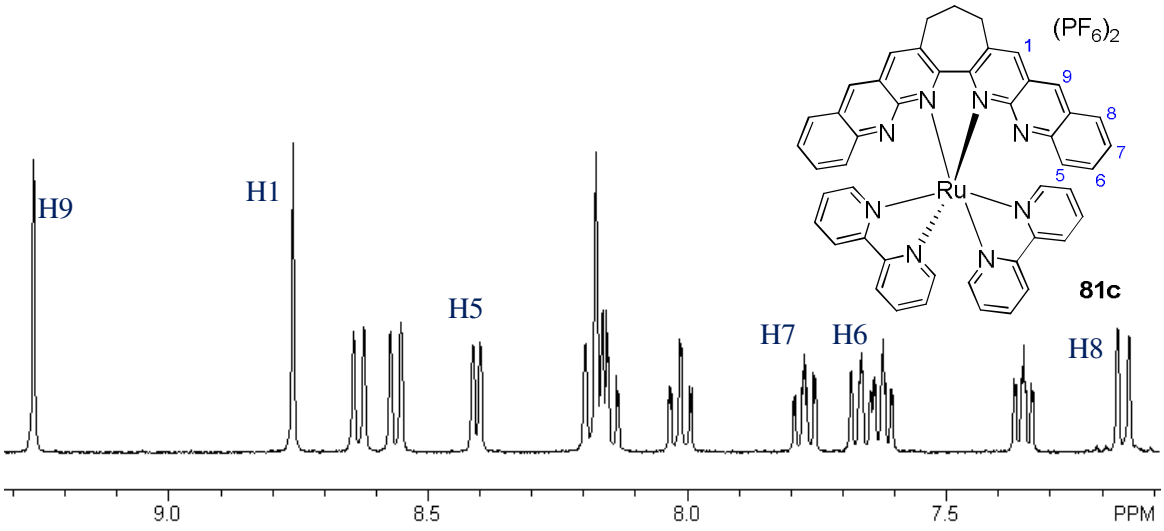

Figure 84. Downfield region of ^{1}H NMR spectrum of **81c** measured in acetone-*d6* (400 MHz, at rt).

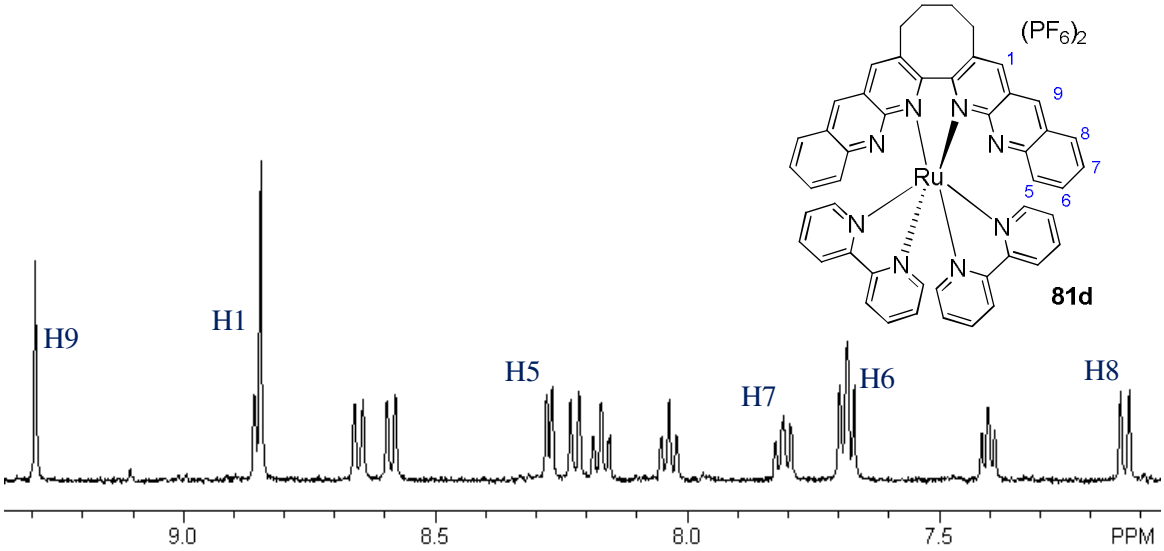

Figure 85. Downfield region of ^{1}H NMR spectrum of **81d** measured in acetone-*d6* (500 MHz, at -80 °C).

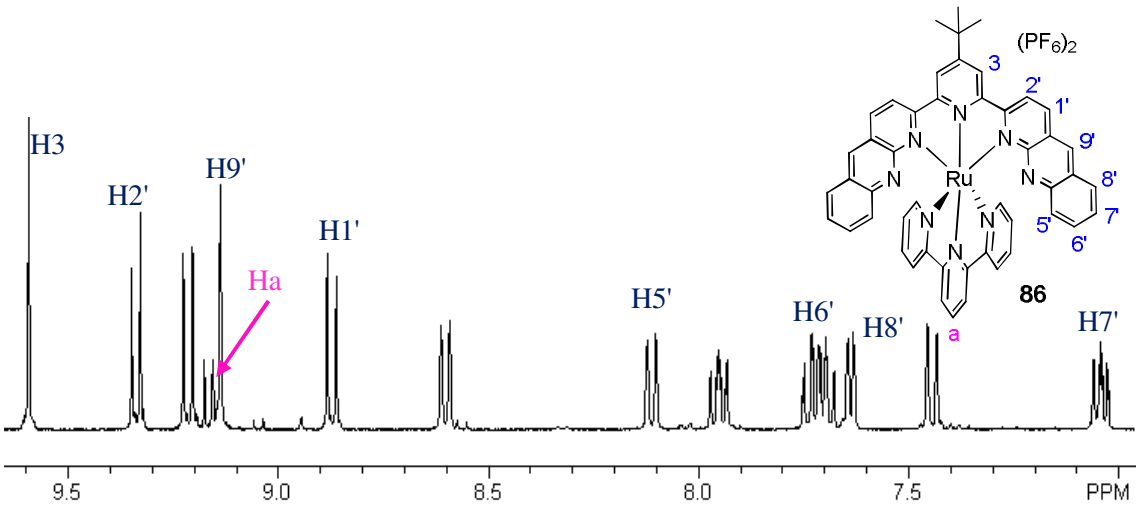

Figure 86. Downfield region of ^{1}H NMR spectrum of **86** in acetone-*d6* (400 MHz, at rt).

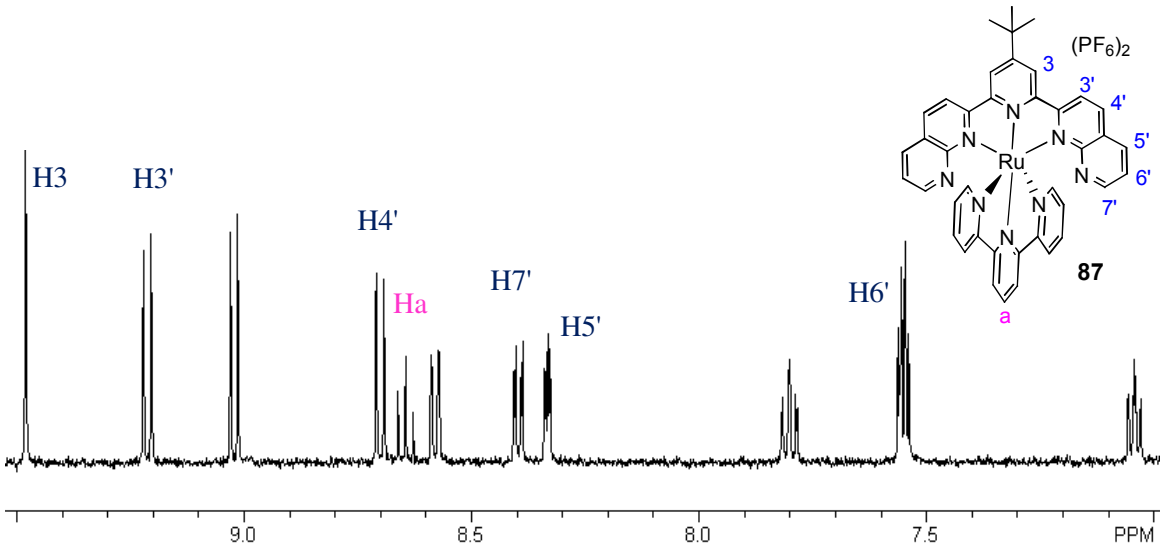

Figure 87. Downfield region of ^{1}H NMR spectrum of **87** in acetone-*d6* (500 MHz, at rt).

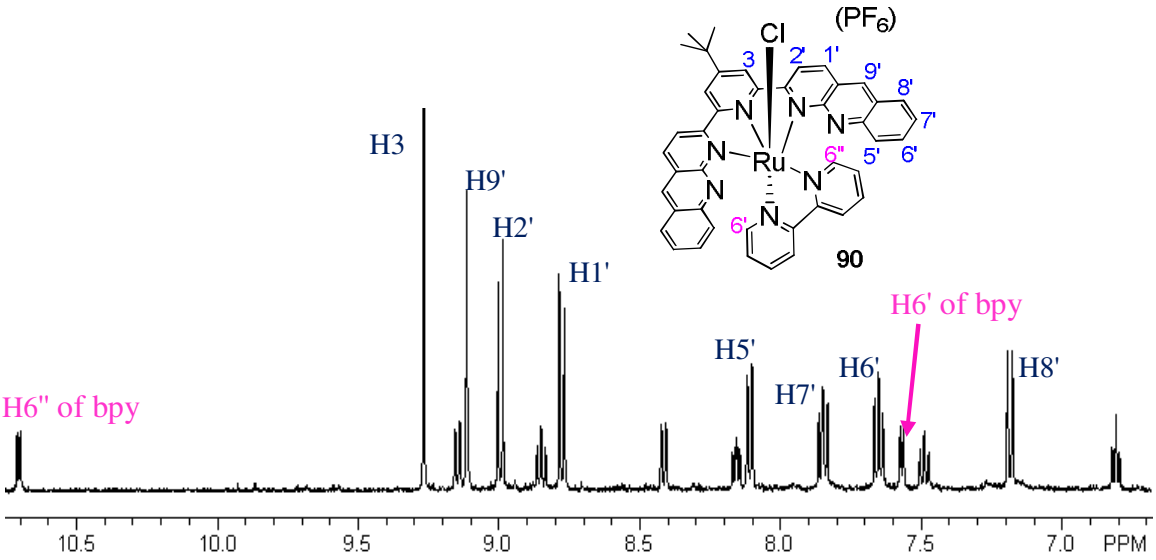

Figure 88. Downfield region of ^{1}H NMR spectrum of **90** in acetone-*d6* (500 MHz, at rt).

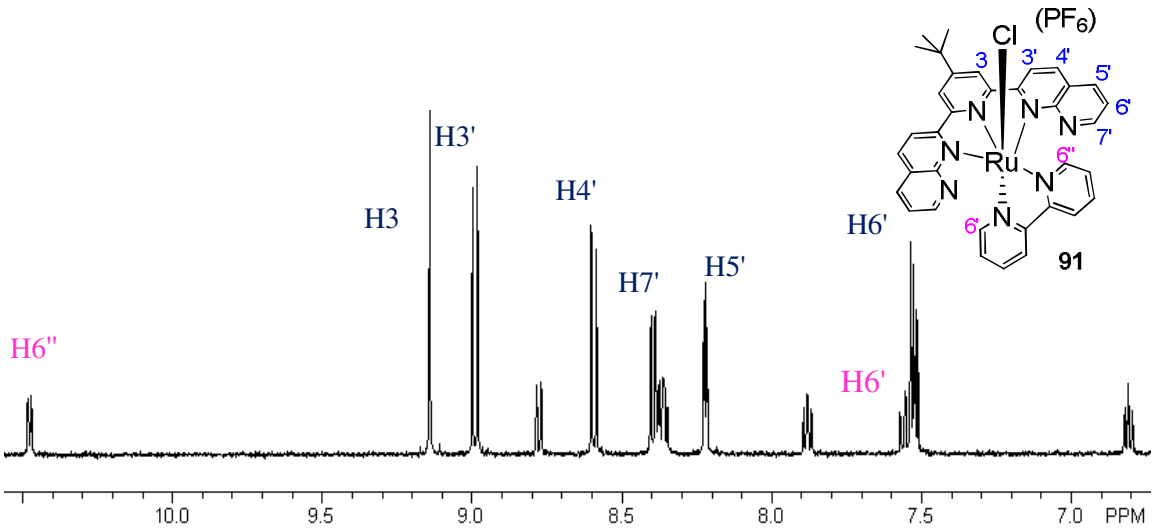

Figure 89. Downfield region of ^{1}H NMR spectrum of **91** in acetone-*d6* (500 MHz, at rt).

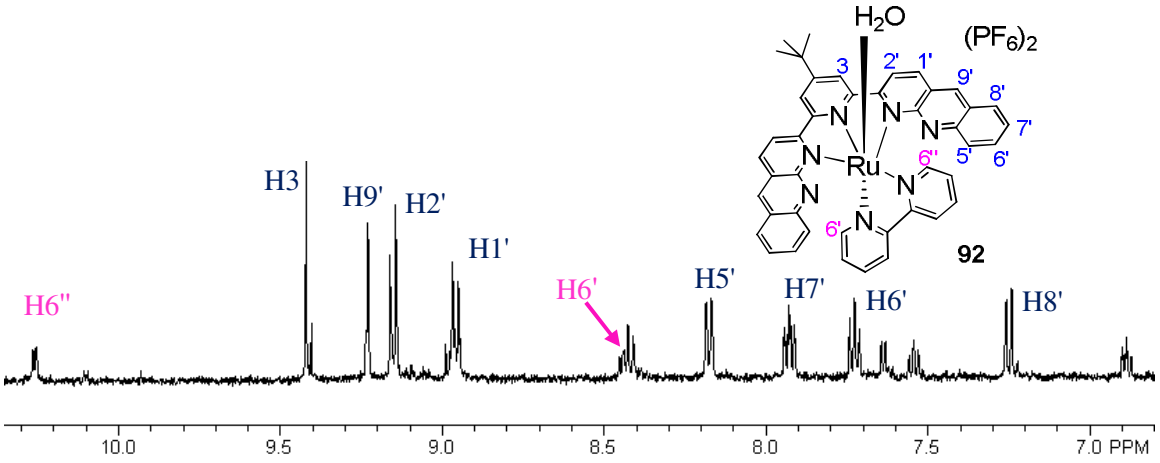

Figure 90. Downfield region of ^{1}H NMR spectrum of **92** in acetone-*d6* (500 MHz, at rt).

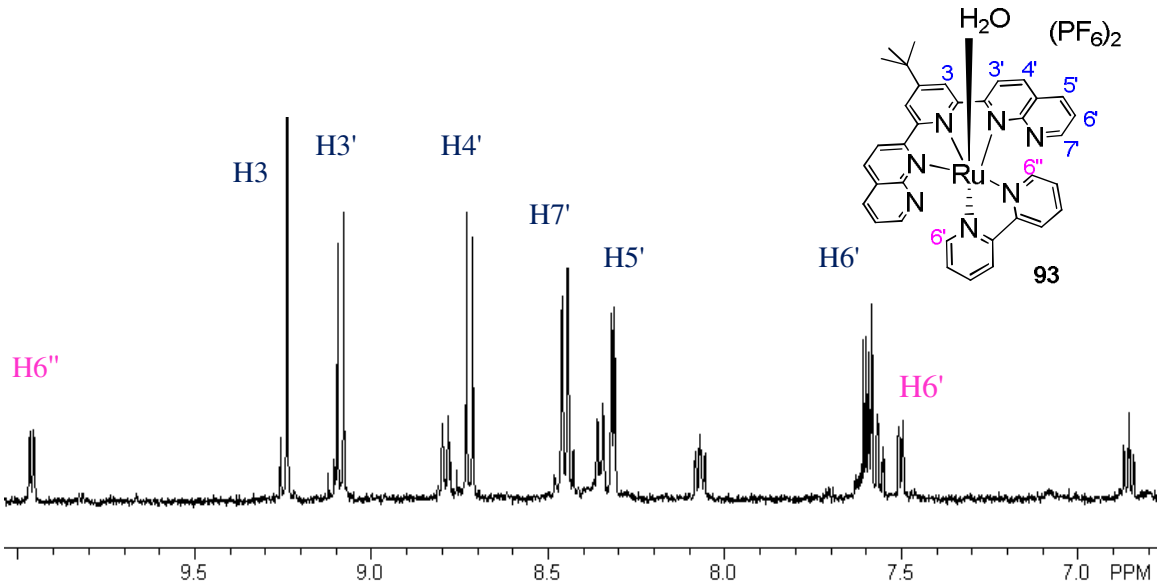

Figure 91. Downfield region of ^{1}H NMR spectrum of **93** in acetone-*d6* (500 MHz, at rt).

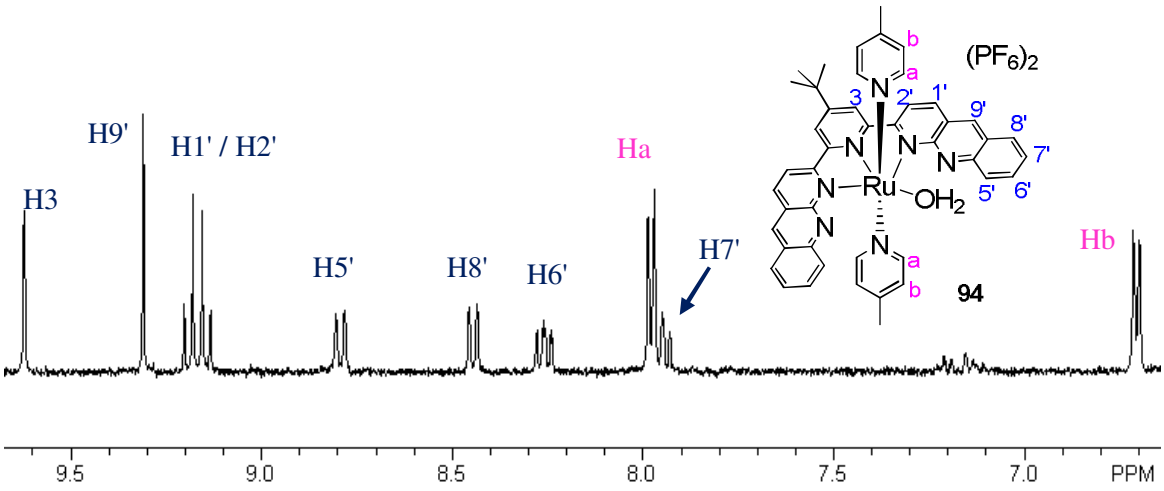

Figure 92. Downfield region of ^{1}H NMR spectrum of **94** in acetone-*d6* (400 MHz, at rt).

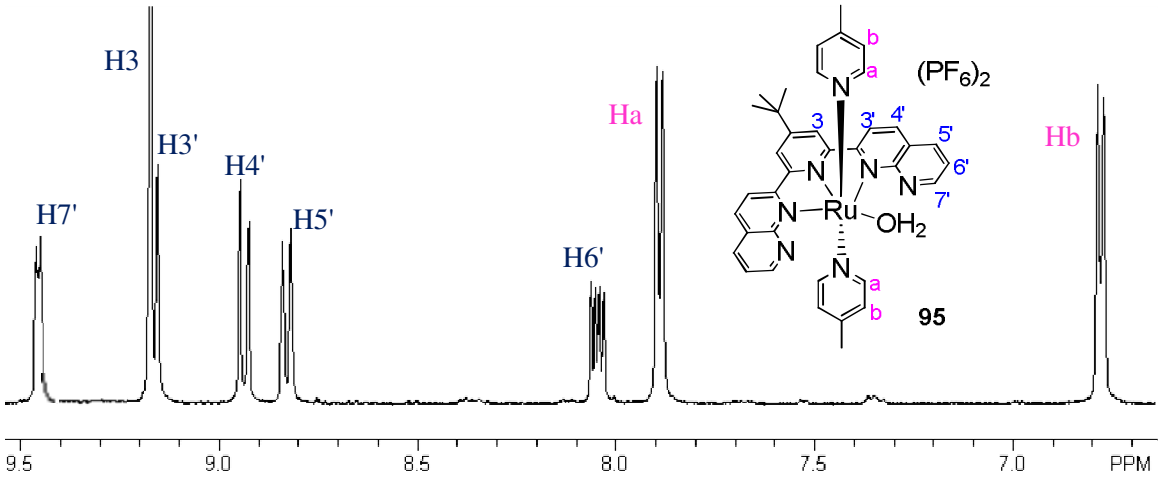

Figure 93. Downfield region of ^{1}H NMR spectrum of **95** in acetone-*d6* (400 MHz, at rt).

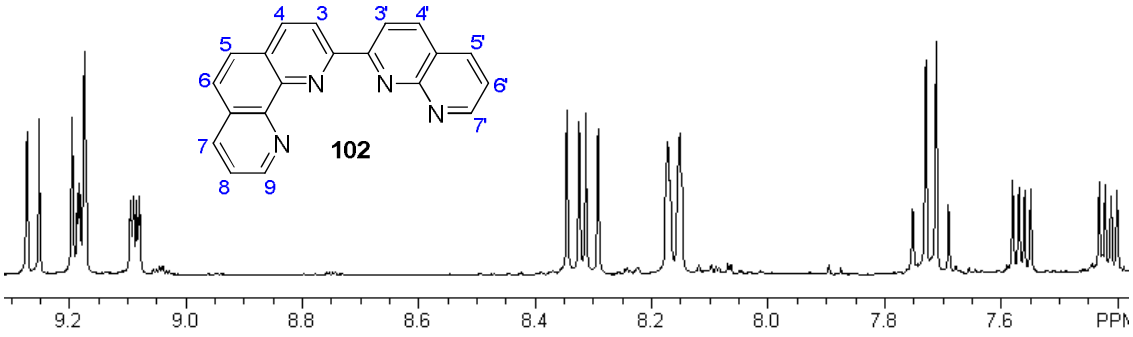

Figure 94. Downfield region of ^{1}H NMR spectrum of **102** in $CDCl_3$ (400 MHz, at rt).

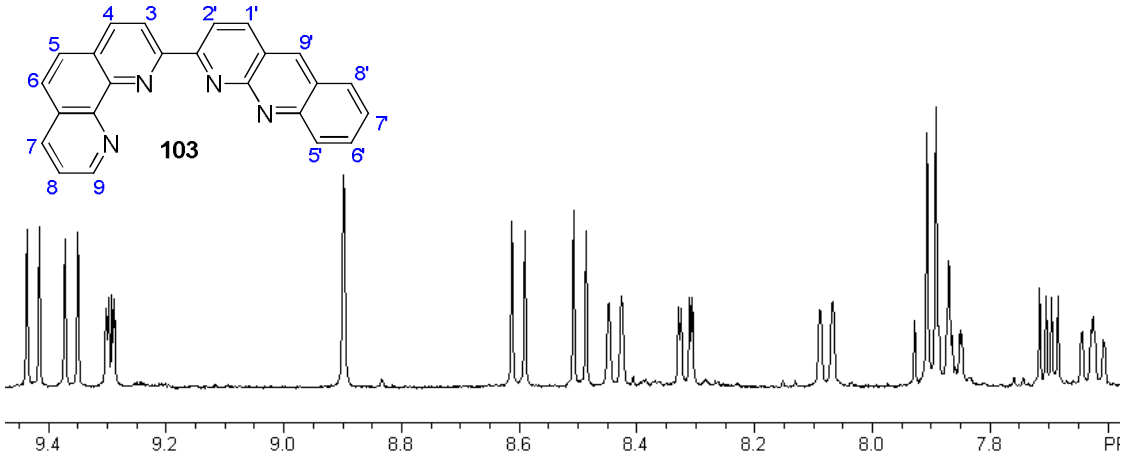

Figure 95. Downfield region of ^{1}H NMR spectrum of **103** in $CDCl_3$ (400 MHz, at rt).

REFERENCES

1. Energy Information Administration, *International Energy Outlook*; US Dept. of Energy: Washington DC, 2011.

2. Lewis, N. S.; Nocera, D. G. *Proc. Natl. Acad. Sci. USA* **2006**, *103*, 15729–15735.

3. Chen, Z. G.; Li, F. Y.; Huang, C. H. *Curr. Org. Chem.* **2007**, *11*, 1241–1258.

4. Kuang, D.; Klein, C.; Ito, S.; Moser, J.; Humphry-Baker, R.; Evans, N.; Duriaux, F.; Grätzel, C.; Zakeeruddin, S. M.; Grätzel, M. *Adv. Mater.* **2007**, *19*, 1133–1137.

5. (a) Smith, Z. A.; Taylor, K. D. *Renewable and Alternative Energy Resources: A Reference Handbook*; ABC-CLIO: Santa Barbara, 2008. (b) Chapin, D. M.; Fuller, C. S.; Pearson, G. L. *J. Appl. Phys.* **1954**, *25*, 676–677.

6. Green, M. A. *J. Mater. Sci.: Mater. Electron*. **2007**, *18*, 15–19.

7. (a) Green, M. A. *Third Generation Photovoltaics: Advanced Solar Energy Conversion*; Springer: New York, 2003. (b) Conibeer, G. *Mater. Today* **2007**, *10*, 42–50.

8. O'Regan, B.; Grätzel, M. *Nature*, **1991**, *353*, 737–740.

9. Nazeeruddin, Md. K.; Kay, A.; Rodicio, I.; Humphry-Baker, R.; Müller, E.; Liska, P.; Vlachopoulos, N.; Grätzel, M. *J. Am. Chem. Soc.* **1993**, *115*, 6382–6390.

10. Bach, U.; Lupo, D.; Comte, P.; Moser, J. E.; Weissörtel, F.; Salbeck, J.; Spreitzer, H.; Grätzel, M. *Nature* **1998**, *395*, 583–585.

11. Duan, L.; Tong, L.; Xu, Y.; Sun, L. *Energy Environ. Sci.* **2011**, *4*, 3296**–**3313.

12. (a) Sun, L.; Hammarström, L.; Åkermark, B.; Styring, S. *Chem. Soc. Rev.* **2001**, *30*, 36–49. (b) Muckerman, J. T.; Polyansky, D. E.; Wada, T.; Tanaka, K.; Fujita, E. *Inorg. Chem*. **2008**, *47*, 1787–1802.

13. (a) Limburg, J.; Vrettos, J. S.; Liable-Sands, L. M.; Rheingold, A. L.; Crabtree, R. H.; Brudvig, G. W. *Science* **1999**, *283*, 1524–1527. (b) Yagi, M.; Narita, K. *J. Am. Chem. Soc.* **2004**, *126*, 8084–8085. (c) Shimazaki, Y.; Nagano, T.; Takesue, H.; Ye, B.; Tani, F.; Naruta, Y. *Angew. Chem., Int. Ed.* **2004**, *43*, 98–100. (d) Rüttinger, W.; Dismukes, G. C. *Chem. Rev.* **1997**, *97*, 1–24.

14. (a) Juris, A.; Balzani, V.; Barigelletti, F.; Campagna, S.; Belser, P.; von Zelewsky, A. *Coord. Chem. Rev.* **1988**, *84*, 85–277. (b) Balzani, V.; Juris, A. *Coord. Chem. Rev.* **2001**,

211, 97–115. (c) Duerr, H.; Bossmann, S. *Acc. Chem. Res.* **2001**, *34*, 905–917. (d) Kalyanasundaram, K. *Photochemistry of Polypyridine and Porphyrin Complexes*; Academic Press: San Diego, CA, 1992.

15. Henry, G. D. *Tetrahedron* **2004**, *60*, 6043–6061.

16. Dumur, F.; Dumas, E.; Mayer, C. R. *Targ. Heterocycl. Syst.* **2007**, *11*, 70–103.

17. Kaes, C.; Katz, A.; Hosseini, M. W. *Chem. Rev.* **2000,** *100,* 3553–3590.

18. Summers, L. A. *Adv. Heterocycl. Chem.* **1984**, *35*, 281–374.

19. Constable, E. C. *Adv. Inorg. Chem. Radiochem.* **1986**, *30*, 69–121.

20. Newkome, G. R.; Patri, A. K.; Holder, E.; Schubert, U. S. *Eur. J. Org. Chem.* **2004**, *2004*, 235–254.

21. Brandt, W. W.; Dwyer, F. P.; Gyarfas, E. D. *Chem. Rev.* **1954**, *54,* 959–1017.

22. Göller, A.; Grummt, U. W. *Chem. Phys. Lett.* **2000**, *321*, 399–405.

23. Bessel, C. A.; See, R. F.; Jameson, D. L.; Churchill, M. R.; Takeuchi K. J. *J. Chem. Soc., Dalton Trans.* **1992**, 3223–3228.

24. Nakamoto, K. *J. Phys. Chem.* **1960**, *64*, 1420–1425.

25. Henry, M. S.; Hoffman, M. Z. *J. Phys. Chem.* **1979**, *83*, 618–625.

26. Albano, G.; Balzani, V.; Constable, E. C.; Maestri, M.; Smith, D. R. *Inorg. Chim. Acta* **1998**, *277*, 225–231.

27. Bandyopadhyay, B. N.; Harriman, A. *J. Chem. Soc., Faraday Trans. 1* **1977**, *73*, 663–674.

28. Leroy-Lhez, S.; Fages, F. *C. R. Chim*. **2005**, *8*, 1204–1212.

29. Steel, P. J. *Coord. Chem. Rev.* **1990***, 106*, 227–265.

30. Smith, G. F. *Anal. Chem.* **1954**, *26*, 1534–1538.

31. Constable, E. C. *Chem. Soc. Rev.* **2007**, *36*, 246–253.

32. Polo, A. S.; Itokazu, M. K.; Iha, N. Y. M. *Coord. Chem. Rev.* **2004**, *248*, 1343–1361.

33. Lo, K. K. W.; Hui, W. K.; Chung, C. K.; Tsang, K. H. K.; Ng, D. C. M.; Zhu, N. Y.; Cheung, K. K. *Coord. Chem. Rev.* **2005**, *249*, 1434–1450.

34. Chelucci, G.; Thummel, R. P. *Chem. Rev.* **2002**, *102*, 3129–3170.

35. Balzani, V.; Bergamini, G.; Ceroni, P. *Coord. Chem. Rev.* **2008***, 252*, 2456–2469.

36. Vos, J. G.; Kelly, J. M. *Dalton Trans.* **2006**, 4869–4883.

37. Kalyanasundaram , K.; Grätzel, M. *Coord. Chem. Rev.* **1998**, *177*, 347–414.

38. O'Regan, B.; Grätzel, M. *Nature* **1991**, *353*, 737–740.

39. Meyer, T. J. *Acc. Chem. Res.* **1989**, *22*, 163–170.

40. Brimblecombe, R.; Dismukes, G. C.; Swiegers, G. F.; Spiccia, L. *Dalton Trans.* **2009**, 9374–9384.

41. Sala, X.; Romero, I.; Rodríguez, M.; Escriche, L.; Llobet, A. *Angew. Chem., Int. Ed.* **2009**, *48*, 2842–2852.

42. Gersten, S. W.; Samuels, G. J.; Meyer, T. J. *J. Am. Chem. Soc.* **1982**, *104*, 4029–4030.

43. Sens,C.; Romero, I.; Rodríguez, M.; Llobet, A.; Parella, T.; Benet-Buchholz, J. *J. Am. Chem. Soc.* **2004**, *126*, 7798–7799.

44. Zong, R.; Thummel, R. P. *J. Am. Chem. Soc.* **2005**, *127*, 12802–12803.

45. Yersin, H. *Top. Curr. Chem.* **2004**, *241* (Transition Metal and Rare Earth Compounds), 1–26.

46. Handy, E. S.; Pal, A. J.; Rubner, M. F. *J. Am. Chem. Soc.* **1999**, *121*, 3525–3528.

47. Buda, M.; Kalyuzhny, G.; Bard, A. J. *J. Am. Chem. Soc.* **2002**, *124*, 6090–6098.

48. Mak, C.; Chan, W. *Highly Efficient OLEDs with Phosphorescent Materials*; Wiley-VCH: Weinheim, 2008, 329–362.

49. Gong, X.; Ng, P. K.; Chan, W. K. *Adv. Mater.* **1998**, *10*, 1337–1340.

50. Leprêtre, J. C.; Deronzier, A.; Stéphan, O. *Synth. Met.* **2002**, *131*, 175–183.

51. Campagna, S.; Puntoriero, F.; Nastasi, F.; Bergamini, G.; Balzani, V. *Top. Curr. Chem.* **2007**, *280*, (Photochemistry and photophysics of coordination compounds I: Ruthenium), 117–214.

52. Balzani, V.; Bergamini, G.; Campagna, S.; Puntoriero, F. *Top. Curr. Chem.* **2007**, *280*, (Photochemistry and photophysics of coordination compounds I: Overview and general concepts), 1–36.

53. Balzani, V.; Juris, A.; Venturi, M. ; Campagna S.; Serroni, S. *Chem. Rev.* **1996**, *96*, 759–833.

54. Crosby, G. A. *Acc. Chem. Res.* **1975**, *8*, 231–238.

55. Kalyanasundaram, K.; Nazeeruddin, Md. K. *Chem. Phys. Lett.* **1992**, *193*, 292–297.

56. Kalyanasundaram, K. *Photochemistry of Polypyridine and Porphyrin Complexes*; Academic Press: Sandiego, 1992.

57. Hofmeier, H.; Schubert, U. S. *Chem. Soc. Rev.* **2004**, *33*, 373–399.

58. Maestri, M.; Armaroli, N.; Balzani, V.; Constable, E. C.; Thompson, A. M. *Inorg. Chem.* **1995**, *34*, 2759–2767.

59. Bard, A. J. *Electrochemical Methods: Fundamentals and Applications*; John Wiley and Sons: New York, 1980.

60. Tokel-Takvoryan, N. E.; Hemingway, R. E.; Bard, A. J. *J. Am. Chem. Soc.* **1973**, *95*, 6582–6589.

61. Lever, A. B. P. *Inorg. Chem.* **1990**, *29*, 1271–1285.

62. Fielder, S. S.; Osborne, M. C.; Lever, A. B. P.; Pietro, W. J. *J. Am. Chem. Soc.* **1995**, *117*, 6990–6993.

63. Nazeeruddin, Md. K.; Kay, A.; Rodicio, I.; Humphry-Baker, R.; Mueller, E.; Liska, P.; Vlachopoulos, N.; Grätzel, M. *J. Am. Chem. Soc.* **1993**, *115*, 6382–6390.

64. Zakeeruddin, S. M.; Nazeeruddin, Md. K.; Péchy, P.; Rotzinger, F. P.; Humphry-Baker, R.; Kalyanasundaram, K.; Grätzel, M. *Inorg. Chem.* **1997**, *36*, 5937–5946.

65. Nazeeruddin, Md. K.; Péchy, P.; Grätzel, M. *Chem. Commun.* **1997**, 1705–1706.

66. Goldemberg, J.; Johansson, T. B. *World Energy Assessment*: Overview 2004 Update, United Nations Development Programme (UNDP), 2004.

67. Klein, J. *Comparative Costs of California Central Station Electricity Generation Technologies*; Commission; C. E., 2009.

68. BP Statistical Review of World Energy June 2009. (accessed July 26, 2010).

69. AM1.5G Global Solar Spectrum (ASTM G173-03) source of data ASTM/NREL, http://rredc.nrel.gov/solar/spectra/am1.5/.

70. Bequerel, A. E. *C. R. Acad. Sci.* **1839**, *9*, 145–149.

71. Haught, A. *J. Sol. Ener. Engine.* **1984**, *106*, 3–15.

72. Nazeeruddin, Md. K.; Grätzel, M. *Compr. Coord. Chem. II* **2004**, *9*, 719–758.

73. Roundhill, D. M. *Photochemistry and Photophysics of Metal Complexes*; Plenum: New York, 1994.

74. Onozawa-Komatsuzaki, N.; Kitao, O.; Yanagida, M.; Himeda, Y.; Sugihara, H.; Kasuga, K. *New J. Chem.* **2006**, *30*, 689–697.

75. Robertson, N. *Angew. Chem. Int. Ed.* **2006**, *45*, 2338–2345.

76. Hagfeldt, A.; Boschloo, G.; Sun, L.; Kloo, L.; Pettersson, H. *Chem. Rev.* **2010**, *110*, 6595–6663.

77. Martinson, A. B. F.; Hamann, T. W.; Pellin, M. J.; Hupp, J. *Chem. Eur. J.* **2008**, *14*, 4458–4467.

78. Kittel, C. *Introduction to Solid State Physics*; Wiley: Hoboken, 2005.

79. Pagliaro, M.; Palmisano, G.; Ciriminna, R.; Loddo, V. *Energy Environ. Sci.* **2009**, *2*, 838–844.

80. Jose, R.; Thavasi, V.; Ramakrishna, S. *J. Am. Ceram. Soc.* **2009**, *92*, 289–301.

81. Reyes-Coronado, D., Rodríguez-Gattorno1, G.; Espinosa-Pesqueira, M. E.; Cab, C.; de Coss, R.; Oskam, G. *Nanotechnology* **2008**, *19*, 145605–145614.

82. Park, N. G.; van de Lagemaat, J.; Frank, A. J. *J. Phys. Chem. B* **2000**, *104*, 8989–8994.

83. Li, G.; Richter, C. P.; Milot, R.; Cai, L.; Schmuttenmaer, C. A.; Crabtree, R.; Brudvig G.; Batista, V. *Dalton Trans.* **2009**, 10078–10085.

84. Ferber, J.; Luther, J. *Solar Energy Mater. Solar Cells* **1998**, *54*, 265–275.

85. Liang, L. Y.; Dai, S. Y.; Hu, L. H.; Kong, F. T.; Xu, W. W.; Wang, K. J. *J. Phys. Chem. B* **2006**, *110*, 12404–12409.

86. Usami, A. *Solar Energy Mater. Solar Cells* **1999**, *59*, 163–166.

87. Barbé, C. J.; Arendse, F.; Comte, P.; Jirousek, M.; Lenzmann, F.; Shklover, V.; Grätzel, M. *J. Am. Ceram. Soc.* **1997**, *80*, 3157–3171.

88. Halaoui, L. I.; Abrams, N. M.; Mallouk, T. E. *J. Phys. Chem. B* **2005**, *109*, 6334–6342.

89. Benkstein, K. D.; Kopidakis, N.; van de Lagemaat, J.; Frank, A. J. *J. Phys. Chem. B* **2003**, *107*, 7759–7767.

90. Galoppini, E. *Coord. Chem. Rev.* **2004**, *248*, 1283–1297.

91. Gillaizeau-Gauthier, I.; Odobel, F.; Alebbi, M.; Argazzi, R.; Costa, E.; Bignozzi, C. A.; Qu, P.; Meyer, G. J. *Inorg. Chem.* **2001**, *40*, 6073–6079.

92. Altobello, S.; Bignozzi, C. A.; Caramori, S.; Larramona, G.; Quici, S.; Marzanni, G.; Lakhmiri, R. *J. Photochem. Photobiol. A Chem.* **2004**, *166*, 91–98.

93. Vittadini, A.; Selloni, A.; Rotzinger, F. P.; Grätzel, M. *J. Phys. Chem. B* **2000**, *104*, 1300–1306.

94. Meyer, T. J.; Meyer, G. J.; Pfennig, B. W.; Schoonover, J. R.; Timpson, C. J.; Wall, J. F.; Kobusch, C.; Chen, X.; Peek, B. *Inorg. Chem.* **1994**, *33*, 3952–3964.

95. Grätzel, M.; McEvoy, A. J. *Asian J. Energ. Env.* **2004**, *5*, 197–210.

96. Clifford, J. N.; Palomares, E.; Nazeeruddin, Md. K.; Grätzel, M.; Nelson, J.; Li, X.; Long, N. J.; Durrant, J. R. *J. Am. Chem. Soc.* **2004**, *126*, 5225–5233.

97. Haque, S. A.; Handa, S.; Peter, K.; Palomares, E.; Thelakkat, M.; Durrant, J. R. *Angew. Chem. Int. Ed.* **2005**, *44*, 5740–5744.

98. Polo, A.; Itokazu, M.; Murakami Iha, N. *Coord. Chem. Rev.* **2004**, *248*, 1343–136.

99. Mishra, A.; Fischer, M. K. R.; Bäuerle, P. *Angew. Chem. Int. Ed.* **2009**, *48*, 2474–2499.

100. Ooyama, Y.; Harima, Y. *Eur. J. Org. Chem.* **2009**, *2009*, 2903–2934.

101. Smestad, G.; Grätzel, M. *J. Chem. Educ.* **1998**, *75*, 752–756.

102. Bignozzi, C. A.; Argazzi, R.; Kleverlaan, C. J. *Chem. Soc. Rev.* **2000**, *29*, 87–96.

103. Nazeeruddin, Md. K.; Zakeeruddin, S. M.; Lagref, J. J.; Liska, P.; Comte, P.; Barolo, C.; Viscardi, G.; Schenk, K.; Grätzel, M. *Coord. Chem. Rev.* **2004**, *248*, 1317–1328.

104. Islam, A.; Sugihara, H.; Arakawa, H. *J. Photochem. Photobiol. A Chem.* **2003**, *158*, 131–138.

105. Heimer, T. A.; Bignozzi, C. A.; Meyer, G. J. *J. Phys. Chem.* **1993**, *97*, 11987–11994.

106. Kuciauskas, D.; Freund, M. S.; Gray, H. B.; Winkler, J. R.; Lewis, N. S. *J. Phys. Chem. B* **2001**, *105*, 392**–**403.

107. Islam, A.; Sugihara, H.; Hara, K.; Singh, L. P.; Katoh, R.; Yanagida, M.; Takahashi, Y.; Murata, S.; ArakawaH.; Fujihashi, G. *Inorg. Chem.* **2001**, *40*, 5371–5380.

108. Geary, E. A. M.; Yellowlees, L. J.; Jack, L. A.; Oswald, I. D. H.; Parsons, S.; Hirata, N.; Durrant, J. R.; Robertson, N. *Inorg. Chem.* **2005**, *44*, 242–250.

109. Hasselmann, G. M.; Meyer, G. J. *J. Phys. Chem. B* **1999**, *103*, 7671–7675.

110. Alonso-Vante, N.; Nierengarten, J.; Sauvage, J. *J. Chem. Soc. Dalton Trans.* **1994**, 1649–1654.

111. Bessho, T.; Constable, E. C.; Grätzel, M.; Redondo, A. H.; Housecroft, C. E.; Kylberg, W.; Nazeeruddin, Md. K.; Neuburger, M.; Schaffner, S. *Chem. Commun.* **2008**, 3717–3719.

112. Ferrere, S. *Chem. Mater.* **2000**, *12*, 1083–1089.

113. Nazeeruddin, Md. K.; De Angelis, F.; Fantacci, S.; Selloni, A.; Viscardi, G.; Liska, P.; Ito, S.; Takeru,B.; Grätzel, M. *J. Am. Chem. Soc.* **2005**, *127*, 16835–16847.

114. Argazzi, R.; Larramona, G.; Contado, C.; Bignozzi, C. A. *J. Photochem. Photobiol. A Chem.* **2004**, *164*, 15–21.

115. Imahori, H.; Umeyama, T.; Ito, S. *Acc. Chem. Res.* **2009**, *42*, 1809–1818.

116. Hagberg, D. P.; Yum, J.; Lee, H.; De Angelis, F.; Marinado, T.; Karlsson, K.; Humphry-Baker, R.; Sun, L.; Hagfeldt, A.; Grätzel, M.; Nazeeruddin, Md. K. *J. Am. Chem. Soc.* **2008**, *130*, 6259–6266.

117. Wang, Z.; Cui, Y.; Dan-oh, Y.; Kasada, C.; Shinpo, A.; Hara, K. *J. Phys. Chem. C* **2007**, *111*, 7224–7230.

118. Yum, J.; Walter, P.; Huber, S.; Rentsch, D.; Geiger, T.; Nüesch, F.; De Angelis, F.; Grätzel, M.; Nazeeruddin, Md. K. *J. Am. Chem. Soc.* **2007**, *129*, 10320–10321.

119. Edvinsson, T.; Li, C.; Pschirer, N.; Schöneboom, J.; Eickemeyer, F.; Sens, R. Boschloo, G.; Herrmann, A.; Müllen, K.; Hagfeldt, A. *J. Phys. Chem. C* **2007**, *111*, 15137–15140.

120. Forneli, A.; Planells, M. A.; Sarmentero, M.; Martinez-Ferrero, E.; O'Regan, B. C.; Ballester, P.; Palomares, E. *J. Mater. Chem.* **2008**, *18*, 1652–1658.

121. Cid, J.; Yum, J.; Jang, S.; Nazeeruddin, Md. K.; Martínez-Ferrero, E.; Palomares, E.; Ko, J.; Grätzel, M.; Torres, T. *Angew. Chem. Int. Ed.* **2007**, *46*, 8358–8362.

122. Calogero, G.; Marco, G. D. *Sol. Energy Mater. Sol. Cells* **2008**, *92*, 1341–1346.

123. Hao, S.; Wu, J.; Huang, Y.; Lin, J. *Sol. Energy* **2006**, *80*, 209–214.

124. Kay, A.; Grätzel, M. *J. Phys. Chem.* **1993**, *97*, 6272–6277.

125. Murakami, T. N.; Grätzel, M. *Inorg. Chim. Acta* **2008**, *361*, 572–580.

126. Papageorgiou, N.; Maier, W. F.; Grätzel, M. *J. Electrochem. Soc.* **1997**, *144*, 876–884.

127. Murakami, T. N.; Ito, S.; Wang, Q.; Nazeeruddin, Md. K.; Bessho, T.; Cesar, I.; Liska, P.; Humphry-Baker, R.; Comte, P.; Péchy, P.; Grätzel, M. *J. Electrochem. Soc.* **2006**, *153*, A2255–A2261.

128. Nogueira, A. F.; Longo, C.; De Paoli, M. A. *Coord. Chem. Rev.* **2004**, *248*, 1455–1468.

129. Frank, A. J.; Kopidakis, N.; van de Lagemaat, J. *Coord. Chem. Rev.* **2004**, *248*, 1165–1179.

130. Nissfolk, J.; Fredin, K.; Hagfeldt, A.; Boschloo, G. *J. Phys. Chem. B* **2006**, *110*, 17715–17718.

131. Kisserwan, H.; Ghaddar, T. H. *Inorg. Chim. Acta* **2010**, *363*, 2409–2415.

132. Islam, A.; Sugihara, H.; Arakawa, H. *J. Photochem. Photobiol., A* **2003**, *158*, 131–138.

133. Anderson, P. A.; Strouse, G. F.; Treadway, J. A.; Keene, F. R.; Meyer, T. J. *Inorg. Chem.* **1994**, *33*, 3863–3864.

134. Islam, A.; Sugihara, H.; Singh, L. P.; Hara, K.; Katoh, R.; Nagawa, Y.; Yanagida, M.; Takahashi, Y.; Murata, S., Arakawa, H. *Inorg. Chim. Acta* **2001**, *322*, 7–16.

135. Juris, A.; Balzani, V.; Barigelletti, F.; Campagna, S.; Belser, P.; von Zelewsky, A. *Coord. Chem. Rev.* **1988**, *84*, 85–277.

136. Alebbi, M.; Bignozzi, C. A.; Heimer, T. A.; Hasselmann, G. M.; Meyer, G. J. *J. Phys. Chem. B* **1998**, *102*, 7577–7581.

137. Treadway, J. A.; Moss, J. A.; Meyer, T. J. *Inorg. Chem.* **1999**, *38*, 4386–4387.

138. Ramamurthy, V.; Schanze, K. S. *Semiconductor Photochemistry and Photophysics*; Marcel Dekker: New York, 2003.

139. (a) Kohle, O.; Grätzel, M.; Meyer, A. F.; Meyer, T. B. *Adv. Mater.* **1997**, *9*, 904–906. (b) Nazeeruddin, Md. K.; Zakeeruddin, S. M.; Humphry-Baker, R.; Jirousek, M.; Liska, P.; Vlachopoulos, N.; Shklover, V.; Fischer, C.; Grätzel, M. *Inorg. Chem.* **1999**, *38*, 6298–6305.

140. Nazeeruddin, Md. K.; Péchy, P.; Renouard, T.; Zakeeruddin, S. M.; Humphry-Baker, R.; Comte, P.; Liska, P.; Cevey, L.; Costa, E.; Shklover, V.; Spiccia, L.; Deacon, G. B.; Bignozzi, C. A.; Grätzel, M. *J. Am. Chem. Soc.* **2001**, *123*, 1613–1624.

141. (a) Lagref, J. J.; Nazeeruddin, Md. K.; Grätzel, M. *Inorg. Chim. Acta* **2008**, *361*, 735–745. (b) Kilså, K.; Mayo, E. I.; Brunschwig, B. S.; Gray, H. B.; Lewis, N. S.; Winkler, J. R. *J. Phys. Chem. B* **2004**, *108,* 15640–15651.

142. Kukrek, A.; Wang, D.; Hou, Y.; Zong, R.; Thummel, R. *Inorg. Chem.* **2006**, *45*, 10131–10137.

143. Nazeeruddin, Md. K.; Péchy, P.; Grätzel, M. *Chem. Comm.* **1997**, *18*, 1705–1706.

144. Nazeeruddin, Md. K.; Péchy, P.; Renouard, T.; Zakeeruddin, S. M.; Humphry-Baker, R.; Comte, P.; Liska, P.; Cevey, L.; Costa, E.; Shklover, V.; Spiccia, L.; Deacon, G. B.; Bignozzi, C. A.; Grätzel, M. *J. Am. Chem. Soc.* **2001**, *123*, 1613–1624.

145. Wang, P.; Zakeeruddin, S. M.; Moser, J. E.; Nazeeruddin, Md. K.; Sekiguchi, T.; Grätzel, M. *Nat. Mater.* **2003**, *2*, 402–407.

146. Schmidt-Mende, L.; Kroeze, J. E.; Durrant, J. R.; Nazeeruddin, Md. K.; Grätzel, M. *Nano Lett.* **2005**, *5*, 1315–1320.

147. Wang, P.; Humphry-Baker, R.; Moser, J. E.; Zakeeruddin, S. M.; Grätzel, M. *Chem. Mater.* **2004**, *16*, 3246–3251.

148. Wang, P.; Zakeeruddin, S. M.; Moser, J. E.; Humphry-Baker, R.; Comte, P.; Aranyos, V.; Hagfeldt, A.; Nazeeruddin, Md. K.; Grätzel, M. *Adv. Mater.* **2004**, *16*, 1806–1811.

149. Wang, P.; Klein, C.; Humphry-Baker, R.; Zakeeruddin, S. M.; Grätzel, M. *J. Am. Chem. Soc.* **2005**, *127*, 808–809.

150. Funaki, T.; Yanagida, M.; Onozawa-Komatsuzaki, N.; Kasuga, K.; Kawanishi, Y.; Kurashige, M.; Sayama, K.; Sugihara, H. *Inorg. Chem. Commun.* **2009**, *12*, 842–845.

151. Bomben, P. G.; Koivisto, B. D.; Berlinguette, C. P. *Inorg. Chem.* **2010**, *49*, 4960–4971.

152. Asghar, M. I.; Miettunen, K.; Halme, J.; Vahermaa, P.; Toivola, M.; Aitola, K.; Lund, P. *Energy Environ. Sci.* **2010**, *3*, 418–426.

153. (a) Yanagida, M.; Yamaguchi, T.; Kurashige, M.; Fujihashi, G.; Hara, K.; Katoh, R.; Sugihara, H.; Arakawa, H. *Inorg. Chim. Acta* **2003**, *351*, 283–290. (b) Yanagida, M.; Yamaguchi, T.; Kurashige, M.; Hara, K.; Katoh, R.; Sugihara, H.; Arakawa, H. *Inorg. Chem.* **2003**, *42*, 7921–7931.

154. Kohle, O.; Ruile, S.; Grätzel, M. *Inorg. Chem.* **1996**, *35*, 4779–4787.

155. Wang, Z.; Yamaguchi, T.; Sugihara, H.; Arakawa, H. *Langmuir* **2005**, *21*, 4272–4276.

156. Bond, A. M.; Deacon, G. B.; MacFarlane, D. R.; Spiccia, L.; Wolfbauer, G. *J. Electrochem. Soc*. **1999**, *146*, 648–656.

157. (a) Gray, H. B.; Maverik, A. W. *Science* **1981**, *214*, 1201–1205. (b) Heyduk, A. F.; Nocera, D. G. *Science* **2001**, *293*, 1636–1639.

158. Grimes, C. A.; Varghese, O.; Ranjan, S. *Light, Water, Hydrogen: The Solar Generation of Hydrogen by Water Photoelectrolysis*; Springer: New York, 2008.

159. Kalyanasundaram, K.; Kiwi, J.; Grätzel, M. *Helv. Chim. Acta* **1978**, *61*, 2720–2730.

160. (a) Cox, J. A.; Jaworski, R. K.; Das, B. K. *Electroanalysis* **1990**, *2*, 617–621. (b) Ledney, M.; Dutta, P. K. *J. Am. Chem. Soc.* **1995**, *117*, 7687–7695.

161. Hurst, J. M.; Carr, P. A. G.; Hovis, F. E.; Richardson, R. J. *Inorg. Chem.* **1981**, *20*, 2435–2438.

162. (a) Lehn, J. M.; Suavage, J. P.; Ziessel, R. *Nouv. J. Chim.* **1979**, *3*, 423–427. (b) Nazeeruddin, Md. K.; Rotzinger, F. P.; Comte, P.; Grätzel, M. *J. Chem. Soc., Chem. Commun.* **1988**, 872–874.

163. (a) Balzani, V.; Moggi, L.; Manfrin, M. F.; Bolletta, F.; Gleria, M.; *Science* **1975**, *189*, 852–856. (b) Bolton, J. R. *Science* **1978**, *202*, 705–710. (c) Grätzel, M. *Acc. Chem. Res.* **1981**, *14*, 376–384.

164. (a) Harriman, A.; Mills, A. *J. Chem. Soc., Faraday Trans. 2* **1981**, *77*, 2111–2124. (b) Prasad, D. R.; Mandal, K.; Hoffman, M. Z. *Coord. Chem. Rev.* **1985**, *64*, 175–190.

165. Takeuchi, K. J.; Thompson, M. S.; Pipes, D. W.; Meyer, T. J. *Inorg. Chem.* **1984**, *23*, 1845–1851.

166. Ryu, C. K.; Wang, R.; Schmehl, R. H.; Ferrere, S.; Ludwikow, M.; Merkert, J. W.; Headford, C. E. L.; Elliot, C. M. *J. Am. Chem. Soc.* **1992**, *114*, 430–438.

167. Balzani, V.; Scandola, F. *Supramolecular Photochemistry*; Horwood: UK, 1991.

168. (a) Mecklenburg, S. L.; Peek, B. M.; Erickson, B. W.; Meyer, T. J. *J. Am. Chem. Soc.* **1991**, *113*, 8540–8542. (b) Strouse, G. F.; Worl, L. A.; Younathan, J. N.; Meyer, T. J. *J. Am. Chem. Soc.* **1989**, *111*, 9101–9102.

169. (a) Rillema, D. P.; Allen, G.; Meyer, T. J.; Conrad, D. *Inorg. Chem.* **1983**, *22*, 1617–1622. (b) Allen, G. H.; White, R. P.; Rillema, D. P.; Meyer, T. J. *J. Am. Chem. Soc.* **1984**, *106*, 2613–2620.

170. Thummel, R. P. *Tetrahedron* **1991**, *47*, 6851–6886.

171. (a) Goswam, S.; Kumar Das, N. *J. Heterocycl. Chem.* **2008**, *46*, 324–326. (b) Litvinov, V. P.; Roman, S. V.; Dyachenko, V. D. *Russ. Chem. Rev.* **2001**, *70*, 299–320. (c) Paudler, W. W.; Sheets, R. M. *Adv. Heterocycl. Chem.* **1983**, *33*, 147–184.

172. Thummel, R. P.; Hery, C.; Williamson, D.; Lefoulon, F. *J. Am. Chem. Soc.* **1988**, *110*, 7894–7896.

173. von Zelewsky, A.; Gremaud, G. *Helv. Chim. Acta* **1988**, *71*, 1108–1115.

174. Thummel, R. P.; Lefoulon, F. *J. Org. Chem.* **1985**, *50*, 666–670.

175. Harris, C. M.; Patil, H. R. H.; Sinn, E. *Inorg. Chem.* **1967**, *6*, 1102–1105.

176. Bessel, C. A.; Margarucci, J. A.; Acquaye, J. H.; Rubino, R. S.; Carndall, J.; Jircitano, A. J.; Takeuchi, K. J. *Inorg. Chem.* **1993**, *32*, 5779–5784.

177. Constable, E. C.; Steel, P. J. *Coord. Chem. Rev.* **1989**, *93*, 205–223.

178. Thummel, R. P.; Lefoulon, F.; Cantu, D.; Mahadevan, R. *J. Org. Chem.* **1984**, *49*, 2208–2212.

179. Rebek, J.; Trend, J. E.; Wattley, R. V.; Chakravorti, S. *J. Am. Chem. Soc.* **1979**, *101*, 4333–4337.

180. Thummel, R. P.; Kohli, D. K. *J. Org. Chem.* **1977**, *42*, 2742–2747.

181. Thummel R. P.; Lefoulon, F. *Inorg. Chem.* **1987**, *26*, 675–680.

182. Scott, S. M.; Burrell, A. K.; Cocks, P. A.; Gordon, K. C. *J. Chem. Soc., Dalton, Trans.* **1998**, 3679–3684.

183. Zong, R.; Naud, F.; Segal, C.; Burke, J.; Wu, F.; Thummel, R. *Inorg. Chem.* **2004**, *43*, 6195–6202.

184. Mayer, J. M.; Rhile, I. J.; Larsen, F. B.; Mader, E. A.; Markle, T. F.; DiPasquale, A. G. *Photosynth. Res.* **2006**, *87*, 3–20.

185. (a) Polyansky, D. E.; Cabelli, D.; Muckerman, J. T.; Fukushima, T.; Tanaka, K.; Fujita, E. *Inorg. Chem.* **2008**, *47*, 3958–3968. (b) Polyansky, D.; Cabelli, D.; Muckerman, J. T.; Fujita, E.; Koizumi, T.; Fukushima, T.; Wada, T.; Koji Tanaka, K. *Angew. Chem. Int. Ed.* **2007**, *46*, 4169–4172. (c) Cohen, B. W.; Polyansky, D. E.; Zong, R.; Zhou, H.; Ouk, T.; Cabelli, D. E.; Thummel, R. P.; Fujita, E. *Inorg. Chem.* **2010**, *49*, 8034–8044.

186. Belser, P.; von Zelewsky, A. *Helv. Chim. Acta* **1980**, *63*, 1675–1702.

187. Juris, A.; Balzani, V.; Belser, P.; von Zelewsky, A. *Helv. Chim. Acta* **1981**, *64*, 2175–2182.

188. Thummel, R. P.; Decloitre, Y. *Inorg. Chim. Acta* **1987**, *128*, 245–249.

189. Thummel, R. P.; Lefoulon, F.; Mahadevan, R. *J. Org. Chem.* **1985**, *50*, 3824–3828.

190. Koizumi, T.; Tanaka, K. *Angew. Chem. Int. Ed.* **2005**, *44*, 5891–5894.

191. Meth-Cohen, O.; Narine, B.; Tarnowski, B. *J. Chem. Soc., Perkin Trans. 1* **1981**, 1520–1530.

192. (a) Cohen, B. W.; Polyansky, D. E.; Zong, R.; Zhou, H.; Ouk,T.; Cabelli, D. E.; Thummel, R. P.; Fujita, E. *Inorg. Chem.* **2010**, *49*, 8034–8044. (b) Kóródi, F. *Synth. Commun*. **1991**, *21*, 1841–1846.

193. Stoessel, S. J.; Elliott, C. M.; Stille, J. K. *Chem. Mater.* **1989**, *1*, 259–268.

194. Suen, H. F.; Wilson, S. W.; Pomerantz, M.; Walsh, J. L. *Inorg. Chem.* **1989**, *28*, 786–791.

195. Spek, A. L.; Gerli, A.; Reedijk, J. *Acta Crystallogr.* **1994**, *C50*, 394–397.

196. Sullivan, B. P.; Salmon, D. J.; Meyer, T. J. *Inorg. Chem.* **1978**, *17*, 3334–3341.

197. Klassen, D. M. *Inorg. Chem.* **1976**, *15*, 3166–3168.

198. Anet, F. A. L.; Yavari, I. *J. Am. Chem. Soc.* **1978**, *100*, 7814–7819.

199. Sandström, J. *Dynamic NMR spectroscopy*; Academic Press: London, 1982.

200. Allerhand, A.; Gutowsky, H. S.; Jonas, J.; Meinzer, R. A. *J. Am. Chem. Soc.* **1966**, *88*, 3185–3194.

201. Anderson, S.; Seddon, K. R.; Wright, R. D.; Cocks, A. T. *Chem. Phys. Lett.* **1980**, *71*, 220–223.

202. Seddon, E. A.; Seddon, K. A. *The Chemistry of Ruthenium*; Elsevier: New York, 1984; Chapter 15.

203. Tseng, H. W.; Zong, R.; Muckerman, J. T.; Thummel R. *Inorg. Chem.* **2008**, *47*, 11763–11773.

204. (a) Hurst, J. K. *Coord. Chem. Rev.* **2005**, *249*, 313–328. (b) Francàs, L.; Sala, X.; Escudero-Adán, E.; Benet-Buchholz, J.; Escriche, L.; Llobet, A. *Inorg. Chem.* **2011**, *50*, 2771–2781.

205. Zong, R.; Zhou, H.; Thummel, R. P. *J. Org. Chem.* **2008**, *73*, 4334–4337.

206. Thummel, R. P.; Hegde, V.; Jahng, Y. *Inorg. Chem.* **1989**, *28*, 3264–3267.

207. Eggleston, M. K.; McMillin, D. R.; Koenig, K. S.; Pallenburg, A. J. *Inorg. Chem.* **1997**, *36*, 172–176.

208. Miller, M. T.; Gantzel, P. K.; Karpishin, T. B. *Inorg. Chem.* **1999**, *38*, 3414–3422.

209. Riesgo, E. C.; Hu, Y. Z.; Bouvier, F.; Thummel, R. P.; Scaltrito, D. V.; Meyer, G. J. *Inorg. Chem.* **2001**, *40*, 3413–3422.

210. Evans, I. P.; Spencer , A. Wilkinson G. *J. Chem. Soc., Dalton Trans.* **1973**, 204–209.

211. Ware, D. C.; Lay, P. A.; Taube, H.; Chou, M. H.; Creutz, C. *Inorg. Syn.* **1986**, *24*, 299–306.

212. Silva, D. O.; Toma, H. E. *Can. J. Chem.* **1994**, *72*, 1705–1708.

213. Matsumura-Inoue, T.; Tanabe, M.; Minami, T.; Ohashi, T. *Chem. Lett.* **1994**, *23*, 2443–2446.

214. Campos-Fernández, C. S.; Thomson, L. M.; Galán-Mascarós, J. R.; Ouyang, X.; Dunbar, K. R. *Inorg. Chem.* **2002**, *41*, 1523–1533.

215. Craig, C. L. *J. Am. Chem. Soc.* **1934**, *56*, 231–232.

216. Ghaffarzadeh, M.; Bolourtchian, M.; Halvagar, M. R.; Hosseini, M. *J. Chem. Res., Synop*. **2003**, 814–815.

217. Nickita, N.; Gasser, G.; Pearson, P.; Belousoff, M. J.; Goh, L. Y.; Bond, A. M.; Deacon, G. B.; Spiccia, L. *Inorg. Chem.* **2009**, *48*, 68–81.

218. Strotmeyera, K. P.; Fritsky I. O.; Otta, R.; Pritzkowa, H.; Krämer, R. *Supramol. Chem.* **2003**, *15*, 529–547.

219. Cui, Y.; Tang, X.B.; Shao, C. X.; Li, J.T.; Sun, W. H. *Chin. J. Chem*. **2005**, *23*, 589–595.

220. Nazeeruddin, Md. K.; Kalyanasundaram, K.; Grätzel, M. *Inorg. Synth*. **1997**, *32*, 181–186.

221. Turner, J., A. *J. Org. Chem.* **1983**, *48*, 3401–3408.

222. Hewawasam, P.; Meanwell, N. A. *Tetrahedron Lett.* **1994**, *35*, 7303–7306.

223. Fontana, F.; Minisci, F.; Nogueira Barbosa, M., C.; Vismara, E. *J. Org. Chem.* **1991**, *56*, 2866–2869.

224. Nyerges, M.; Pintér, Á.; Virányi, A.; Blaskó, G.; Tőke, L. *Tetrahedron* **2005**, *61*, 8199–8205.

225. Godard, A; Queguiner, G. *J. Heterocyclic Chem.* **1980**, *17*, 465–473.

226. Vander Haar, R. W.; Voter, R. C.; Banks, C. V. *J. Org. Chem.* **1949**, *14*, 836–838.

227. Sun, W. H.; Jie, S.; Zhang, S.; Zhang, W.; Song, Y.; Ma H. *Organometallics* **2006**, *25*, 666–677.